

# ADVANCED STEEL CONSTRUCTION

*An International Journal*

Volume 9 Number 4

December 2013

## CONTENTS

### Technical Papers

Inelastic Stability Analysis for Framed Structures Subjected to Nonconservative Forces  
*Nam-Il Kim and Dong-Ho Choi*

Modified One Zone Model for Fire Resistance Design of Steel Structures  
*Chao Zhang and Guo-qiang Li*

Temperature Distribution and Structural Behavior of Box-Sectional Arch Structures under Solar Radiation  
*Hongbo Liu, Zhihua Chen and Ting Zhou*

Experimental and Numerical Study on Mechanical Behavior of Composite Girders under Hogging Moment  
*Weiwei Lin and Teruhiko Yoda*

Design Motivation, Mechanical Modeling, and Nonlinear Analysis for Composite PR Moment Frames with Smart SMA Connection Systems  
*Jong Wan Hu*

Design of Steel and Composite Open Car Parks under Fire  
*Cécile Haremza, Aldina Santiago and Luís Simões da Silva*

Research on a New Double-Wall Steel Insulation Silo with Multiple Bolted Joints: Part I, Structure System  
*Lingfeng Yin, Gan Tang, Xiaoming Guo and Haibin Lai*

Research on a New Double-Wall Steel Insulation Silo with Multiple Bolted Joints: Part II, Experimental Verification  
*Gan Tang, Lingfeng Yin, Xiaoming Guo and Haibin Lai*

Copyright © 2013 by :

The Hong Kong Institute of Steel Construction

Website: <http://www.hkisc.org>

ISSN 1816-112X

Science Citation Index Expanded, Materials Science Citation Index and ISI Alerting

Cover: The Tamar Headquarters of Hong Kong SAR Government

*Top five floors spanning over the two mega cores are made of composite trusses with concrete infilled rectangular sections and designed by second-order direct analysis*

ADVANCED STEEL CONSTRUCTION

VOL.9, NO.4 (2013)

# ADVANCED STEEL CONSTRUCTION

*an International Journal*

ISSN 1816-112X

Volume 9 Number 4

December 2013



### Editors-in-Chief

**S.L. Chan**, The Hong Kong Polytechnic University, Hong Kong

**W.F. Chen**, University of Hawaii at Manoa, USA

**R. Zandonini**, Trento University, Italy



ISSN 1816-112X

Science Citation Index Expanded,  
Materials Science Citation Index  
and ISI Alerting

#### EDITORS-IN-CHIEF

**Asian Pacific, African  
and organizing Editor**  
S.L. Chan  
*The Hong Kong Polyt. Univ.,  
Hong Kong*

**American Editor**  
W.F. Chen  
*Univ. of Hawaii at Manoa, USA*

**European Editor**  
R. Zandonini  
*Trento Univ., Italy*

#### INTERNATIONAL EDITORIAL BOARD

F.G. Albermani  
*The Univ. of Queensland, Australia*

I. Burgess  
*Univ. of Sheffield, UK*

F.S.K. Bijlaard  
*Delft Univ. of Technology, The Netherlands*

R. Bjorhovde  
*The Bjorhovde Group, USA*

M.A. Bradford  
*The Univ. of New South Wales, Australia*

D. Camotim  
*Technical Univ. of Lisbon, Portugal*

C.M. Chan  
*Hong Kong Univ. of Science & Technology, Hong Kong*

T.H.T. Chan  
*Queensland Univ. of Technology, Australia*

S.P. Chiew  
*Nanyang Technological Univ., Singapore*

W.K. Chow  
*The Hong Kong Polyt. Univ., Hong Kong*

K.F. Chung  
*The Hong Kong Polyt. Univ., Hong Kong*

G.G. Deierlein  
*Stanford Univ., California, USA*

L. Dezi  
*Univ. of Ancona, Italy*

D. Dubina  
*The Politehnica Univ. of Timisoara, Romania*

R. Greiner  
*Technical Univ. of Graz, Austria*

L. Gardner  
*Imperial College of Science, Technology and Medicine, UK*

L.H. Han  
*Tsinghua Univ. China*

S. Herion  
*University of Karlsruhe, Germany*

G.W.M. Ho  
*Ove Arup & Partners Hong Kong Ltd., Hong Kong*

B.A. Izzuddin  
*Imperial College of Science, Technology and  
Medicine, UK*

J.P. Jaspart  
*Univ. of Liege, Belgium*

S. A. Jayachandran  
*IIT Madras, Chennai, India*

S.E. Kim  
*Sejong Univ., South Korea*

S. Kitipornchai  
*The Univ., of Queensland, Australia*

D. Lam  
*Univ. of Bradford, UK*

G.Q. Li  
*Tongji Univ., China*

J.Y.R. Liew  
*National Univ. of Singapore, Singapore*

E.M. Lui  
*Syracuse Univ., USA*

Y.L. Mo  
*Univ. of Houston, USA*

J.P. Muzeau  
*CUST, Clermont Ferrand, France*

D.A. Nethercot  
*Imperial College of Science, Technology and  
Medicine, UK*

Y.Q. Ni  
*The Hong Kong Polyt. Univ., Hong Kong*

D.J. Oehlers  
*The Univ. of Adelaide, Australia*

J.L. Peng  
*Yunlin Uni. of Science & Technology, Taiwan*

K. Rasmussen  
*The Univ. of Sydney, Australia*

J.M. Rotter  
*The Univ. of Edinburgh, UK*

C. Scawthorn  
*Scawthorn Porter Associates, USA*

P. Schaumann  
*Univ. of Hannover, Germany*

G.P. Shu  
*Southeast Univ. China*

L. Simões da Silva  
*Department of Civil Engineering, University of  
Coimbra, Portugal*

J.G. Teng  
*The Hong Kong Polyt. Univ., Hong Kong*

G.S. Tong  
*Zhejiang Univ., China*

K.C. Tsai  
*National Taiwan Univ., Taiwan*

C.M. Uang  
*Univ. of California, USA*

B. Uy  
*University of Western Sydney, Australia*

M. Veljkovic  
*Univ. of Lulea, Sweden*

F. Wald  
*Czech Technical Univ. in Prague, Czech*

Y.C. Wang  
*The Univ. of Manchester, UK*

Y.L. Xu  
*The Hong Kong Polyt. Univ., Hong Kong*

D. White  
*Georgia Institute of Technology, USA*

E. Yamaguchi  
*Kyushu Institute of Technology, Japan*

Y.B. Yang  
*National Taiwan Univ., Taiwan*

Y.Y. Yang  
*China Academy of Building Research, Beijing, China*

B. Young  
*The Univ. of Hong Kong, Hong Kong*

X.L. Zhao  
*Monash Univ., Australia*

Z.H. Zhou  
*Alpha Consultant Ltd., Hong Kong*

Cover: The Tamar Headquarters of Hong Kong SAR Government

Top five floors spanning over the two mega cores are made of composite trusses with concrete infilled rectangular sections and designed by second-order direct analysis

## General Information

### *Advanced Steel Construction, an international journal*

#### **Aims and scope**

The International Journal of Advanced Steel Construction provides a platform for the publication and rapid dissemination of original and up-to-date research and technological developments in steel construction, design and analysis. Scope of research papers published in this journal includes but is not limited to theoretical and experimental research on elements, assemblages, systems, material, design philosophy and codification, standards, fabrication, projects of innovative nature and computer techniques. The journal is specifically tailored to channel the exchange of technological know-how between researchers and practitioners. Contributions from all aspects related to the recent developments of advanced steel construction are welcome.

#### **Instructions to authors**

**Submission of the manuscript.** Authors may submit double-spaced manuscripts preferably in MS Word by emailing to one of the chief editors as follows for arrangement of review. Alternatively papers can be submitted on a diskette to one of the chief editors.

Asian Pacific, African and organizing editor: Professor S.L. Chan, Email: [ceslchan@polyu.edu.hk](mailto:ceslchan@polyu.edu.hk)  
American editor: Professor W.F. Chen, Email: [waifah@hawaii.edu](mailto:waifah@hawaii.edu)  
European editor: Professor R. Zandonini, Email: [riccardo\\_zandonini@ing.unitn.it](mailto:riccardo_zandonini@ing.unitn.it)

All manuscripts submitted to the journal are recommended to accompany with a list of four potential reviewers suggested by the author(s). This list should include the complete name, address, telephone and fax numbers, email address, and at least five keywords that identify the expertise of each reviewer. This scheme will improve the process of review.

#### **Style of manuscript**

**General.** Author(s) should provide full postal and email addresses and fax number for correspondence. The manuscript including abstract, keywords, references, figures and tables should be in English with pages numbered and typed with double line spacing on single side of A4 or letter-sized paper. The front page of the article should contain:

- a) a short title (reflecting the content of the paper);
- b) all the name(s) and postal and email addresses of author(s) specifying the author to whom correspondence and proofs should be sent;
- c) an abstract of 100-200 words; and
- d) 5 to 8 keywords.

The paper must contain an introduction and a conclusion. The length of paper should not exceed 25 journal pages (approximately 15,000 words equivalents).

**Tables and figures.** Tables and figures including photographs should be typed, numbered consecutively in Arabic numerals and with short titles. They should be referred in the text as Figure 1, Table 2, etc. Originally drawn figures and photographs should be provided in a form suitable for photographic reproduction and reduction in the journal.

**Mathematical expressions and units.** The Systeme Internationale (SI) should be followed whenever possible. The numbers identifying the displayed mathematical expression should be referred to in the text as Eq. (1), Eq. (2).

**References.** References to published literature should be referred in the text, in the order of citation with Arabic numerals, by the last name(s) of the author(s) (e.g. Zandonini and Zanon [3]) or if more than three authors (e.g. Zandonini et al. [4]). References should be in English with occasional allowance of 1-2 exceptional references in local languages and reflect the current state-of-technology. Journal titles should be abbreviated in the style of the Word List of Scientific Periodicals. References should be cited in the following style [1, 2, 3].

Journal: [1] Chen, W.F. and Kishi, N., "Semi-rigid Steel Beam-to-column Connections, Data Base and Modelling", Journal of Structural Engineering, ASCE, 1989, Vol. 115, No. 1, pp. 105-119.

Book: [2] Chan, S.L. and Chui, P.P.T., "Non-linear Static and Cyclic Analysis of Semi-rigid Steel Frames", Elsevier Science, 2000.

Proceedings: [3] Zandonini, R. and Zanon, P., "Experimental Analysis of Steel Beams with Semi-rigid Joints", Proceedings of International Conference on Advances in Steel Structures, Hong Kong, 1996, Vol. 1, pp. 356-364.

**Proofs.** Proof will be sent to the corresponding author to correct any typesetting errors. Alternations to the original manuscript at this stage will not be accepted. Proofs should be returned within 48 hours of receipt by Express Mail, Fax or Email.

**Copyright.** Submission of an article to "Advanced Steel Construction" implies that it presents the original and unpublished work, and not under consideration for publication nor published elsewhere. On acceptance of a manuscript submitted, the copyright thereof is transferred to the publisher by the Transfer of Copyright Agreement and upon the acceptance of publication for the papers, the corresponding author must sign the form for Transfer of Copyright.

**Permission.** Quoting from this journal is granted provided that the customary acknowledgement is given to the source.

**Page charge and Reprints.** There will be no page charges if the length of paper is within the limit of 25 journal pages. A total of 30 free offprints will be supplied free of charge to the corresponding author. Purchasing orders for additional offprints can be made on order forms which will be sent to the authors. These instructions can be obtained at the Hong Kong Institute of Steel Construction, Journal website: <http://www.hkisc.org>

The International Journal of Advanced Steel Construction is published quarterly by non-profit making learnt society, The Hong Kong Institute of Steel Construction, c/o Department of Civil & Structural Engineering, The Hong Kong Polytechnic University, Hung Hom, Kowloon, Hong Kong.

**Disclaimer.** No responsibility is assumed for any injury and / or damage to persons or property as a matter of products liability, negligence or otherwise, or from any use or operation of any methods, products, instructions or ideas contained in the material herein.

**Subscription inquiries and change of address.** Address all subscription inquiries and correspondence to Member Records, IJASC. Notify an address change as soon as possible. All communications should include both old and new addresses with zip codes and be accompanied by a mailing label from a recent issue. Allow six weeks for all changes to become effective.

#### **The Hong Kong Institute of Steel Construction**

HKISC

c/o Department of Civil and Environmental Engineering,

The Hong Kong Polytechnic University,

Hunghom, Kowloon, Hong Kong, China.

Tel: 852- 2766 6047 Fax: 852- 2334 6389

Email: [ceslchan@polyu.edu.hk](mailto:ceslchan@polyu.edu.hk) Website: <http://www.hkisc.org/>

ISSN 1816-112X

Science Citation Index Expanded, Materials Science Citation Index and ISI Alerting

Copyright © 2013 by:

The Hong Kong Institute of Steel Construction.



ISSN 1816-112X

Science Citation Index Expanded,  
Materials Science Citation Index and  
ISI Alerting

## EDITORS-IN-CHIEF

### Asian Pacific, African and organizing Editor

S.L. Chan

*The Hong Kong Polyt. Univ.,  
Hong Kong*

Email: [ceslchan@polyu.edu.hk](mailto:ceslchan@polyu.edu.hk)

### American Editor

W.F. Chen

*Univ. of Hawaii at Manoa, USA*

Email: [waifah@hawaii.edu](mailto:waifah@hawaii.edu)

### European Editor

R. Zandonini

*Trento Univ., Italy*

Email: [riccardo.zandonini@ing.unitn.it](mailto:riccardo.zandonini@ing.unitn.it)

# Advanced Steel Construction

*an international journal*

VOLUME 9 NUMBER 4

DECEMBER 2013

## Technical Papers

- |   |     |
|---|-----|
| Inelastic Stability Analysis for Framed Structures Subjected to Nonconservative Forces<br><i>Nam-Il Kim, Dong-Ho Choi</i>   | 259 |
| Modified One Zone Model for Fire Resistance Design of Steel Structures<br><i>Chao Zhang and Guo-qiang Li</i>  | 282 |
| Temperature Distribution and Structural Behavior of Box-Sectional Arch Structures under Solar Radiation<br><i>Hongbo Liu, Zhihua Chen and Ting Zhou</i>                           | 298 |
| Experimental and Numerical Study on Mechanical Behavior of Composite Girders under Hogging Moment<br><i>Weiwei Lin and Teruhiko Yoda</i>  | 309 |
| Design Motivation, Mechanical Modeling, and Nonlinear Analysis for Composite PR Moment Frames with Smart SMA Connection Systems<br><i>Jong Wan Hu</i>                             | 334 |
| Design of Steel and Composite Open Car Parks under Fire<br><i>Cécile Haremza, Aldina Santiago and Luís Simões da Silva</i>  | 350 |
| Research on a New Double-Wall Steel Insulation Silo with Multiple Bolted Joints: Part I, Structure System<br><i>Lingfeng Yin, Gan Tang, Xiaoming Guo and Haibin Lai</i>           | 369 |
| Research on a New Double-Wall Steel Insulation Silo with Multiple Bolted Joints: Part II, Experimental Verification<br><i>Gan Tang, Lingfeng Yin, Xiaoming Guo and Haibin Lai</i> | 383 |



# INELASTIC STABILITY ANALYSIS FOR FRAMED STRUCTURES SUBJECTED TO NONCONSERVATIVE FORCES

Nam-Il Kim<sup>1</sup> and Dong-Ho Choi<sup>2\*</sup>

<sup>1</sup>*Department of Architectural Engineering, Sejong University,  
98 Kunja Dong, Kwangjin Ku, Seoul 143-747, S. Korea*

<sup>2</sup>*Department of Civil and Environmental Engineering, Hanyang University,  
17 Haengdang-dong, Seoungdong-gu, Seoul, 133-791, South Korea*

*\*(Corresponding author: E-mail: samga@hanyang.ac.kr)*

*Received: 5 November 2011; Revised: 1 June 2012; Accepted: 8 June 2012*

---

**ABSTRACT:** In this study, the inelastic system buckling analysis is developed to evaluate the buckling loads and the effective length factors for columns in steel frames subjected to nonconservative forces. For this purpose, the finite element model for the nonconservative system is presented based on an extended Hamilton principle. The traditional elastic and inelastic stability analyses are briefly introduced for the conservative systems. Then evaluation procedure for the critical value of buckling load and its corresponding effective length factor for the nonconservative system are proposed based on the inelastic system buckling approach. In numerical examples, the buckling loads and the effective length factors for the inelastic conservative or nonconservative steel frames are evaluated and compared with results by other researchers. Particularly, the effects of various parameters such as the nonconservativeness parameter, the stiffness and span ratios of beam to column of frames on the inelastic stability behavior of nonconservative systems are newly addressed.

**Keywords:** Effective length factor, Inelastic column, Nonconservative force, Finite element method

---

## 1. INTRODUCTION

For decades, many researchers have explored various approaches for assessing column and frame stability in the design of steel structures. Among these approaches, the stability design method based on the effective length factor ( $K$ -factor) was quite a common practice to engineers for many years.

Up to the present, various methods have been reported for the evaluation of  $K$ -factor and the most widely accepted method is the alignment chart method that was proposed by Julian and Lawrence [1]. And now, various design codes such as AISC [2], ACI [3], and AASHTO [4] adopt this method. The isolated subassembly approach, as an alternative method, has also been applied extensively following the early works of Galambos [5] and adopted in specifications such as DIN 18800 [6] and Eurocode 3 [7]. These alignment chart method and isolated subassembly approach are the traditional methods used to assess the rotational end restraints of the isolated column, which represent the stiffness ratio between the column and the beam. However in spite of its popularity, these approaches have major drawback in that they do not properly reflect the interaction effects of neighboring members except for the very closely adjacent columns and beams. Since these approaches are based on several fundamental assumptions, which basically limit the use of these methods only for the idealized cases, they may lead to inadequate estimation of the  $K$ -factor when these assumptions are not satisfied. To overcome this drawback, many studies have been carried out. Duan and Chen [8, 9] evaluated the  $K$ -factor of the three-story subassemblage of the frame using the same assumptions as the traditional effective length method, but considering the true boundary conditions at far ends of the top and bottom columns. The story-interaction of columns in no-sway frames was studied by Bridge and Fraser [10] and they extended the nomograph for effective lengths of non-sway buckling to a range where the rotational spring had a negative rigidity and proposed an iterative approach to calculate this interaction. Mahini and Seyyedien [11] presented a new iterative approach with a high convergence

rate to improve the effectiveness of the  $G$ -factor method developed by Bridge and Fraser [10]. They replaced the explicit forms of the stability functions by more simple rational forms using the curve-fitting principles and converted members with the non-hinged far-end condition to the equivalent hinged far-end ones, considering the rotational stiffness in each case. The improved analytical expressions for  $K$ -factors of columns in multi-story sway frames were also proposed by Gantes and Mageirou [12]. They considered all possible rotational and translational boundary conditions at the far end of these members, as well as the eventual presence of axial force.

Another improved approach to evaluate the  $K$ -factor is the so called “story-based approach” which accounts for the horizontal interaction between columns in a story. In the Commentary of the AISC [2], two methods of determining the story-based  $K$ -factor, namely the story buckling method [13] and the story stiffness method [14,15], were presented. LeMessurier [14,15] provided comprehensive discussion for story stability behavior and proposed a practical approach for obtaining  $K$ -factors to consider the story stability behavior. Also the in-plane buckling characteristics of the unbraced frames under the non-proportional loading adopting the story-based buckling concept were investigated by Xu *et al.* [16]. To get over the difficulty associated with the non-proportional loading, the problem of the lateral buckling of unbraced frames was expressed as a minimization problem subjected to stability constraints. Liu and Xu [17] presented a practical method for evaluating  $K$ -factors for columns in multi-story unbraced frames based on the story-based buckling concept, which decomposes a multi-story frame into a series of single-story partially-restrained frames.

The stability of the column in the frame structures, although often expressed as a stability problem restricted to an individual column, can be regarded as a problem in related with the whole stability of the structures by considering interactions between all members. Thus the column design is a system-related problem, not an individual member-restricted problem. Özmen and Girgin [18] developed the method for determining  $K$ -factors of columns in multi-story frames based on computing on approximate values for system buckling load by using the results of a fictitious lateral loading. Girgin *et al.* [19] applied their previous method [18] to irregular frames and obtained good results with errors less than 5% for all examples considered. Geschwindner [20] reviewed a wide range of analytical approaches including the elastic system buckling analysis and Roddis *et al.* [21] pointed out the practical limitations of the alignment chart method using the elastic system buckling analysis. Despite significant achievements, all of these studies were devoted only to the elastic stability of the overall frame systems and did not consider the inelastic effects of columns.

To account for the effects of inelastic behavior on evaluation of  $K$ -factor, several researchers have studied the inelastic stability design of steel structures. Yura [13] proposed an iterative procedure to determine the  $K$ -factor in the inelastic range of column behavior. Choi *et al.* [22] presented the numerical method determining the inelastic effective length of each member in three-dimensional steel frames based on iterative schemes and the stiffness reduction factors considering a fictitious axial force factor. Kim and Lee [23] investigated the influence of the  $P$ - $\Delta$  effect on the behavior of middle-rise unbraced steel frames using the refined plastic hinge method with an arc length algorithm. Essa [24] developed a design approach, to predict  $K$ -factors for columns in unbraced frames, considering the inelastic behavior, semi-rigid connections, far-end conditions, and differentiated stiffness parameters of the connected columns. He used a slope-deflection equation with the column stiffness reduction factors, which were evaluated from the column-strength curve proposed by the Structural Stability Research Council (SSRC) [25]. In AISC [2], inelastic  $K$ -factors are determined from the alignment chart method with the stiffness reduction factor applied to elastic modulus in the equation for  $G$ -factor. Depending on how the stiffness reduction factors are calculated, they might account for both the reduction in the stiffness of columns due to geometric imperfections and the spread of plasticity due to residual stresses under high compression loading. However, these studies

were based on the alignment chart method, which adopted several simplifying assumptions and restricted to the stability analysis of frames under the conservative forces.

The nonconservative forces are forces whose line of action is affected by the deformation of the system on which they act and some examples of the nonconservative systems are the frame structures, the members of bridges, and aircraft which are subjected to aerodynamic force. The submarines and ships are also subjected to hydrodynamic forces which are nonconservative. The nonconservative forces are present in basically every engineering field such as civil engineering and bioengineering (spinal chord) among others and considerable attention has been devoted to the stability of columns subjected to these nonconservative forces. The first review of this branch of applied mechanics has been made in a book form by Bolotin [26]. Gasparini *et al.* [27] discussed the transition between the stability and instability of a cantilevered beam subjected to the partially follower force. Ryu *et al.* [28] employed the finite element method to perform the numerical analyses on the stability of a cantilevered column subjected to the triangularly distributed subtangential forces. Wang [29] studied the effect of the follower force on the buckling capacities of the beam structure subjected to the concentrated follower force. Imielowski [30] performed the sensitivity analysis of a stepped column under the subtangential force depending on the nonconservativeness parameter and investigated the influence of joint stiffness, variation of segment cross-sections and their length. But these works only dealt with the elastic stability problems of a single column under the nonconservative forces. Lee *et al.* [31] investigated the dynamic stability behavior of the Beck's column resting on elastic foundation by using the finite element method.

From the previously cited references, it can be noted that even though a significant amount of research has been extensively conducted on the evaluation of  $K$ -factor for the stability design of frames, there still has been no study reported on the elastic or inelastic instability analyses of steel frames subjected to nonconservative forces. The main purpose of this study is to present a more reliable procedure to determine  $K$ -factors of columns in steel frames subjected to nonconservative forces based on the elastic and inelastic system buckling analyses by using the column strength curves. The important points considered in this study are summarized as follows:

1. Based on the extended Hamilton principle, the finite element model is formulated. For this, the generalized displacements are expressed over each element as a linear combination of the one-dimensional Lagrange interpolation function for the axial displacement and the cubic Hermite interpolation function for the lateral displacement.
2. Traditional elastic and inelastic stability analyses such as the isolated subassembly approach and the story-based one are briefly presented for the conservative systems.
3. Inelastic system buckling analysis procedure using the AISC-LRFD and Eurocode 3 column strength curves under nonconservative forces is proposed based on a nonlinear eigenvalue analysis algorithm.
4. To illustrate the accuracy and the effectiveness of the proposed method from numerical examples, buckling loads or  $K$ -factors of steel columns in frame structures subjected to the conservative or nonconservative forces are evaluated and compared with those by available references.
5. Especially, emphasis is given in showing the effects of the nonconservativeness parameter, the stiffness and span ratios of beam to column on buckling loads.  $K$ -factors are also investigated for the inelastic nonconservative systems.

## 2. FINITE ELEMENT MODEL FOR NONCONSERVATIVE SYSTEM

Figure 1 shows the cantilevered column of the length  $L$  subjected to the combined conservative force  $P_c$  and the tangential follower force  $P_t$  acting at the tip. The former may be thought of as a dead load, while the latter can be considered as a typical follower force and the two forces  $P_c$  and  $P_t$  are assumed to be constant along the elastic line. For a small deflection, the angle between the  $x$ -axis and the tangent to the elastic line of column can be approximated by  $\partial v / \partial x$  where  $v$  is the lateral displacement. The direction of the resultant subtangential force  $P$  is specified by  $\alpha \partial v(L) / \partial x$ . Thus the parameter  $\alpha$  can also be referred to as the nonconservativeness parameter and one can easily derive the following relation.

$$\mathbf{P} = \mathbf{P}_c + \mathbf{P}_t, \quad \alpha = \frac{P_t}{P} \quad (1)$$

Note that the force is conservative for  $\alpha=0$ , while it is nonconservative for  $\alpha \neq 0$  and is a purely tangential follower force for  $\alpha=1$ .

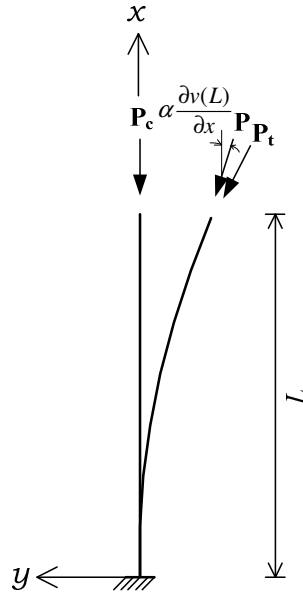


Figure 1. Column subjected to the Nonconservative Force

In order to present the finite element formulation of the element with the length  $l_e$ , three nodal displacements at nodal end points  $p$  and  $q$  ( $u^p, v^p, \theta^p; u^q, v^q, \theta^q$ ) are considered in which  $u$ ,  $v$  and  $\theta$  are the axial displacement, the lateral displacement, and the angle of rotation, respectively. In this study, the strain energy  $\Pi_E$  of the system, the potential energy  $\Pi_G$  including the work done by the conservative component of the subtangential force and the virtual work  $\delta \Pi_{NC}$  by the nonconservative component of the acting force are considered. Here the type of instability is only divergence and the critical flutter load from the dynamic criterion is not considered. These terms are expressed as follows:

$$\Pi_E = \sum_e \frac{1}{2} \int_0^{l_e} \left\{ E_t A \left( \frac{\partial u}{\partial x} \right)^2 + E_t I \left( \frac{\partial^2 v}{\partial x^2} \right)^2 \right\} dx \quad (2a)$$

$$\Pi_G = -\sum_e \frac{1}{2} \int_0^{l_e} P \left( \frac{\partial v}{\partial x} \right)^2 dx \quad (2b)$$

$$\delta \Pi_{NC} = -\alpha P \frac{\partial v(L)}{\partial x} \delta v(L) \quad (2c)$$

where  $E_t$  is the tangent modulus;  $A$  and  $I$  are the cross-sectional area and the second moment of inertia, respectively;  $\delta$  is the variation. The extended Hamilton principle of the column can be presented by

$$\int_{t_1}^{t_2} [\delta(\Pi_E + \Pi_G) - \delta \Pi_{NC}] dt = 0 \quad (3)$$

The present column theory is implemented via a displacement-based finite element method. For this, the generalized displacements are expressed over each element as an one-dimensional Lagrange interpolation function for the axial displacement  $u$  and the third-order Hermitian interpolation function for the lateral displacement  $v$ . By substituting the interpolated displacements into Eq. 3, the resulting equation for a single element is obtained in a matrix form as

$$\int_{t_1}^{t_2} [\delta \mathbf{U}_e (\mathbf{K}_e + \mathbf{K}_g - \mathbf{K}_{nc}) \mathbf{U}_e - \delta \mathbf{U}_e \mathbf{F}_e] dt = 0 \quad (4)$$

where  $\mathbf{U}_e$  and  $\mathbf{F}_e$  are the nodal displacement and force vectors, respectively;  $\mathbf{K}_e$  and  $\mathbf{K}_g$  are the elastic stiffness matrix and the geometric stiffness matrix due to conservative compressive forces, respectively;  $\mathbf{K}_{nc}$  is the load correction stiffness matrix due to the directional change of nonconservative forces.

Finally, the equilibrium equation for whole column members is expressed in a matrix form using the direct stiffness method as follows:

$$(\mathbf{K}_E + \mathbf{K}_G - \mathbf{K}_{NC}) \mathbf{U} = \mathbf{F} \quad (5)$$

where  $\mathbf{K}_E$ ,  $\mathbf{K}_G$ , and  $\mathbf{K}_{NC}$  are respectively the elastic and geometric stiffness matrices, and the load correction stiffness matrix due to the nonconservative forces in the global coordinate system.

### 3. TRADITIONAL ELASTIC AND INELASTIC STABILITY APPROACHES

A wide range of methods have been suggested in the engineering literature for the design calculation of column buckling loads and their corresponding  $K$ -factors. This section outlines the broad categories of the traditional elastic and inelastic stability approaches based on the physical extent of the structure under the conservative forces.

#### 3.1 Isolated Subassembly Approach

The effective length of an end-restrained column is defined as the length of an equivalent pinned-ended column that will give the same critical load as the end-restrained column. This effective length can be visualized as the distance between the two inflection points (real and imaginary) of the buckled shape of the end-restrained member. The most widely used method for evaluating  $K$ -factor is probably the isolated subassembly approach, also commonly referred to as the alignment chart method or the  $G$ -factor method since it offers a straightforward method of obtaining  $K$  of the column.

The transcendental equations of the buckling solution of the subassembly for the sideway inhibited and uninhibited frames subjected to conservative compressive forces are given in Eq. 6 and the detailed step-by-step derivation of equations governing the buckling of this assembly is presented by Chen and Lui [32] based on the slope deflection equations.

$$\frac{G_A G_B}{4} \left( \frac{\pi}{K} \right)^2 + \left( \frac{G_A + G_B}{2} \right) \left( 1 - \frac{\pi / K}{\tan(\pi / K)} \right) + \frac{2 \tan(\pi / 2K)}{\pi / K} - 1 = 0 \quad (6a)$$

$$\frac{G_A G_B (\pi / K)^2 - 36}{6(G_A + G_B)} - \frac{\pi / K}{\tan(\pi / K)} = 0 \quad (6b)$$

where  $G_A$  and  $G_B$  are the stiffness ratios ( $G$ -factors) of columns and beams at joints  $A$  and  $B$ , respectively, and the detailed expressions are as follows:

$$G_A = \frac{\sum_c (E_c I_c / L_c)}{\sum_b (E_b I_b / L_b)} \quad \text{and} \quad G_B = \frac{\sum_c (E_c I_c / L_c)}{\sum_b (E_b I_b / L_b)} \quad (7a,b)$$

where subscript  $c$  and  $b$  denote the column and the beam, respectively. Note that Eq. 6 may be analytically derived under several fundamental assumptions that the structure should follow in order to guarantee a reasonable result.

It is well known that the significant economy may be gained by utilizing inelastic buckling solutions in many design situations [13,15], although the column strength calculations are often based on the elastic models. This is because the slenderness of the columns in typical steel buildings is usually small enough such that the distributed yielding occurs along the column lengths before the design strength of the most critically-loaded components is reached. To reflect the inelastic effects into the design of steel frames, the elastic modulus can be lowered with the inelastic stiffness reduction factor  $\tau_a$  as follows (AISC [2]):

$$E_t = \tau_a E \quad (8)$$

where

$$\tau_a = 1.0 \quad \text{for} \quad P_n / P_y \leq 0.39 \quad (9a)$$

$$\tau_a = -2.724(P_n / P_y) \ln(P_n / P_y) \quad \text{for} \quad P_n / P_y > 0.39 \quad (9b)$$

where  $E$  is the elastic modulus;  $P_n$  and  $P_y$  are the nominal column strength and the yielding axial force, respectively. Thus the inelastic  $K$ -factor can be determined by using  $\tau_a$  times  $E_c$  for  $E_c$  in the equations for  $G_A$  and  $G_B$  in Eq. 7

### 3.2 Story-based Approach

Since the isolated subassembly approach assumes that the shear force of the column does not transfer to other columns in the same story, each of columns in any story buckles in the sidesway mode, independent of the adjacent columns. This assumption may be inadequate in some real cases, such as a structural system with leaning columns. To account for the interaction effect between the columns



in the story, the inelastic  $K$ -factor can be inferred from the elastic  $K$ -factor which the commentary of AISC [2] recommends based on the story buckling method as follows:

$$K = \sqrt{\frac{\pi^2 \tau_a EI / L^2}{P_r} \left( \frac{\sum P_r}{\sum \frac{\pi^2 \tau_a EI}{(K_{n2} L)^2}} \right)} \geq \sqrt{\frac{5}{8}} K_{n2} \quad (10)$$

where  $K_{n2}$  is defined as the  $K$  value determined directly from the alignment chart,  $P_r$  is the required axial compressive force for the rigid column, and  $\sum P_r$  is the total axial compressive force of columns in the story. The  $K$ -factor obtained from Eq. 10 inherently account for the inelastic effects and the interactions within and between stories at incipient buckling of the system subjected to conservative forces.

On the other hand, the story stiffness method considers later displacements of the story instead of the sum of the compressive force. The inelastic  $K$ -factor can be deduced from the Equation C-C2-5 in AISC [2] as follows:

$$K = \sqrt{\frac{\sum P_r}{(0.85 + 0.15 R_L) P_r} \left( \frac{\pi^2 \tau_a EI}{L^2} \right) \left( \frac{\Delta_H}{\sum HL} \right)} \geq \sqrt{\frac{\pi^2 \tau_a EI}{L^2} \left( \frac{\Delta_H}{1.7 HL} \right)} \quad (11)$$

where  $H$  and  $\Delta_H$  are respectively the shear in the column and the lateral displacement of the story under consideration.  $R_L$  is the ratio of the vertical column load for all leaning columns in the story to the vertical load of all the columns in the story expressed by

$$R_L = \frac{\sum P_r \text{ leaning columns}}{\sum P_r \text{ all columns}} \quad (12)$$

#### 4. SYSTEM BUCKLING APPROACH UNDER NONCONSERVATIVE FORCES

In this section, the elastic and inelastic system buckling approaches for calculating buckling loads and  $K$ -factors for columns in steel frames subjected to nonconservative forces are presented.

##### 4.1 Column Strength Curves for AISC-LRFD and Eurocode 3

The inelastic buckling of columns can lead to system collapse prior to the formation of a plastic hinge on beam members as external loads are increased on the steel frames. In several design specifications, the load-carrying capacity of the column member is modified based on such information as theoretical buckling analysis results, various experimental results come from initial imperfections due to manufacturing or constructional errors, residual stress due to welding, dependency on cross-sectional shape and etc.

In this study, two kinds of load-carrying capacity curves are presented for further development in inelastic buckling formulation, one from the AISC-LRFD [33] and the other from the Eurocode 3 [7]. In the development of the LRFD specification, the AISC specification uses a column strength curve as

$$f^* = 0.658\lambda^{*2} \quad \text{for } 0 \leq \lambda^* \leq 1.5 \quad (13a)$$

$$f^* = \frac{0.877}{\lambda^{*2}} \quad \text{for } \lambda^* > 1.5 \quad (13b)$$

where

$$f^* = \frac{f_{cr}}{f_y}, \quad \lambda^* = \frac{KL}{\pi r} \sqrt{\frac{f_y}{E}} \quad (14a,b)$$

In which  $f^*$  and  $\lambda^*$  are the dimensionless strength of the column and the slenderness parameter, respectively;  $f_{cr}$  and  $f_y$  are the critical buckling stress and the specified minimum yield stress, respectively;  $r$  the governing radius of gyration about the axis of buckling. This equation was calibrated to fit closely the SSRC curve 2 [34], which was modified to reflect an initial out-of-straightness of about 1/1500. This strength curve of AISC-LRFD [33] is depicted in Figure 2 together with the Euler hyperbola curve and the strength curves of Eurocode 3 [7].

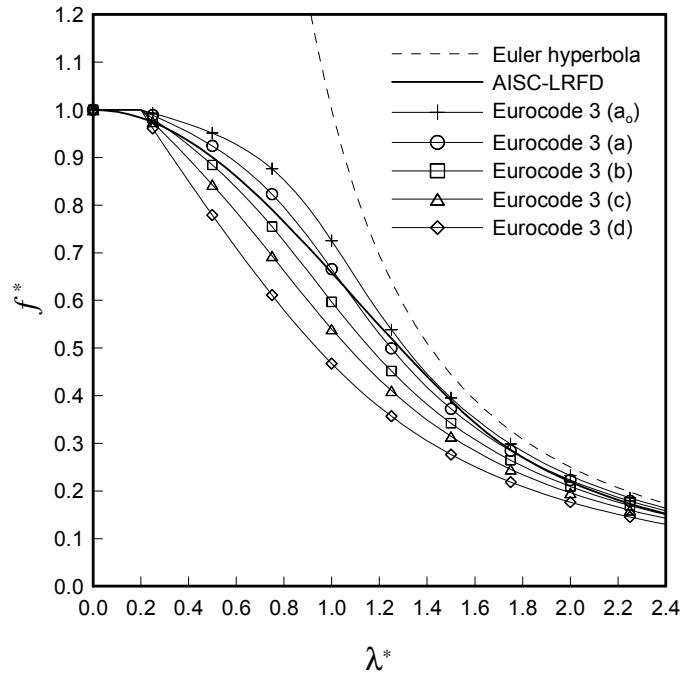


Figure 2. Load-carrying Capacity Curves in AISC-LRFD and Eurocode 3

The simplified design predictions for the maximum load (or resistance) were also used in Eurocode 3 [7] that had been developed from the results of computer analyses and correlations with available test data considering the residual stresses and the initial imperfection in design of compression members. The Eurocode 3 approach to determine the buckling resistance of compression member is based on the same principles as that of BS 5950 [35]. Although minor technical differences exist, the primary difference between the two codes is in the presentation of the method. The basic formulations for buckling curves are given by

$$f^* = \frac{1}{\phi + \sqrt{\phi^2 - \lambda^{*2}}} \quad \text{but } f^* \leq 1.0 \quad (15)$$

where

$$\phi = 0.5 \left[ 1 + \beta (\lambda^* - 0.2) + \lambda^{*2} \right] \quad (16)$$

In which  $\beta$  is the imperfection factor which shifts the resistance curve, as shown in Figure 2, for different cross-section types, properties, thicknesses, buckling axes, and material strengths and the five values of  $\beta$  for each of these curves are given in Table 1. The advantage of this approach is that the buckling resistances of a particular group of sections can be determined by assigning an appropriate value of  $\beta$  to them.

Table 1. Imperfection Factors for Buckling Curves

Buckling curve	$a_o$	$a$	$b$	$c$	$d$
Imperfection factor $\beta$	0.13	0.21	0.34	0.49	0.76

#### 4.2 Elastic and Inelastic System Buckling Analyses

According to the study by Chen and Lui [32], the best way to evaluate the more accurate  $K$ -factor for each individual member of the frame structure should be the stability analysis of the entire structure as a whole. The followings describe the elastic and inelastic system buckling analysis procedure proposed by this study.

**Step 1)** Constitute the system elastic stiffness matrix  $\mathbf{K}_E$  for the whole structure. For a given load condition, the following linear elastic analysis is performed from Eq. 5 to evaluate the axial force  $P_j$  for each member where subscript  $j$  denotes the number of member.

$$\mathbf{K}_E \mathbf{U} = \mathbf{F} \quad (17)$$

**Step 2)** Solve the linear eigenvalue problem in Eq. 18 and calculate the minimum eigenvalue  $\xi_{cr}^i$  where superscript  $i$  means the number of iteration.

$$\mathbf{K}_E^i (E_t^i) \Delta \mathbf{U} = \xi_{cr}^i (\mathbf{K}_G^i - \mathbf{K}_{NC}^i) \Delta \mathbf{U} \quad (18)$$

Then the elastic buckling load of each member is calculated as  $\xi_{cr}^i P_j$ .

**Step 3)** Evaluate the slenderness parameter  $\lambda_j^{*i}$  of each member as follows:

$$\lambda_j^{*i} = \frac{L_e^i}{\pi r} \sqrt{\frac{f_y}{E}} \quad (19)$$

where the effective length is defined as

$$L_e^i = K^i L = \pi \sqrt{\frac{E_{t,j}^i I_j}{\xi_{cr}^i P_j}} \quad (20)$$

**Step 4)** Calculate the inelastic critical buckling stress  $f_{cr,j}^i$  of each member from the AISC-LRFD and Eurocode 3 column strength curves by utilizing the slenderness parameter  $\lambda_j^{*i}$ .

**Step 5)** Calculate the refined tangent modulus of each member as

$$E_{t,j}^{i+1} = \frac{f_{cr,j}^i}{f_{cr,in,j}^i} E_{t,j}^i \quad (21)$$

where  $f_{cr,in,j}^i$  is the inelastic buckling stress of each member obtained from Eq. 18. Next check the convergence designated as  $(E_{t,j}^{i+1} - E_{t,j}^i) / E_{t,j}^i < \varepsilon$ . In case that the convergence is not achieved, go back to the step 2).

**Step 6)** Determine the final  $K$ -factor of each member.

In addition, Figure 3 shows the schematic procedures for the evaluation of  $K$ -factor in inelastic stability analysis.

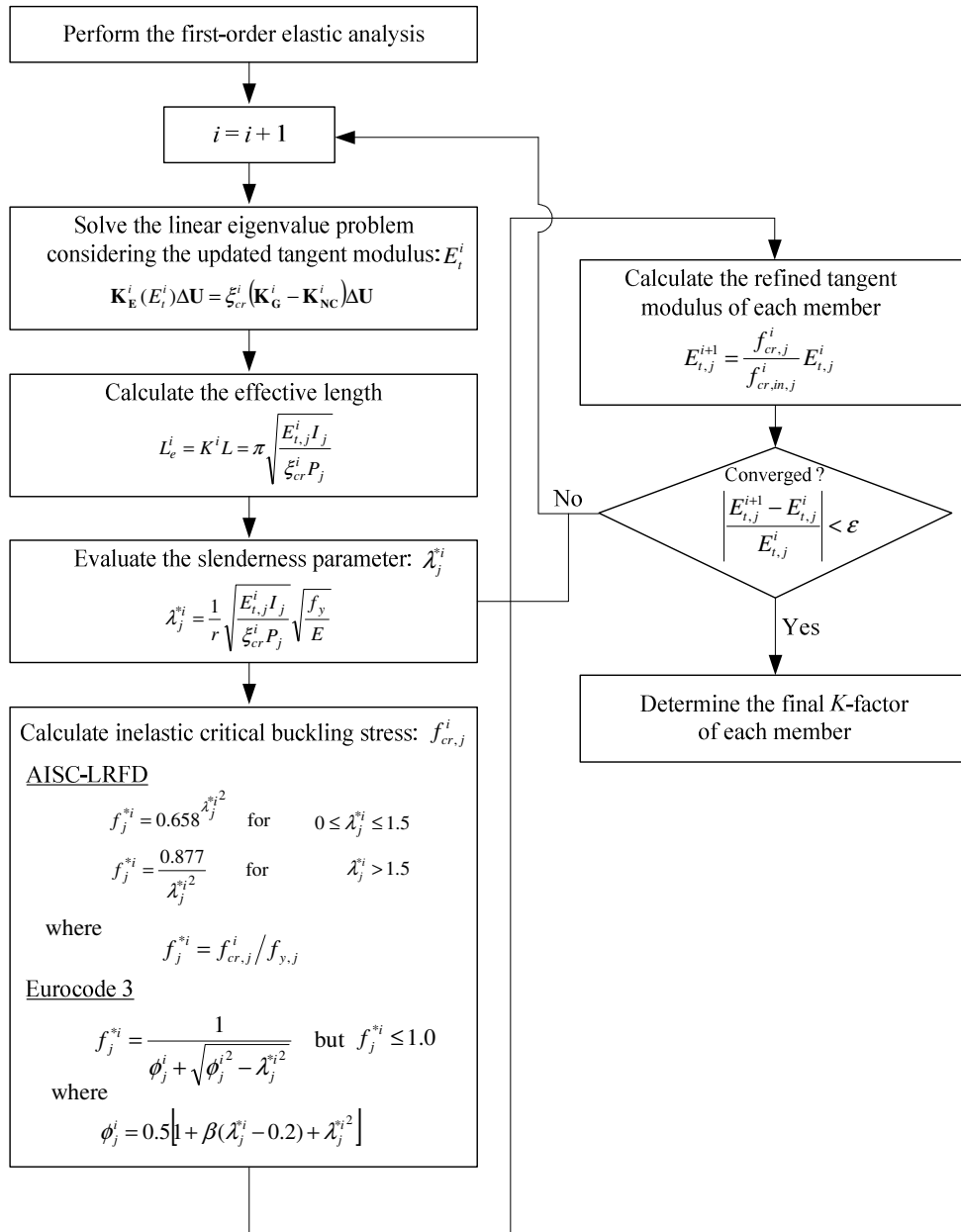


Figure 3. Flowchart of the Evaluation of  $K$ -factor in Inelastic Stability Analysis

## 5. NUMERICAL EXAMPLES

In numerical examples, to show the accuracy and the usefulness of the present study, the elastic and inelastic stability analyses of the frame structures subjected to conservative or nonconservative forces are performed and compared with other available references. The effects of various parameters on buckling loads and  $K$ -factors for columns in steel frames are investigated. In subsequent examples, each column is modeled with the five finite beam elements and the yield stress  $f_y$  of all columns is 344.7 MPa (50 ksi).

### 5.1 Three-story Frame Subjected to Conservative Forces

The stability analysis is carried out on the three-story frame subjected to conservative forces to illustrate the validity of the present method to predict  $K$ -factors of columns. Figure 4 shows the configuration of the frame with W-shape section, and its material and sectional properties are as follows:  $E = 2 \times 10^5$  MPa; W8×35:  $A = 6.645 \times 10^{-3} \text{ m}^2$ ,  $I = 5.286 \times 10^{-5} \text{ m}^4$ ; W8×48:  $A = 9.097 \times 10^{-3} \text{ m}^2$ ,  $I = 7.659 \times 10^{-5} \text{ m}^4$ ; W14×30:  $A = 5.71 \times 10^{-3} \text{ m}^2$ ,  $I = 1.2112 \times 10^{-4} \text{ m}^4$ ; W21×44:  $A = 8.387 \times 10^{-3} \text{ m}^2$ ,  $I = 3.5088 \times 10^{-4} \text{ m}^4$ . The  $K$ -factors evaluated by present elastic and inelastic stability analyses are presented in Table 2. For comparison, the  $K$ -factors by Liu and Xu [17] who uses the geometrical stiffness distribution approach for elastic analysis and AISC [2] using the modified equation for determining  $K$ -factors based on the story buckling approach and the alignment chart method for elastic and inelastic analyses are presented. It can be seen that the results by the present Euler hyperbola curve show fairly good agreement with those by Liu and Xu [17]. When the inelastic behavior is considered, the  $K$ -factor for column  $C_1$ , on which the highest axial force acts, becomes smaller. On the other hand, the inelastic system buckling analysis introduces the higher  $K$ -factor for column  $C_3$  having the relatively small axial force.

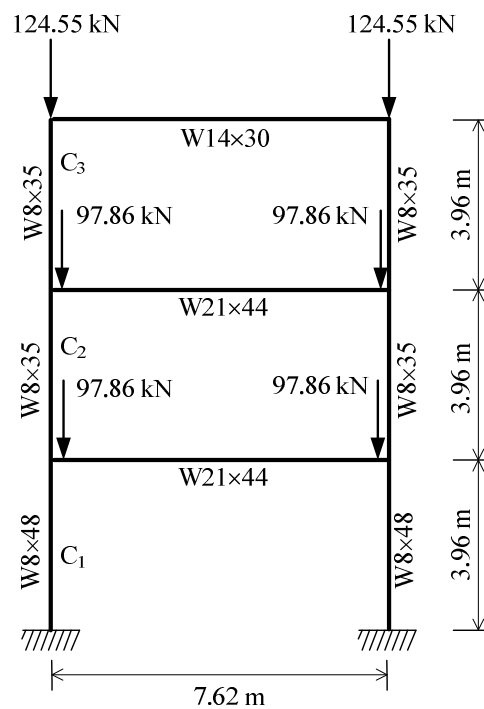


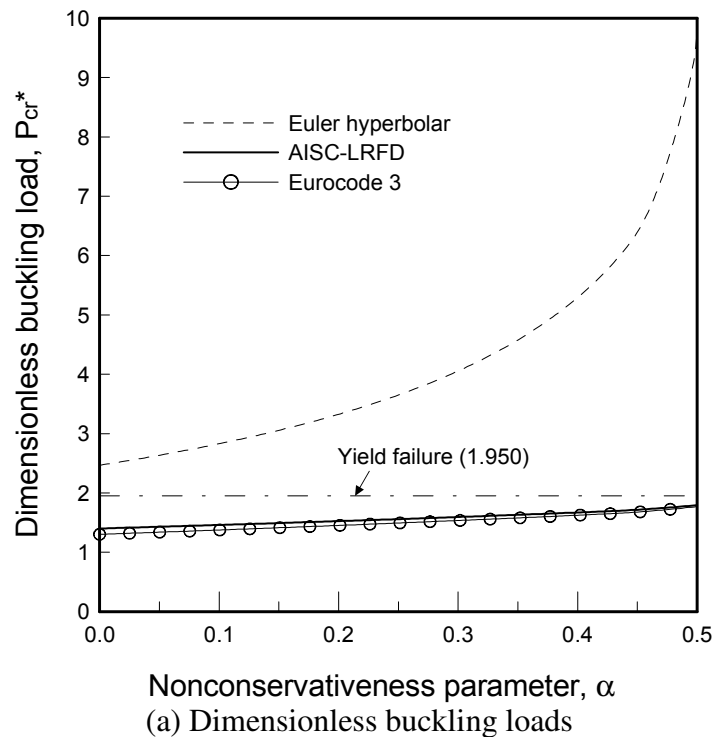
Figure 4. Three-story Frame subjected to Conservative Forces

Table 2.  $K$ -factors of the Three-story Frame Subjected to Conservative Forces ( $\alpha = 0$ )

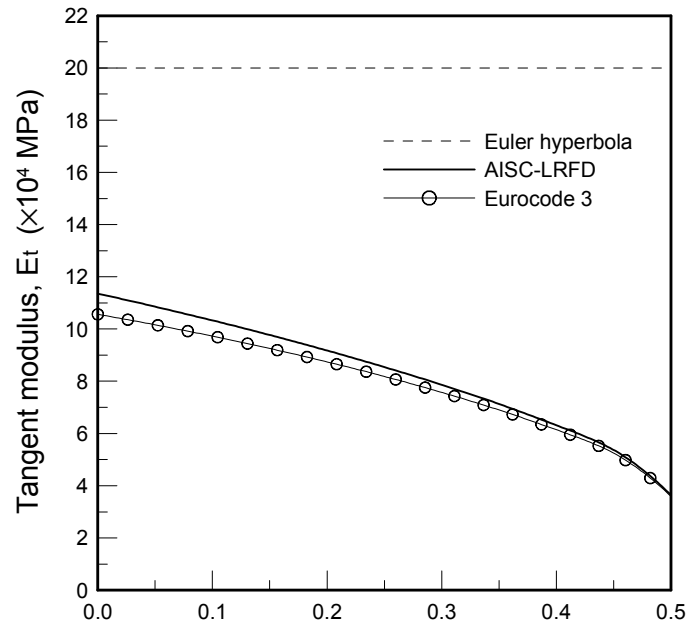
Methods	Elastic analysis			Inelastic analysis		
	$C_1$	$C_2$	$C_3$	$C_1$	$C_2$	$C_3$
Liu and Xu [17]	1.15	1.15	1.53	-	-	-
Story buckling approach [2]	1.11	1.21	1.23	1.07	1.14	1.21
Alignment chart method	1.11	1.21	1.23	1.07	1.14	1.21
This study	Euler hyperbola	1.15	1.14	1.53	-	-
	AISC-LRFD	-	-	-	1.03	1.11
	Eurocode 3	-	-	-	1.03	1.10

## 5.2 Cantilevered Column

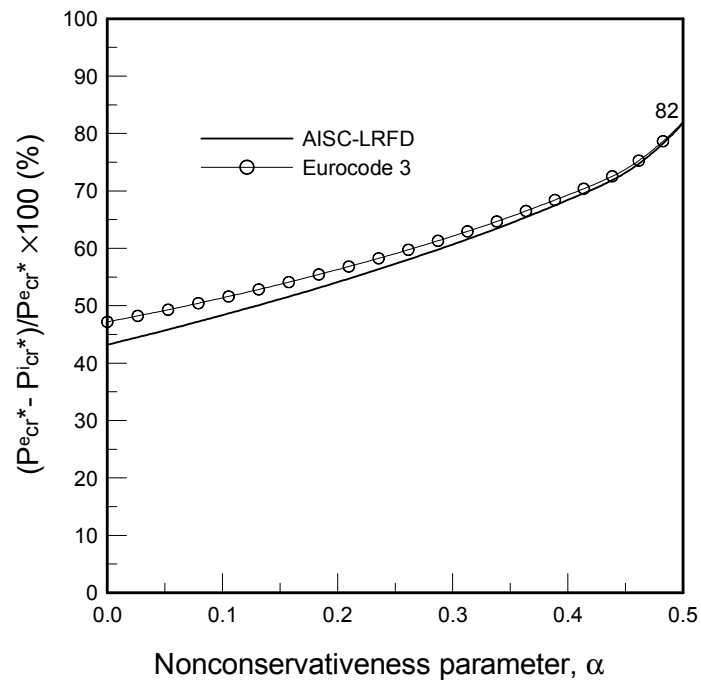
For verification purpose of the present study in evaluation of buckling load for the column subjected to the nonconservative force, we consider the cantilevered column with W-shape section (W8×35) subjected to the compressive tangential force  $P$  acting at the top of the column as shown in Figure 1. The length of column is 3 m and the material and sectional properties are as follows:  $E = 2 \times 10^5$  MPa,  $A = 6.645 \times 10^{-3}$  m<sup>2</sup>,  $I = 5.286 \times 10^{-5}$  m<sup>4</sup>. For simplicity the dimensionless buckling load  $P_{cr}^* = P_{cr} L^2 / (EI)$ , in which  $P_{cr}$  denotes the critical buckling load, is introduced. In Table 3, the dimensionless buckling loads by this study are compared with results obtained by Rao and Rao [36] deriving the exact solutions, with the solutions given by Leipholz [37], and with those proposed by Kikuchi [38] via a finite element technique. It can be found from Table 3 that the results by this Euler hyperbola curve are in excellent agreement with other literature results for whole  $\alpha$  considered.







(b) Variation of the tangent modulus



(c) Effects of inelasticity on the dimensionless buckling loads

Figure 5. Dimensionless Buckling Loads and Its Corresponding Tangent Modulus, and the Effects of Inelasticity on the Dimensionless Buckling Loads for the Cantilevered Column with Respect to  $\alpha$

Table 3. Dimensionless Buckling Loads for the Cantilevered Column Subjected to the Nonconservative Force

Methods		Nonconservativeness parameter $\alpha$					
		0.0	0.1	0.2	0.3	0.4	0.5
	Rao and Rao [36]	2.467	2.830	3.325	4.055	5.292	9.870
	Leipholtz [37]	2.467	2.830	3.325	4.055	5.292	9.870
	Kikuchi [38]	2.467	2.830	3.325	4.055	5.293	9.872
This study	Euler hyperbola	2.467	2.830	3.325	4.055	5.293	9.871
	AISC-LRFD	1.401	1.461	1.526	1.595	1.671	1.795
	Eurocode 3	1.303	1.376	1.453	1.536	1.625	1.771

Figure 5(a) shows the variation of the dimensionless buckling loads with respect to  $\alpha$ . It can be observed from Figure 5(a) that the buckling loads from both elastic and inelastic stability analyses increase as  $\alpha$  increases, so the conservative case ( $\alpha = 0$ ) is the more susceptible of instability. Also the increase ratio of buckling load with respect to  $\alpha$  for the Euler hyperbola curve is larger than those for AISC-LRFD and Eurocode 3 curves. As is expected, this is due to the fact that as  $\alpha$  increases, the critical buckling loads from the inelastic stability analyses increases slowly with significant degradation of the tangent modulus as seen in Figure 5(b). In Figure 5(c), the inelastic effects on the dimensionless buckling load are plotted with  $\alpha$ . Here  $P_{cr}^{e*}$  and  $P_{cr}^{i*}$  denote the dimensionless buckling loads from the elastic and inelastic stability analyses, respectively. As the results show, the inelastic effects on the buckling loads increase as  $\alpha$  increases up to around 82% at  $\alpha = 0.5$  for both of AISC-LRFD and Eurocode 3 curves.

### 5.3 Frame with Semirigid Connections

The frame with semirigid connections as shown in Figure 6 is considered. The frame consists of columns with W14×22 section and the modulus of elasticity is  $2 \times 10^5$  MPa. The moment of inertia for columns ( $I_c$ ) and beams ( $I_{b1}, I_{b2}$ ) are as follows:  $I_c = 82.83 \times 10^{-6} \text{ m}^4$ ,  $I_{b1} = 83.25 \times 10^{-6} \text{ m}^4$ , and  $I_{b2} = 10.41 \times 10^{-6} \text{ m}^4$ .

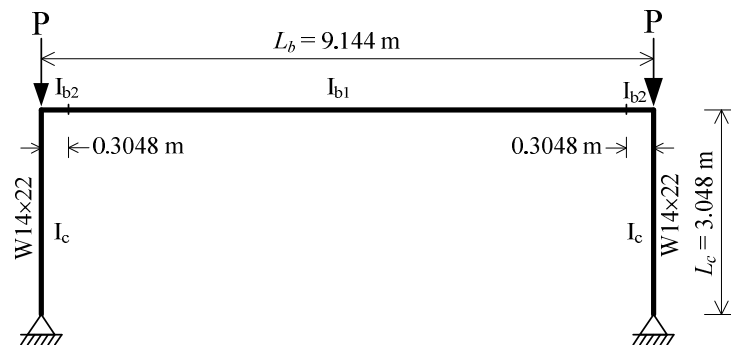


Figure 6. Frame with Semirigid Connections

When the columns are subjected to conservative forces ( $\alpha = 0$ ), the present  $K$ -factors are compared with one obtained by Cheong-Siat-Moy [39] in Table 4. Cheong-Siat-Moy [39] proposed a new design method employing a fictitious lateral load that was a fraction of the gravity loads. As can be seen in Table 4, the result from this Euler hyperbola curve is in good agreement with that from Cheong-Siat-Moy [39]. It can also be found that the inelastic effects decrease the  $K$ -factor by 16.6% and 15.6% for AISC-LRFD and Eurocode 3 curves, respectively.

Table 4.  $K$ -factors for the Column of Frame with Semirigid Connections Subjected to Conservative Forces

Cheong-Siat-Moy [39]	This study		
	Euler hyperbola	AISC-LRFD	Eurocode 3
3.8	3.85	3.21	3.25

Table 5 summarizes buckling loads and  $K$ -factors for columns with respect to  $\alpha$ . It is seen that the buckling load increases by tangential follower forces ( $\alpha = 1.0$ ) by 269.8% for the elastic analysis. On the other hand, for the inelastic columns, the buckling loads increase by 23.1% and 25.6% for AISC-LRFD and Eurocode 3 curves, respectively, due to the tangential forces. In case of  $K$ -factors, as  $\alpha$  increases, the  $K$ -factors converge to the value of 2.0 for both of the elastic and inelastic analyses. This  $K$ -factor of 2.0 corresponds to one in column with clamped boundary condition at the base, and the rotation fixed and translation free one at upper end. It is also seen that the tangential forces decrease  $K$ -factor by 48.1% for Euler hyperbola and 37.7% and 38.5% for AISC-LRFD and Eurocode 3 curves, respectively.

Table 5. Buckling Loads and  $K$ -factors for the Column of Frame with Semirigid Connections Subjected to Nonconservative Forces

Methods		Nonconservativeness parameter $\alpha$					
		0.0	0.2	0.4	0.6	0.8	1.0
Buckling loads	Euler hyperbola	1189.8	1402.0	1704.0	2164.9	2938.9	4399.7
	AISC-LRFD	1021.7	1092.7	1158.0	1200.4	1235.3	1258.2
	Eurocode 3	1034.5	1125.8	1198.3	1245.0	1279.1	1299.1
$K$ -factors	Euler hyperbola	3.85	3.54	3.21	2.85	2.45	2.00
	AISC-LRFD	3.21	2.87	2.58	2.34	2.15	2.00
	Eurocode 3	3.25	2.92	2.61	2.35	2.15	2.00

Figure 7 shows buckling loads and inelastic effects on buckling loads with respect to  $\alpha$ . It is observed from Figure 7(a) that the buckling loads increase with increase of  $\alpha$  and the elastic buckling load is smaller than the yield failure load at  $0 \leq \alpha \leq 0.24$  and it is larger at  $\alpha > 0.24$ . In Figure 7(b),  $P_{cr}^e$  and  $P_{cr}^i$  mean the buckling loads obtained from the elastic and inelastic analyses, respectively. The effects of inelasticity on buckling loads increase for increasing values of  $\alpha$  by 71.4% and 70.5% for AISC-LRFD and Eurocode 3, respectively. Figure 8 presents the variation of  $K$ -factors and the effects of inelasticity on  $K$ -factors. The  $K$ -factors decrease with increase of  $\alpha$ , as shown in Figure 8(a). In Figure 8(b),  $K^e$  and  $K^i$  are the  $K$ -factors evaluated from the elastic and inelastic analyses, respectively. It is observed from Figure 8(b), the effects of inelasticity increase with increase of  $\alpha$  and have the maximum values of 19.6% and 18.7% for AISC-LRFD and Eurocode 3 curves, respectively, at  $\alpha = 0.4$ . These effects decrease thereafter and become to be zero at  $\alpha = 1.0$ .

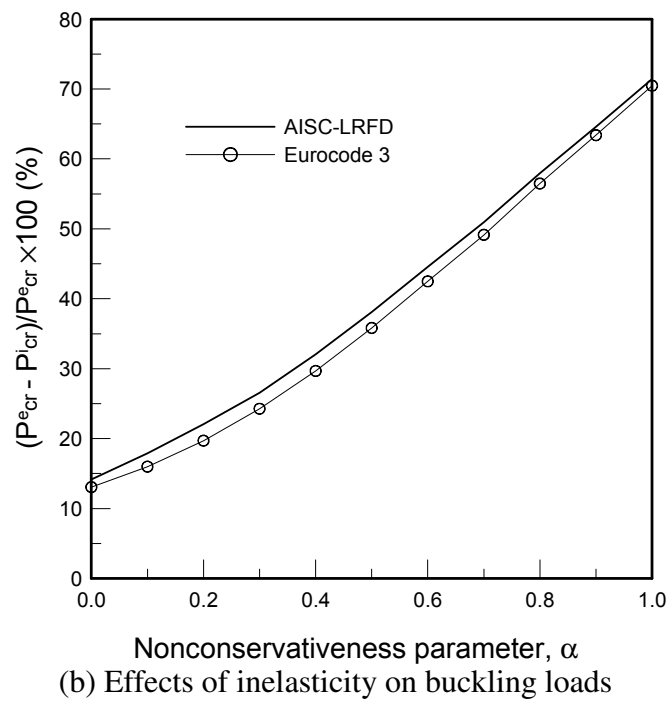
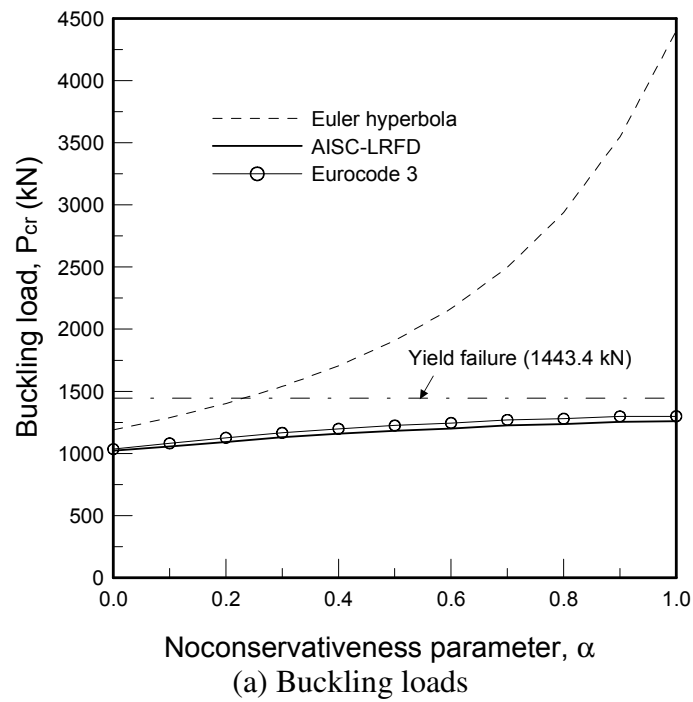


Figure 7. Buckling Loads and the Effects of Inelasticity on Buckling Loads for the Frame with Semirigid Connections with Respect to  $\alpha$

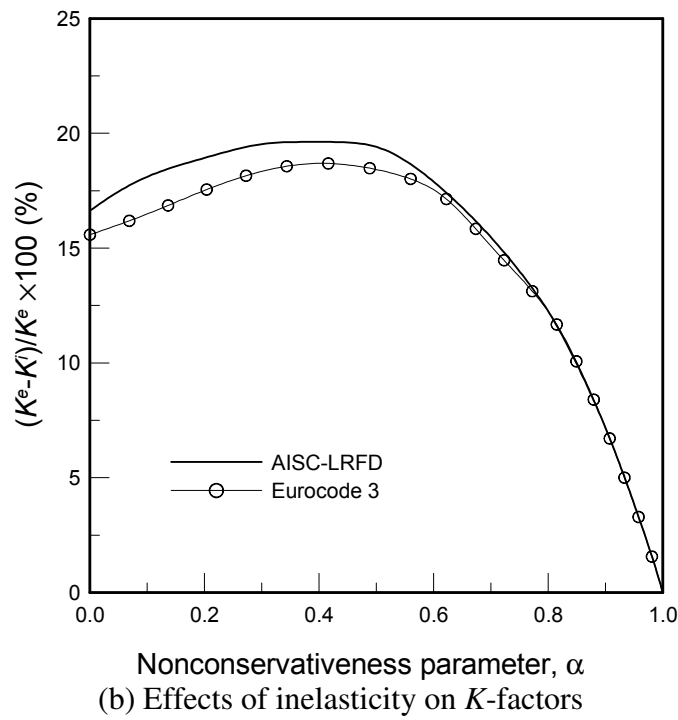
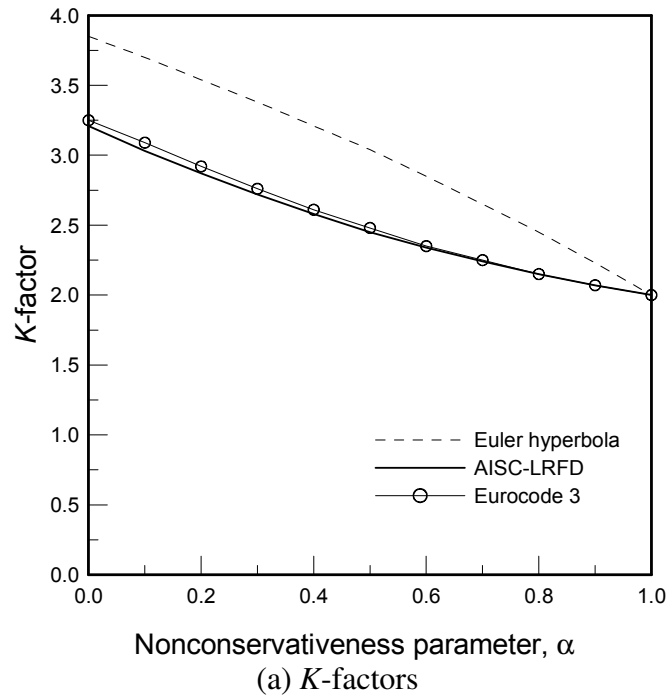
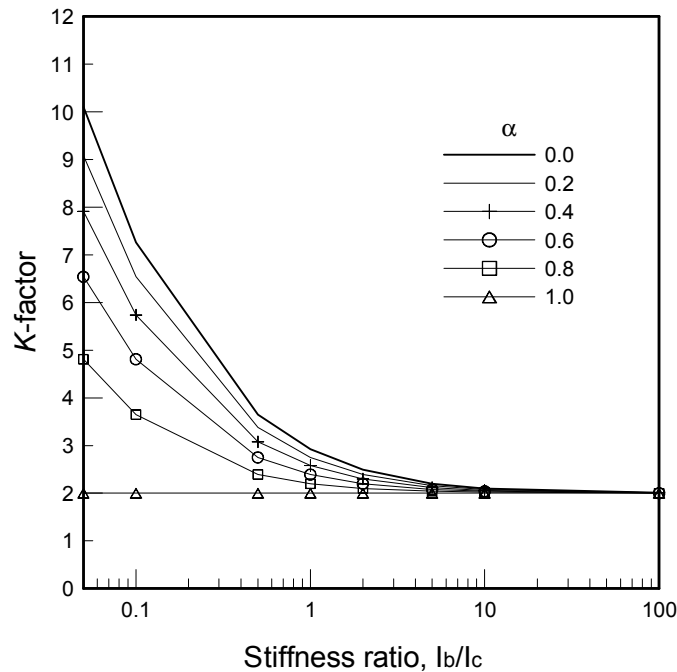


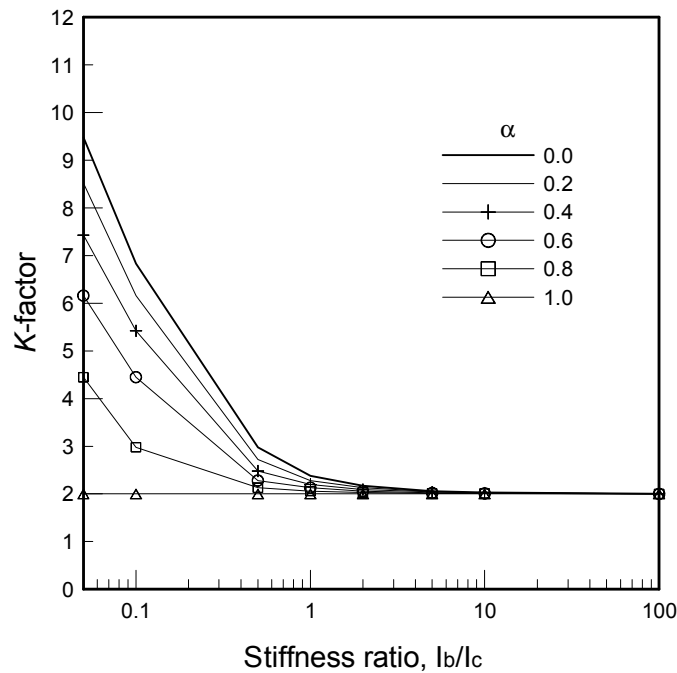
Figure 8.  $K$ -factors and the Effects of Inelasticity on  $K$ -factors for the Frame with Semirigid Connections with Respect to  $\alpha$

Now for the frame with rigid connections ( $I_{b2} = I_{b1} = 83.25 \times 10^{-6} \text{ m}^4$ ) subjected to nonconservative forces, the variation of  $K$ -factors and the effects of inelasticity on  $K$ -factors are investigated with respect to various values of the stiffness ratio  $I_b/I_c$  and the span ratio  $L_b/L_c$  of beam to column. First, Figures 9(a) and 9(b) show the variation of  $K$ -factors with values of  $\alpha$  versus the stiffness ratio for the Euler hyperbola and AISC-LRFD curves, respectively. In this example, we keep the moment of inertia of column  $I_c$  constant and change the value of  $I_b$ . It is observed that  $K$ -factors from the present elastic and inelastic stability analyses decrease as  $I_b/I_c$  increases and converge to the value

of 2.0 after  $I_b/I_c$  of 10. This means that if the stiffness of the beam approaches infinity, the columns will behave like a member with a hinged boundary condition at the base, and a rotation fixed and translation free one at the upper end. The effects of inelasticity on  $K$ -factors are plotted in Figure 9(c) with respect to  $I_b/I_c$  where  $K^A$  is the  $K$ -factor evaluated from AISC-LRFD curve. It can also be seen that the  $K$ -factors from the inelastic analysis is smaller than those from elastic one except for  $\alpha = 1.0$ . It is interesting to observe from Figure 9(c) that the maximum values of inelastic effects are about 19.8% for whole  $\alpha$  considered except for  $\alpha = 1.0$ . The values of  $I_b/I_c$  corresponding to the largest effects of inelasticity are on the decrease as  $\alpha$  increases. This is due to the fact that as  $\alpha$  increases, the total stiffness decreases, as shown in Eq. 5, and therefore the maximum inelastic effect occurs at the stiffness ratio with more flexible beam stiffness.



(a)  $K$ -factors from the Euler hyperbola curve



(b)  $K$ -factors from the AISC-LRFD curve



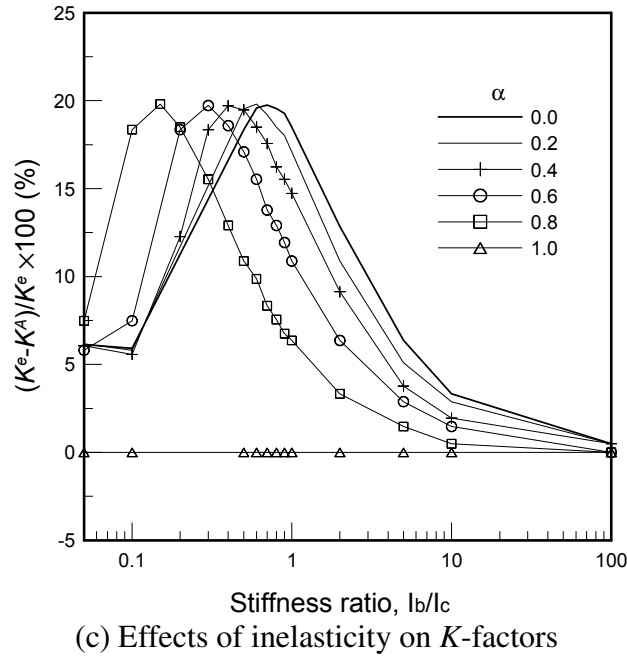
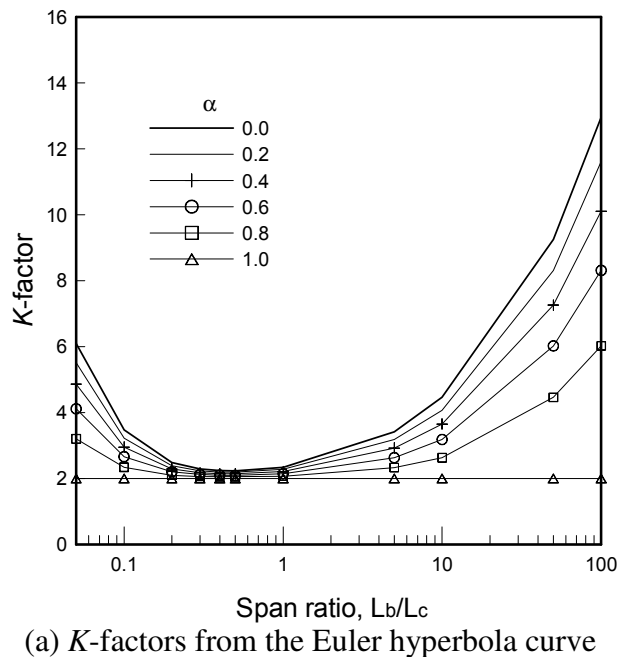


Figure 9.  $K$ -factors and the Effects of Inelasticity on  $K$ -factors for the Frame with Rigid Connections with Respect to  $I_b/I_c$

Next, the variation of  $K$ -factors from the Euler hyperbola and AISC-LRFD curves are presented in Figures 10(a) and 10(b), respectively, with respect to the span ratio  $L_b/L_c$  as the length of column remains constant and that of beam is varied. As can be seen, the  $K$ -factors for the frame subjected to tangential forces ( $\alpha = 1.0$ ) are irrespective of  $L_b/L_c$ . It is interesting to observe that as  $L_b/L_c$  increases, the  $K$ -factors decrease and have the minimum values at  $L_b/L_c$  of 0.5 and increase thereafter for both of the Euler hyperbola and AISC-LRFD curves. As shown in Figure 10(c), the values of inelastic effects on  $K$ -factors increase with increase of  $L_b/L_c$  and have the maximum value of 19.7% for whole  $\alpha$  except  $\alpha = 1.0$ , and decrease thereafter. The values of  $L_b/L_c$  corresponding to the largest effects of inelasticity are on the increase as  $\alpha$  increases.



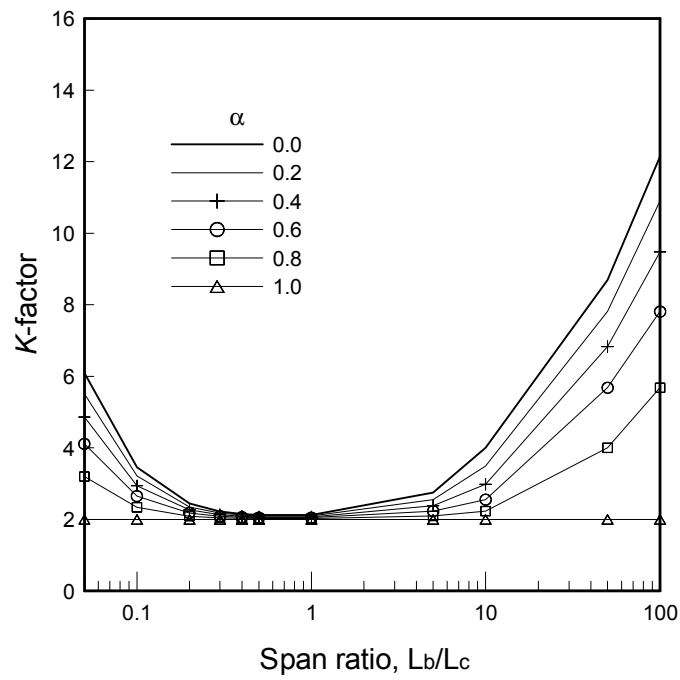
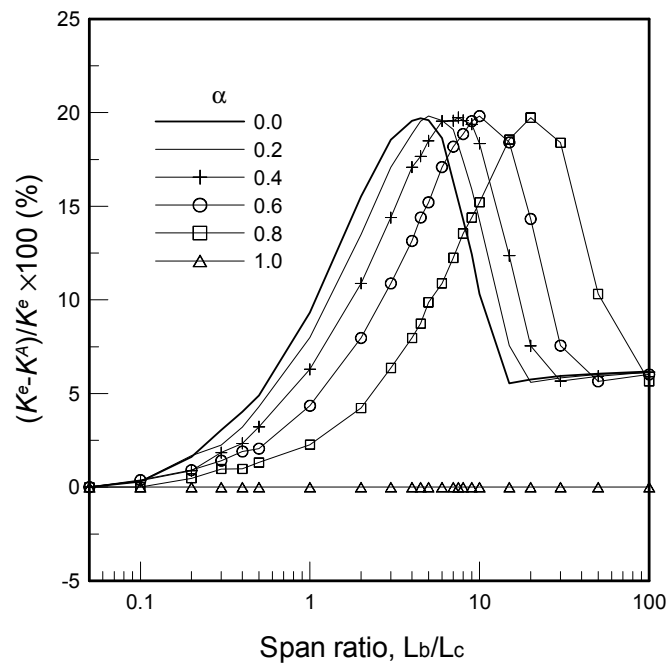
(b)  $K$ -factors from the AISC-LRFD curve(c) Effects of inelasticity on  $K$ -factors

Figure 10.  $K$ -factors and the Effects of Inelasticity on  $K$ -factors for the Frame with Rigid Connections with Respect to  $L_b/L_c$

## 6. CONCLUSIONS

The present paper proposes the inelastic system buckling analysis method to determine buckling loads and  $K$ -factors for columns of steel frames subjected to nonconservative forces by generalizing the iterative buckling procedures. This study overcomes the limit of traditional elastic and inelastic stability analyses using the many unrealistic assumptions which may lead to unreasonable  $K$ -factor if the frame structure does not satisfy these assumptions. Moreover this study is the first attempt to perform the stability analysis of the frame structures subjected to nonconservative forces considering column strength curve which considers the geometric imperfections and the residual stresses of the compression members. Throughout numerical examples, comparative examples and parametric studies are conducted and the following conclusions are drawn.

- 1) For evaluation of buckling loads and  $K$ -factors for the elastic conservative and nonconservative systems, the results by this study are in good agreement with those from other researchers.
- 2) For column subjected to the smaller axial force of in frame, the  $K$ -factor from inelastic analysis is larger than that from elastic analysis but it is the reverse for column subjected to the larger axial force.
- 3) For both elastic and inelastic analyses, the critical buckling loads of the frame increase with increase of  $\alpha$ , and so the conservative case ( $\alpha = 0$ ) is the more susceptible of instability.
- 4) The increase ratio of the inelastic buckling load of the frame with respect to  $\alpha$  is smaller than that of the elastic buckling load due to the significant degradation of the tangent modulus in inelastic analysis.
- 5) For all  $\alpha$ , the  $K$ -factors from the elastic and inelastic analyses decrease and converge to the specified value as  $I_b/I_c$  increases.
- 6) The maximum values of inelastic effects on  $K$ -factors of the frame are same for all  $\alpha$  considered except for  $\alpha = 1.0$  and the values of  $I_b/I_c$  corresponding to the largest effects of inelasticity are on the decrease as  $\alpha$  increases.
- 7) As  $L_b/L_c$  increases, the  $K$ -factors have the minimum values at  $L_b/L_c = 0.5$  and increase thereafter for both elastic and inelastic analyses. The values of inelastic effects on  $K$ -factors increase with  $L_b/L_c$  and have the same maximum values for whole range of  $\alpha$ .

## ACKNOWLEDGEMENTS

This work is a part of a research project supported by the Korea Ministry of Land, Transportation Maritime Affairs (MLTM) through Core Research Project 1 of Super Long Span Bridge R&D Center. The authors wish to express their gratitude for the financial support.

## REFERENCES

- [1] Julian, O.G. and Lawrence, L.S., "Notes on J and L Nomographs for Determination of Effective Lengths", Unpublished Report, Jackson and Moreland Engineers, Boston, 1959.
- [2] AISC, Steel Construction Manual, 13th ed. American Institute of Steel Construction, Inc., Chicago, Illinois, 2005.
- [3] ACI, Building Requirements for Structural Concrete, American Concrete Institute, Farmington Hill, MI, 2005.
- [4] AASHTO, Load and Resistance Factor Design Specifications for Highway Bridges, 2nd ed., American Association of State Highway and Transportation Officials, Washington, DC, 1998.

- [5] Galambos, T.V., *Structural Members and Frames*, Prentice-Hall, New York, 1968.
- [6] DIN 18800, Part 2: *Analysis of Safety Against Buckling of Linear Members and Frames*, Beuth Verlag GmbH, Berlin, 1990.
- [7] Eurocode 3, *Design of Steel Structures*, Final Draft, CEN, Brussels, Belgium, 2002.
- [8] Duan, L. and Chen, W.F., "Effective Length Factors for Columns in Unbraced Frames", *Journal of Structural Engineering*, ASCE, 1989, Vol. 115, pp. 149-165.
- [9] Duan, L. and Chen, W.F., "Effective Length Factors for Columns in Braced Frames", *Journal of Structural Engineering* ASCE, 1988, Vol. 114, pp. 2357-2370.
- [10] Bridge, R.Q. and Fraser, D., "Improved G-factor Method for Evaluating Effective Lengths of Columns", *Journal of Structural Engineering*, ASCE, 1987, Vol. 113, pp. 1341-1356.
- [11] Mahini, M.R. and Seyyedian, H., "Effective Length Factor for Columns in Braced Frames Considering Axial Forces on Restraining Members", *Structural Engineering and Mechanics*, 2006, Vol. 22, pp. 685-700.
- [12] Gantes, C.J. and Mageirou, G.E., "Improved Stiffness Distribution Factors for Evaluation of Effective Buckling Lengths in Multi-story Sway Frames", *Engineering Structures*, 2005, Vol. 27, pp. 1113-1124.
- [13] Yura, J.A., "The Effective Length of Columns in Unbraced Frames", *Engineering Journal*, AISC, 1971, Vol. 8, pp. 37-42.
- [14] LeMessurier, W.J., "A Practical Method of Second-order Analysis, Part 1: Pin-jointed Frames", *Engineering Journal*, AISC, 1976, Vol. 13, pp. 89-96.
- [15] LeMessurier, W.J., "A Practical Method of Second-order Analysis, Part 2: Rigid Frames", *Engineering Journal*, AISC, 1977, Vol. 14, pp. 49-67.
- [16] Xu, L., Liu, Y. and Chen, J., "Stability of Unbraced Frames under Non-proportional Loading", *Structural Engineering and Mechanics*, 2001, Vol. 11, pp. 1-16.
- [17] Liu, Y. and Xu, L., "Storey-based Stability Analysis of Multi-storey Unbraced Frames", *Structural Engineering and Mechanics*, 2005, Vol. 19, pp. 679-705.
- [18] Özmen, G. and Girgin, K., "Buckling Lengths of Unbraced Multi-storey Frame Columns", *Structural Engineering and Mechanics*, 2005, Vol. 19, pp. 55-71.
- [19] Girgin, K., Ozmen, G. and Orakdogan, E., "Buckling Lengths of Irregular Frame Columns", *Journal of Constructional Steel Research*, 2006, Vol. 62, pp. 605-613.
- [20] Geschwindner, L.F., "A Practical look at Frame Analysis, Stability and Leaning Columns", *Engineering Journal*, AISC, 2002, Vol. 31, pp. 167-181.
- [21] Roddis, W.M.K., Hamid, H.A. and Guo, C.Q., "K Factors for Unbraced Frames: Alignment Chart Accuracy for Practical Frame Variations", *Engineering Journal*, AISC, 1998, Vol. 8, pp. 81-93.
- [22] Choi, D.H., Na, H.S., Jung, J.W. and Yoo, H., "Iterative Eigenvalue Analysis for Stability Design of Three-dimensional Frames Considering a Fictitious Axial Force Factor", *International Journal of Steel structures*, 2010, Vol. 10, pp. 325-335.
- [23] Kim, H.D. and Lee, M.J., "Analytic Investigation of the P-Delta Effect of Middle-rise Unbraced Steel Frames", *International Journal of Steel structures*, 2010, Vol. 10, pp. 221-232.
- [24] Essa, H.S., "New Stability Equation for Columns in Unbraced Frames", *Structural Engineering and Mechanics*, 1998, Vol. 6, pp. 411-425.
- [25] Johnston, B.G., *Structural Stability Research Council, Guide to Stability Design Criteria for Metal Structures*, 3rd Ed., John Wiley & Sons, Inc., New York.
- [26] Bolotin, V.V., "Non-conservative Problems of the Theory of Elastic Stability", Pergamon Press, Oxford, 1963.
- [27] Gasparini, A.M., Saetta, A.V. and Vitaliani, R.V., "On the Stability and Instability Regions of Non- Conservative Continuous System under Partially Follower Forces", *Computer Methods in Applied Mechanics and Engineering*, 1995, Vol. 124, pp. 63-78.
- [28] Ryu, B.J., Sugiyama, Y., Yim, K.B. and Lee, G.S., "Dynamic Stability of An Elastically

- Restrained Column Subjected to Triangulary Distributed Subtangential Forces”, *Computers and Structures*, 2000, Vol. 76, pp. 611-619.
- [29] Wang, Q., “Effect of the Follower Force on the Static Buckling of Beams”, *International Journal of Structural Stability and Dynamics*, 2002, Vol. 2, pp. 425-430.
  - [30] Imielowski, Sz., “Sensitivity Analysis of a Stepped Column under Circulatory Load”, *ZAMM*, 1993, Vol. 73, pp. T186 -T189.
  - [31] Lee, J.S., Kim, N.I. and Kim, M.Y., “Sub-tangentially Loaded and Damped Beck’s Columns on Two- Parameter Elastic Foundation”, *Journal of Sound and Vibration*, 2007, Vol. 306, pp. 766-789.
  - [32] Chen, W.F. and Lui, E.M., “Structural Members and Frames”, Elsevier Inc., New York, 1987.
  - [33] AISC, *Manual of Steel Construction*, 3rd ed., Load and Resistance Factor Design, American Institute of Steel Construction, Inc., Chicago, Illinois, 2001.
  - [34] Galambos, T.V., *Guide to Stability Design Criteria for Metal Structures*, 5th. ed., John Wiley and Sons, New York, 1998.
  - [35] Gardner, L. and Nethercot, D.A., *Designers’ Guide to EN 1993-1-1; Eurocode 3: Design of Steel Structures General Rules and Rules for Buildings*, Thomas Telford Ltd, London, 2005.
  - [36] Rao, B.N. and Rao, G.V., “Applicability of the Static or the Dynamic Criterion for the Stability of a Cantilever Column under a Tip-concentrated Subtangential Follower Force”, *Journal of Sound and Vibration*, 1987, Vol. 120, pp. 197-200.
  - [37] Leipholz, H., “Über die befreiung der Ansatzfunktionen des Ritzschen und galerkinschen verfahrens von den Randbedingungen”, *Archive of Applied Mechanics (Ingenieur Archiv)*, 1967, Vol. 36, pp. 215-261 (in German).
  - [38] Kikuchi, F., “A Finite Element Method for Non-self-adjoint Problem”, *International Journal for Numerical Methods in Engineering*, 1973, Vol. 6, pp. 39-54.
  - [39] Cheong-Siat-Moy, F., “K-factor Paradox”, *Journal of Structural Engineering*, 1986, Vol. 112, pp. 1747- 1760.

# MODIFIED ONE ZONE MODEL FOR FIRE RESISTANCE DESIGN OF STEEL STRUCTURES

Chao Zhang <sup>1,\*</sup> and Guo-qiang Li <sup>2</sup>

<sup>1</sup>College of Civil Engineering, Tongji University, 1239 Siping Road, Shanghai 200092, China

<sup>2</sup>State Key Laboratory for Disaster Reduction in Civil Engineering, 1239 Siping Road, Shanghai, China

\*(Corresponding author: E-mail: 08\_chao\_zhang@tongji.edu.cn)

Received: 23 February 2012; Revised: 8 July 2012; Accepted: 13 July 2012

**ABSTRACT:** A modified one-zone model has been proposed for structural fire safety design. In the model, a quantity which considers the heat sink effect of steel members in fire compartment is added to the heat balance equation for one-zone compartment fire model. In this paper, the proposed model is solved by FEM simulations. The results from FEM simulations are verified by program OZone (V2.0). Case studies have been conducted with investigating parameters including number of steel members, compartment dimension, opening area, fire load density and steel insulation thickness. The results of the studies show that for fire compartments with bare steel members, the steel heat sink effect is greater for compartments with smaller floor area, larger opening, lower fire load density, and more steel members; and for fire compartments with insulated steel members, the steel heat sink effect is greater for compartments with larger floor area, smaller opening, higher fire load density, and more steel members with thinner insulation. Correspondingly, the over-predictions of the maximum steel temperatures by the current model are comparatively more severe for those compartments. The proposed model can yield more economical fire resistance design than the current model, which is recommended for practical usage.

**Keywords:** Temperature calculation; Steel structures; Post-flashover fires; Fire resistance; Modified one-zone model

## 1. INTRODUCTION

Currently, performance-based method is very popular in fire safety engineering. In a performance-based fire resistance design, the temperature of building components exposed to the potential real fires should be determined scientifically.

The behavior of a real fire is complex, which depends on many parameters such as sprinkler, fire load, combustion, ventilation, compartment size and geometry, and thermal properties of compartment boundaries [1]. So far, with increase in complexity, empirical correlations (e.g. nominal fire curves and parameter fire curve [2]), zone models (e.g. one-zone model for post-flashover fires [3,4] and two-zone model for preflashover fires [4,5]), and sophisticated CFD models (e.g. Fire Dynamic Simulation [6]) have been developed to model the fire behavior.

In fire resistance design, post-flashover fires are usually considered because they provide the worst case scenario (however, localized heating of key elements of structure in pre-flashover fires must also be considered). The temperature of a steel member exposed to a post-flashover fire is usually determined by first representing the fire environment by a fire curve obtained from solving the one-zone compartment fire model, then substituting the fire curve into a one-dimensional (1D) condensed heat transfer model to obtain the steel temperature [7]. The temperature of steel members in a fire can also be determined by advanced compute simulations [8].

Figure 1 shows the one-zone compartment fire model. In this model, the heat balance equation within the compartment is given by [9]

$$HRR = \dot{q}_g + \dot{q}_w + \dot{q}_{o,c} + \dot{q}_{o,r} \quad (1)$$



where  $HRR$  is heat release rate due to combustion;  $\dot{q}_g$  is rate of heat storage in the gas volume;  $\dot{q}_w$  is rate of heat loss through the walls, ceiling and floor;  $\dot{q}_{o,c}$  is rate of heat loss due to replacement of hot gases by cold; and  $\dot{q}_{o,r}$  is rate of heat loss by radiation through the openings. Based on this model, both analytical expressions and compute programs were developed to give fire curves for structural design [10].

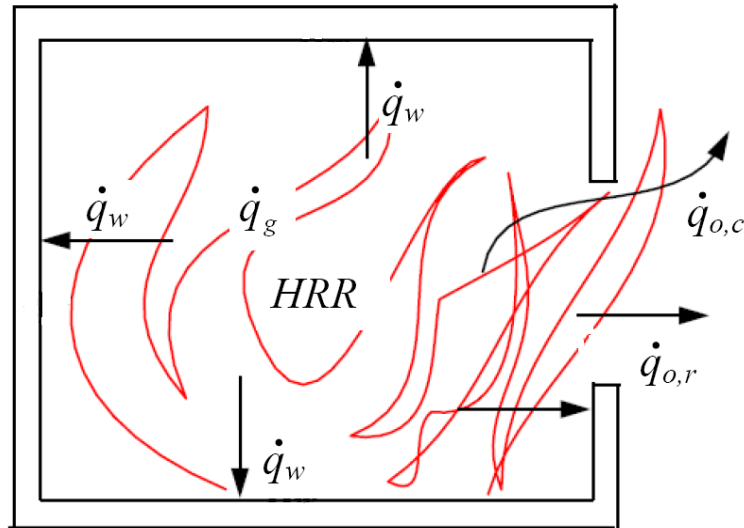


Figure 1. Illustration of Compartment One Zone Model

Figure 2 shows the 1D condensed heat transfer model used to calculate the temperature of insulated steel members. The temperature specified by a fire curve ( $T_f$ ) is interpreted as the effective black body radiation temperature for radiation calculation and as the same gas temperature for convection calculation. The radiation and convection effects are considered by using a thermal resistor  $R_f$ . The heat insulation effect of the fire protection is considered by using a thermal resistor  $R_i$  (for bare steel members without fire protection,  $R_i = 0$ ). The internal steel is represented by a lumped mass that temperature gradient within the steel is ignored. Based on this model, using various mathematical techniques, different formulas were developed for calculating the average steel temperatures [7].

It is obvious that the steel members in a fire compartment will absorb a portion of the energy released by combustion. That portion of energy will heat the steel members on one hand and cool the compartment on the other hand. As a result, the temperature of a steel member within a fire compartment is dependent on the heating mechanism of the compartment. However, in current models, as shown in Figures 1 and 2, the temperature of a steel member within a fire compartment is related to the fire curve which is determined without considering the heat sink effect of the steel member.

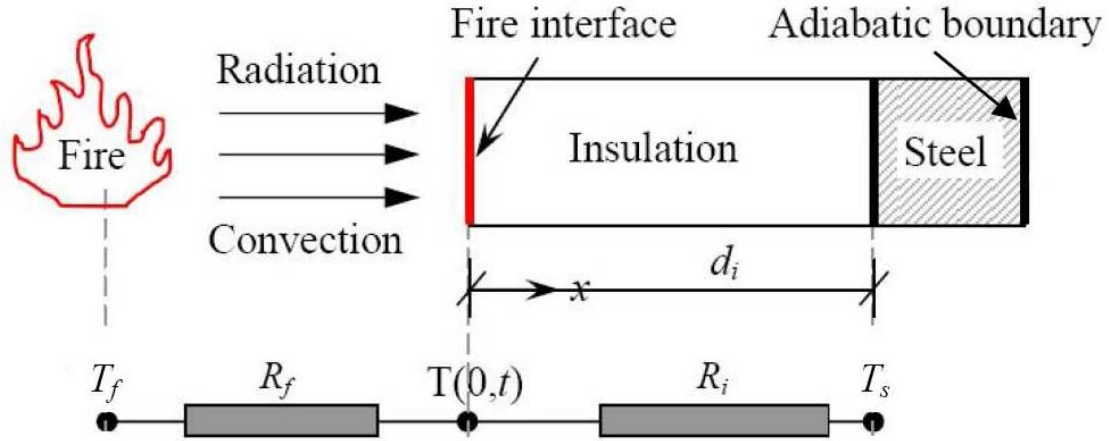


Figure 2. Illustration of 1D Condensed Heat Transfer Model

In this paper, a modified one-zone model is proposed to calculate the temperature of steel members in post-flashover fires. By the model, heat sink effect of steel members in fire compartment has been investigated.

## 2. THE MODIFIED ONE-ZONE MODEL

### 2.1 Heat Balance Equation

In the modified one-zone model, the heat sink effect of steel members in fire compartments has been considered by adding a quantity to the heat balance equation for one zone compartment model (Eq. 1), thus

$$HRR = \dot{q}_g + \dot{q}_w + \dot{q}_{o,c} + \dot{q}_{o,r} + \dot{q}_s \quad (2)$$

where,  $\dot{q}_s$  is rate of heat storage in steel members.

### 2.2 Sub-models

#### 2.2.1 Heat release rate (HRR)

Heat release rate ( $HRR$ ) is the most important variable in measuring fire severity, which can be calculated by

$$HRR = \dot{m}_f \Delta H_c \quad (3)$$

where,  $\dot{m}_f$  is the mass burning rate of the fuel; and  $\Delta H_c$  is the net heat of combustion of the fuel. In ventilation controlled fires (fully-developed compartment or post-flashover fires), the  $HRR$ s are alternatively calculated by [1]

$$HRR = \dot{m}_{air} \Delta H_{air} \quad (4)$$

where,  $\dot{m}_{air}$  is the mass rate of air inflow and  $\Delta H_{air}$  is the heat released per unit mass air consumed.

The *HRR* of a real fire can be measured by cone calorimeter designed by Babrauskas et al. [11]. In design work, the natural fire safety concept (*NFSC*) is widely used to represent the fire conditions [2,4]. As shown in Figure 3, the *NFSC* fire is assumed to be t-square in the growth stage and decay stage begins at the time when 70% of design fire load is consumed.

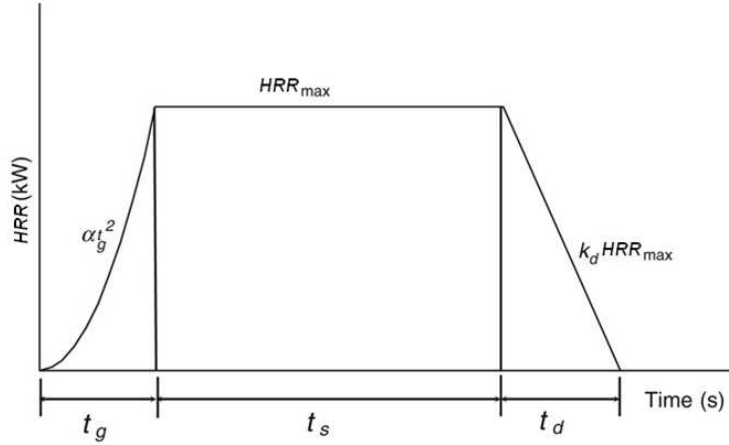


Figure 3. Illustration of the HRR History in a NFSC Fire

In a *NFSC* fire, at the growth stage, the *HRR* is given by

$$HRR = \alpha t^2 \quad (5)$$

the fire growth time  $t_g$  is given by

$$t_g = \sqrt{\frac{HRR_{\max}}{\alpha}} \quad (6)$$

and the fuel energy consumed at the fire growth stage,  $Q_g$ , is

$$Q_g = \int_0^{t_g} \alpha t^2 dt = \frac{\alpha t_g^3}{3} \quad (7)$$

where,  $\alpha$  is the fire intensity coefficient, taken as 0.00293, 0.0117 and 0.0466 for slow, medium and fast growth fires, respectively.

The duration time of steady burning in a *NSFC* fire is given by

$$t_s = \frac{0.7q_f A_f - Q_g}{HRR_{\max}} \quad (8)$$

and the duration of decaying stage is given by

$$t_d = \frac{0.6q_f A_f}{HRR_{\max}} \quad (9)$$

where,  $q_f$ ,  $A_f$  are design fire load density and floor area, respectively; and  $HRR_{\max}$  is the maximum heat release rate, for ventilation controlled fires [1],

$$HRR_{\max} = 1500 A_o \sqrt{H_o} \quad (10)$$

where,  $A_o = W_o H_o$  is the area of the ventilation opening, in which  $W_o$  and  $H_o$  are the width and height, respectively. For fuel-controlled fires, EC1 [2] gives some values of maximum heat release rates for different occupancies.

### 2.2.2 Heat loss due to convective flow ( $\dot{q}_{o,c}$ )

Pressure in a compartment fire is essentially atmospheric, and flows occur at openings due to hydrostatic pressure differences. The mass rates of out and in flows are calculated by [1]

$$\dot{m}_{gas} = \frac{2}{3} C_d W_o \rho_{\infty} \left[ 2g \frac{T_{\infty}}{T_f} \left( 1 - \frac{T_{\infty}}{T_f} \right) \right]^{1/2} (H_o - X_N)^{3/2} \quad (11)$$

And

$$\dot{m}_{air} = \frac{2}{3} C_d W_o \rho_{\infty} \left[ 2g \left( 1 - \frac{T_{\infty}}{T_f} \right) \right]^{1/2} (X_N - X_d)^{1/2} (X_N + X_d / 2) \quad (12)$$

, respectively. The heat loss due to replacement of hot gases by cold at openings is calculated by

$$\dot{q}_{o,c} = \dot{m}_{gas} c_p T_f - \dot{m}_{air} c_p T_{\infty} \quad (13)$$

The flow coefficient,  $C_d$ , is approximately 0.7. The neutral plane height,  $X_N$ , can be approximated as the half height of the opening. For post-flashover fires, the height of the interface  $X_d$  is approximately zero. Taken those values into Eq. 12, the inflow mass rate for post-flashover fires can be approximated as

$$\dot{m}_{air} = 0.5 A_o \sqrt{H_o} \quad (14)$$

In many calculations [1], the mass rate of outflow is taken as equal to the mass rate of inflow given by Eq. 14. Correspondingly, the heat loss due to replacement of hot gases by cold is calculated by

$$q_{o,c} \approx 0.5 A_o \sqrt{H_o} c_p (T_f - T_{\infty}) \quad (15)$$

where,  $c_p$  is the specific heat of the gas;  $T_f$  and  $T_{\infty}$  are fire and environment temperatures, respectively.

### 2.2.3 Heat loss by radiation through the openings ( $\dot{q}_{o,r}$ )

The heat loss by radiation through the openings of a fire compartment is usually calculated by adopting homogeneous gray gas approximations for fire environment and using Stefan-Boltzmann law, that,

$$\dot{q}_{o,r} = A_o \varepsilon_f \sigma (T_f^4 - T_\infty^4) \quad (16)$$

where,  $\varepsilon_f$  is the effective emissivity of the gases within the compartment, which can be calculated from

$$\varepsilon_f = 1 - e^{-\kappa L} \quad (17)$$

where,  $\kappa$  is the emission coefficient, usually taken as  $1.1 \text{ m}^{-1}$  [9]; and  $L$  is the mean beam length for the enclosure, which is approximated as the height of the compartment.

### 2.2.4 Heat loss through wall ( $\dot{q}_w$ )

The heat transfer into the boundary surface of a compartment occurs by convection and radiation from the enclosure, and then conduction through the walls. In calculating heat transfer from fire to boundary surface ( $\dot{q}_w$ ), the following assumptions are adopted,

- In radiation calculation, the fire and the boundary surface are represented as two infinitely parallel grey planes that the view factor is taken as unit;
- In unsteady conduction calculation, The boundaries (walls, ceiling and floor) are usually assumed to be semi-infinite solids

Theoretically, for semi-infinite behavior, the exposure time must be less than the penetration time which for a slab exposed to a Dirichlet boundary condition is about  $\frac{1}{\alpha_w} \left(\frac{d_w}{4}\right)^2$  [1]. Here,

$\alpha_w = k_w / (\rho_w c_w)$  is the thermal diffusivity of the slab, in which  $k_w$ ,  $\rho_w$  and  $c_w$  are conductivity, density and specific heat, respectively.  $d_w$  is the thickness of the slab. In practice, if the thickness of a slab is greater than  $2\sqrt{\alpha_w t}$ , the semi-infinite solid assumption is used [1,12]. In the proposed model, however, the semi-infinite solid assumption is not adopted, that the heat transfer from unexposed surfaces of compartment boundaries to outside environment is considered.

The governing equation for 1D wall conduction is given by

$$\frac{\partial^2 T_w(x,t)}{\partial x^2} = \frac{1}{\alpha_w} \frac{\partial T_w(x,t)}{\partial t} \quad (18)$$

At fire and environment exposed sides, the Neumann boundary conditions are given by Eq. 19 and Eq. 20, respectively.

$$\dot{q}_w = -k_w \frac{\partial T_w(0,t)}{\partial x} = (h_{c,l} + h_{r,l})[T_f - T_w(0,t)] \quad (19)$$

$$-k_w \frac{\partial T_w(d_w, t)}{\partial x} = (h_{c,r} + h_{r,r})[T_w(d_w, t) - T_\infty] \quad (20)$$

Here,  $T_w(0, t)$  and  $T_w(d_w, t)$  are temperatures of fire and environment exposed surfaces, respectively;  $h_{c,l}$  and  $h_{c,r}$  are convective heat transfer coefficients at fire and environment exposed surfaces, taken as 35 W/(m<sup>2</sup>K) and 9 W/(m<sup>2</sup>K) [2], respectively; and  $h_{r,l}$  and  $h_{r,r}$  are radiative heat transfer coefficients at fire and environment exposed surfaces, given by Eq. 21 and Eq. 22, respectively.

$$h_{r,l} = \varepsilon_{res} \sigma [T_f^2 + T_w(0, t)^2][T_f + T_w(0, t)] \quad (21)$$

$$h_{r,r} = \varepsilon_w \sigma [T_\infty^2 + T_w(d_w, t)^2][T_\infty + T_w(d_w, t)] \quad (22)$$

Here,  $\varepsilon_{res}$  is the resultant emissivity at fire exposed surface, given by

$$\varepsilon_{res} = \frac{1}{1/\varepsilon_f + 1/\varepsilon_w - 1} \quad (23)$$

in which,  $\varepsilon_w$  is the emissivity of the wall.

### 2.2.5 Heat storage in gas volume ( $\dot{q}_g$ )

The heat stored in the gas volume within the compartment is calculated by

$$\dot{q}_g = \rho_\infty c_p V_g \frac{\Delta T_f}{\Delta t} \quad (24)$$

where,  $\rho_\infty$  is the density of the gas; and  $V_g$  is the gas volume.

### 2.2.6 Heat absorbed by steel members ( $\dot{q}_s$ )

For bare steel, using lumped capacitance method, the heat absorbed by the steel members within the compartment is calculated by

$$\dot{q}_s = c_s m_s \frac{\Delta T_s}{\Delta t} \quad (25)$$

where,  $c_s$  is the specific heat of steel;  $m_s$  is the total mass of steel members; and  $T_s$  is the average steel temperature.

For insulated steel, 1D condensed model (Figure 2) is adopted to calculate heat transfer. At fire-insulation interface, the Neumann boundary condition is adopted. By lumped capacitance concept, the boundary condition at the steel-insulation interface is given by

$$-k_i \frac{\partial T(d_i, t)}{\partial x} = \frac{c_s \rho_s}{A_i / V_s} \frac{\partial T(d_i, t)}{\partial t} \quad (26)$$

$$T_s = T(d_i, t) \quad (27)$$

where,  $T(d_i, t)$  is the temperature of insulation at steel-insulation interface;  $c_s \rho_s$  is the volumetric specific heat of steel;  $A_i / V_s$  is the section factor, in which  $A_i$  is the appropriate area of the fire insulation, and  $V_s$  is the volume of steel; and  $d_i$  is the thickness of the insulation.

For steel members insulated by thin, light weight coatings, the heat absorbed by the coatings are usually ignored, that the heat absorbed by the members are calculated by Eq. 25.

### 3. SIMULATING THE MODIFIED ONE-ZONE MODEL BY FEM

#### 3.1 Numerical Tool

The proposed model given above can be solved using technologies like finite differential method (FDM) and finite element method (FEM). In this paper, the FEM program ANSYS with powerful capacity to solve steady-state or transient heat transfer problems, is employed to simulate the proposed model. Validation of the program has been conducted by many works, e.g. [7, 13].

#### 3.2 Basic Elements

##### 3.2.1 LINK32-2D conduction bar

LINK 32 is a uniaxial element with the ability to conduct heat between its nodes. The element has a single degree of freedom, temperature, at each node point. The conducting bar is applicable to a 2D, steady-state or transient thermal analysis.

The element is defined by two nodes, a cross-sectional area, and the material properties. The thermal conductivity is in the element longitudinal direction. Heat generation rates may be input as element body loads at the nodes.

##### 3.2.2 LINK34-convection link

LINK34 is a uniaxial element with the ability to convect heat between its nodes. The element has a single degree of freedom, temperature, at each node point. The convection element is applicable to a 2D or 3D, steady-state or transient thermal analysis. The element is defined by two nodes, a convection surface area, two empirical terms, and a film coefficient.

##### 3.2.3 LINK31-radiation link

LINK31 is a uniaxial element which models the radiation heat flow rate between two points in space. The link has a single degree of freedom, temperature, at each node. The radiation element is applicable to a 2D or 3D, steady-state or transient thermal analysis.

The element is defined by two nodes, a radiating surface area, a geometric form factor, the emissivity, and the Stefan-Boltzmann constant.

### 3.2.4 MASS71-thermal mass

MASS71 is a point element with one degree of freedom, temperature, at the node. The element may be used in a transient thermal analysis to represent a body having thermal capacitance capability but negligible internal thermal resistance, that is, no significant temperature gradients within the body. The lumped thermal mass element is applicable to a 1D, 2D, or 3D steady-state or transient thermal analysis.

The lumped thermal mass element is defined by one node and a thermal capacitance.

### 3.3 FEM Model

Figure 4 illustrates the FEM model. The heat source is modeled by a perfect conductor, which is represented by one LINK32 element. The heat generation rate of the source is input as  $HRR$  specified by  $NFSC$ . The compartment boundaries and the insulation coatings of the steel members are modeled using LINK32. Convection and radiation at fire or environment exposed surfaces are modeled using LINK34 and LINK31, respectively. Gas and steel volumes are modeled using MASS71. Radiation at opening is modeled using LINK31. Convection at opening by mass exchange is modeled using LINK34 with film coefficient of  $c_p \dot{m}_{gas} / A_o$ .

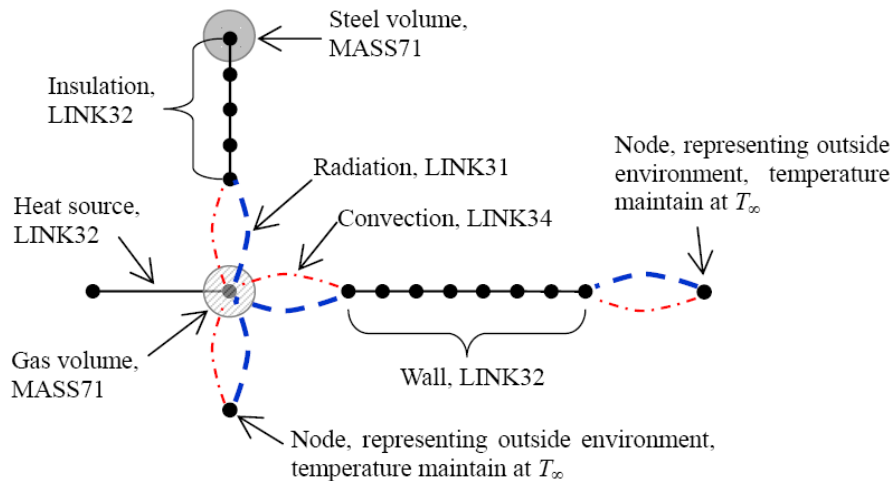


Figure 4. Illustration of the FEM Model

## 4. CASE STUDIES

### 4.1 Verification of FEM Model

Not including steel members in the proposed model, the results predicted by the proposed model simulated by FEM are compared with those predicted by the program OZone [4], Lie method [14] and EC1 parameter fire [2].

In the study, a compartment with dimensions of 3 m width, 4 m length and 2.7 m height are considered. The compartment has a vent of 2 m width and 1 m height. The compartment boundaries are made of normal weight concrete (NWC) with thickness of 200 mm. The properties of NWC are  $\rho_w=2300 \text{ kg/m}^3$ ,  $c_w=1000 \text{ J/(kg K)}$ , and  $k_w=1.6 \text{ W/(m K)}$ . The floor fire load density is  $800 \text{ MJ/m}^2$  and the fire intensity coefficient is 0.0117. The maximum heat release rate per unit area for fuel controlled fire is taken as  $250 \text{ kW/m}^2$ . Correspondingly, the calculated  $HRR_{max}$  for fuel and ventilation controlled fires are 2.25 MW and 3.0 MW respectively.



Figure 5 shows the comparison among the results of fire temperatures predicted by different methods. The FEM model and OZone give consistent results for both fuel ( $HRR_{max}=2.25$  MW) and ventilation ( $HRR_{max}=3$  MW) controlled fires, whilst in the heating phases the fire temperatures predicted by the FEM model are slightly higher than those predicted by OZone. The differences among the results by FEM model and OZone are due to different mathematic technologies adopted by them in solving sub-models in one zone post-flashover fire model [4]. Results by Lie method agree well with those by FEM model using  $HRR_{max}=2.25$  MW in the heating phases. Lie method and EC1 parameter fire give same results for fuel and ventilation controlled fires.

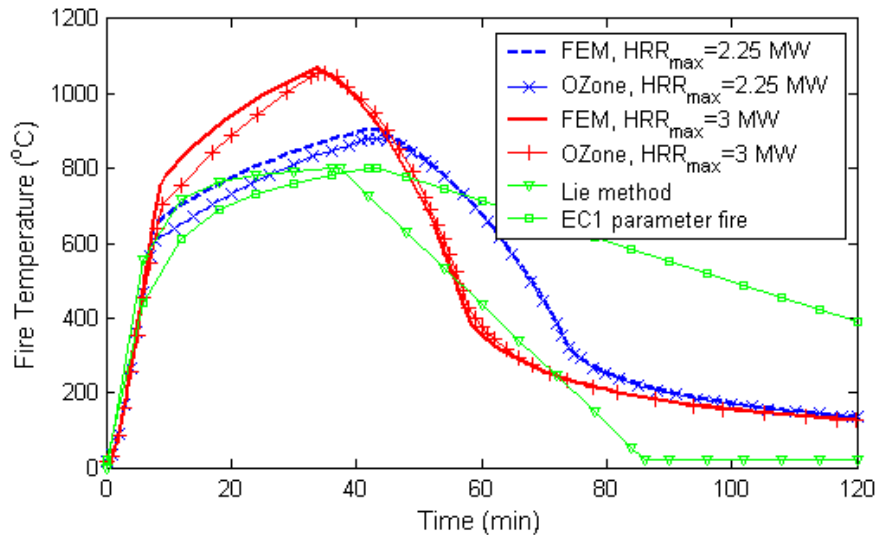


Figure 5. Comparison among Results of Fire Temperatures Predicted by Different Methods

## 4.2 Bare Steel Members

The fire compartment is 4.8 m width, 6.0 m depth and 3.6 m height. The compartment boundaries are made of 200 mm gypsum board, the properties of which are  $\rho_w=800$  kg/m<sup>3</sup>,  $c_w=1700$  J/(kg K) and  $k_w=0.2$  W/(m K). The compartment has a vent of 4.8 m width and 1.8 m height. The floor fire load density is 600 MJ/m<sup>2</sup> and the fire intensity coefficient is 0.0117. Including steel members in the FEM model, the effect of steel members within the compartment on gas and steel temperatures are investigated. Ventilation controlled fires are considered in the following studies. The cross section of the steel member is H300×300×10×15 and the length of the member is taken as the height of the compartment.

Figure 6 shows the results of gas temperatures with different number of steel members in the compartment. The more the number of steel members, the lower is the gas temperatures. For the case with 4 steel members, the predicted maximum gas temperature is about 46 °C lower than that for the case with no steel member. Figure 7 shows the results of steel temperatures. For the case with no steel in the compartment, the steel temperature is calculated by solving the 1D condensed heat transfer model (Figure 2) with using the predicted fire curve. The more the number of steel members, the lower is the steel temperatures. For the case with no steel member, the predicted maximum steel temperature is about 31 °C higher than that for the case with 4 steel members.

Figures 8 and 9 show the results of steel temperatures for compartments with different floor and opening areas, respectively. Taking  $\Delta T_{s,max}$  as the difference between the maximum steel temperatures for the same compartment with no steel member and with 4 steel members,  $\Delta T_{s,max}$  decreases with compartment floor area increases, and increases with opening area increases.

Figure 10 shows the results of steel temperatures for compartments with different fire loads.  $\Delta T_{s,max}$  decreases with fire load increases.

For the investigated cases, the maximum value of  $\Delta T_{s,max}$  is 219 °C, which is for the case with  $q_f=300$  MJ/m<sup>2</sup> and is shown in Figure 10.

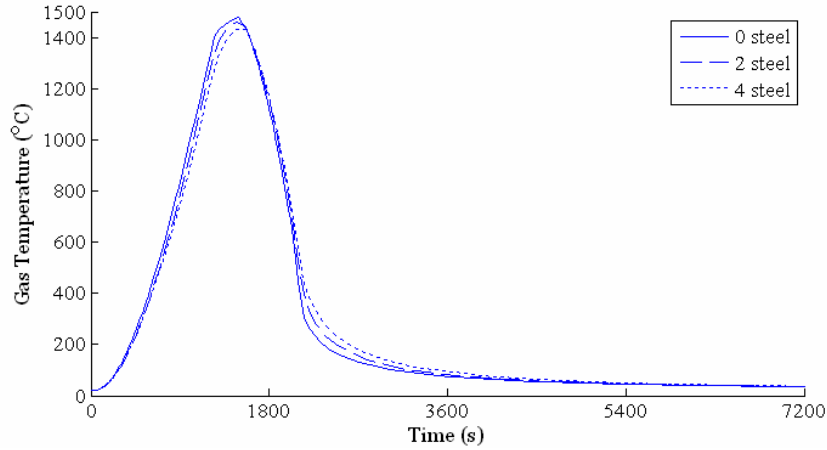


Figure 6. Results of Gas Temperatures for a Compartment with Different Number of Steel Members in it

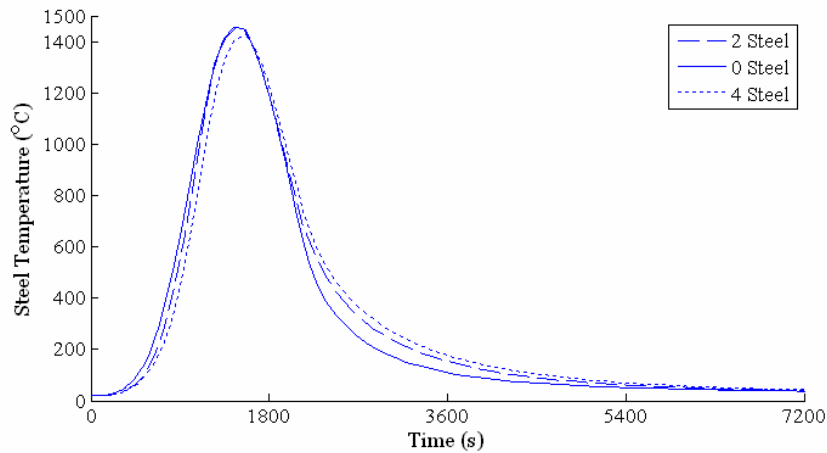


Figure 7. Results of Steel Temperatures for a Compartment with Different Number of Steel Members in it

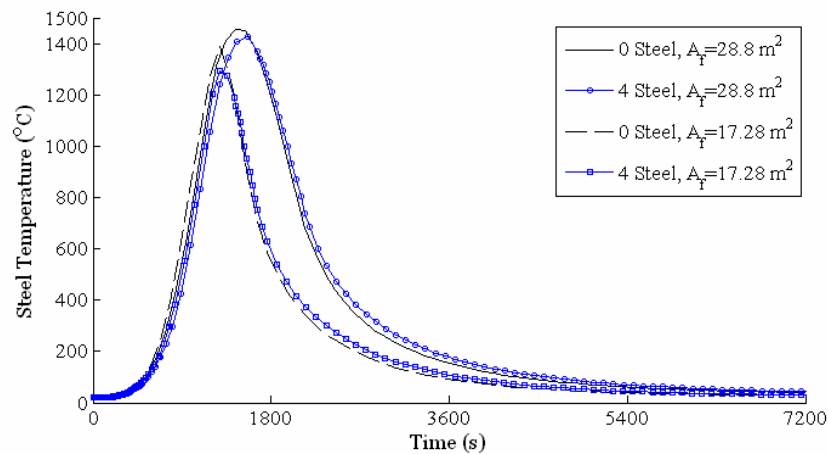


Figure 8. Results of Steel Temperatures for Compartments with Different Floor Areas

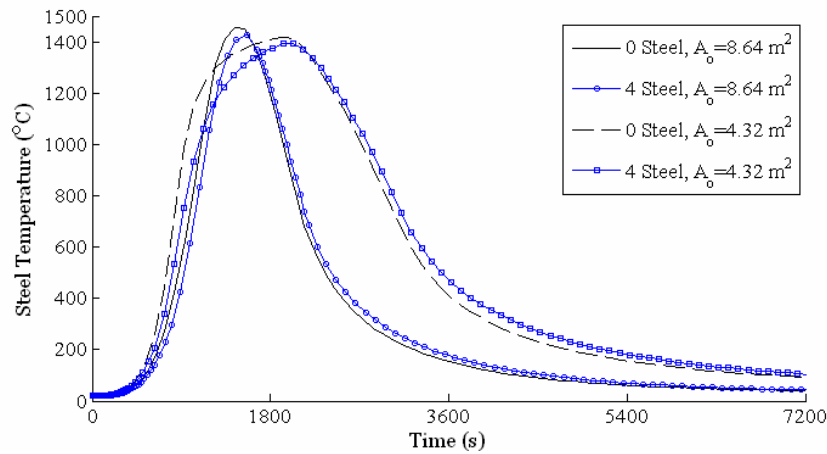


Figure 9. Results of Steel Temperatures for Compartments with Different Opening Areas

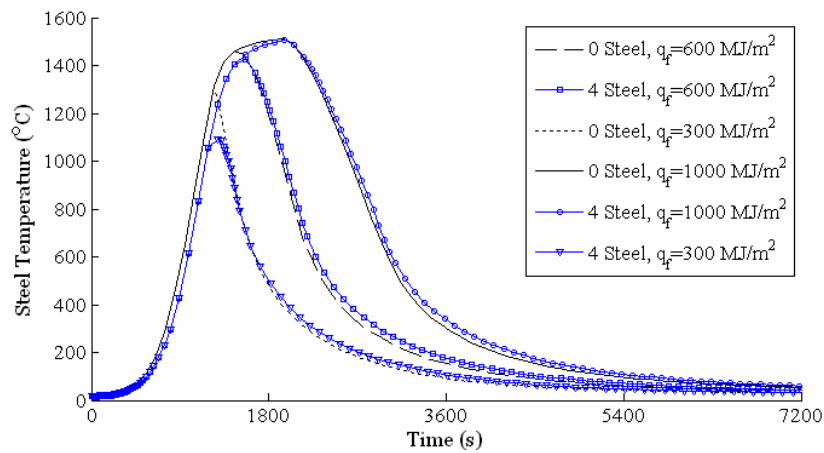


Figure 10. Results of Steel Temperatures for Compartments with Different Fire Loads

### 4.3 Insulated Steel Members

Figures 11 to 14 show the results for insulated steel members in fire compartments. The insulation material is a commonly used SFRM, the properties of which are  $\rho_i=250 \text{ kg/m}^3$ ,  $c_i=800 \text{ J/(kg K)}$  and  $k_i=0.12 \text{ W/(m K)}$ . The difference between the maximum steel temperatures for cases with no insulated member and with 4 insulated member,  $\Delta T_{s,max}$ , decreases with floor area decreases, opening area increases, fire load decreases, and insulation thickness increases.

For the investigated cases, the maximum value of  $\Delta T_{s,max}$  is  $38^\circ\text{C}$ , which is for the case with  $A_o=4.32 \text{ m}^2$  and is shown in Figure 12.

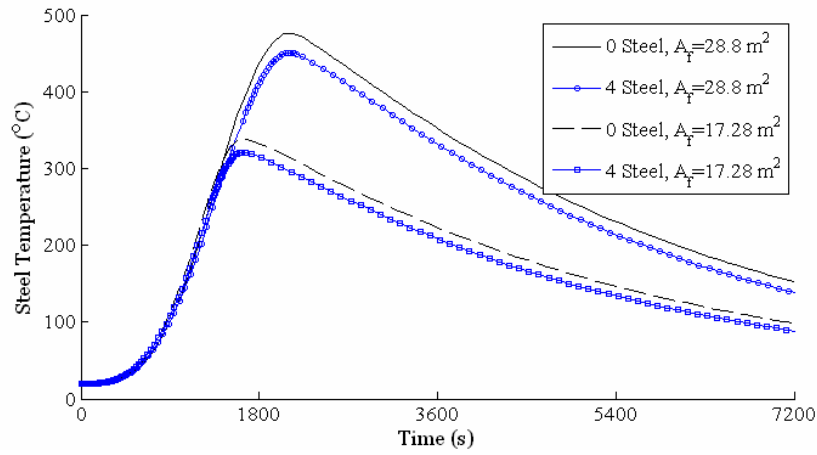


Figure 11. Results of Steel Temperatures of Insulated Members in Compartments with Different Floor Areas

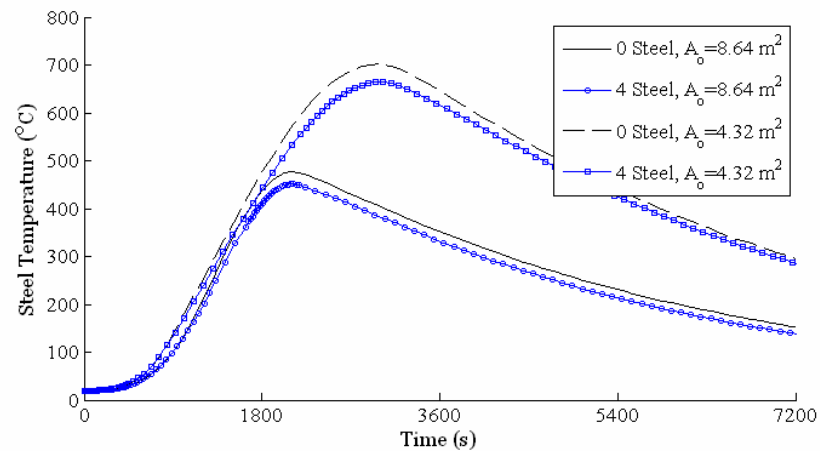


Figure 12. Results of Steel Temperatures of Insulated Members in Compartments with Different Opening Areas

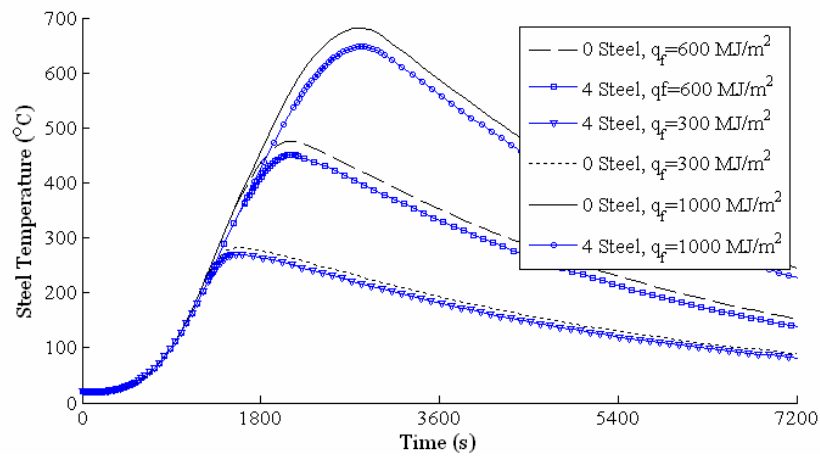


Figure 13. Results of Steel Temperatures of Insulated Members in Compartments with Different Fire Loads

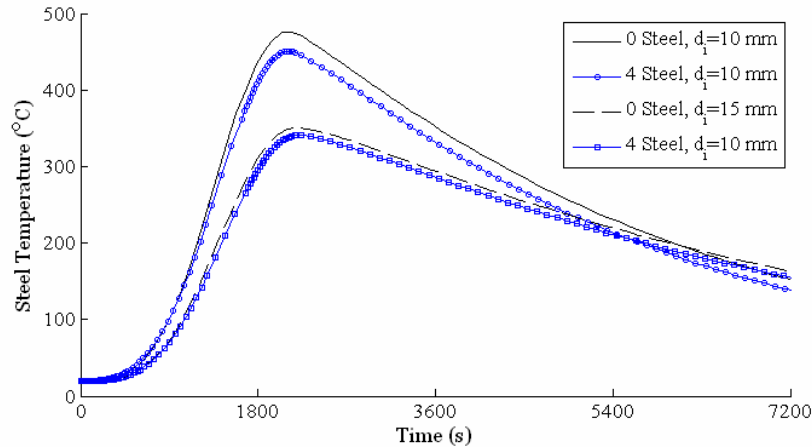


Figure 14. Results of Steel Temperatures of Insulated Members with Different Insulation Thicknesses

## 5. DESIGN EXAMPLE

**Problem:** 4 steel columns are located at different corners of a fire compartment in an office building. The compartment is 4.8 m width, 6.0 m length and 3.6 m height, and is made of gypsum board with thickness of 200 mm. The compartment has a window with dimensions of 2.4 m width and 1.8 m height. The compartment has two fire doors which are assumed to be closed in fire condition. The design fire load density is taken as  $600 \text{ MJ/m}^2$ . The dimensions of the columns are designed to be  $\text{H}400 \times 400 \times 15 \times 20$ . Take column failure temperature as  $550^\circ\text{C}$ , determine the fire protection of the columns.

**Design by the proposed model:** The calculated bare steel column temperature obtained through solving the modified one-zone model,  $T_{s,max}$ , is close to the fire temperature and taken as  $1356^\circ\text{C}$ . Adopting the commonly used SFRM considered above as the fire protection material, the calculated minimum insulation thickness is 9.7 mm ( $T_{s,max}=548^\circ\text{C} < 550^\circ\text{C}$ ).

**Design by the current model:** The calculated fire temperature obtained through solving the traditional one-zone model is  $1422^\circ\text{C}$ . Adopting the commonly used SFRM, the calculated minimum insulation thickness through solving the 1D condensed heat transfer model given in Figure 2 is 10.8 mm ( $T_{s,max}=549^\circ\text{C} < 550^\circ\text{C}$ ).

The difference between the minimum insulation thickness determined by the traditional and proposed model is 1.1 mm.

## 6. CONCLUSIONS

In real conditions, the steel members in a fire compartment will absorb a portion of the heat released by combustion. That position of heat is the reason that causes steel temperature elevation, and in turn it has effect of cooling the compartment. In this paper, a modified one-zone model has been proposed for calculating the temperature of steel members in post-flashover fires. Based on the results of this study, the following conclusions can be drawn:

- The proposed model has capacity of modeling the heating mechanism of steel members in post-flashover fires, which is recommended for practical usage. Based on the proposed model, computing program or analytical formulae can be derived for daily design work.

- The proposed model can yield more economical fire resistance design than the current model. For the considered design example of an office building, the proposed model can save 1.1 mm fire protection material for each steel column.
- For fire compartments with bare steel members, the steel heat sink effect is greater for compartments with smaller floor area, larger opening, lower fire load density, and more steel members. Correspondingly, the over-predictions of the maximum steel temperatures by the current model are comparatively more severe for those compartments.
- For fire compartments with insulated steel members, the steel heat sink effect is greater for compartments with larger floor area, smaller opening, higher fire load density, and more steel members with thinner insulation. Correspondingly, the over-predictions of the maximum steel temperatures by the current model are comparatively more severe for those compartments.

## NOMENCLATURE

$HRR$	heat release rate (kW)
$\dot{q}_g$	rate of heat storage in the gas volume (kW)
$\dot{q}_w$	rate of heat loss through the walls, ceiling and floor (kW)
$\dot{q}_{o,c}$	rate of heat loss due to replacement of hot gases by cold (kW)
$\dot{q}_{o,r}$	rate of heat loss by radiation through the openings (kW)
$\dot{q}_s$	rate of heat storage in steel members (kW)
$\dot{m}_{air}$	mass rate of inflow (kg/s)
$\dot{m}_{gas}$	mass rate of outflow (kg/s)
$\Delta H_{air}$	heat released per unit mass air consumed (MJ/kg)
$t$	time
$q_f$	floor fire load density (kJ/m <sup>2</sup> )
$A_f$	floor area (m <sup>2</sup> )
$A_o$	vent area (m <sup>2</sup> )
$W_o$	vent width (m)
$H_o$	vent height (m)
$C_d$	flow coefficient
$X_N$	neutral plane height (m)
$X_d$	height of interface (m)
$T_\infty, T_f$	ambient and hot gas temperature (°C or K)
$T_w, T_s$	wall and steel temperature (°C or K)
$c_p$	specific heat of air (kJ/kg K)
$c_w, c_i$	specific heat of wall or slab, and insulation (kJ/kg K)
$k_w, k_i$	thermal conductivity of wall or slab, and insulation (W/m K)
$\rho_\infty$	density of air (kg/m <sup>3</sup> )
$\rho_w, \rho_i$	density of wall or slab, and density of insulation (kg/m <sup>3</sup> )
$\alpha$	fire intensity coefficient
$\alpha_w$	thermal diffusivity of wall or slab
$\varepsilon_f, \varepsilon_w$	emissivity of fire and wall

$\sigma$	Stefan-Boltzmann constant
$d_w, d_i$	wall or slab thickness, and insulation thickness (mm)
$h_c, h_r$	convective and radiative heat transfer coefficient ( $\text{W/m}^2 \text{ K}$ )

## REFERENCES

- [1] Drysdale, D., "An introduction to Fire Dynamics", 2nd Edition, John Wiley and Sons, 1999.
- [2] EC1-1-2. Eurocode 1: Actions on Structures - Part 1-2: General Actions - Actions on Structures Exposed to Fire, British Standards Institution (BSI), 2002.
- [3] Babrauskas, V., "COMPF2: A Program for Calculating Post-flashover Fire Temperatures", NBS Technical Note 991, National Bureau of Standards, 1979.
- [4] Cadorin, J.F. and Franssen, J.M., "A Tool to Design Steel Elements Submitted to Compartment Fires - OZone V2, Part 1: Pre- and Post-flashover Compartment Fire Model", Fire Safety Journal, 2003, Vol. 38, pp. 395-427.
- [5] Jones, W.W., Peacock, R.D., Forney, G.P. and Reneke, P.A., "CFAST - Consolidated Model of Fire Growth and Smoke Transport (Version 6): Technical Reference Guide", NIST Special Publication 1026, Gaithersburg : National Institute of Standard and Technology, 2009.
- [6] McGrattan, K., McDermott, R., Hostikka, S. and Floyd, J., "Fire Dynamics Simulator (Version 5) User's Guide", NIST Special Publication 1019-5, National Institute of Standards and Technology (NIST), 2010.
- [7] Li, G.Q. and Zhang, C., "Thermal Response to Fire of Uniformly Insulated Steel Members: Background and Verification of the Formulation Recommended by Chinese Code CECS200", Advanced Steel Construction, 2010, Vol. 6, pp. 788-802.
- [8] Zhang, C. and Li, G.Q., "Thermal Response of Steel Columns Exposed to Localized Fires – Numerical Simulation and Comparison with Experimental Results", Journal of Structural Fire Engineering, 2011, Vol. 2, pp. 311-7.
- [9] Pettersson, O., Magnusson, S.E. and Thor, J., "Fire Engineering Design of Steel Structures", Swedish Institute of Steel Construction, Publication 50, Stockholm, 1976.
- [10] Buchanan, A.H., "Structural Design for Fire Safety", John Wiley and Sons, Ltd, 2001.
- [11] Babrauskas, V., SFPE Handbbok of Fire Protection Engineering, 3rd edition, Section 3-1:Heat Release Rates, Society of Fire Protection Engineers, 2002.
- [12] McCaffrey, B.J., Quintiere, J.G. and Harkleroad, M.F., "Estimating Room Temperatures and Likelihood of Flashover using Fire Test Data Correlations", Fire Technology, 1981, Vol. 17, pp. 98-119.
- [13] Zhang, C., Li, G.Q. and Wang, Y.C., "Sensitivity Study on using Different Formulas for Calculating the Temperatures of Insulated Steel Members in Natural Fires", Fire Technology, 2012, Vol. 48, pp. 343-66.
- [14] Lie, T.T., "Fire Temperature-time Relations", SFPE Handbook of Fire Protection Engineering, 3rd Edition, Society of Fire Protection Engineers, 2002.

# TEMPERATURE DISTRIBUTION AND STRUCTURAL BEHAVIOR OF BOX-SECTIONAL ARCH STRUCTURES UNDER SOLAR RADIATION

Hongbo Liu<sup>1</sup>, Zhihua Chen<sup>1,2,\*</sup> and Ting Zhou<sup>1</sup>

<sup>1</sup> Department of Civil Engineering, Tianjin University, Tianjin 300072, China

<sup>2</sup> Tianjin Key Laboratory of Civil Engineering Structure & New Materials, Tianjin University, Tianjin 300072, China

\*(Corresponding author: E-mail: zhchen@tju.edu.cn)

Received: 24 March 2012; Revised: 25 May 2012; Accepted: 31 May 2012

**ABSTRACT:** The temperature change of large-span steel arch structures normally appears when the structures are exposed to solar radiation, which may result in large displacement and stress. Therefore, there has been growing attention to both temperature distribution and structural response of the structures under the solar radiation. In order to investigate the response of large-span box-sectional steel arch structures formed by rectangular steel tubes, one rectangular steel tube specimen was designed and its temperature was measured under solar radiation. A numerical method was presented according to transient thermal analysis and then verified by experimental results. Both experimental and numerical results showed that the solar radiation had a significant effect on the temperature distribution of rectangular steel tubes. Considering the solar radiation, the temperature of rectangular steel tubes is about 18.1°C higher than the corresponding ambient air temperature in summer. Moreover, the temperature distribution under solar radiation is extremely nonlinear. In order to study the structural response induced by the temperature change due to the solar radiation, a steel arch structure model is designed and the structural response due to temperature change is also investigated on this model. The results showed that the solar radiation has a remarkable effect on the thermal load response of large-span steel structures. The effect of the solar radiation has to be considered in the design process of large-span steel arch structures.

**Keywords:** Effective box-sectional steel arch structures, Temperature change, Solar radiation, Rectangular steel tube, Numerical analysis, Structural response

## 1. INTRODUCTION

In recent years, large-span steel structures, such as arch structures, beam string structures, suspen-dome structures, lattice shell structures and cable-strut structures, are widely adopted as the roof structures of stadiums, gymnasiums, conference, exhibition center, train stations, airport and so on. Most constructed steel structures have a span more than 200 m. For example, the arch structures of the Baita Airport, Inner Mongolia, China is 205 m as shown in Figure 1. Due to the large span, the steel structure is sensitive to the thermal change, especially when exposed to solar radiation. Therefore, the thermal load is usually the control load for large-span steel structures and there has been growing attention to the structural behavior of steel structures under thermal change.



Figure 1. Baita Airport, Inner Mongolia, China



Alinia and Kashizadeh conducted some work on the structural behavior of spherical double layer space truss domes under uniform thermal load [1-3]. However, for the steel structures exposed to solar radiation, its temperature is much larger and more non-uniformly distributed than the corresponding ambient air temperature in summer. If the effect of solar radiation on the temperature of steel structures is not considered properly, the steel structure may potentially fail due to over-large temperature change. However, only a few published papers were reported on the temperature distribution of steel structures under solar radiation. In addition, a number of researchers drew inconsistent conclusions on this problem. For example, three maximal temperatures under solar radiation for steel structures proposed by Fan et al. [4], Wang et al. [5] and Xiao et al. [6] are  $50^{\circ}\text{C}$ ,  $60^{\circ}\text{C}$  and  $80^{\circ}\text{C}$ , respectively. Therefore, this inconsistency may make the one confused to determine the thermal effect in the design process.

The available references, on the thermal effect due to the solar radiation, have focused on bridges [7-8], dams [9-10] and pavements [11-12]. Considering the large structural difference among large-span steel structures, bridges, dams and pavements, the proposed numerical methods in these papers are not directly applied to large-span steel structures. Therefore, it is important to understand the temperature distribution of large-span steel structures under solar radiation through both experimental and numerical studies.

In this study, an experiment first was conducted to provide insights into the temperature distribution of steel members under solar radiation in summer, as well as to verify a following numerical simulation method. And then the numerical simulation method is presented for the temperature distribution analysis of steel members under solar radiation. This method is further verified by the test data. Using the numerical simulation method, the temperature distribution of an arch structure under solar radiation in summer is analyzed. Meanwhile, the structural behavior under thermal effect is also studied to give the temperature-induced response of large-span steel arch structures.

## 2. EXPERIMENTAL STUDY

### 2.1 Experiment Program

A rectangular steel tube specimen was designed and measured to obtain its temperature distribution under solar radiation as shown in Figure 2. Figure 3 presents twelve measured points designed for this specimen. In this test, infra-red temperature meter was used to obtain the temperature value of each measured point.



Figure 2. Specimen in Test Site

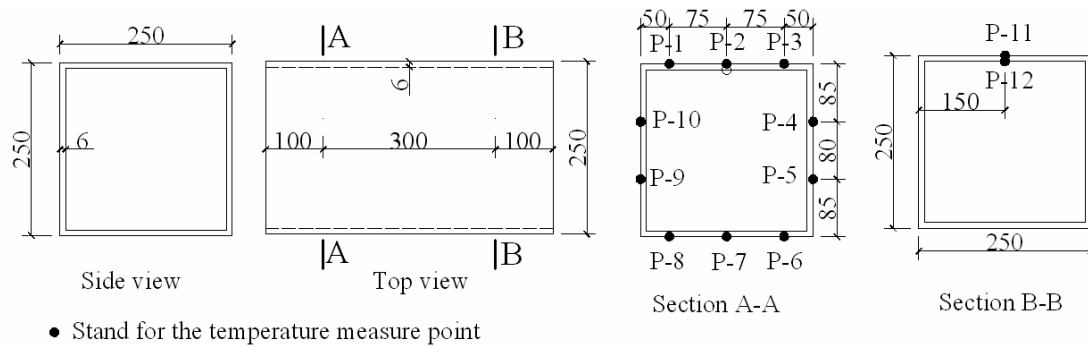


Figure 3. Arrangement of Temperature Measure Points of the Rectangular Steel Tube Specimen

## 2.2 Experiment Result

For the rectangular steel tube specimen, the temperature values of all measure points arranged in Figure 3 were obtained at 6:00 am, 8:00 am, 10:00 am, 12:00 am, 13:00 pm, 14:00 pm, 15:00 pm, 16:00 pm, 17:00 pm, 18:00 pm and 19:00 pm on 22th, 23th and 24th July, 2010.

The temperature-time curve for the maximal temperature point (Point 2) and the minimal temperature point (Point 7) are shown in Figure 4 and Figure 5. The temperature values for all measure points at 14 pm are given in Figure 6 and Figure 7. The following conclusions can be drawn on the test results:

- 1) The temperature-time curve for Point 2 and Point 7 is similar to sine curve as shown in Figure 4 and Figure 5.
- 2) The maximal temperature value obtained in this experiment is  $52.3^{\circ}\text{C}$ ,  $18.1^{\circ}\text{C}$  higher than the corresponding ambient air temperature with a value of  $34.2^{\circ}\text{C}$ ; and the maximal temperatures usually occur at 12:00~14:00 as shown in Figure 4, Figure 5 and Table 1.
- 3) The temperature of the specimen begins to increase and then decrease from Point 1 to Point 10 at 14:00 pm as shown in Figure 6. Therefore, the temperature distribution is non-uniform on the whole specimen. However, for the upper steel plate and low steel plate in the rectangular steel tube specimen, their temperature distribution is almost uniform.
- 4) The temperature-time curve of Point 11 is identical to that of Point 12 as shown in Figure 7. Therefore, the temperature distribution in thickness direction is uniform.
- 5) The temperature-time curve of Point 2 is identical to that of Point 11 as shown in Figure 7. Therefore, the temperature in the longitudinal direction is uniform if the two ends of rectangular steel tubes are close to each other.

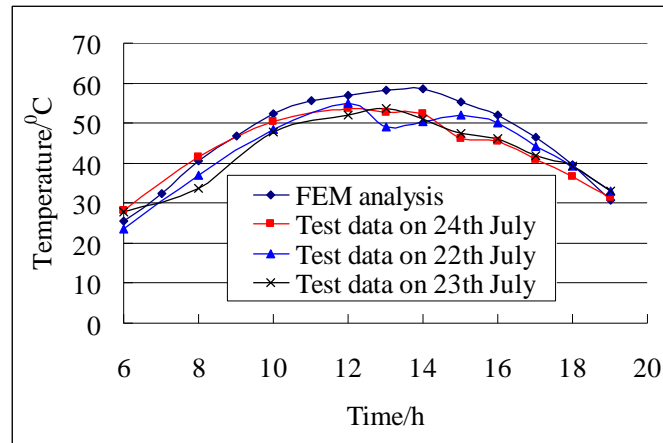


Figure 4. Time-temperature Curve of Point 2

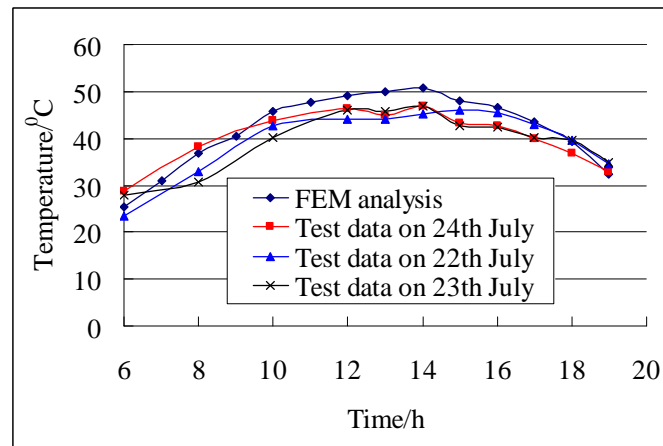


Figure 5. Time-temperature Curve of Point 7

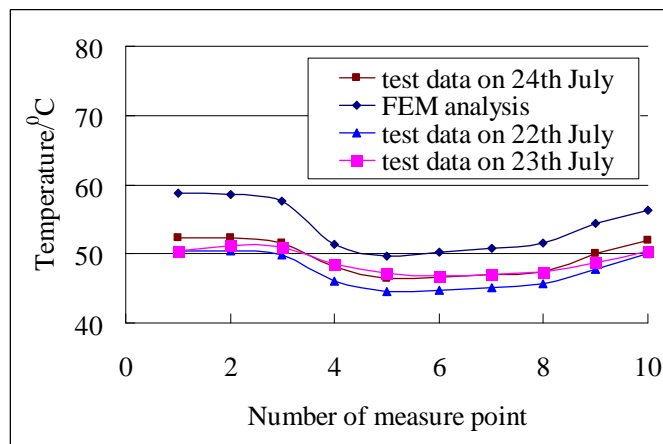


Figure 6. Temperature of All Points at 14:00 pm

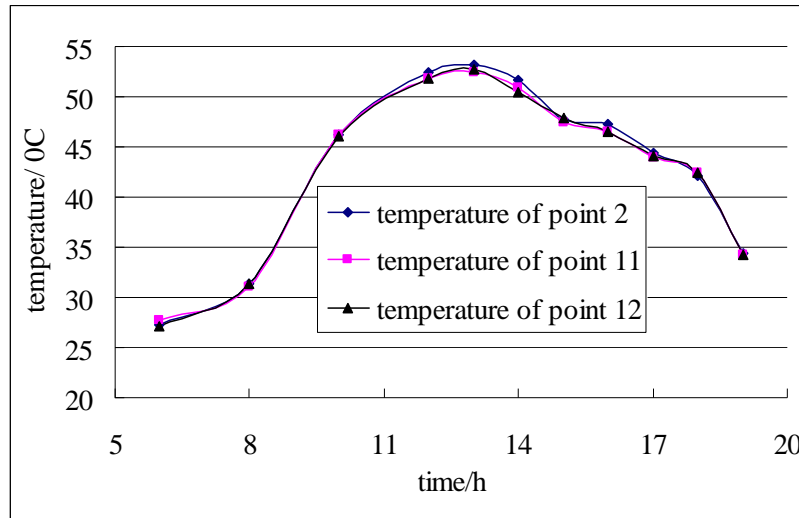


Figure 7. Time-temperature Curves of Point 1 and Point 10 on 22th July, 2010

Table 1. Minimal and Maximal Temperature Values of the Rectangular Steel Tube Specimen at 14:00

Item	$T_{\text{test22}}$	$T_{\text{test23}}$	$T_{\text{test24}}$	$T_{\text{FEM}}$	error-max
Min temperature	44.7	46.9	46.4	48.98	8.74%
Max temperature	50.4	51.1	52.3	59.07	14.68%

### 3. NUMERICAL SIMULATION

#### 3.1 Heat Conduction Equation

According to previous references, the thermal properties of steel material are assumed to be uniform and isotropic. Considering that there is no heat generation within rectangular steel tubes, the general transient governing equation for heat conduction in a three dimensional solid region  $\Omega$  can be expressed as follows:

$$\alpha \left( \frac{\partial^2 T}{\partial x^2} + \frac{\partial^2 T}{\partial y^2} + \frac{\partial^2 T}{\partial z^2} \right) = \frac{\partial T}{\partial t} \quad (1)$$

where  $\alpha = \lambda / \rho c$ ;  $\lambda$  is thermal conductivity ( $\text{W}/\text{m}^2 \cdot ^\circ\text{C}$ );  $\rho$  is material's density ( $\text{kg}/\text{m}^3$ );  $c$  is specific heat ( $\text{J}/\text{kg} \cdot ^\circ\text{C}$ ).

#### 3.2 Boundary Conditions

In the process of thermal analysis using a three-dimensional finite element, the temperature boundary conditions should be first determined. For the rectangular steel tubes, the temperature is affected by solar radiation, convection heat transfer and long wave radiation heat transfer. Therefore, the temperature boundary condition is defined as:

$$\lambda \frac{\partial T}{\partial n} \Big|_{\Gamma} = h [T_a(t) - T] + q_s(t) + q_L(t) \quad (2)$$

Where  $h$  is heat convection coefficient ( $W/m^2 \cdot ^\circ C$ );  $T_a$  is ambient air temperature;  $q_s$  is solar radiation ( $W/m^2$ );  $q_l$  is long wave radiation ( $W/m^2$ ).

### 3.3 Solar Radiation Model

The ASHRAE clear-sky model was adopted in this study to evaluate the solar radiation on the surface of rectangular steel tubes [13]. In this model, the total global solar radiation is assumed to be the sum of direct radiation, diffuse radiation, and the solar radiation reflected from the surrounding surface. On a clear day, the value of solar radiation at the earth's surface is defined as

$$G_{ND} = \frac{A}{\exp(B/\sin \beta)} C_N \quad (3)$$

Where:  $G_{ND}$  = normal direct radiation,  $W/m^2$ ;  $A$  = apparent solar radiation at air mass equal to zero,  $W/m^2$ ;  $B$  = atmospheric extinction coefficient;  $\beta$  = solar altitude;  $C_N$  = clearness number  
Based on the ASHRAE model, the total solar radiation incident on a non-vertical surface can be evaluated by Eq. 4 :

$$q_s = \varepsilon \left[ \max(\cos \theta, 0) + CF_{ws} + \rho_g F_{wg} (\sin \beta + C) \right] G_{ND} \quad (4)$$

$$F_{ws} = (1 + \cos \alpha)/2 \quad (5)$$

$$F_{wg} = (1 - \cos \alpha)/2 \quad (6)$$

Where  $\varepsilon$  is the solar radiation absorptivity;  $\theta$  is the angle of incidence between the sun's rays and the normal to the surface;  $\alpha$  is tilt angle;  $C$  is obviously the ratio of diffuse irradiation on a surface to direct normal radiation;  $F_{ws}$  the angle factor between the surface and the sky;  $F_{wg}$  is the configuration or angle factor from surface wall to ground;  $\rho_g$  is the solar radiation reflectance of ground or horizontal surface

Similarly, the total solar radiation incident on a vertical surface can be given by following equations:

$$q_s = \varepsilon \left[ \max(\cos \theta, 0) + \frac{G_{dV}}{G_{dH}} C + \rho_g F_{wg} (\sin \beta + C) \right] G_{ND} \quad (7)$$

$$\frac{G_{dV}}{G_{dH}} = \begin{cases} 0.55 + 0.437 \cos \theta + 0.313 \cos^2 \theta & \theta > -0.2 \\ 0.45 & \text{otherwise} \end{cases} \quad (8)$$

The parameters A, B, and C can be determined according to the characteristics of solar radiation at the experiment site. Unfortunately, this information is not yet available. To overcome this problem, the following expressions of parameters A, B, and C for Beijing, near to test site, were adopted to evaluate solar radiation [14].

### 3.4 Long Wave Radiation

The long wave radiation on the surface of rectangular steel tubes can be expressed by the Stefan-Boltzmann equation [13]:

$$q_l = \varepsilon_f \sigma (F_{wg} (T_g^4 - T^4) + F_{ws} (T_{sky}^4 - T^4)) \quad (9)$$

Where  $\varepsilon_f$  is the ratio of the radiation emitted by a surface;  $\sigma$  is Stefan-Boltzmann constant  $= 5.67 \times 10^{-8} \text{ W}/(\text{m}^2 \cdot \text{K}^4)$ ;  $T_{sky}$  is the effective temperature of sky, usually calculated by  $T_a - 6$ ;  $T_g$  is the ground temperature.

### 3.5 Numerical Investigation

A finite element model is established using ANSYS software, and a three-dimensional thermal conduction element SOLID70 is used to simulate the rectangular steel tube specimen. The physical properties of steel material and the main parameters used in the study are listed in Table 2.

Table 2. Parameters Adopted in Calculation

Parameters	Convection coefficient $\text{W}/(\text{m}^2 \cdot ^\circ\text{C})$	Specific heat capacity $\text{J}/(\text{kg} \cdot ^\circ\text{C})$	Thermal conductivity $\text{W}/(\text{m} \cdot ^\circ\text{C})$
Values	13.3	480	56
Parameters	Absorptivity	Density ( $\text{kg}/\text{m}^3$ )	Emissivity
Values	0.6	7850	0.8
Parameters	Coefficient A	Coefficient B	Coefficient C
Values	1326.54	0.404	0.181
Parameters	Ground radiation reflectance $\rho_g$	$c_N$	
Values	0.15	1.0	

The temperature obtained from the transient thermal analysis of the specimen was also shown in Figure 4 through Figure 7 and Table 1.  $T_{\text{FEL}}$  (obtained from the finite element analysis) was generally larger than  $T_{\text{T}}$  (obtained from test) by a factor of 1.0 to 1.5. Therefore, the strength  $T_{\text{FEL}}$  was generally consistent with the test results, with a maximum difference of 14.68%.

Reasons attributing to the discrepancies may include variance in the solar radiation model, variance in solar radiation absorption and ground reflectance, precision of infra-red temperature meter, etc. In the test process, the clouds might shelter against solar radiation, and it decreased the temperature of the rectangular steel tube specimen. Considering the above arguments, the numerical results for the rectangular steel tube specimen were then considered generally precise, and the transient models can be used for the following parametric study.

The temperature distribution of the rectangular steel tube specimen at 14:00 on 22th July 2010 is shown in Figure 8(a). From this figure, the temperature field under solar radiation is found to be very non-uniform. However, because the two ends of rectangular steel tubes are close to each other in practice, the temperature field of the specimen is analyzed under the condition that the solar radiation cannot irradiate the inner surface of specimen. The corresponding temperature field is shown in Figure 8(b). The numerical results showed the temperature is longitudinally uniform if the two ends of rectangular steel tube is close to each other.

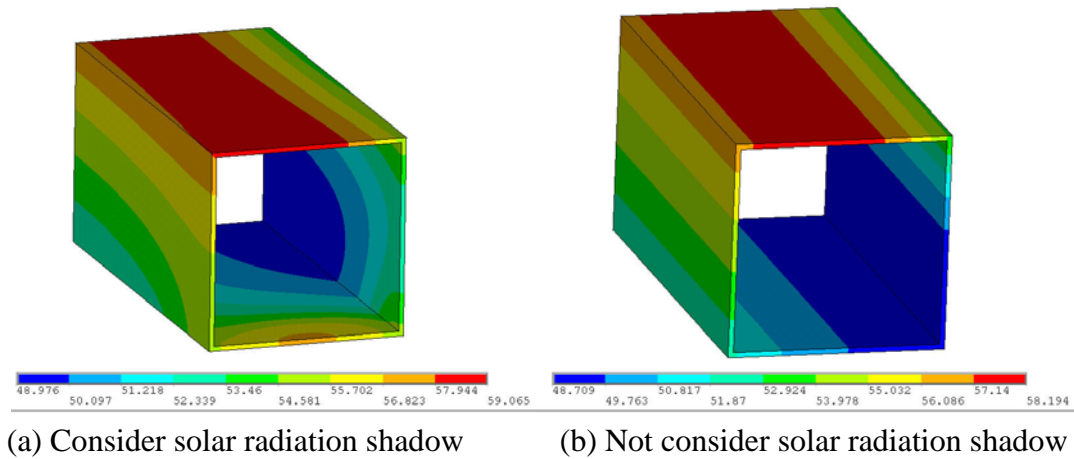


Figure 8. Temperature Distribution of the Rectangular Steel Tube Specimen at 14:00 pm on 22th July 2010

## 4. APPLICATION

### 4.1 A Steel Arch Structure Model

In order to understand the temperature distribution and thermal behavior of large-span arch structures, a steel arch structure was designed as shown in Figure 10. Its span and rise is 200 m and 40 m, respectively. The tapered rectangular steel tubes were used as the members. For the tapered rectangular steel tube, its flange width is constant with a value of 1.4 m, and its web height ranges from 1.4 m at the mid-span to 1.8 m at both ends.

The model consists of 89 structural members with rectangular sections. Each structural member includes four areas. Therefore, 356 areas are included in this model. The area number of Area A is 1 ~ 89 from End J to End I. The area number of Area B is 90 ~ 178 from End J to End I. The area number of Area C is 179 ~ 267 from End J to End I. The area number of Area D is 268 ~ 356 from End J to End I.

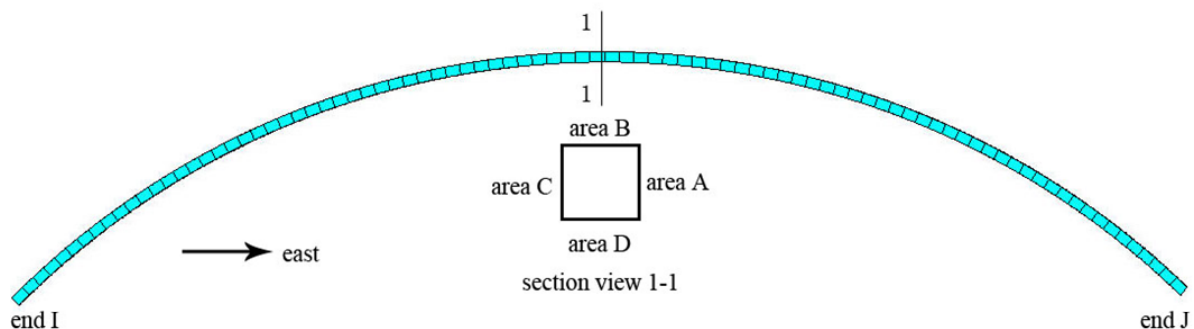


Figure 10. The Model of the Arch Structure in ANSYS

### 4.2 Temperature Distribution Simulation

Using the numerical simulation method presented in this paper, the temperature distribution of the steel arch structure model on 21th June was analyzed. The temperature distribution of the model at 14:00 p.m. is shown in Figure 11. The average temperatures for all areas at 6:00 a.m., 14:00 p.m. and 19:00 p.m. are shown in Figure 12. From the figures, the following conclusions are obtained:

- 1) The maximal temperature for the studied model occurred at 14:00 p.m. and the value is  $65.28^{\circ}\text{C}$ .
- 2) The temperature distribution is very no-uniform and the temperature variance is up to  $20^{\circ}\text{C}$ . At 14:00 p.m., the average temperature of Area B is the largest; the average temperature of Area D is the smallest.
- 3) The temperature change is large from sunrise to sundown. It is up to  $40^{\circ}\text{C}$  during a day

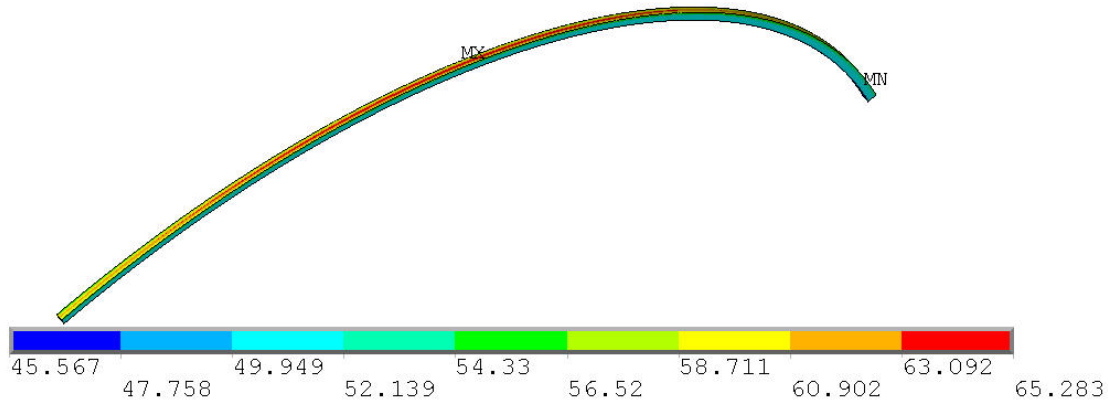


Figure 11. The Temperature Distribution of the Studied Model at 14:00 p.m.

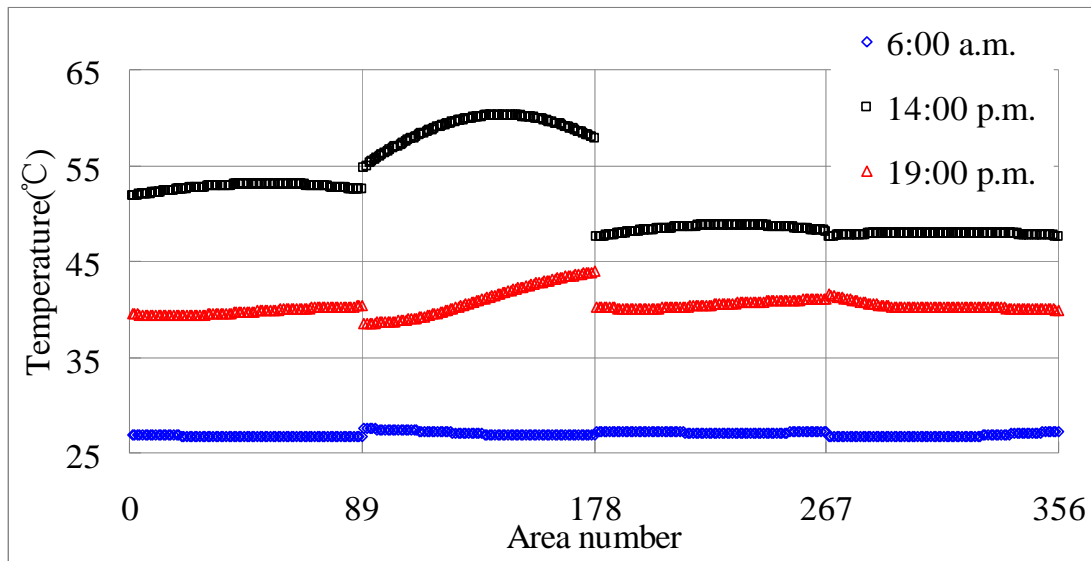


Figure 12. The Average Temperatures for All Areas at 6:00 a.m., 14:00 p.m. and 19:00 p.m.

### 4.3 Thermal Behavior

Assume that the highest and the lowest air temperature for the steel arch structure model location is  $40^{\circ}\text{C}$  and  $-20^{\circ}\text{C}$ , respectively. If the effect of solar radiation is not considered, the heating temperature should be  $10^{\circ}\text{C}$ . In order to investigate the effect of solar radiation on the thermal-induced response of the model, two cases are designed. The solar radiation is not considered in the first case, and this case denote as Case A. The positive thermal value in Case A is uniform and the value is  $30^{\circ}\text{C}$ . The solar radiation is considered in the other case, and this case denote as Case B. The positive thermal value in Case B is no-uniform load and the value fluctuates from  $35.57^{\circ}\text{C}$  to  $55.28^{\circ}\text{C}$ .



The support conditions at the two ends are assumed to be pinned. Compared with the maximum equivalent stress of 84.2 MPa and the maximum node displacement of 99 mm of Case A, the corresponding values of Case B are 150.6 MPa (78.86% increased) and 165 mm (66.67% increased), respectively. Therefore, the solar radiation has a remarkable effect on the thermal-induced response of large span steel structures.

## 5. CONCLUSIONS

- 1) From the test result, the following conclusions are drawn: i) the temperature-time curve is similar to a sine curve; ii) the temperature obtained in this experiment is  $52.3^{\circ}\text{C}$ , it is  $18.1^{\circ}\text{C}$  higher than the corresponding ambient air temperature; iii) the maximal temperatures usually occur during 12:00~14:00 ; iv) the temperature field is very non-uniform under solar radiation.
- 2) The presented numerical simulation method on the temperature distribution of steel members under solar radiation is verified by the test data.
- 3) The solar radiation has a remarkable effect on the temperature-induced response of large-span steel structures.

## ACKNOWLEDGEMENTS

This work was supported by the National Natural Science Foundation of China (No. 51208355), China Postdoctoral Science Foundation funded project (No. 2012M510751) and the Independent innovation foundation of Tianjin University (No. 1102, No. 1104).

## REFERENCES

- [1] Alinia, M.M., Kashizadeh, S., "Effect of Flexibility of Substructures Upon Thermal Behaviour of Spherical Double Layer Space Truss Domes, Part I : Uniform Thermal Loading", *Journal of Constructional Steel Research*, 2006, Vol. 62, pp. 359-368.
- [2] Alinia, M.M., Kashizadeh, S., "Effect of Flexibility of Substructures upon Thermal Behaviour of Spherical Double Layer Space Truss Domes, Part II : Gradient & Partial Loading", *Journal of Constructional Steel Research*, 2006, Vol. 62, pp. 675-681.
- [3] Alinia, M.M., Kashizadeh, S., "Effects of Support Positioning on the Thermal Behaviour of Double Layer Space Truss Domes", *Journal of Constructional Steel Research*, 2007, Vol. 63, pp. 375-382.
- [4] Fan, Z., Wang, Z. and Tian, J., "Analysis on Temperature Field and Determination of Temperature upon Healing of Large-span Steel Structure of the National Stadium", *Journal of Building Structures*, 2007, Vol. 28, No. 2, pp. 32-40. (in Chinese)
- [5] Wang, Y.Q., Lin, C.C. and Shi, Y.J., "Experimental Study on the Temperature of Steel Members in Sunshine", *Journal of Building Structures*, 2010, Supplementary Issue 1, pp. 140-147. (in Chinese)
- [6] Xiao, J.C., Xu, H., Liu, J.K. and Ma, K.J., "The Influence of Intense Solar Radiation on Long-span Spatial Steel Structures", *Chinese Journal of Solid Mechanics*, 2010, Vol. 31 (Issue), pp. 275-280. (in Chinese)
- [7] Xu, Y.L., Chen, B., Ng, C.L., Wong, K.Y. and Chan, W.Y., "Monitoring Temperature Effect on a Long Suspension Bridge", *Structural Control and Health Monitoring*, 2010, Vol. 17, pp. 632-653.
- [8] Tong, M., Tham, L.G. and Au, F.T.K., "Numerical Modeling for Temperature

- Distribution in Steel Bridges”, *Computers and Structures*, 2000, Vol. 79. pp. 583-593.
- [9] Jin, F., Chen, Z., Wang, J.T. and Yang, J., “Practical Procedure for Predicting Non-uniform Temperature on the Exposed Face of Arch Dams”, *Applied Thermal Engineering*, 2010, Vol. 20, pp. 2146-2156.
- [10] Noorzaei, J., Bayagoob, K.H., Thanoon, W.A., et al., “Thermal and Stress Analysis of Kinta RCC Dam”, *Engineering Structures*, 2006, Vol. 28, No. 13, pp. 1795-802.
- [11] Briss, K. Diefenderfer, Imad, L. Al-Qadi, Stacey, D. Diefenderfer, “Model to Predict Pavement Temperature Profile : Development and Validation”, *Journal of Transportation Engineering*, Vol. 132, No. 2, pp. 162-167.
- [12] Chiasson, Andrew D., Yavuzturk, Cenk, Ksaibati, Khaled, “Linearized Approach for Predicting Thermal Stresses in Asphalt Pavements due to Environmental Conditions”, *Journal of Materials in Civil Engineering*, Vol. 20, No. 2, pp. 118-127.
- [13] McQuiston, Faye C., Parker, Jerald D., Spitler, Jeffrey D., “Heating, Ventilating, and Air Conditioning Analysis and Design”, USA : John Wiley and Sons, 2005.
- [14] Li, J.P. and Song, A.G., “Compare of Clear Day Solar Radiation Model of Beijing and ASHRAE”, *Journal of Capital Normal University*, 1998, Vol. 19, No. 1, pp. 35-38.(in Chinese).

# EXPERIMENTAL AND NUMERICAL STUDY ON MECHANICAL BEHAVIOR OF COMPOSITE GIRDERS UNDER HOGGING MOMENT

Weiwei Lin<sup>1</sup> and Teruhiko Yoda<sup>2,\*</sup>

<sup>1</sup>Assistant Professor, Department of Civil and Environmental Engineering,  
Waseda University, Shinjuku-ku, Tokyo 169-8555, Japan

<sup>2</sup>Professor, Department of Civil and Environmental Engineering,  
Waseda University, Shinjuku-ku, Tokyo 169-8555, Japan

\*(Corresponding author: E-mail: yoda1914@waseda.jp)

Received: 24 March 2012; Revised: 10 July 2012; Accepted: 13 July 2012

**ABSTRACT:** In continuous steel-concrete composite structures, cracking of the concrete slab in the hogging bending moment region decreases the global stiffness of composite structures and reduces the effect of continuity, resulting in making the structural behaviors highly nonlinear even for low stress levels. Because of this, special consideration is necessary. The purpose of the present study is to investigate the effects of rubber-latex mortar and different types of shear connectors on inelastic behavior of composite girders subjected to hogging moment. Two overturned simply supported steel-concrete composite girders with different shear connectors such as Studs and Perfo-Bond Strips (PBLs) were tested under concentrated load in the mid-span. Based on the experimental observations, a three-dimensional FE model capable of analyzing the composite beams subjected to negative bending moment was built. Strength and load bearing capacity, sectional strain distribution and movement of composite neutral axis before and after cracking were observed in the test and compared with the numerical results, and the results predicted by this modeling method are in good agreement with those obtained from the tests. Research results indicate that the PBL connectors could slightly improve the rigidity of the composite girder under both the serviceability limit state and the ultimate limit state, while Stud specimens have relatively better mechanical behavior in regard to the initial crack and the “crack closure” of the test specimens. Besides, research results indicate that the current specifications such as AASHTO, JSCE, and EUROCODE-4 can provide appropriate values for ultimate strength of a composite girder under negative bending moment. Moreover, noise reduction, shear stud stiffness increase and the adhesion bonding effect of rubber-latex mortar on interface slip were confirmed in the tests.

**Keywords:** Steel-concrete composite girder, hogging moment, rubber-latex mortar coating, studs, PBLs

## 1. INTRODUCTION

In recent years, the composite steel and concrete structures are used extensively for construction of both building and bridge structures due to their benefits of combining the advantages of component materials and obtaining efficient lightweight structural members, not only for simply supported girders, but also for continuous composite girders. For simply supported composite beams, the ultimate loading capacity is usually dominated by either flexural or shear bearing capacity, which will be governed by the compressive strength of the concrete and tensile strength of the joist steel girder. However, for continuous composite girders or composite girders subjected to hogging moment, this condition may not be fully satisfied. Negative bending moment acting in the support regions of continuous composite beams generate tensile stresses in the concrete slab and compressive stresses in the lower steel profile. As a result, the mechanical behavior of these girders is strongly nonlinear even for low stress levels, due not only to the slip at the beam-slab interface, but also to cracking in the slab, which generally has shortcomings in view of durability and service life of the structures [1,2]. Therefore, special considerations for composite girders under negative bending moment are necessary. For this reason, experimental studies about inelastic behavior of composite girder under negative bending have been done widely. Special attentions were generally

given to crack control methods [3, 4], failure modes [5, 6], and long-term behaviors [7] and so on. In addition, some numerical models were also created to simulate the composite girders under negative bending. Those numerical models keep a watchful eye on the effect of slip on the steel-slab interface [8, 9], partial shear connection [10], or improved numerical methods [11].

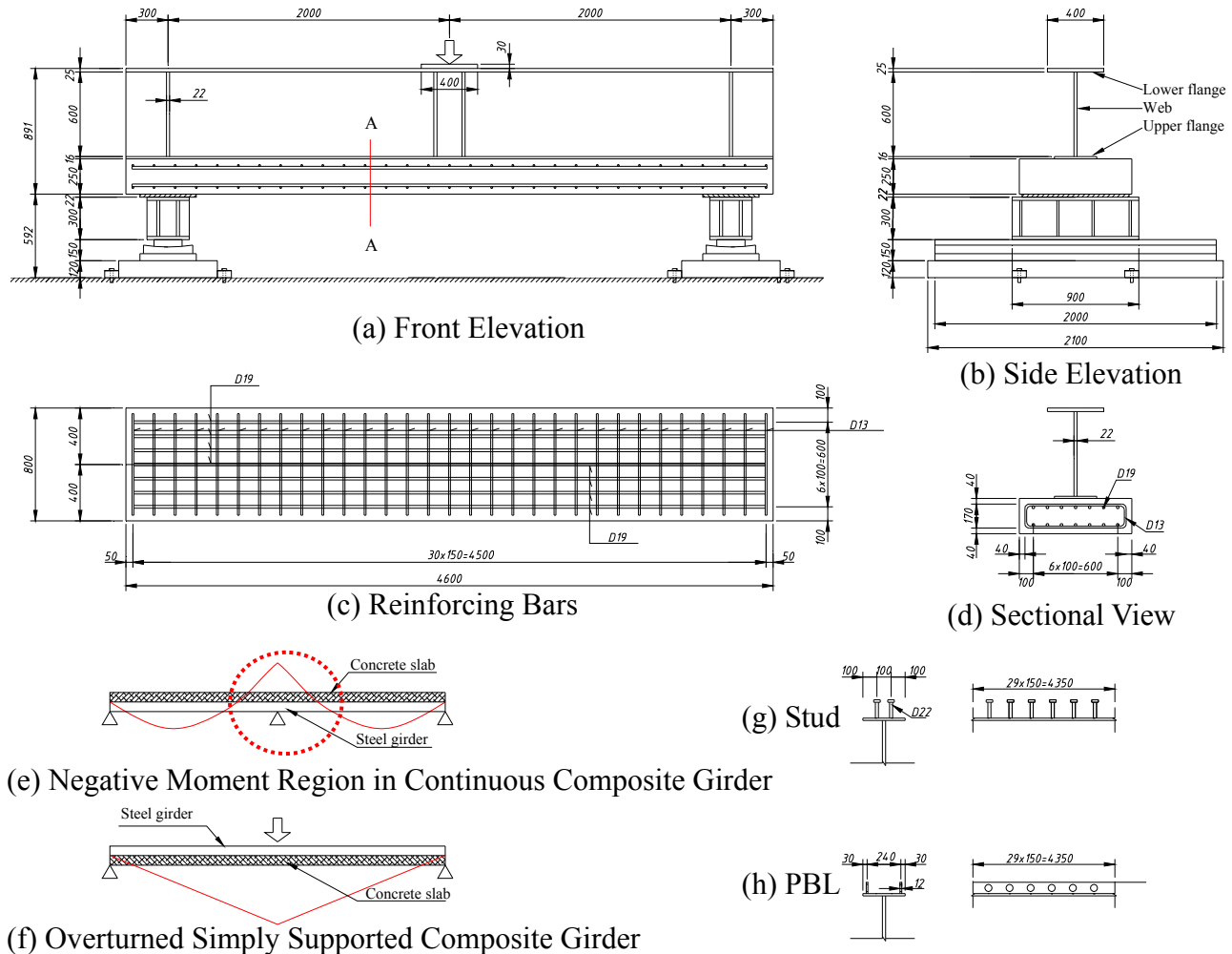


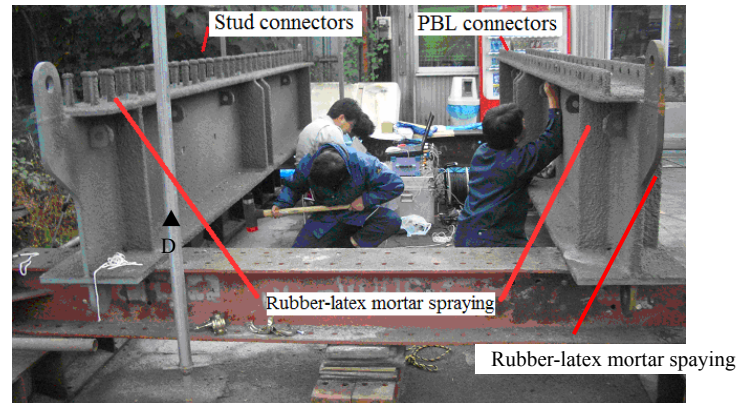
Figure 1. Dimensions of Test Specimen

Table 1. Details of Test Specimens

Specimen	Connection device	Shear connectors spacing(mm)		Reinforcing bars spacing (mm)		Rubber-latex spraying
		Longitudinal	Transverse	Longitudinal bars	Stirrup	
CBS	Stud	150	100	100	150	Yes
CBP	PBL	150	240	100	150	Yes

Table 2. Rubber-Latex Mortar Spraying Details

Details Locations	Spraying thickness (mm)		Spraying times
	CBS	CBP	
Top surface of upper flange	7.7	6.6	2
Bottom surface of upper flange	3.0	4.8	2
Web	6.7	6.4	2
Shear connector	2.1	6.7	2
Top surface of lower flange	3.0	4.8	2
Bottom surface of lower flange	5.0	7.0	3



(a) Steel Girder and Shear Connectors



(b) Rubber-Latex Mortar Spaying Construction

Figure 2. Shear Connectors and Rubber-Latex Mortar Spaying



Figure 3. Static Loading Test Set-Up

Shear connectors, sometimes known generally as Perfo-Bond Strips (PBLs) or Nelson Studs, are used in steel-concrete composite structures. They act as reinforcing members, connecting the steel girder with the concrete slab. Stud and Perfo-Bond Strips (PBLs), generally known as flexible and rigid shear connectors, are most frequently-used shear connectors in steel-concrete composite girders. Current studies mainly pay attention to mechanical behavior of the shear connector itself, such as the ultimate load carrying capacity and load-deformation response. Recently, the effects of shear connectors on structural behavior of composite girders were performed by some researchers [4, 12, and 13].

Concrete and mortar, including SBR latex, shows various abilities especially in adhesion bonding, waterproofing, shock absorption and abrasion resistance. The rubber-latex mortar was used for steel

structures to reduce the noise as well as the interface slip, enhance the integrity and improve the durability of the composite structures. Moreover, the composite structures with rubber-latex mortar coating are also reported to have the good impact resistance, weather resistance as well as the good constructability and operability behaviors. Some experimental studies were performed recently to study the effects of rubber-latex mortar on the mechanical behavior of composite structures [12, 13, and 14].

For this kind of background, this paper presents the experimental and numerical results of test composite girders subjected to negative bending, including the strain distribution at salient sections along the span and strain development process of reinforcements, load-displacement response, and load-carrying capacity as well as the interface slip distribution. The objective of the present study is to investigate the influence of rubber-latex mortar coating and to clarify the difference between Studs and PBLs on inelastic mechanical behavior of composite girders subjected to negative bending or support regions of continuous steel-concrete composite girders.

## **2. EXPERIMENTAL PROGRAMME**

### **2.1 Details of Test Specimens**

Two overturned simply supported steel-concrete composite beams CBS and CBP were tested under concentrated load in mid-span, which were used to simulate the support regions of continuous composite steel and concrete girder as shown in Figure 1 (e and f). CBS was designed with studs as shear connectors whilst CBP was designed with PBLs as shear connection devices. Each of the specimens was 4.6m in length and was simply supported at a span of 4m. The concrete slab thickness was 250mm with a width of 800mm. Vertical stiffeners were welded at supports, loading points to prevent shear buckling failure and crippling of the web before flexural failure. Different shear connectors, including 22mm nominal diameter headed shear studs and 12mm thickness PBLs were used to connect the concrete slab and the steel girder, and the composite section was designed as full shear connection according to JSCE specifications [15]. The typical geometry of test specimen is shown in Figure 1, and the detailed sectional properties were illustrated in Table 1. Besides, it is worth noting that upper flange, web and lower flange of steel girder are named as shown in Figure 1 (b). Moreover, rubber-latex mortar was sprayed on the surface of the steel girder, concrete slab and the shear connectors including PBLs and shear studs, as shown in Figure 2 and with details listed Table 2.

### **2.2 Instrumentation**

Measurement of strains in the reinforcements, steel girder and concrete slab were conducted by mean of electric resistance gauges at sections located at mid-span, 20cm and 60cm from the mid-span, respectively. Strain gauges were also employed at the root of the shear studs to measure the flexural strain during the loading process. Deflections and transverse deformations were measured by mean of deformation gauges at key sections. Since reaction supporting beams were set up at the ends, deflections were also measured at the end sections. Measurement of slips between the concrete slab and steel beams were also conducted by mean of deformation gauges, and the  $\pi$ -gauges for measuring the crack width on the concrete slab were also employed in the test. In addition, impact test was performed on the steel girder before the concrete casting to confirm the effect of rubber-latex mortar on noise reduction, and the accelerometers were arranged on the middle center of the web in the 1/4 span section.

## 2.3 Test Set-up and Loading Procedure

The experiment was performed in the Structural Laboratory of Waseda University. The 5000kN loading capacity equipment of “Two Axes Large-scale Apparatus used for Performance Evaluation of Structures” was used in the experiment to apply a point load in the mid-span of the overturned composite beams. The test specimen was supported by a roller system at two ends. The set-up for the steel-concrete composite girder test is illustrated in Figure 3. After the drying shrinkage had stabilized, pre-loading was applied to check the reliability of the measure equipment and the stability of the test specimen. The behavior of composite girders in elastic, cracking, and inelastic ranges was carefully observed through the static tests. The test girder was loaded in four cycles with the maximum loads of 200, 400, 700, 1300 kN before the ultimate load was reached. For unloading process, the load was removed at the calculated initial cracking load (200 kN) and at the stationary cracking load (700 kN) to check the cracking of the concrete slab [16]. The loading was terminated when either the maximum stroke of the jack was reached or when the load level of the test specimen dropped significantly.

## 3. NUMERICAL SIMULATION OF EXPERIMENT

### 3.1 Model Building

The modeling of each numerical model was carried out in three dimensions by using the finite-element method and the *DIANA* software, as shown in Figure 4. Solid elements, shell elements, spring elements were used to simulate the concrete slab, steel girder and PBLs, stud connectors respectively. For each stud, three springs were employed to simulate the shear and axial forces in three directions. Re-bar elements were used for modeling reinforcing bars in the concrete slab, and perfect bond between reinforcements and surrounding concrete was assumed. 3cm thickness loading plate was also modeled by using shell element. In order to predigest complicated numerical simulation, the rubber-latex mortar was not modeled as the separate structural member but considered as special treatment for the steel-slab interface and it will enhance the bond stiffness as well as the bond strength of the steel-slab interface. Therefore, with the purpose of accounting for the slip and the composite action between concrete slab and steel girder, interface elements that considering the adhesion bonding effects of rubber-latex mortar were employed in the numerical models. Rigid supporting plate and simplified line support were employed to simulate the simply supported boundary conditions.

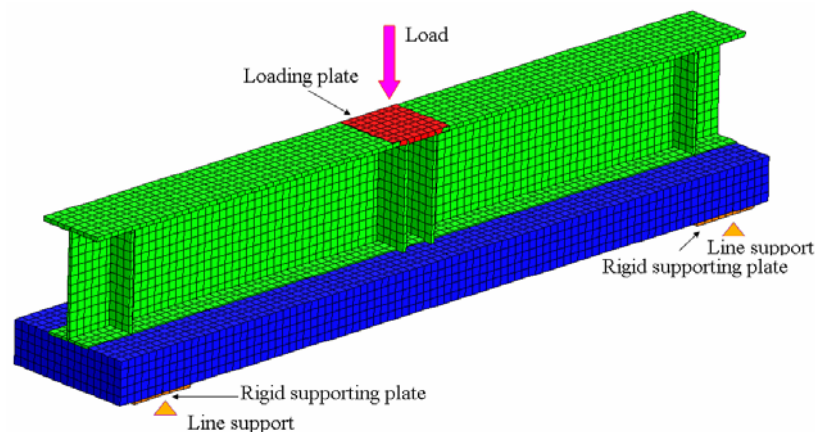


Figure 4. FE Model of Test Specimen

Table 3. Mix Proportion of Concrete

Specimen	Design strength (N/mm <sup>2</sup> )	Aggregate size (mm)	Slump (mm)	W/C (%)	Air (%)	Unit cement (kg/m <sup>3</sup> )	Unit salinity (kg/m <sup>3</sup> )
CBS & CBP	27	<20	80±25	<55	4.5±1.5	>230	<0.3

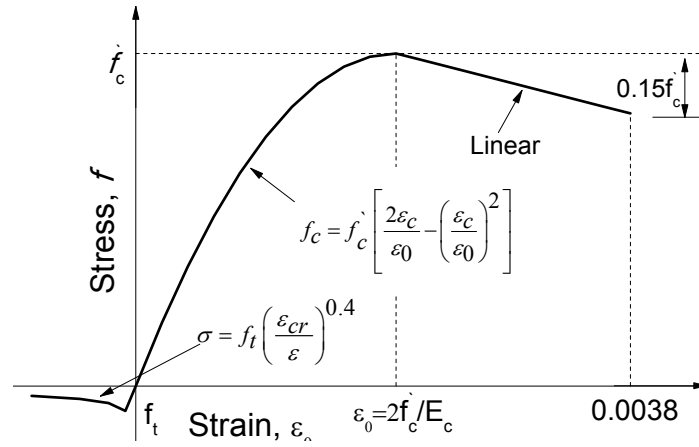


Figure 5. Stress-Strain Curve for Concrete

### 3.2 Material Properties

#### 3.2.1 Concrete

Material property of concrete is determined from material test. Mix proportion of concrete for test specimen was illustrated in Table 3. The nominal concrete compressive strengths achieved after twenty-eight days of curing for CBS and CBP was 29.1N/mm<sup>2</sup>. Tensile strength of the concrete was calculated according to Eq. (1) suggested by JSCE (2002), in which the  $f_t$  and  $f_c$  denote tensile and compressive strengths of concrete, respectively. The often quoted stress-strain curve due to Hognestad [17, 18] was employed to simulate the compression behavior of concrete, shown in Figure 5. Experimental tension-stiffness curve proposed by Nakasu et al. [19] is used in the numerical analysis to reflect the softening of concrete due to crack.

$$f_t = 0.23f_c^{2/3} \quad (1)$$

#### 3.2.2 Structural steel and reinforcing bars

The uniaxial stress-strain relationships for structural steel and reinforcing bars shown in Figure 6 were adopted in numerical models based on the material tests. Three steel beam coupons were cut out from different components of the upper flange, web, lower flange and PBL with different nominal thickness of 16, 22, 25 and 12mm respectively, and the tensile tests were performed. Fourteen reinforcing bars of D19 nominal diameter were used for two layers as longitudinal reinforcing bars in the concrete slabs, whilst D13 stirrup reinforcing bars were used as torsional reinforcement with a nominal diameter of 13mm. Multi-linear stress-strain relationships for structural steel and rebar used in the numerical models are shown in Figure 6(b).



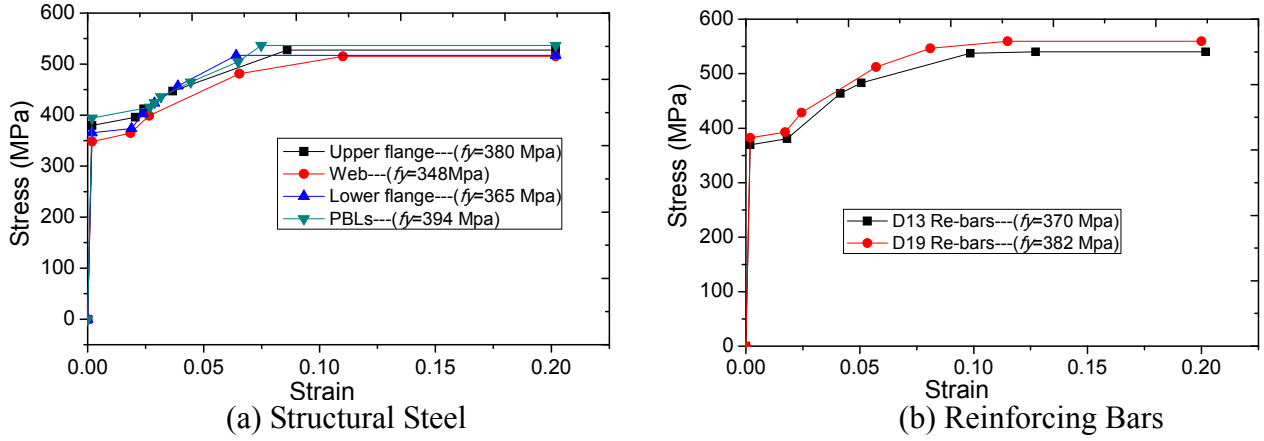


Figure 6. Multi-Linear Stress-Strain Relationship for Structural Steel and Rebar

### 3.2.3 Shear connectors

Studs and PBL shear connectors during the concrete casting are shown in Figure 7. In the test specimen, it was intended that the shear connections were installed to achieve full shear connections, which means the shear connectors should be still reliable even when the test specimens are in the ultimate state. Therefore, the present study is limited to full shear connection specimens (or the shear degree is larger than 1.0).

In the numerical study, the shear studs were modeled by 3D nonlinear spring elements. For each stud, three springs are used, two in horizontal direction and one in vertical direction. A previous study [20] shown that the shear force-slip curve is generally nonlinear and it is reasonable to use a nonlinear spring in modeling the mechanical behavior of the connectors. The constitutive relationship of the spring is given by Eq. (2) suggested by Ollgaard et al. [21] and illustrated in Figure 8, in which the ultimate shear force loading capacity of studs was specified by JSCE specifications [15], shown as Eq. (3).

$$Q = Q_u (1 - e^{-0.7S})^{0.4} \quad (2)$$

$$Q_u = \min \left( \frac{(31A_{ss} \sqrt{(h_{ss}/d_{ss}) f_{cd}} + 10000) / \gamma_b}{A_{ss} f_{ss} / \gamma_b} \right) \quad (3)$$

where  $S$ : slip of the shear stud (mm),  $A_{ss}$ : area of the shank of the stud ( $\text{mm}^2$ ),  $d_{ss}$ : diameter of the shank of the stud (mm),  $h_{ss}$ : height of the stud (mm),  $f_{cd}$ : design compressive strength of concrete ( $\text{N/mm}^2$ ) ( $=f_{ck} / \gamma_c$ ),  $f_{ck}$ : the characteristic compressive strength of concrete ( $\text{N/mm}^2$ ),  $f_{ss}$ : design tensile strength of the stud ( $\text{N/mm}^2$ ) ( $=f_{sk} / \gamma_s$ ),  $f_{sk}$ : characteristic tensile strength of the stud ( $\text{N/mm}^2$ ),  $\gamma_c$ : material factor of concrete ( $=1.3$ ),  $\gamma_s$ : material factor of stud ( $=1.0$ ),  $\gamma_b$ : member factor ( $=1.3$ ).



(a) Stud Connectors



(b) PBL Connectors

Figure 7. Shear Connectors during the Concrete Casting

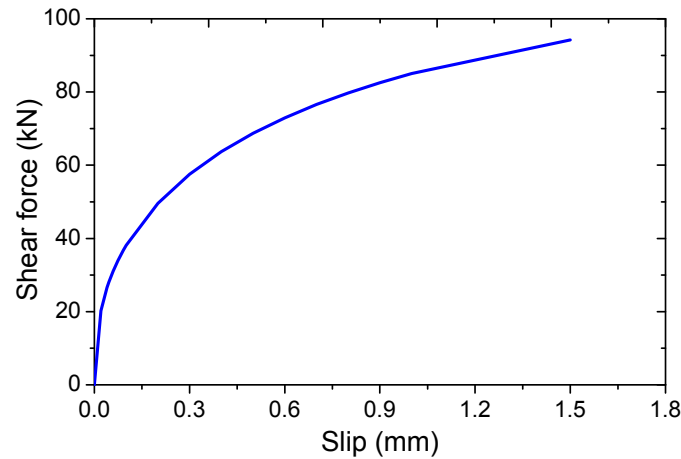


Figure 8. Constitutive Relation of Shear Stud

Several authors, such as Ahna et al. [22], Al-Darzi et al. [23], Iwasaki et al. [24], Machacek and Studnika [25], Medberry and Shahrooz [26], Ushijima et al. [27], and Valente and Cruz [28] have recently studied the behaviour of the PBL connector. And the resistance capacity of PBL shear connectors was proposed by JSCE (2007) as follows [15]

$$Q_u = \left[ 1.45 \left\{ (d^2 - \phi_{st}^2) f'_{cd} + \phi_{st}^2 f_{st} \right\} - 106.1 \times 10^3 \right] / \gamma_b \quad (4)$$

with the application limit in the following:

$$73.2 \times 10^3 < (d^2 - \phi_{st}^2) f'_{cd} + \phi_{st}^2 f < 488 \times 10^3$$

where  $d$  is the diameter of the Perfo-Bond strip holes (mm),  $f'_{cd}$  is the design concrete compressive strength (N/mm<sup>2</sup>),  $\phi_{st}$  and  $f_{st}$  are the diameter (mm) and tensile strength (N/mm<sup>2</sup>) of re-bar. The member factor  $\gamma_b$  can be taken as 1.3.

However, the previous mentioned tests also proved that the PBL shear connector has relatively larger stiffness and smaller slip during the whole loading process (especially when reinforcement pass through the holes, like the present PBL specimen as shown Figure 7(b)) in comparison with the other types of shear connectors. Thus, in order to predigest complicated calculation, the PBL connector was simulated by using shell element and perfect bond was assumed between PBLs and surrounding concrete. The goal of the numerical analysis is not to get exact resemblance between modeled and measured results on the complicated local behavior on the shear connectors, but to model the global behavior of the test specimens.

Table 4. Material Property of Rubber-Latex Mortar

Appearance	oyster white
Solid content	45.0±1.0%
PH	9±1
Viscosity (20°C)	<200mPa·s
Mean specific gravity	1.00±0.05
Compressive strength	32.3N/mm <sup>2</sup>
Elastic modulus	21kN/mm <sup>2</sup>

### 3.2.4 Rubber-latex mortar

Styrene-Butadiene-Rubber (SBR) is a synthetic rubber copolymer consisting of styrene and butadiene. It has good abrasion resistance and good aging stability when protected by additives. The rubber-latex mixing with SBR was applied for both CBS and CBP, and its material properties were illustrated in Table 4. As mentioned above, the rubber-latex mortar was not considered as the separate structural member in the numerical analysis, but considered as the potential material for increasing the bond stiffness and strength of the steel-slab interface.

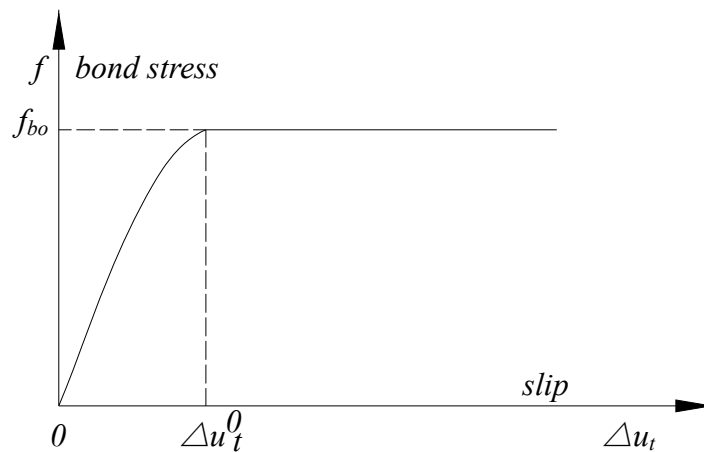


Figure 9. Material Properties of Interface

### 3.2.5 Composite action or interface

In order to account for the composite action between steel girder and concrete slab, the interface element was used in the numerical analysis. And the bond-friction interface model suggested by Okada et al. [29] was employed in this study, as shown in Figure 9 and Eq. (5)-(6). As can be seen, constant bond or friction stress is supposed after breaking of the chemical bond on the steel-slab interface, which is developed from Dörr's bond-slip model [30] and has been verified by the previous push-out tests as well as numerical studies.

$$0 \leq \Delta u_t \leq \Delta u_t^0 :$$

$$f_{\tan} = \frac{f_{bo}}{1.9} \left( 5 \left( \frac{\Delta u_t}{\Delta u_t^0} \right) - 4.5 \left( \frac{\Delta u_t}{\Delta u_t^0} \right)^2 + 1.4 \left( \frac{\Delta u_t}{\Delta u_t^0} \right)^3 \right) \quad (5)$$

$$\Delta u_t \geq \Delta u_t^0 :$$

$$f = f_{bo} \quad (6)$$

The maximum bond stress  $f_{bo}$  is taken as  $2.4 \text{ N/mm}^2$  by considering the adhesion bonding effects of rubber-latex mortar [12, 13]. Concerning the corresponding slip to the peak bond stress,  $0.06 \text{ mm}$ , this is the standard value of Dörr's model as well as Okada's model.

## 4. RESULTS AND DISCUSSION

### 4.1 Strength and Deformation Response

Totally 12 deformation gauges were employed for measurement of vertical displacement. The load-displacement curves obtained from the numerical analyses were compared with the experimental data as shown in Figure 10. Both numerical and experimental displacements are taken from the vertical deflection at the bottom mid-point of the composite beam, which is the bottom point of the concrete slab (Point D in Figure 1(a)). The loads corresponding to the theoretical yield and full plastic moments are plotted as the horizontal lines indicated by  $P_y$  and  $P_p$ , respectively. The ultimate pure bending moments,  $M_{u,t}$  is to be calculated following the procedure for computing the plastic bending moment of composite sections under negative moment specified in Appendix D6.1 of AASHTO LRFD, 2007 [31].

It is found that in the linear region, the load-displacement curves from numerical studies agree well with the measured results. However, in the nonlinear region after girder yielding, the rigidity of FE model is a little bit stronger than the test girder. This is presumably because the residual stress is not considered in the finite element analysis, which may result in slightly larger stiffness of FE model than that of the test girder. And also, the present modeling method for shear connectors assumes the perfect bond between PBL connectors and concrete. At the final stage, the concrete can not sustain any increase in applied loading and eventually fails by through crack in the mid-span. The numerical results and experimental results are summarized and compared in Table.5.

Table 5. Loading Capacity of the Test Specimens

Specimen No	Initial cracking moment (kN·m)			Yielding moment (kN·m)			Crack closure moment (kN·m)	Ultimate bending moment (kN·m)		
	$M_{c,e}$	$M_{c,t}$	$M_{c,f}$	$M_{y,e}$	$M_{y,t}$	$M_{y,f}$	$M_{c,c}$	$M_{u,e}$	$M_{u,t}$	$M_{u,f}$
CBS	220	247	260	2702	2000	3100	3500	3801	3104	3720
CBP	120	247	224	2505	2000	3260	3203	3999	3104	3900

Note:  $M_{c,e}$ ,  $M_{c,t}$  and  $M_{c,f}$  = Initial cracking bending moment from experiments, theoretical calculation and numerical values;  $M_{y,e}$ ,  $M_{y,t}$  and  $M_{y,f}$  = Yielding moment from experiments, theoretical calculation and numerical values;  $M_{c,c}$  = Crack closure bending moment from experiments;  $M_{u,e}$ ,  $M_{u,t}$  and  $M_{u,f}$  = ultimate bending moment from experiments, theoretical calculation and numerical calculation, respectively.

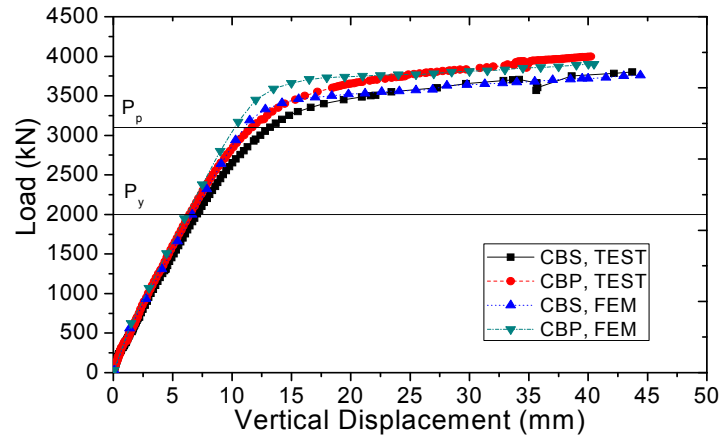


Figure 10. Load-Deflection Relationship

The initial cracking load calculated with reference to the slab exhibiting maximum negative moment of composite section under elastic state has been estimated to be 247kN for CBS and CBP, were close to numerical results but larger than experimental values. It seems to indicate that the initial cracking load is very small for composite beams under negative bending moment and thus making the structural behavior highly nonlinear even for very low stress levels. Besides, experimental girder yielding moment seems larger than theoretical values but smaller than those of numerical results, which might be caused by the neglect of concrete slab in theoretical calculation and perfect bond assumption on rebar-concrete interface in numerical simulation. Furthermore, a phenomenon of “crack closure” was observed in the tests and the corresponding loads were given, and the details will be discussed below. Regarding to the ultimate bending moment, as strain hardening of the steel girder and reinforcing bars was not considered in the theoretical analysis, resulting in that the experimental results was approximate to numerical results but much larger than the theoretical values. However, as the “crack closure” load is a little larger but relatively close to the theoretically ultimate load, current specifications can provide appropriate values in regard to the ultimate strength of a composite girder under negative bending moment. Moreover, comparison of load-deformation response of each specimen indicates that the displacement of CBP becomes a little less at around 1000kN than those of CBS, which is presumably because the PBL dowels affect the rigidity of the entire girder when cracking has progressed to a certain extent.

In addition, comparison between the numerical and experimental results of CBP and CBS also indicates that the initial cracking and crack closure moments of PBL specimen are much smaller in comparison with those of Stud specimen. It seems to demonstrate that the PBL connectors could be helpful to increase the girder stiffness and the ultimate loading capacity, but composite beams using studs as shear connectors have better mechanical behavior in regard to concrete cracking. This is presumably because the flexible behavior of studs is profitable for internal force and deformation redistribution. Besides, by comparison with the previous test results that without rubber-latex

mortar, there is no obvious effects of rubber-latex mortar coating on the loading capacity, deformation behavior, or the failure modes of composite girders subjected to hogging moment [32].

## 4.2 Composite Neutral Axes

Figure 11 illustrates the movement of sectional neutral axis in both linear and nonlinear stage for test specimens. During testing, the sectional strain was measured in five characteristic sections located at span center, 60 and 20 cm from the span center respectively. In order to avoid the effect of 30mm thickness loading plate, sectional strains were generated and compared with the experimental values on section A-A' shown in Figure 1. Numerical strain results of steel and concrete elements were generated and compared with the measured strain values of the steel and the reinforcement from the tests. Elastic neutral axis (ENA) and plastic neutral axis (PNA) according to AASHTO LRFD (2007) [31] were given to make a comparison with the movement of the composite neutral axis of each test specimen.

It is observed that the strain distribution was linear for steel-concrete composite beams during the early stage of the tests, as shown in Figures 12 and 13. However, with the load increase, the strain distribution of the reinforcement has exhibited a different curvature compared with the strain distribution of the steel beam. Due to the presence of interface slip and the crack of the concrete slab, the plane cross-section assumption is not satisfied and the strain distribution difference could be produced between different portions of steel girder, concrete and the reinforcing bars. Furthermore, the movement of composite neutral axis can be divided into three stages, as shown in Figure 11. Firstly, when sectional bending moment is smaller than the cracking bending moment, the composite neutral axis is similar to the calculated elastic neutral axis. However, the test results show that the first stage is relatively small for composite girders subjected to negative bending moment. This is presumably because of the negative bending moment as well as the initial cracks in the test specimens, which will cause the structural behavior of composite girders highly nonlinear and the movement of composite neutral axis even when the load is relatively small. With the load increase, the composite neutral axis changes expeditiously and move towards the plastic neutral axis, which might be caused by the development of the cracks in the concrete slab and can be treated as the second stage. In the third stage, with the load increase the crack on the concrete slab becomes stable and the cross-sectional stress of composite girders will mainly withstand by the reinforcing bars and the steel girder, and the composite neutral axis begin to keep as constant at around the plastic neutral axis.

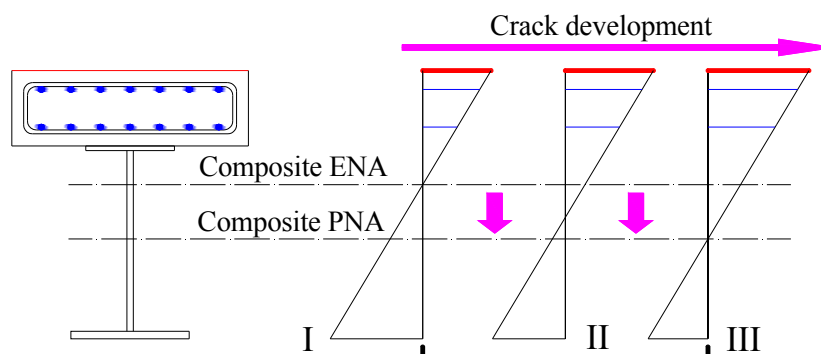


Figure 11. Movement of Neutral Axis

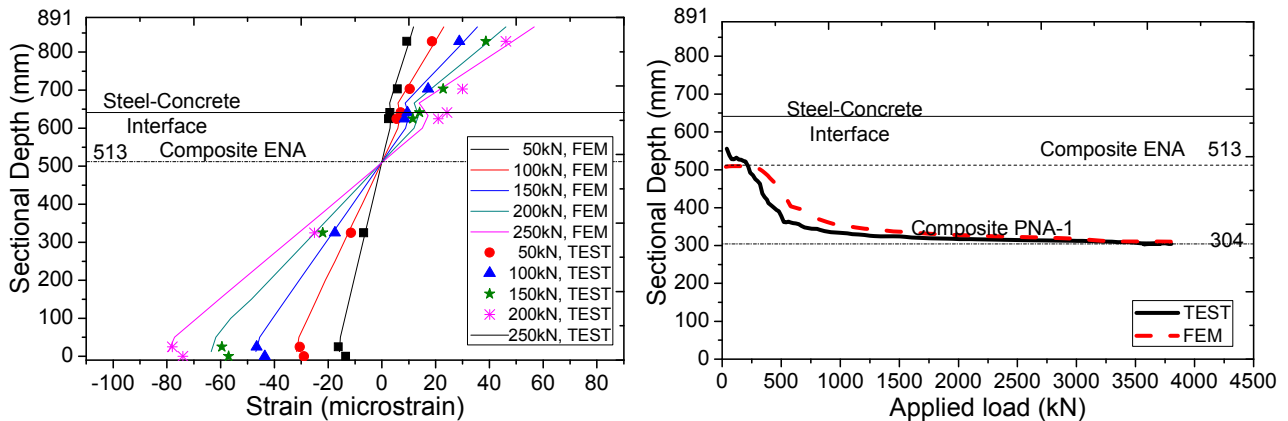


Figure 12. Strain Distribution and Neutral Axis Movement of CBS

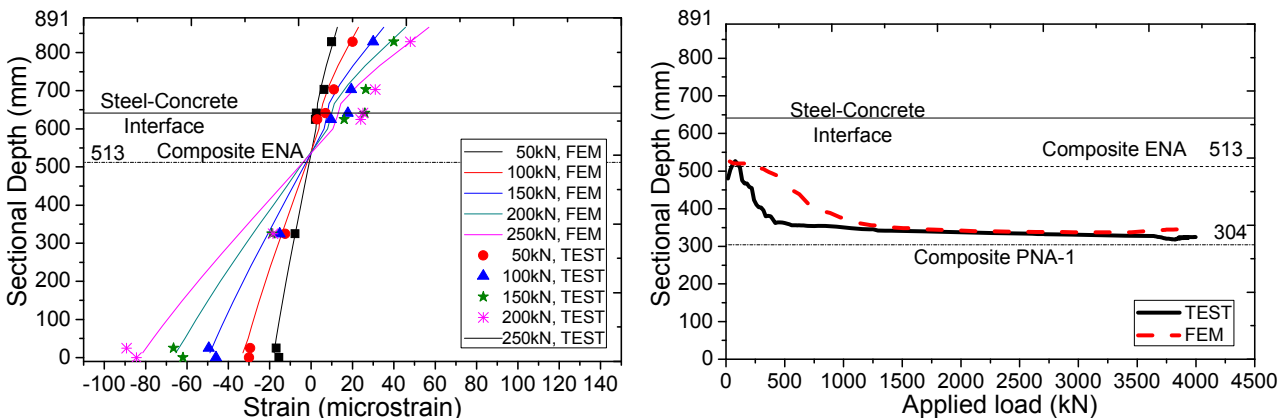


Figure 13. Strain Distribution and Neutral Axis Movement of CBP

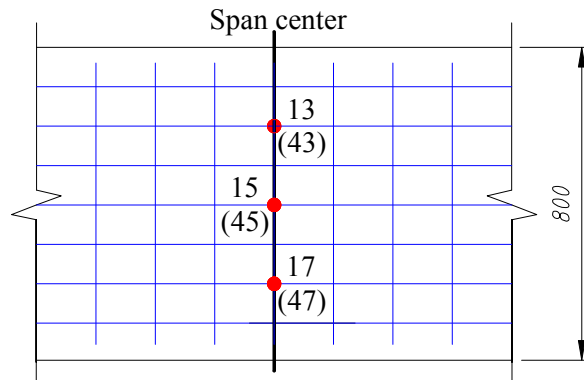


Figure 14. Position of Reinforcement Strain Gauges

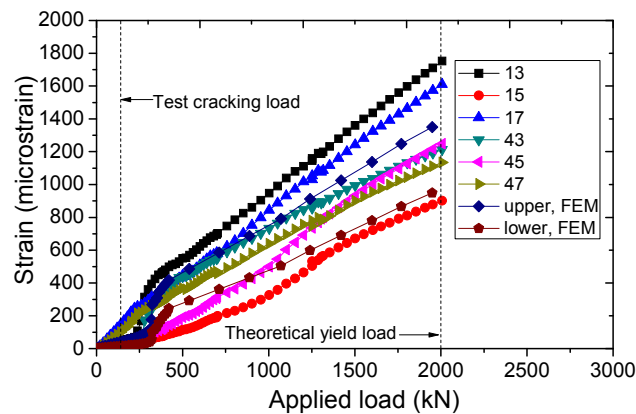
### 4.3 Strain of Reinforcements

The strains of longitudinal reinforcements in the mid-span near the loading point were measured in the tests, and the results of CBS and CBP were presented herein. Figure 14 shows gauges' number (gauges 13, 15, 17 were arranged for the upper layer reinforcements, and gauge 43, 45, 47 were employed for the lower layer reinforcements) as well as their positions, and the load-strain relationships were depicted in Figures 14 and 15. Strain development of the reinforcement before theoretical girder yielding load as well as the strain results during the whole loading process were illustrated separately. Numerical strain results of reinforcements were also given. During the whole loading process, no obvious difference of numerical strain results was found between different reinforcements in the same layer. Average values for both upper and lower layers were given separately to compare with the test results.

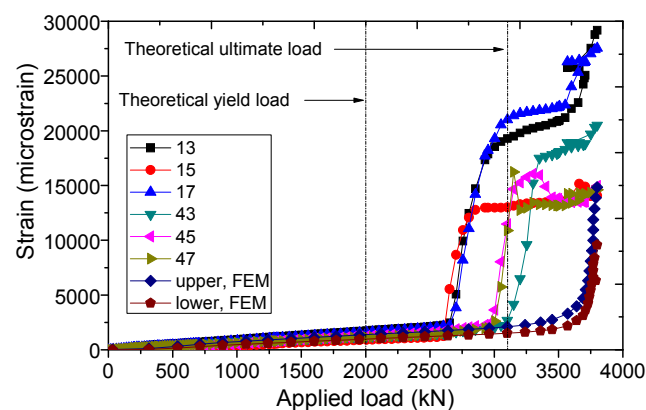


The strain increased linearly and slowly before the concrete slab cracking. After the initial cracking, the strain near the point where the crack has occurred increased rapidly (often referred to as strain jump). Similar phenomenon was also confirmed in the numerical studies, shown in Figure 15(a) and Figure 16(a). In regard to the initial cracking moment, results in Table 4 indicate that the numerical results agree well with the theoretical values, but larger than the test values. It demonstrates that for steel-concrete composite structures subjected to hogging moment, the concrete slab will crack and thus making the structural behavior highly nonlinear even for low stress levels.

Until the theoretical girder yielding load of the specimen, the reinforcements were continuously deformed and the strain of upper layer reinforcements was found larger than those of lower reinforcement. Comparison between numerical and theoretical results indicates that numerical strain results of reinforcements had a similar variation trend but a little bit smaller than test values, which might be caused by the initial cracks in the concrete slab that cannot be considered in the numerical simulation. Beside, as the concrete in tension zone are usually suggested to be ignored for girder yielding and ultimate strength calculation, resulting in theoretical yielding loads were smaller than the test values, as shown in Figure 15(b) and Figure 16(b). Thus, the tension stiffening effect between cracks should be considered in order to evaluate the more exact flexural stiffness of the composite section under hogging moments.



(a)  $P < 2000\text{kN}$



(b) Whole Loading Process

Figure 15. Strain Development of Reinforcing Bars of CBS



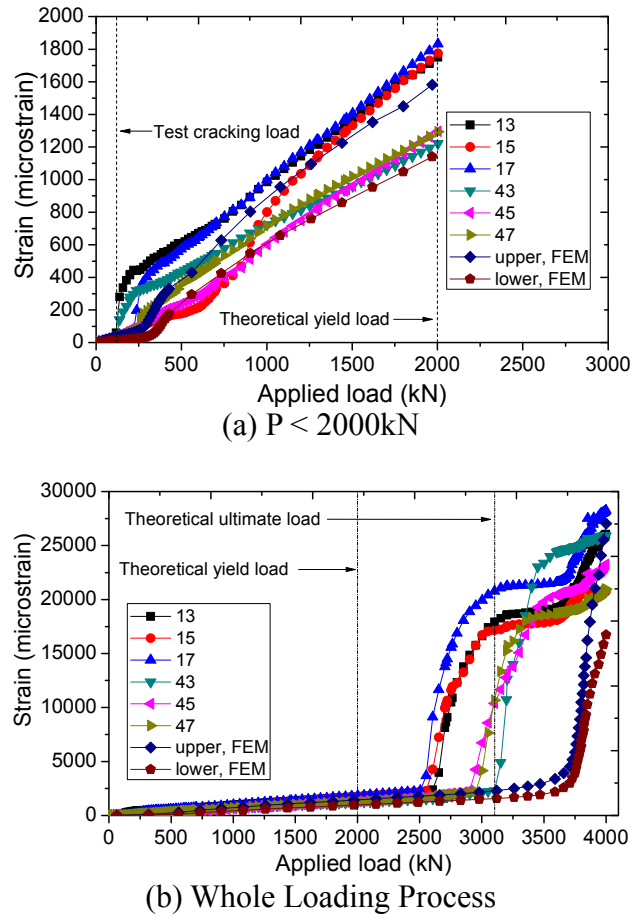


Figure 16. Strain Development of Reinforcing Bars of CBP

Furthermore, as perfect bond was assumed for interface between reinforcing bars and surrounding concrete, resulting in smaller strain during the loading process and deferred Re-bar yielding in the numerical analysis. Also, strain hardening of the reinforcements was confirmed in the experiment for some reinforcements. However, for some other reinforcements, the strain was declined before strain hardening was obtained, which could be caused by the bond effect failure between the concrete and the reinforcement. Therefore, strain hardening effect of reinforcement for composite girders in negative bending moment region seems can be ignored.

#### 4.4 Crack Formation and Development on Concrete Slab

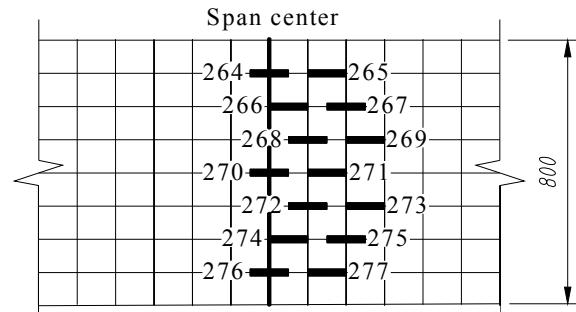
Initial crack formation, crack width development during the loading process and distribution on the concrete slab were recorded by using 14  $\pi$ -gauges on the top surface of the concrete slab. Numbers, locations as well as arrangement of  $\pi$ -gauges in the experiments were shown in Figure 17. CBS was taken as an example. As mentioned earlier, loading, unloading and reloading process were applied in this experiment, thus, recorded results during the loading process of 0-400kN, and final reloading process until the ultimate load were presented in Figure 18 in order to show the initial cracking behavior of concrete and crack development of composite beam during the whole loading process. Detailed experimental results of initial cracking and cracking width development were illustrated in Figures 18 (a) and (c). Besides, crack width calculated by considering the maximum crack spacing (taken as 217mm according to JSCE specification [15]) and rebar strains from numerical models was illustrated as numerical results, shown in Figures 18 (b) and (d), in which the average experimental values of crack width were given to make a comparison.

The crack width jump shown in Figure 18(a) indicates that the initial cracks occurred at the top of concrete slab near loading position when applied load reached to 220kN, which is a little bit smaller than the numerical and theoretical results, as shown in Figure 18(b). The comparison indicates that the proposed numerical model can simulate the un-cracked section well and give similar results to experimental values, although there is a small difference between experimental and numerical responses just after initial cracking.

Figure 18(c) shows the crack width development during the whole loading process. With increasing of the load, the cracks propagated and distributed. At a crack, the rebar strain is maximum and the concrete strain is zero. In between cracks, the rebar strain is minimum and the concrete strain is maximum. If, under increasing load, the concrete strain reaches the limiting tensile strain, an intermediate crack forms between two previously formed cracks. When new crack occurs, “crack jump” for existing cracks was confirmed in the experiments. The results shown in Figure 18(d) demonstrate that before rebar yielding, the assumption of perfect bond between rebar and surrounding concrete will not affect the crack width and the numerical simulation has similar results in comparison with test values. Also, the results indicate that the smeared crack model that usually used in commercial software is capable for simulating the crack development process. However after Re-bar yielding, non-ignorable slip is produced between rebar and concrete, resulting in larger difference between numerical and experimental results.

In addition, a very interesting phenomenon of “crack closure” was observed in the test for both CBS and CBP, and the crack width was found suddenly to become small and keep as constant for all large cracks before the ultimate load was reached, shown as Figure 18(d). This might be because the sectional through cracks were generated, and the bond on the steel-slab interface and the rebar-surrounding concrete interface was broken. For the concrete between through cracks, no tension transfer mechanism between through cracks causes the reduction of the crack width, which is experimentally observed as “crack closure” in the test. Due to the strain hardening of the steel girder and some reinforcing bars, the section could continue to sustain more loads after the “crack closure” was observed. However, as the concrete was out of service, the girder stress as well as its deformation increased rapidly until the ultimate load was reached. Nevertheless, similar phenomenon cannot be obtained in the numerical analysis due to perfect bond assumption between concrete and reinforcing bars. A similar load-crack width response during the whole loading process was also confirmed in results of CBP specimen, as shown in Figure 19.

Results of PBL specimen were illustrated in Figure 19, which have the similar behavior with stud specimen. But it should be noted that both numerical and experimental initial cracking and girder yielding loads of CBP is smaller than those of CBS. Furthermore, as this experimental behavior of “crack closure” is similar to the assumptions for the calculation of ultimate load in current specifications such as AASHTO[31], JSCE[15], Eurocode-4[33] and GB-2003[34], thus “crack closure” load of each test specimen was presented and made a comparison with theoretically and experimental ultimate load, as listed in Table 5. The results indicate that the “crack closure” loads are always slightly larger than the code specified (theoretical) ultimate strength but smaller than the experimentally ultimate loads, which seems to indicate that the current codes for ultimate loading capacity of composite girder under negative bending moment is suitable for practical design because “crack closure” always happen after the theoretically ultimate loading capacity was reached.

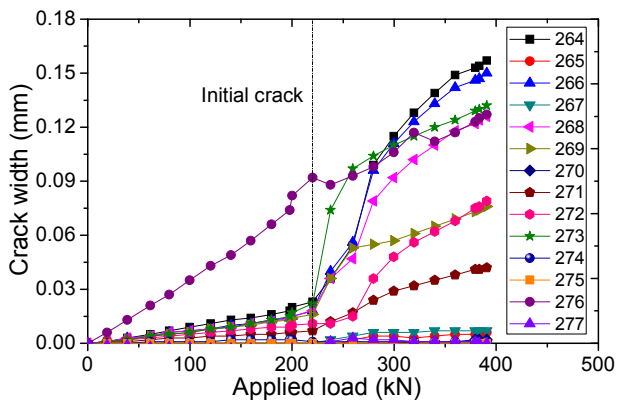


(a) II-Gauge Locations and Gauge Numbers

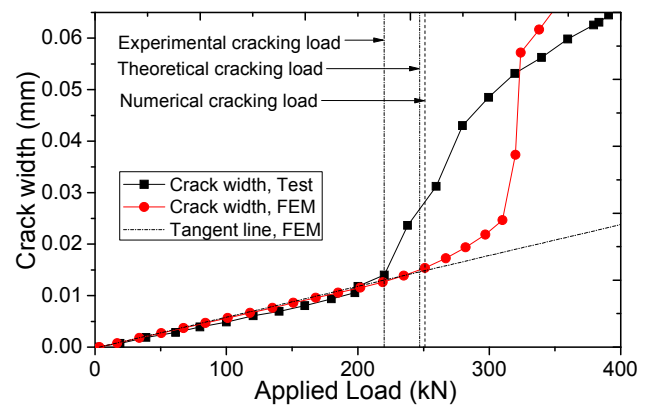


(b) II-Gauge Arrangement in the Test

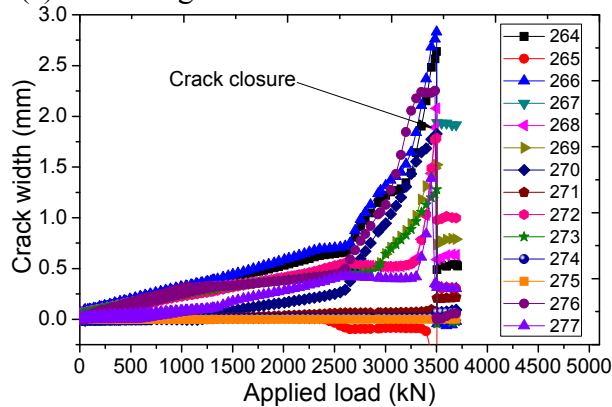
Figure 17. Locations and Arrangement of II-Gauges (100mm square meshes on the surface of the concrete slab)



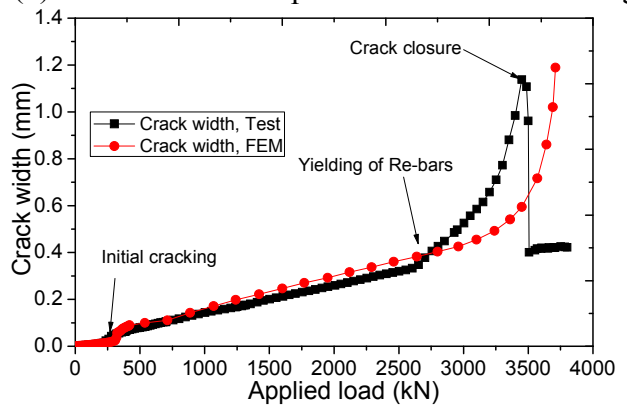
(a) Reloading Process from 0 to 400kN



(b) Numerical and Experimental Initial Cracking

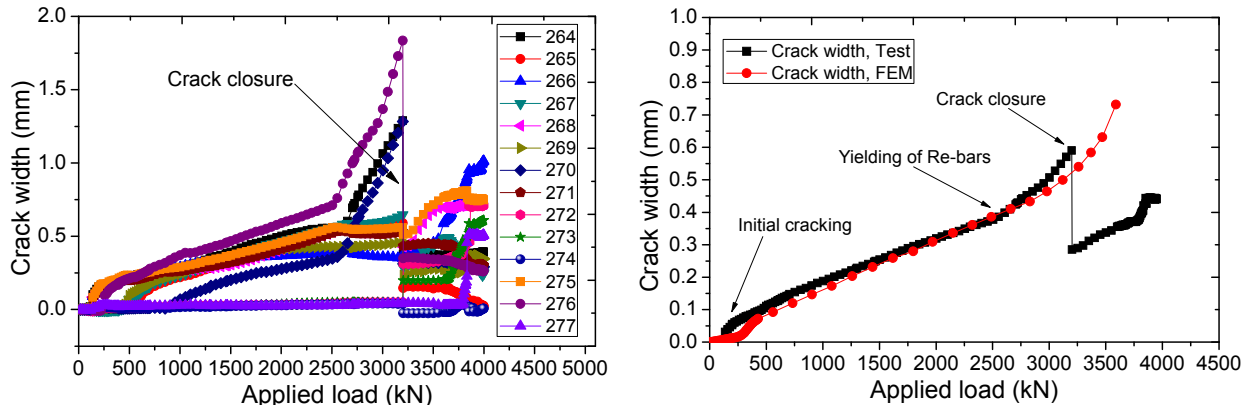


(c) Reloading Process from 0 to Ultimate Load



(d) Numerical and Experimental Crack Width

Figure 18. Crack Width Development Process of CBS



(a) Reloading Process from 0 to Ultimate Load (b) Numerical and Experimental Crack Width  
Figure 19. Crack Width Development Process of CBP

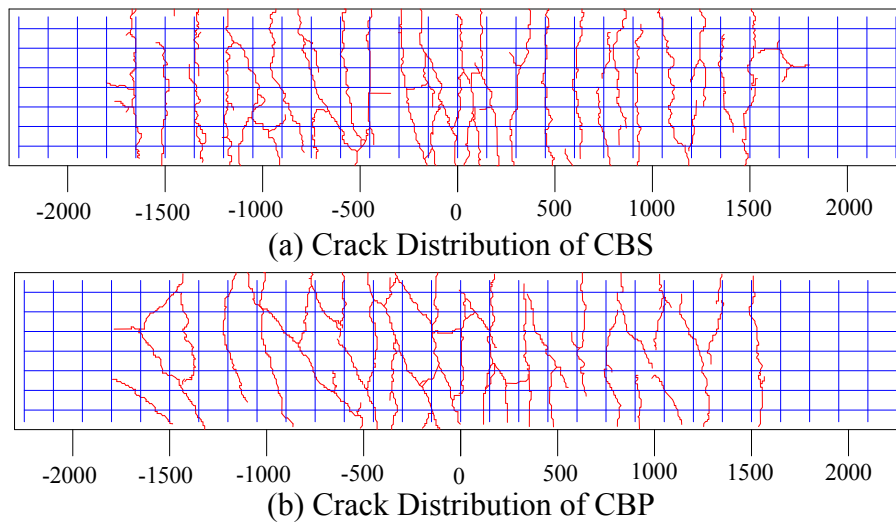


Figure 20. Crack Distribution on the Surface of Concrete Slab After Loading Test (Note: The horizontal coordinate represents the distance from the loading point, the grid in blue stands for the place of reinforcement, and the line colored in red shows the cracks.)

Table 6. Crack Spacing of Test Specimens

Test crack spacing (mm)		CEB-FIP crack spacing (mm) [35]		JSCE maximum crack spacing $L_{max}$ (mm)	
Maximum	Average	Maximum	Average	JSCE(2007) [15]	MLIT(2009) [36]
200	150	265.9	177.3	217	204

Figure 20 shows the crack distribution on the concrete slab surface of each specimen after the loading test. It was observed that in the ultimate stage, the cracks mainly distributed in a direction perpendicular to the girder axis, which means the cracks were mainly dominated by bending moment. With the entire specimens, crack spacing ranges from 100 to 200mm, with an average value of 150mm, coinciding with the spacing between the reinforcement stirrups. Also, it was found that the maximum experimental crack spacing is almost twice the minimum, which is consistent with the theoretical findings [37]. Furthermore, no obvious difference about crack distribution was observed between Studs and PBLs specimens.

The test crack spacing was also compared with the maximum crack spacing specified by CEB-FIP and JSCE, as summarized in Table.6. The comparison indicates that code specified cracking spacing is relatively close to the test values and can be regarded as appropriate values. The comparison shown in Figures 18(d) and 19(d) also demonstrate that the code-based crack spacing results are appropriate values in predicting the cracking width on the concrete slab.

## 4.5 Effects of Rubber-Latex Mortar Coating

As the key point in this research, effects of rubber-latex mortar on mechanical behavior of steel-concrete composite girders subjected to hogging moment were studied from the following three aspects: impact test of the steel girder (about the noise reduction), interface slip on key sections and flexural strain of the shear studs.

### 4.5.1 Impact test

Impact test was performed for steel girder before and after rubber-latex mortar coating. Previous researches show that the steel girder noise was mainly produced from the steel web [38], so that accelerometers were arranged on the middle center of the web in the 1/4 span. Impact force by using harmer was applied in the bottom plate in the span-center section. The test set-up was shown in Figure 21. Also, as for steel girders the structure borne noise was remarkable when the frequencies from 125 to 2000Hz, sound pressure levels within this range was recorded, and the all pass value (AP) was also calculated within this range.

The 1/3 octave filters results shown in Figure 22 indicates that the sound pressure level of 5-15 dB was reduced after rubber-latex mortar painting, and about 10 dB sound level reduction can also be confirmed for AP values. With the application of rubber-latex mortar coating, damping performance of the structural members will be enhanced, and the mass of the structures will be increased, which might be the reasons for noise reduction of the test specimens.

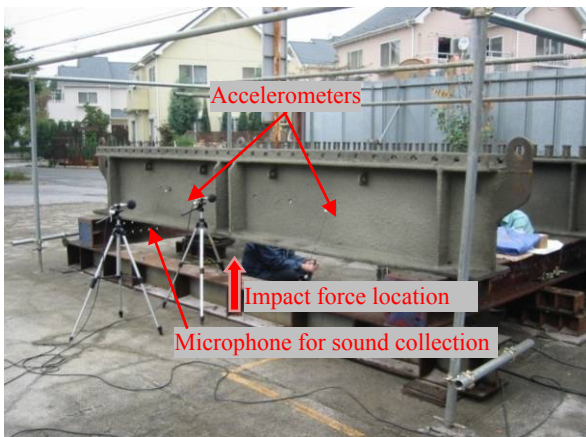


Figure 21. Set-Up of the Impact Test

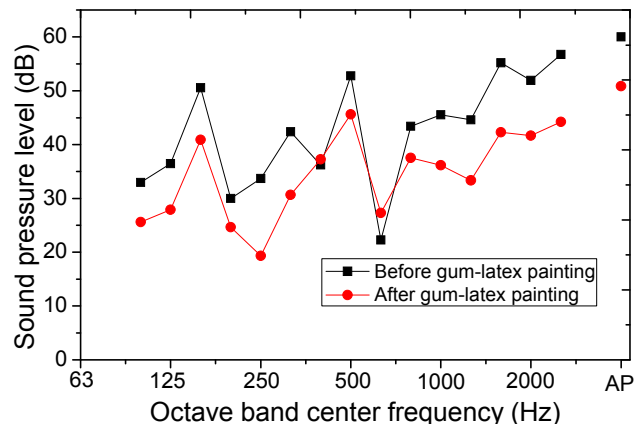


Figure 22. Impact Noise Before and After Rubber-Latex Coating



Figure 23. Arrangement of the Linear Variable Differential Transducers (LVDTs)

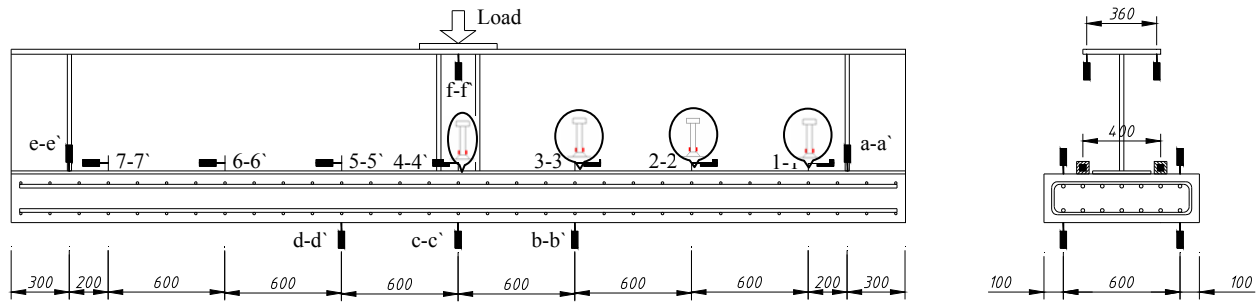
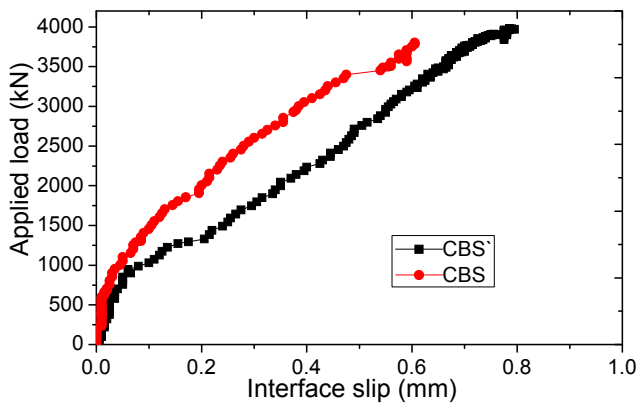
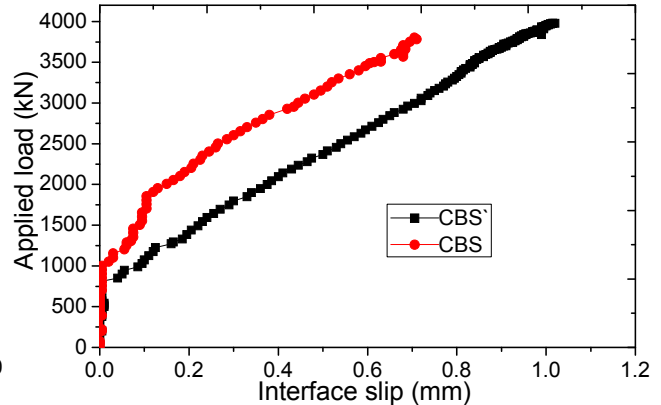


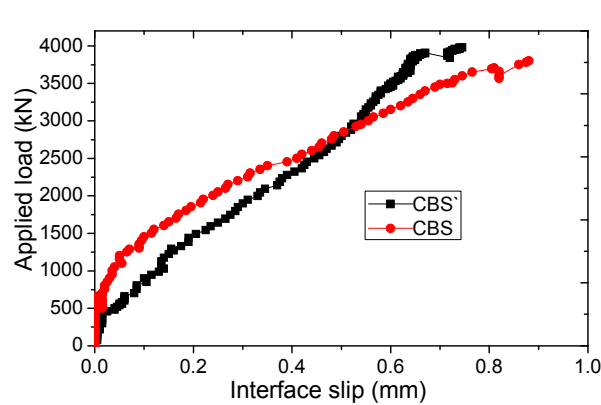
Figure 24. Arrangement of Linear Variable Differential Transducers (LVDTs)



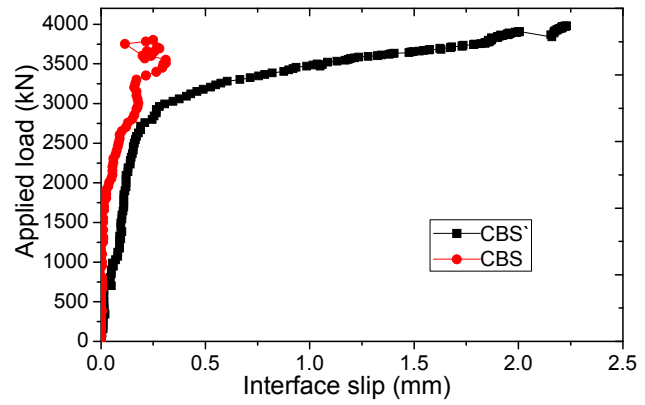
(a) Interface Slip on Section 1-1'



(b) Interface Slip on Section 2-2'

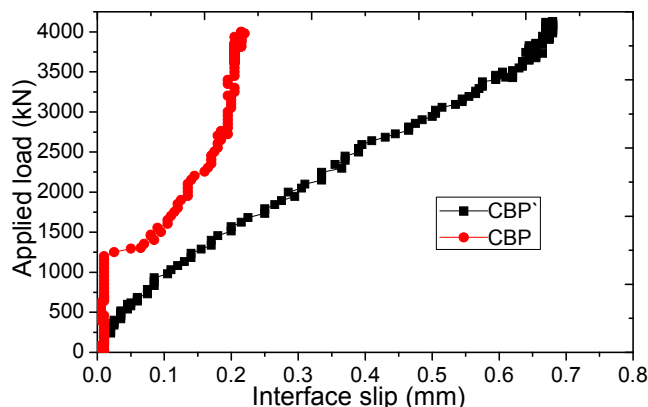


(c) Interface Slip on Section 3-3'

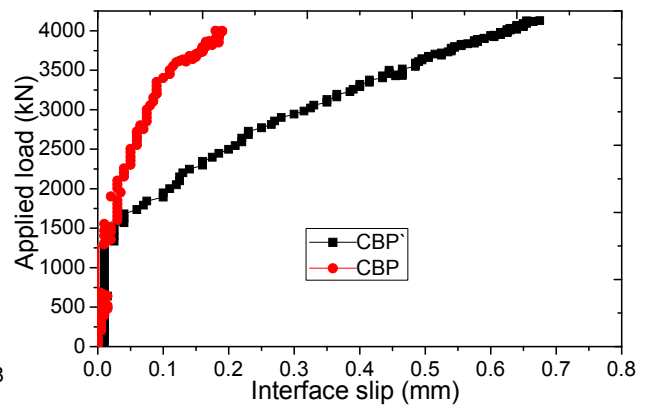


(d) Interface Slip on Section 4-4'

Figure 25. Comparison of Slip Developing Process between CBS and CBS'



(a) Interface Slip on Section 1-1'



(b) Interface Slip on Section 2-2'



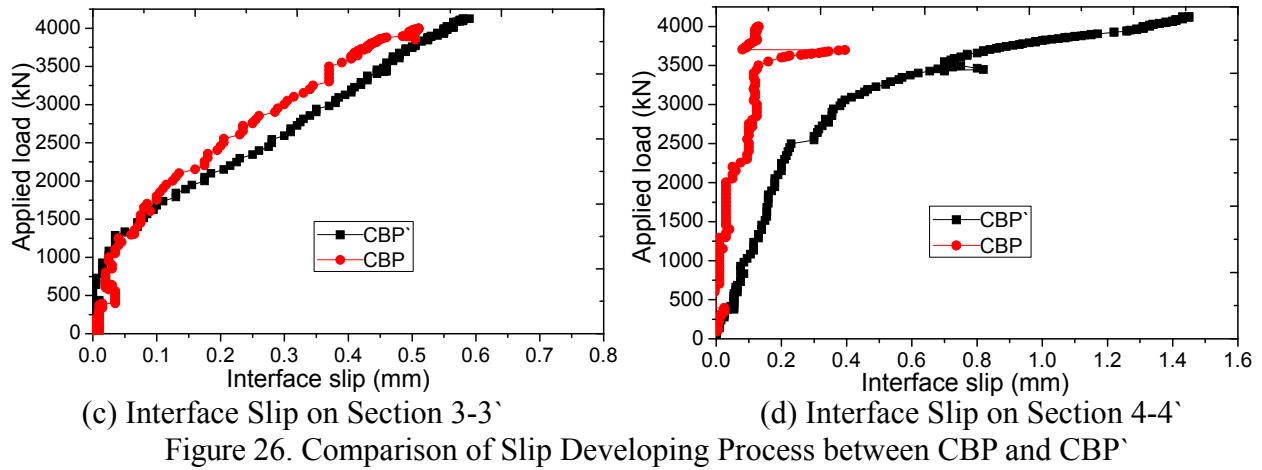


Figure 26. Comparison of Slip Developing Process between CBP and CBP'

#### 4.5.2 Interface slip

In order to learn the influence of rubber-latex mortar coating, slip development on key sections was observed and recorded in the test and compared with previous experimental results [32, 39]. CBS' and CBP', which have same size dimension and similar material with CBS and CBP, were not sprayed with rubber-latex mortar. Interface slip was measured on seven different sections along the longitudinal direction by mean of linear variable differential transducers (LVDTs), as shown in Figures.23 and 24.

The interface slip at the different sections of 1-1', 2-2', 3-3', 4-4' of these four test specimens was generated respectively and compared as shown in Figures 25 and 26. The results indicate that the slip increases with the load increase and the interface slip is relatively small when both the studs and PBLs beyond their yield load. Comparison indicates that the girders CBS and CBP have much smaller interface slip, which demonstrates that the rubber-latex mortar coating has a significant effect on reducing the interface slip, thus the adhesion bonding effects of rubber-latex mortar coating was confirmed. Besides, slip results comparison between CBS and CBP also illustrate that PBL connectors have relatively smaller slip in comparison with that of stud connectors.

#### 4.5.3 Flexural strain results of shear studs

Moreover, shear studs were also painted with rubber-latex mortar, and two strain gauges were arranged in the vertical direction at the root of each stud in sections of 1-1', 2-2', 3-3', 4-4' (shown in Figures 24, 27 and 28). Flexural strain was taken as the average of the tension and compression strains. Previous test results of CBS' (similar design of CBS without rubber-latex mortar) were given and compared with results of CBS.

The flexural strain of studs in sections of 2-2', 3-3', 4-4' during the loading process was compared between CBS and CBS' in Figure 29 (the gauges were failed on sections 1-1' of CBS during the test), it was found that the strain increased approximately bi-linear as the load increased, while the increase of slope after cracking was larger than that before cracking. Under the ultimate state, however, the values of strain for shear connectors were less than the yield strain. Therefore, the connection between the steel girder and concrete slab was reliable until the ultimate state. Besides, the comparison also indicates that the flexural strain of the stud in CBS was much smaller than that of CBS', and the flexural stiffness of studs with rubber-latex mortar seems to increase by using rubber-latex mortar.



Figure 27. Rubber-Latex Mortar on Studs

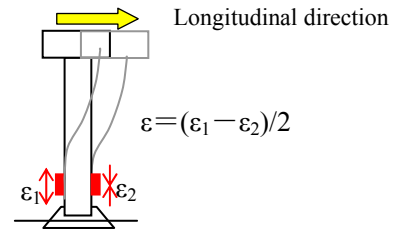


Figure 28. Arrangement of Strain Gauges on Stud

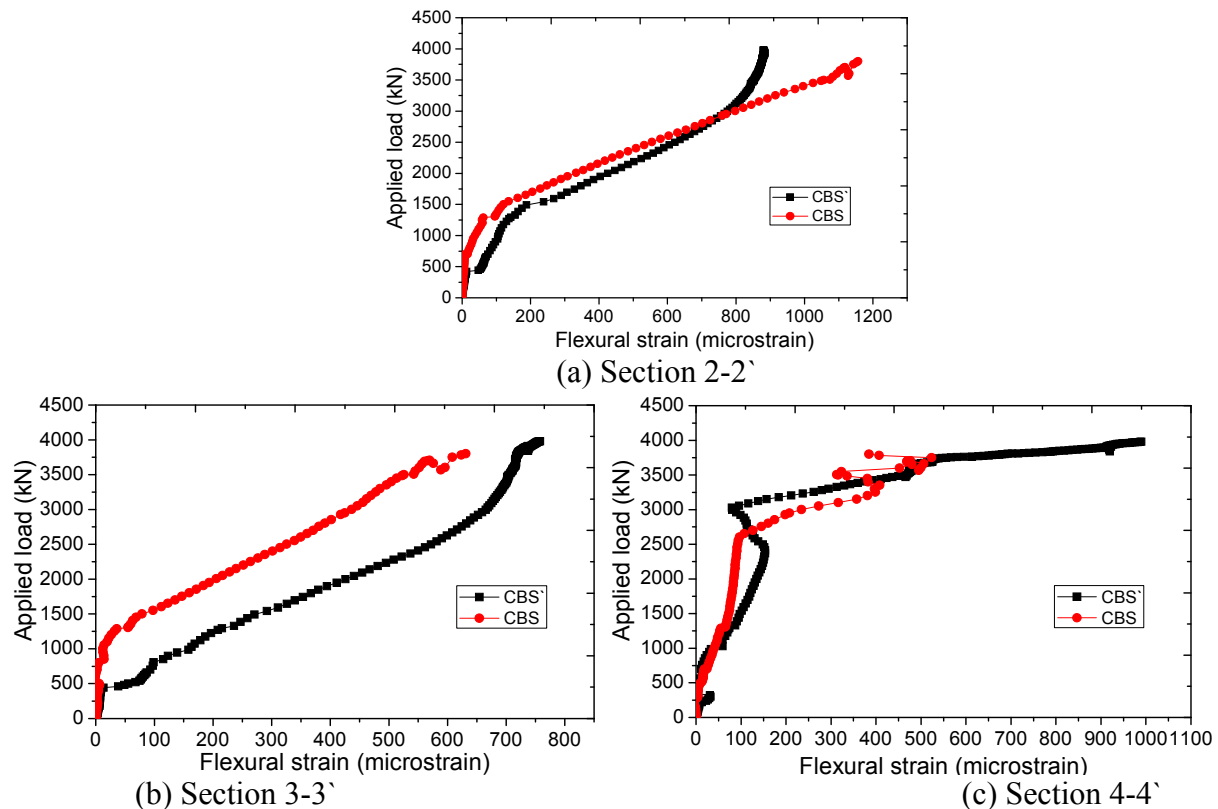


Figure 29. Comparison of Flexural Strain between Studs with (CBS) and without (CBS') Rubber-Latex Mortar

## 5. CONCLUDING REMARKS

The experimental and numerical studies were performed to investigate the inelastic behavior of steel-concrete composite girder subjected to hogging moment. The load-displacement relations, strain distribution and movement of the sectional neutral axis as well as the crack and interface slip developing process were presented in this paper. Experiments based 3-D nonlinear finite element models were also established. From the present results, the following conclusions and recommendations deserving priority are made:

- (1) Proposed numerical models can simulate the test specimens well on the basis of the present load-deformation response, sectional strain distribution, rebar yielding and crack developing process on the concrete slab, thus it follows that proposed numerical method can be served as a basis for the design of steel-concrete composite girders under hogging moment. Besides, perfect bond assumption for concrete-reinforcement interface was proved suitable before rebar yielding, but relatively large difference was produced after rebar yielding.



- (2) Results from the impact test indicate that the application of rubber-latex mortar can be beneficial to reducing the noise pressure levels (about 10 dB in the present test). Flexural stiffness of the shear connectors was also found to be enhanced by using rubber-latex mortar. Besides, adhesion bonding effects of rubber-latex mortar on the interface were confirmed in the tests by comparing with specimens without using rubber-latex mortar.
- (3) Both PBLs and Stud connectors are effective shear connective devices for composite girders subjected to negative bending moment, and no obvious differences were found except that PBL connectors could slightly improve the rigidity of the composite girder under both the serviceability limit state and the ultimate limit state in comparison with stud connectors according to the experimental load-displacement relationship as well as the interface slip. Stud specimens have relatively better mechanical behavior in regard to concrete cracking, such as initial cracking and crack closure.
- (4) It is considered that the composite neutral axis moves between the cross-sectional elastic neutral axis and the plastic neutral axis. The location of the composite neutral axis was found to be the same as un-cracked section before cracking. After cracking, tension stiffening of the concrete between cracks is suggested to be considered when determining the location of the neutral axis.
- (5) Average crack spacing on concrete slab was found mainly dependent on the transverse reinforcement, and the maximum crack spacing specified by current specifications was proved to be appropriate in comparison with test values. Furthermore, code-based ultimate loads were similar to test results, and current specifications based on the plastic analysis were proved to be appropriate as a design method on the safe side.

## ACKNOWLEDGMENTS

The experimental work was carried out in the Structural Laboratory of Waseda University, Tokyo, Japan. The financial support sponsored by Ministry of Land, Infrastructure, Transport and Tourism of Japan is gratefully acknowledged. Special thanks were given to Assoc. Prof. Taniguchi from Maebashi Institute of Technology in Japan (Formerly, senior researcher at Railway Technical Research Institute) for his suggestions and test supports to this study.

## REFERENCES

- [1] Manfredi, G., Fabbrocino, G. and Cosenza, E., "Modeling of Steel-concrete Composite Beams under Negative Bending", *Journal of Engineering Mechanics*, ASCE, 1996, Vol. 125, No. 6, pp. 654-662.
- [2] Ryu, H.K., Chang, S.P., Kim, Y.J. and Kim, B.S., "Crack Control of a Steel and Concrete Composite Plate Girder with Prefabricated Slabs under Hogging Moments", *Engineering Structures*, 2005, Vol. 27, No. 11, pp. 1613-1624.
- [3] Ryu, H.K., Kim, Y.J. and Chang, S.P., "Crack Control of a Continuous Composite Two-girder Bridge with Prefabricated Slabs under Static and Fatigue Loads", *Engineering Structures*, 2007, Vol. 29, No. 6, pp. 851-864.
- [4] He, J., Liu, Y., Chen, A. and Yoda, T., "Experimental Study on Inelastic Mechanical Behaviour of Composite Girders under Hogging Moment", *Journal of Constructional Steel Research*, 2010, Vol. 66, No. 1, pp. 37-52.
- [5] Chen, S. and Jia, Y., "Required and Available Moment Redistribution of Continuous Steel-concrete Composite Beams", *Journal of Constructional Steel Research*, 2008, Vol. 64, No. 2, pp. 167-175.

- [6] Chen, S., Jia, Y. and Wang, X., "Experimental Study of Moment Redistribution and Load Carrying Capacity of Externally Prestressed Continuous Composite Beams", *Structural Engineering and Mechanics*, 2009, Vol. 31, No. 5, pp. 605-619.
- [7] Fan, J., Nie, J., Li, Q. and Wang, H., "Long-Term Behavior of Composite Beams under Positive and Negative Bending. I : Experimental Study", *Journal of Structural Engineering*, ASCE, 2010, Vol. 136, No. 7, pp. 849-857.
- [8] Fabbrocino, G., Manfredi, G. and Cosenza, E., "Analysis of Continuous Composite Beams including Partial Interaction and Bond", *Journal of Structural Engineering*, ASCE, 2000, Vol. 126, No. 11, pp. 1288-1294.
- [9] Nie, J., Fan, J. and Cai, S., "Stiffness and Deflection of Steel–Concrete Composite Beams under Negative Bending", *Journal of Structural Engineering*, ASCE, 2004, Vol. 130, No. 11, pp.1842-1851.
- [10] Loh, H.Y., Uy, B. and Bradford, M.A., "The Effects of Partial Shear Connection in the Hogging Moment Regions of Composite Beams Part II—Analytical Study", *Journal of Constructional Steel Research*, 2004, Vol. 60, No. 6, pp. 921-962.
- [11] Nguyen, Q.H., Hjiat, M., Uy, B. and Guezouli, S., "Analysis of Composite Beams in the Hogging Moment Regions using a Mixed Finite Element Formulation", *Journal of Constructional Steel Research*, 2009, Vol. 65, No. 3, pp. 737-748.
- [12] Lin, W. and Yoda, T., "Inelastic Behavior of Continuous Steel-Concrete Composite Beams with Gum-Latex Mortar Coating", *Proceedings of the 2011 World Congress on Advances in Structural Engineering and Mechanics (ASEM+)*, 2011, pp. 5451-5459.
- [13] Lin, W., Yoda, T., Taniguchi, T. and Hansaka, M. "Performance of Strengthened Hybrid Structures Renovated from Old Railway Steel Bridges." *Journal of Constructional Steel Research*, 2013, Vol. 85, pp. 130-139.
- [14] Taniguchi, N., Hansaka, M., Koide, N., Ogaki, K., Okubo, F. and Saeki, T., "Study of the Hybrid Structures changed from the Steel Bridges for Railroad which Considered Construction", *Journal of Structural Engineering*, JSCE, 2011, Vol. 57A, pp. 1052-1059. [in Japanese].
- [15] Japan Society of Civil Engineers, "Standard Specifications for Steel and Composite Structures 2007", 2007, pp.250-259.
- [16] Taniguchi, N. and Ikeda, M., "Experimental Study on a Crack Formation for Railway Composite Girders with Negative Bending", *Proceedings of the Third International Conference on Steel and Composite Structures ICSCS07*, Manchester, UK, 2007, pp. 915-920.
- [17] Hognestad, E., "A Study of Combined Bending and Axial Load in Reinforced Concrete Members", *University of Illinois Engineering Experiment Station, Bulletin Series*, 1951, No. 399, pp. 40-54.
- [18] Park, R. and Paulay, T., "Reinforced Concrete Structures", John Wiley and Sons, Inc., 1975, pp.11-36.
- [19] Nakasu, M. and Iwatate, J., "Fatigue Experiment on Bond between Concrete and Reinforcement", *Transaction of JSCE*, 1996, Vol. 426, pp. 852-853.
- [20] Wang, Y. C., "Deflection of Steel-concrete Composite Beams with Partial Shear Interaction", *Journal of Structural Engineering*, 1998, Vol. 124, No. 10, pp. 1159–1165.
- [21] Ollgaard, J.G., Slutter, R.G. and Fisher, J.W., "Shear Strength of Stud Connectors in Lightweight and Normal Weight Concrete", *Engineering Journal of AISC*, 1971, Vol. 8, No.2, pp. 55-64.
- [22] Ahna, J., Leeb, C., Wona, J. and Kima, S., "Shear Resistance of the Perfobond-rib Shear Connector Depending on Concrete Strength and Rib Arrangement", *Journal of Constructional Steel Research*, 2010, Vol. 66, No. 10, pp. 1295-1307.

- [23] Al-Darzi, S.Y.K., Chen, A.R. and Liu, Y.Q., "An Experimental Investigation on Stud and Perfobond Connectors with Push-out test", *Proceeding of the 13th International Conference on Steel and Composite Structures*, UK, 2007, pp. 455-462.
- [24] Iwasaki, H., Fujii, K., Fukada, K., Toyota, T. and Nakamura, H., "A Consideration on Slip Test Methods for Perfobond Shear Connector Focusing on Concrete Confinements", *1st International Conference on Advances in Experimental Structural Engineering*, 2005. pp. 871-76.
- [25] Machacek J, Studnicka J., "Perforated shear connector", *Steel and Composite Structures*, 2002, Vol.2, No. 1, pp.51-66.
- [26] Medberry SB, Shahrooz BM., "Perfobond shear connector for composite construction", *AISC Journal*, 2002, Vol.1, pp.2-12.
- [27] Ushijima Y, Hosaka T, Mitsuki K, Watanabe H, Tachibana Y, Hiragi H., "An experimental study on shear characteristics of perfobond strip and its rational strength equations", *International symposium on connections between steel and concrete*, 2001, pp.1066-1075.
- [28] Valente MIB, Cruz PJS., "Experimental analysis of Perfobond shear connection between steel and lightweight concrete", *Journal of Constructional Steel Research*, 2004, Vol.60, pp.465-479.
- [29] Okada, J., Yoda, T., and Lebet, J.P., "A study of the grouped arrangement of stud connectors on the shear strength", *Journal of the Japan Society of Civil Engineers*, 2004, Vol.766, pp.81-95. [in Japanese].
- [30] DÖRR, K., "Ein Beitrag zur Berechnung von Stahlbetonscheiben unter besonderer Berücksichtigung des Verbundverhaltens", PhD thesis, University of Darmstadt, 1980.
- [31] AASHTO., "AASHTO LRFD Bridge Design Specifications", Washington, DC, 2007.
- [32] Lin, W., and Yoda, T., "Mechanical Behaviour of Composite Girders Subjected to Hogging Moment: Experimental Study", *Journal of Japan Society of Civil Engineers*, 2011, Vol.67, No.3, pp.583-596.
- [33] Eurocode 4. Design of composite steel and concrete structures. General rules and rules for buildings, British-Adopted European Standard, 2005.
- [34] Ministry of Construction of People's Republic of China, "Code for design of steel structures. GB50017-2003", China Planning Press, Beijing, 2003. [in Chinese].
- [35] CEP-FIP., "Model Code 90, Model Code for Concrete Structures, Comité Euro-International du Béton (CEB) - Fédération Internationale de la Précontrainte (FIP)", Thomas Telford Ltd., London, UK; 1993.
- [36] Ministry of Land, Infrastructure, Transport and Tourism, "Standard specification for railway structures", Japan, 2009.
- [37] Frosch, R.J., "Another Look at Cracking and Crack Control in Reinforced Concrete", *ACI Structural Journal*, 1999, Vol.96, No.3, pp.437-442.
- [38] Taniguchi, N., Hansaka, M., Koide, N., Ogaki, K., and Saeki, T., "Study of the hybrid structures changed from the steel bridges for railroad which considered construction", *Journal of Structural Engineering, JSCE*, 2011, Vol.57A, pp.1052-59. [in Japanese].
- [39] Kouzuki, T., Tanahashi, A., Taniguchi, N., Ikariyama, H., Yoda, T., "Experimental study of shear connector for negative bending composite girders with the rubber-latex mortar coating", *Journal of Structural Engineering, JSCE*, 2009, Vol.56A: 1161-68. [in Japanese].

# DESIGN MOTIVATION, MECHANICAL MODELING AND NONLINEAR ANALYSIS OF COMPOSITE PR MOMENT FRAMES WITH SMART SMA CONNECTION SYSTEMS

Jong Wan Hu

*Assistant Professor, Department of Civil and Environmental Engineering, College of Urban Science,  
University of Incheon, Incheon, 406-840, Republic of Korea  
(Head of Center, Incheon Disaster Prevention Research Center, University of Incheon, Incheon, 406-840,  
Republic of Korea)  
E-mail: jongp24@incheon.ac.kr*

---

*Received: 27 March 2012; Revised: 8 July 2012; Accepted: 13 July 2012*

---

**ABSTRACT:** This paper focuses on seismic design and behavior of hybrid structures composed of partially restrained (PR) steel-concrete composite-moment frames (C-MFs). The innovative aspects of this research are to introduce new smart connections between steel beams and concrete-filled tube (CFT) columns that utilize a combination of low-carbon steel and shape memory alloy (SMA) components in the C-MF design. In these new connections, we can exploit the recentering effect provided by super-elastic SMA tension bars to reduce both building damage and residual drift after a major earthquake event, while the low-carbon steel components provide excellent energy dissipation. The results of corresponding component tests were used to develop cyclic stiffness models for individual components in the connection. The seismic behavior of the composite moment-resisting frames with new connection systems was reproduced by performing nonlinear pushover and time-history analyses. The analysis results suggest that these frames are very effective in resisting seismic events due to the structural advantages of the smart SMA PR-CFT connections.

**Keywords:** Composite moment frames, Shape memory alloys (SMAs), Partially restrained (PR) connections, Concrete-filled tube (CFT) columns, Stiffness models, Mechanical modeling, Nonlinear frame analyses

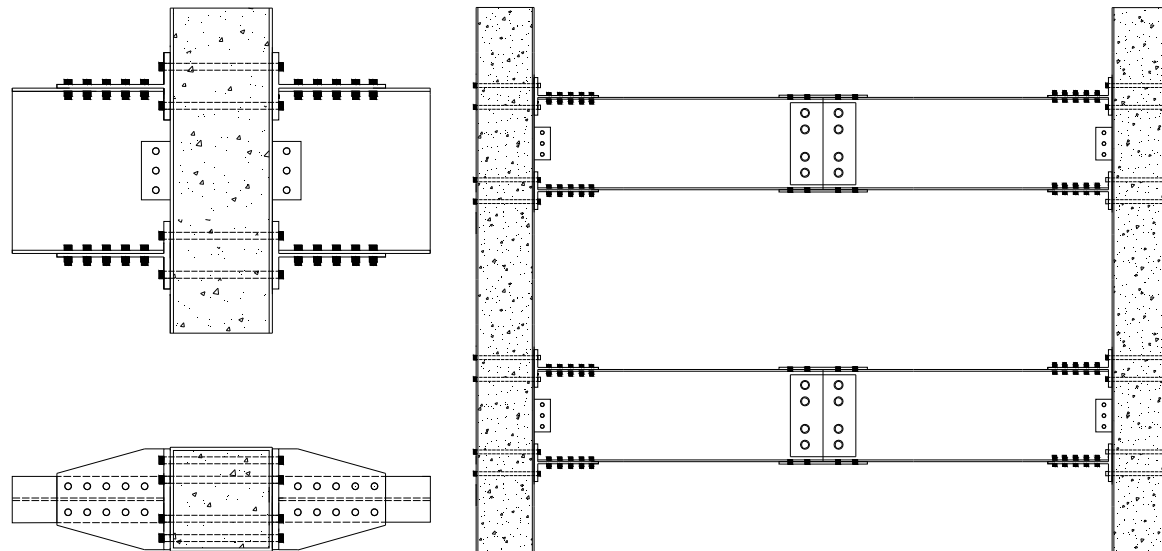
---

## 1. INTRODUCTION

Composite-partially restrained frames (C-PRMFs) are composed of I-shape steel beams and composite concrete-filled steel tube (CFT) columns, which are interconnected with PR composite connections (e.g. Tsai et al. [1]; Wu et al. [2]). The C-PRMFs were originally proposed for use in the areas of low to moderate seismicity, classified as seismic design categories (SDC) C and below (e.g. AISC (2005) [3]; ASCE [4]). However, they can be utilized at the areas of higher seismicity in the western United States (SDC D and over) with appropriate detailing and analysis. Recently developed bidirectional bolted CFT column-to-beam connections have been widely used in modern steel structures because they provide superior seismic performance with respect to strength, ductility, energy dissipative capacity, and stiffness (e.g. Wu et al. [2]; Wu et al. [5]; Park et al. [6]; Hu et al. [7]). Studies have demonstrated that their seismic resistance exceeds requirements stipulated in the seismic design codes of Taiwan and US (e.g. Tsai et al. [1]; Wu et al. [2]; Wu et al. [5]). T-sub connections were used as the main component for the composite bolted PR-CFT connections used in this study (see Figure 1).

For the smart PR-CFT connections proposed in this study, three design concepts were integrated: (a) the use of CFT columns, (b) the use of PR connections, and (c) the introduction of new smart materials (i.e. Shape memory alloys). Mixed or hybrid systems such as CFT columns combine the synergetic advantages of ductility and toughness associated with steel structures and high compressive strength associated with confined concrete components. CFT columns in the moment resisting frame are very suitable as the vertical elements to resist high gravity loading because they have a high strength-to-weight ratio (e.g. Tsai et al. [1]; Wu et al. [5]; Park et al. [6]; Hu et al. [7]).

They are especially efficient in high seismic areas because of excellent dynamic resistance under biaxial bending plus axial force and good damping characteristics (e.g. Hu et al. [8]). Moreover, the steel tube can be used as a formwork for casting concrete; therefore, this design improves constructability over conventional reinforced concrete structures. CFT columns have gained wide acceptance in China, Japan, Korea, Taiwan, and in some areas of the USA for use in high-rise construction. Circular and rectangular shapes can be used in CFT column sections (CCFT or RCFT).



(a) Composite bolted PR-CFT connection

(b) Composite PR moment frames (C-PRMF) using PR-CFT connections

Figures 1 (a) and (b). Connection Details and Composite PR Moment Frames (C-PRMF)

Major failures of fully restrained (FR) moment frames with welds during the 1994 Northridge and 1995 Kobe earthquakes led to the conclusion that traditional buildings suffer from brittle fracture problems in the moment connections (e.g. Leon [9]). When using PR connections, improved performance is derived from a combination of (a) a decrease in the seismic forces stemming from the additional flexibility of component members due to the PR nature of the connections, and (b) an increase in the structural strength reserve capacity due to the lack of brittle connection failure modes. Although PR connections are not as stiff as FR connections, it has been demonstrated that well-detailed PR structures can provide similar or superior seismic behavior compared to their FR counterparts (e.g. Leon [9]; Green et al. [10]; Rassati et al. [11]).

More recently, beam-to-column connections using super-elastic (SE) Nitinol (NiTi) tendons have been investigated at the Georgia Institute of Technology (Georgia, USA). The goal is to use these new materials in the design of moment connections (e.g. Penar [12]; Hu [13]). SE Nitinol is a type of SMA with the unique ability to sustain large strain that is fully reversible, thereby automatically returning the structural element to its original position without residual deformation when stresses are removed, as shown in Figure 2 (e.g. DesRoches et al. [14]). The characteristics of the stress-strain curve largely depend on a phase transformation process that is controlled by heat treatment and chemical composition. A recentering effect from the connections can be expected due to the SE effect of these new materials.

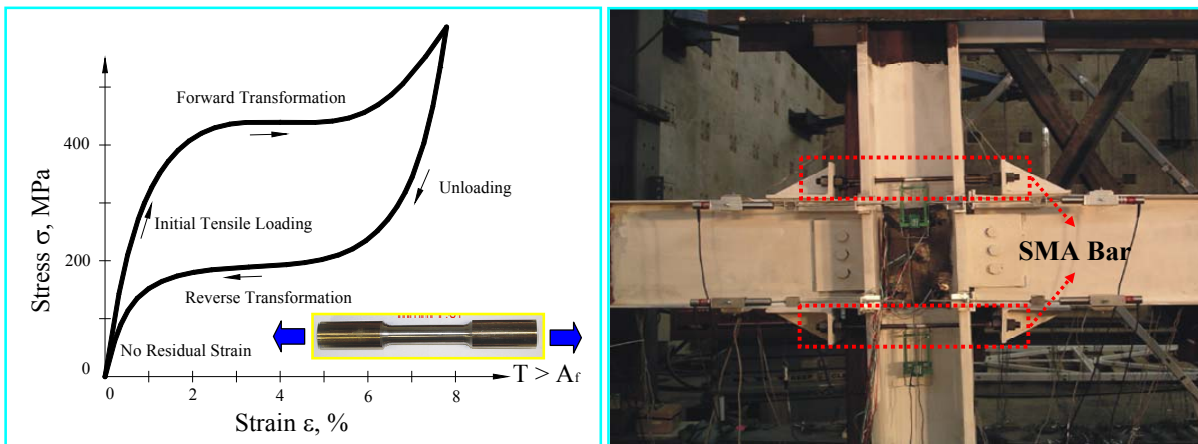


Figure 2. Stress and Strain Behavior and Connection Application for Super-elastic (SE) SMA Materials (e.g. DesRoches et al. [14])

A new type of connection, which is called the SMA PR-CFT connection in this study (see Figure 3), combines the advantages of bolted PR connections, new smart SMA materials, and the aforementioned composite structures. Contrary to the existing PR connection, this new connection exploits the combination of steel bars and SE Nitinol bars as connection elements to CFT columns. The combination of CFT columns, SMA bars, and PR connections will achieve upgraded strength, local buckling prevention, recentering capability, and excellent ductility.

This paper is divided into three parts. We describe (a) a simplified two dimensional (2D) joint model for cyclic tests, (b) numerical composite-moment frame models with joint models, and (c) nonlinear frame analyses. The seismic performance of the composite moment frame with the proposed SMA PR-CFT connections is compared with the seismic performance of other composite moment frames with commonly used connections in order to show the adequacy of numerical simulations and the structural advantage of the proposed connection design. Most of the numerical tests were performed using finite element (FE) models for connections and composite frames using the OpenSEES program (e.g. Mazzoni et al. [15]).

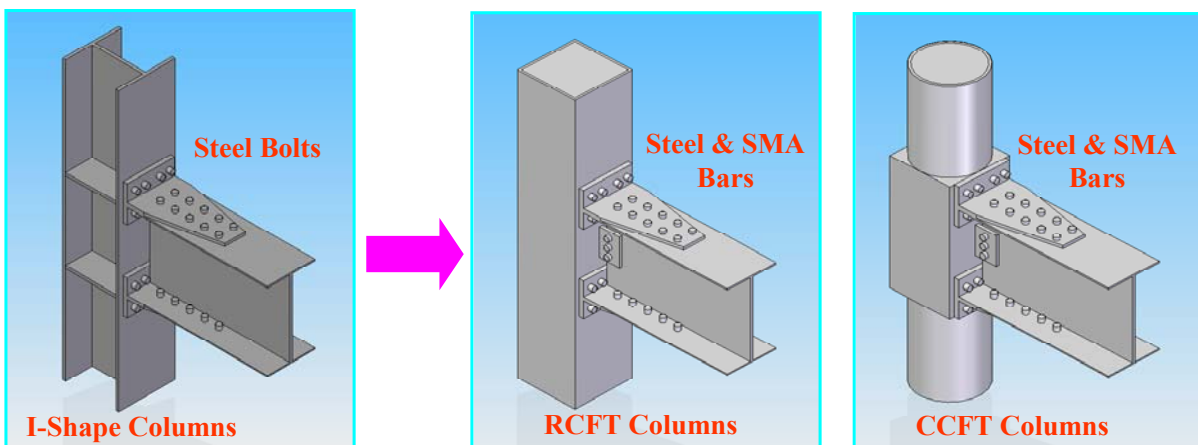


Figure 3. New Smart PR-CFT Connections Compared with the Previous PR Connection

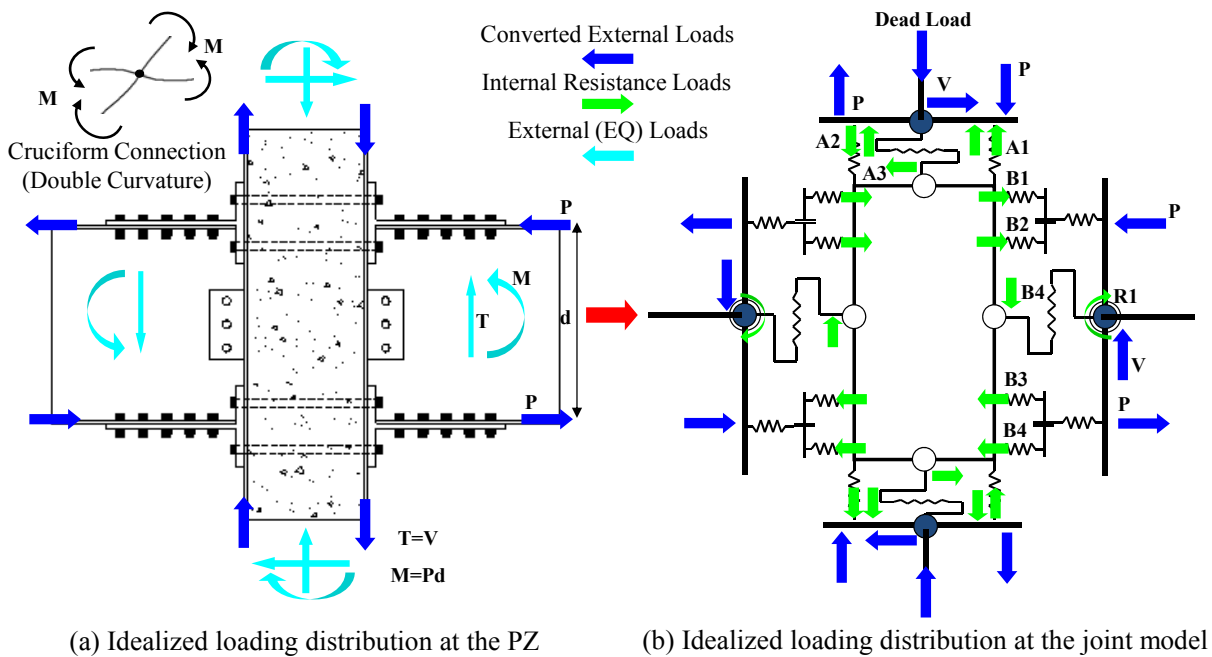
## 2. JOINT MODEL

Joint models suitable for use in nonlinear frame analyses are able to accurately reproduce the inelastic response of moment frame structures under cyclic loading. In this study, joints were modeled as user-defined 2D joint elements that are composed of assemblies of springs, linked to each other in series or parallel to mimic the connection behavior. The primary purpose is to develop simplified, numerically efficient, accurate joint models that simulate the real non-linear connection, and frame behavior.

### 2.1 Basic Mechanisms

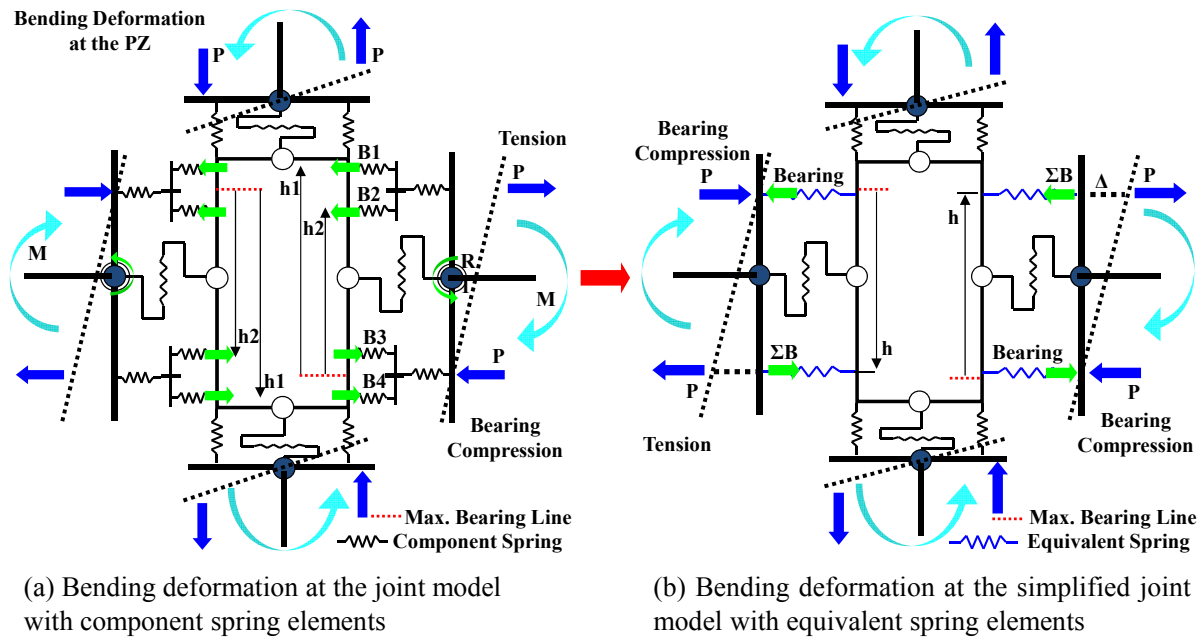
A moment frame structure should provide adequate stiffness, strength, and energy dissipation capacity to withstand both gravity loads and lateral loads. The random seismic inertial forces introduced into a building by an earthquake can be converted into a set of equivalent lateral loads for design (e.g. ASCE [4]). As lateral loads dominate the behavior, the joints are mostly deformed in a shear mode (a scissors-line manner) due to double curvature bending. The double curvature moments resulting from lateral loads are delivered into the connections as equivalent axial forces (e.g. Braconi et al. [16]).

Figure 4 show the idealized force distribution at the perimeter of the joint for a T-stub connection subjected to seismic loads. Connection components such as tension bars, flanges, T-stems, and shear tabs were modeled as corresponding nonlinear-axial or nonlinear-rotational spring elements. The slip mechanism was simulated using sliding elements (see Figure 4 (b)). Generally, the beam develops flexural strength, while the column carries the axial gravity loads elastically. These member forces are shown as equivalent concentrated forces acting on the joint (see blue arrows in Figure 4 (a)). The internal reactions in the connection components (see yellowish green arrows in Figure 4 (b)) act against these converted external forces to satisfy force equilibrium ( $\sum B_i = P$ ).



Figures 4 (a) and (b). Force Distribution at the Joint Model for the Composite PR-CFT Connection

The response of the joint model under shear deformations resulting from the bending forces in the framing members is shown in Figure 5. The internal tension loads are carried by tension bars, which correspond to the top springs on the right side of the connection, as shown in Figure 5 (a). Internal compression loads resulting from the bearing forces between the beam flange and the CFT column surface are transferred into the bottom springs on the right side of the connection. The bars inside the compression zone do not produce a significant contribution to the response mechanism of the joint model. The deformations of the tension bars located above bearing compression are proportional to their distance from the centerline of the bottom flange ( $\Delta = \Delta_i h/h_i$ ).

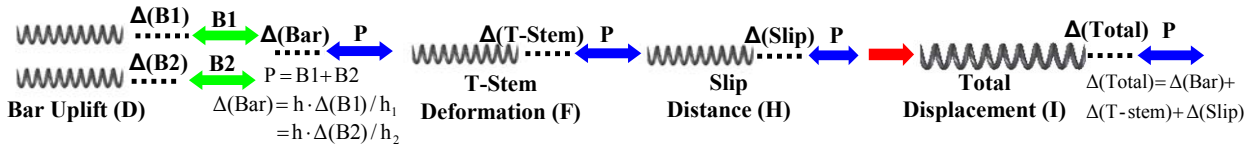


Figures 5 (a) and (b). Force and Deformation Response Mechanism of the Joint Model

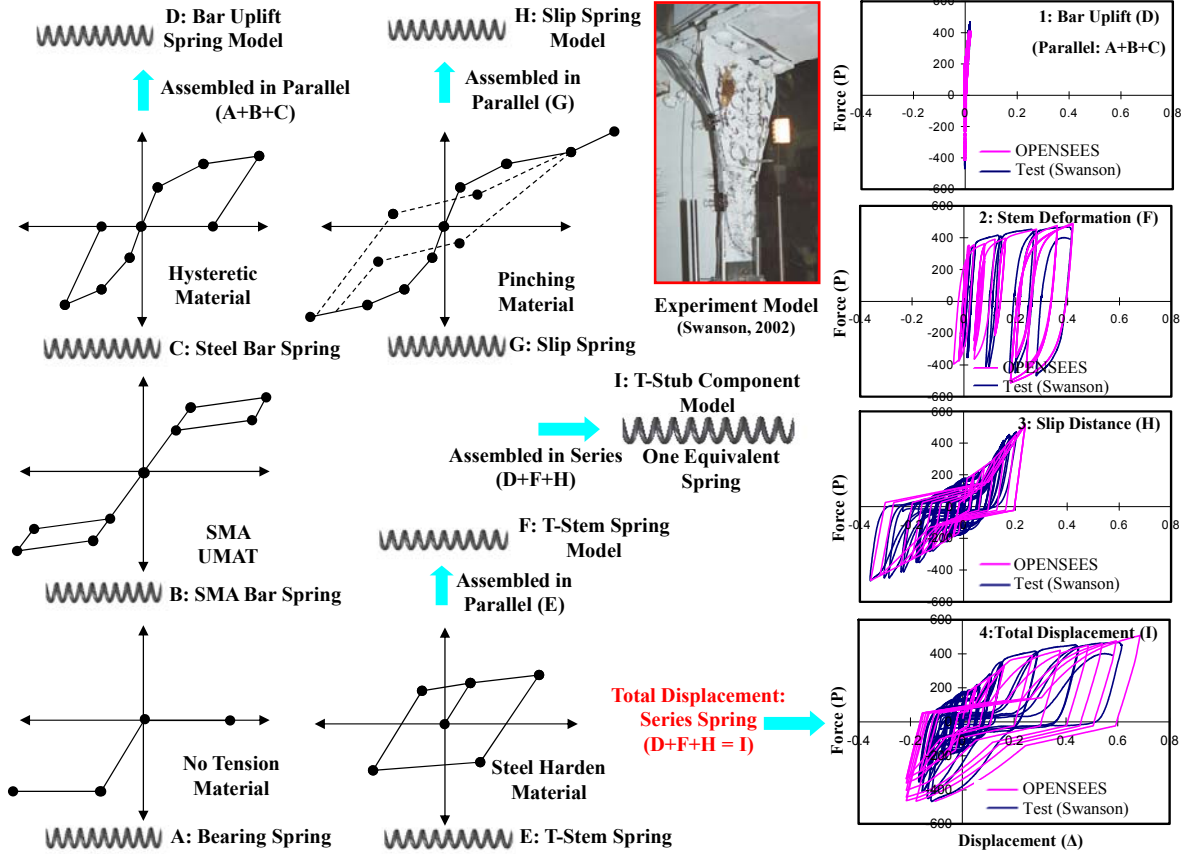
## 2.2 Component Springs

Detailed procedures for the formation of an equivalent spring element are illustrated in Figure 6, including the behavior of individual component springs. The main properties are modeled as idealized stiffnesses, as presented in Figure 6 (a). The stiffness models for tension bars were determined from their own material properties, whereas those for bearing compression, T-stem deformation, and slip-sliding were obtained via established stiffness models (e.g. Kurak et al. [17]; Rex and Easterling [18]; Astaneh-Asl [19]; Hu et al. [20] ) and curve fitting to existing test data (e.g. Swanson [21]; Swanson [22] ) (see Figure 6 (c)). For numerical analyses, the curves were generated using default material commands available in the OpenSEES program. The behavioral properties for slip springs and T-stem springs were generated using pinching materials and steel hardening materials, respectively (e.g. Mazzoni et al. [15]). The stiffness model for the superelastic SMA materials, on the other hand, was simulated by user-defined material codes (e.g. Davide [23]) because an appropriate material command was not available in the program. These stiffness models were assigned to corresponding component springs to simulate the behavior of component members during cyclic loading tests.





(b) The assemblage of the spring components



(a) The behavioral property of individual components

(c) The calibration of stiffness models to experimental results

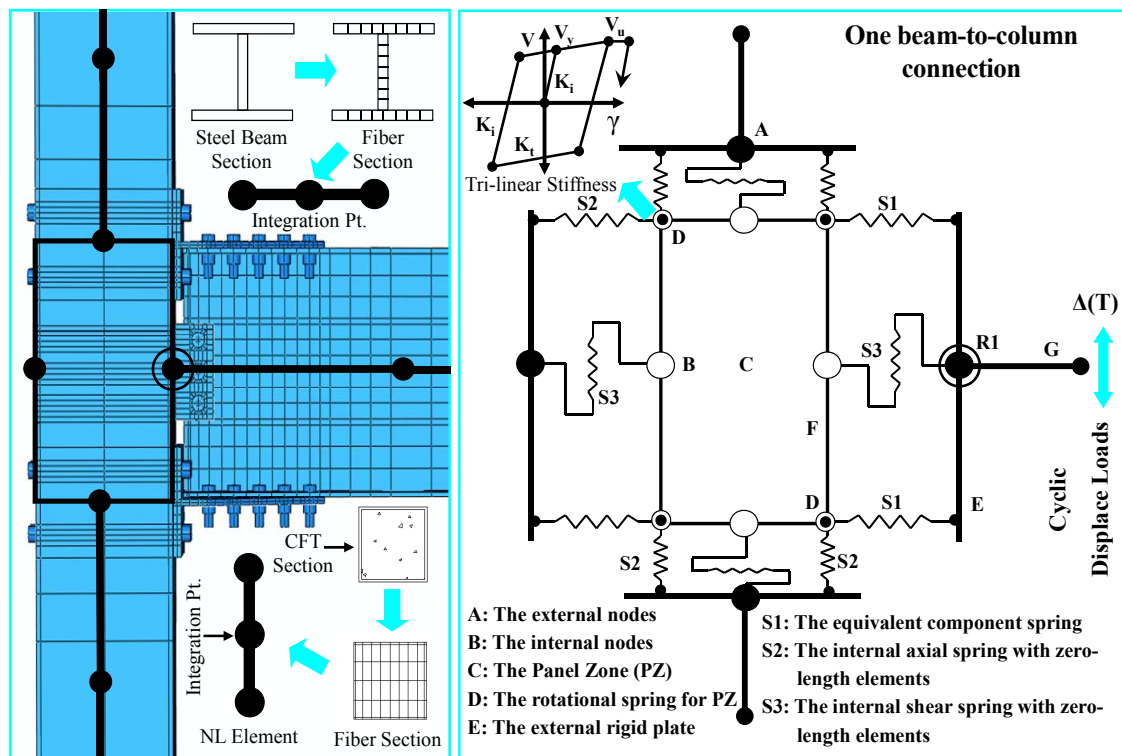
Figures 6 (a), (b), and (c). Behavioral Properties and Assembly Procedures for the Component Spring Elements

The total displacement of the T-stub was constructed by adding the deformations from three basic mechanisms together under the converted axial load ( $P$ ). The mechanisms are (a) bar uplift and flexural deformation of the T-flange, (b) T-stem deformation, and (c) slip. The individual basic mechanisms occurring in the connection components were ideally modeled by using nonlinear spring elements. These different spring elements in the connection component can be assembled in parallel or series depending on how they interact with each other (see Figures 6 (a) and (b)). This methodology offers the possibility of component assemblies and condensed-mechanical models so as to achieve a simplified model for numerical analyses. The response mechanisms acting on the tension bars were combined in parallel so that internal bar reaction forces correspond to the converted axial force ( $B1+B2=P$ ). As this converted axial force ( $P$ ) was transmitted into consecutive component springs, each of the deformations was added to the total displacement by the use of a series system ( $\Delta(Bar) + \Delta(T-stem) + \Delta(Slip) = \Delta(Total)$ ). Their stiffnesses were also assembled into the final, total rigidity, which is the overall stiffness of the T-stub component. Therefore, the total displacement of the T-stub component was simulated through a cyclic loading test carried out by using the equivalent spring element as can be seen in Figure 6 (c). Furthermore, the cyclic curves reproduced by using the spring elements were compared with the resulting curves obtained from the experimental component tests in an effort to validate the component spring

element model for simulation. The experimental component tests were performed by Swanson (e.g. Swanson [21]). In this study, the TA01 specimen for the experimental test was selected for comparison. Both results compared to each other show good agreements in terms of initial stiffness, shape of the envelope, ultimate capacity, and even location of pinching points, and thus result in a good visual match of the shape of the hysteresis loops.

### 2.3 User-defined 2D Joint Elements

The data from experimental connection tests (e.g. Swanson [21]) were employed to develop a simplified 2D joint element for use in the OpenSEES program. This program allows the implementation of refined joint elements such as the one proposed herein as shown in Figure 7. The composition of the joint element for a general beam-to-column connection is illustrated in this figure. This element includes (a) two equivalent spring elements (S1) to reproduce the behavior of the connection components, (b) six internal spring elements (S2) to reproduce the axial deformation of the CFT column, (c) four internal shear springs (S3) to reproduce the shear deformation of the CFT column and the beam, (d) one shear panel zone element (C) to reproduce the failure of the panel zone under severe loading, and (e) two rotational spring elements (D) that are intended to reproduce the shear deformation at the composite panel zone (e.g. Hu [13]). Additional rotational spring elements can be used if shear tabs are present in the connection model. All spring elements were formulated using zero-length elements with their stiffness properties. Thus, they are implemented with the interior and exterior planes coincident.



(a) The element formulation on the connection (b) The joint element of one beam-to-column connection

Figures 7 (a) and (b). Typical Joint Element for a Joint Model (One Beam-to-column Connection) (e.g. Hu [13])

### 3. NUMERICAL MODELS FOR COMPOSIT-MOMENT FRAMES

#### 3.1 Connection Design

The connections were fabricated with an assembly of various members cut from standard shapes provided in the current design specification (e.g., AISC [3]). A572 Grade 50 steel with strain hardening was used for beam members, shear tabs, and T-stub components. The T-stub connections accepted herein were composed of thick T-stub components cut from a W16X100 section and 114X228X14mm plate for the shear tabs. Standard tube sections constructed with A500 Grade C steel material were used for CFT columns. A490 high strength bolt material was used to fabricate steel bars, washers, and nuts. The diameter of web and shear bolts was 25mm. For the purpose of maximizing the recentering mechanism, super-elastic SMA bars were installed at the parts where large deformations were feasibly to occur. The panel zones were designed as rectangular shape in order to allow for bidirectional T-stub connections with steel and SMA tension bars completely running through the connections. These tension bars include 25mm diameter, either 510mm length for RCFT columns or 560mm one for CCFT columns. The details for connection design are described in Figure 8.

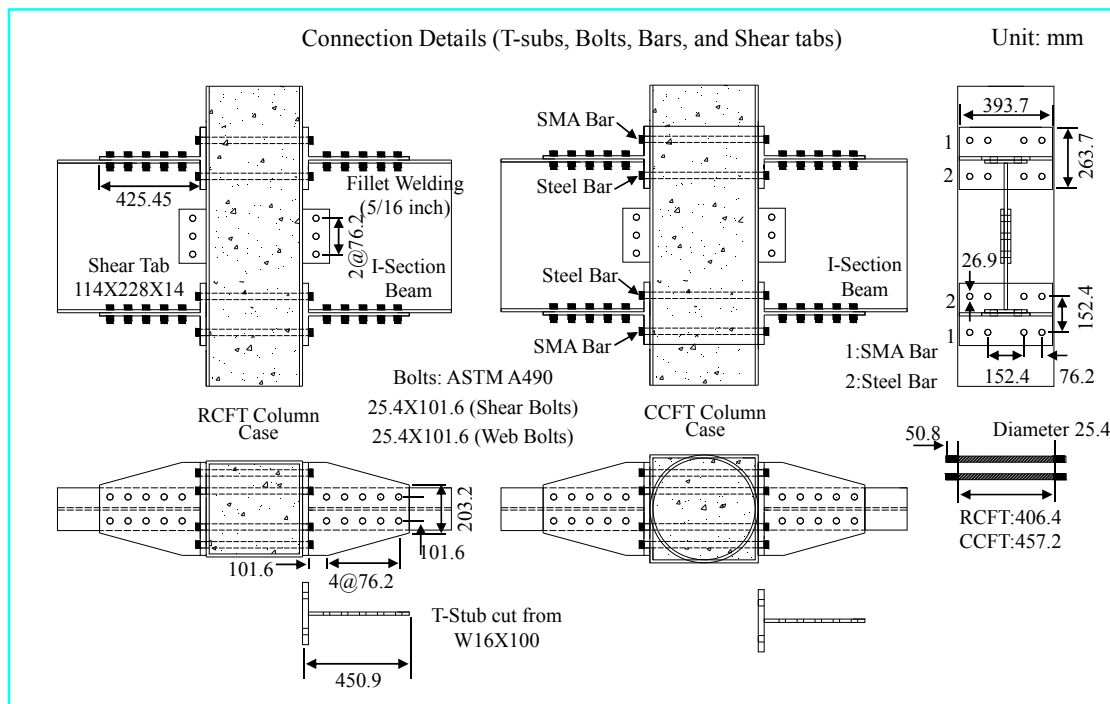
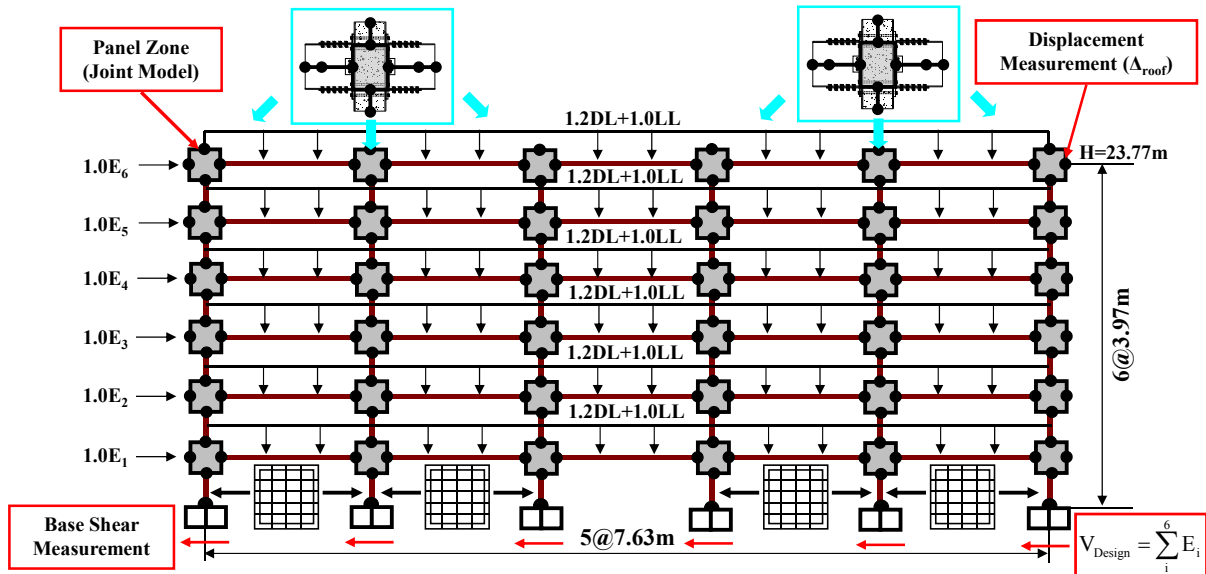


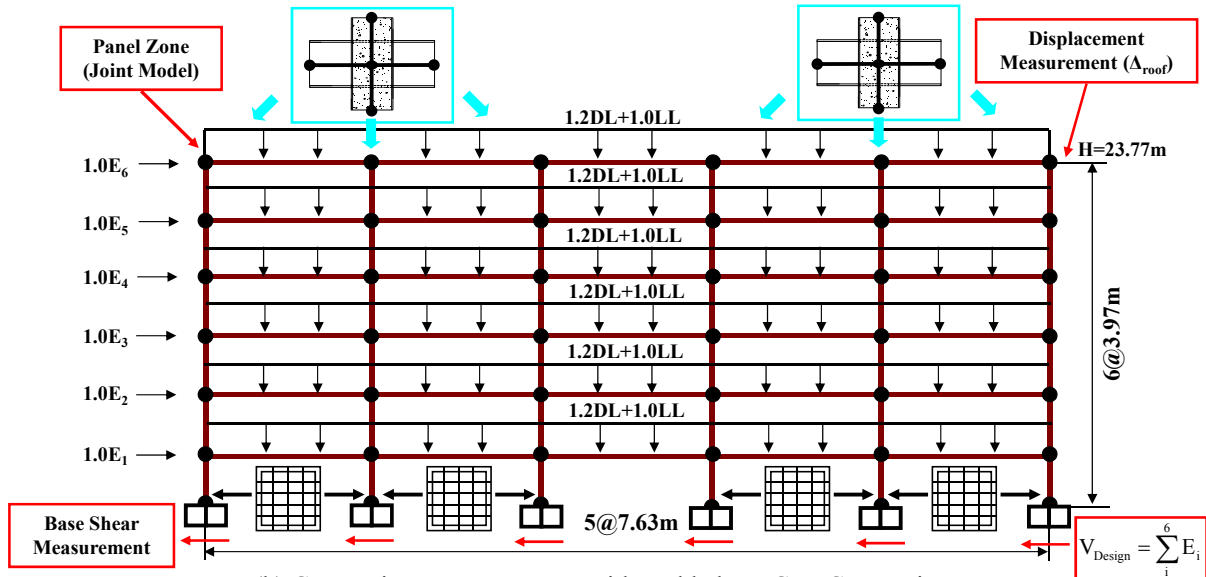
Figure 8. Details of the Connection Models (T-stubs, Bolts, Bars, and Shear Tabs)

#### 3.2 Frame Design

All buildings were designed as 6-story composite structures with 3 by 5 long bays, and were located in the Los-Angeles (LA) area. Consistent dead loads, live loads, seismic design category (SDC), and occupancy category were used for all buildings. Based on the mapped maximum spectral acceleration in the LA area, the SDC for LA area was assumed to be as defined for the D class in the IBC 2003 code (e.g. ICC [24]). The composite-moment frames have a 9.15- m by 7.63-m span length with a 3.97-m story height (see Figure 9). The CFT columns were considered to be fixed at the basement. Perimeter moment resisting frames were used to resist all lateral loads. Overall, all buildings had a symmetric configuration at all story levels.



(a) Composite Moment Frame with Smart PR-CFT Connections



(b) Composite Moment Frame with Welded FR-CFT Connections

Figures 9 (a) and (b). Modeling Attributes for Load Combination, Response Measurement, Panel Zone, and Elevation View

The composite frame members were designed in accordance with the AISC-LRFD specification (e.g. AISC [25]) and the AISC 2005 Seismic Provisions (e.g. AISC [3]). The steel beams were designed with two different member sizes, W24X62 and W24X55, according to the story level. The CFT columns were continuous for all story frames. Member sizes and design details are given in Table 1. In this table, the number 6 shown in the model ID indicates the total number of stories. The letter of the acronym following this number indicates the connection types used: the new PR-CFT connections (PRT: Partially restrained T-stub connections) or welded connections (FRW: Fully restrained welded connections). The last identifier (RC or CC) represents the model combination determined by the CFT column system (RCFT=RC and CCFT=CC). The ideal failure mode by the full plastic yielding of beam members after the considerable hardening of the connections was expected for the C-PRMF models.

Table1. Design Results for Composite Frame Buildings

Model ID	Connection Type	Column System	Column Size (All Stories)	Beam Size	
				1 <sup>st</sup> to 3 <sup>rd</sup> Story	4 <sup>th</sup> and 6 <sup>th</sup> Story
6PRT-RC	T-Stub	RCFT	HSS16X16X375	W24X62	W24X55
6PRT-CC	T-Stub	CCFT	HSS18X375	W24X62	W24X55
6FRW-RC	Welded	RCFT	HSS16X16X375	W24X62	W24X55
6FRW-CC	Welded	CCFT	HSS18X375	W24X62	W24X55

### 3.3 Numerical Frame Models

In the building plan, composite floors have symmetric configurations at all story levels and behave as rigid diaphragms. Therefore, perimeter moment resisting frames have the same lateral deformation as all internal frames under lateral forces and 3D building models can be replaced with 2D frame models. The modeling attributes for the 2D numerical frame models are given with more details in Figure 9. Perimeter moment resisting frames along the W-E direction were used for nonlinear frame analyses.

The modeling attributes for elements, fiber sections, and material models follows the previous studies for local connection models (check Secs. 2.2 and 2.3). Thus, steel beams and CFT columns were modeled as nonlinear beam-column elements with 2D fiber sections and nonlinear uni-axial materials. For the C-PRMF models (e.g. 6PRT-RC and -CC), composite panel zones were modeled using 2D joint elements to introduce the new smart PR-CFT connections into these numerical frame models (see Figure 9 (a)). The connections for the welded composite moment frames (e.g. 6FRW-RC and -CC) were modeled with the beam flange, web, or entire cross section penetrating through the composite column. Welded FR-CFT connections were assumed to be fixed where the nodal points of the beam elements were directly attached to those of the column elements, as shown in Figure 9 (b). The size of the welded panel zones was controlled by the rigid-end offsets.

In our nonlinear pushover analyses, earthquake or wind loads were converted into a set of equivalent lateral loads ( $E_i$ ) as stipulated by the ASCE 07-02 (e.g. ASCE [4]). The determination of these equivalent lateral forces depends on several code design factors such as ground motion parameters, site classification, the classification of the structural system, and the fundamental period of vibration. They were determined from Sections 9.4 and 9.5 in the ASCE 07-02. The summation of static lateral forces results in the design seismic base shear ( $V_{Design}$ ). The design dead loads (DL) and live loads (LL) were assumed as 4.74kPa and 3.83kPa, respectively. As stipulated in the ASCE 07-02, the load combination 5 (LC 5:  $1.2DL+1.0E_i+1.0LL$ ), which commonly dominated over other load combinations was used for the nonlinear pushover analyses. At the C-PRMF model (i.e. 6PRT-RC model), the force-deformation curves of individual components under static pushover are given as a reference in Figure 10.

For nonlinear dynamic analyses, a long time period ground motion (e.g., LA 21) assuming a 2.0% probability of exceedance in 50 year was used. This ground motion was constructed from historical records for the western US area (e.g. Somerville et al. [26]). As commonly recommended for code-designed frame buildings (e.g. ASCE [4]; ICC [24]), lumped masses composed of 1.0 times dead loads plus 0.2 times live loads were taken into consideration. To solve the time dependent-dynamic problem, a transient equilibrium analysis was performed using the Newmark method (e.g. Newmark [27]). A value of 2.5% was used for the damping as defined by the Rayleigh

command in the OpenSEES program. It ensures that this damping ratio is slightly greater than the recommended value of 2.0% for reinforced concrete (RC) frames (e.g. Mazzoni et al. [15]). The second-order effects (P-Delta effect) due to gravity loads were also taken into consideration by adding dead loads and live loads to the beam elements. The data of interest such as nodal displacements, member forces, and base shear forces were collected using the recorder command in the program.

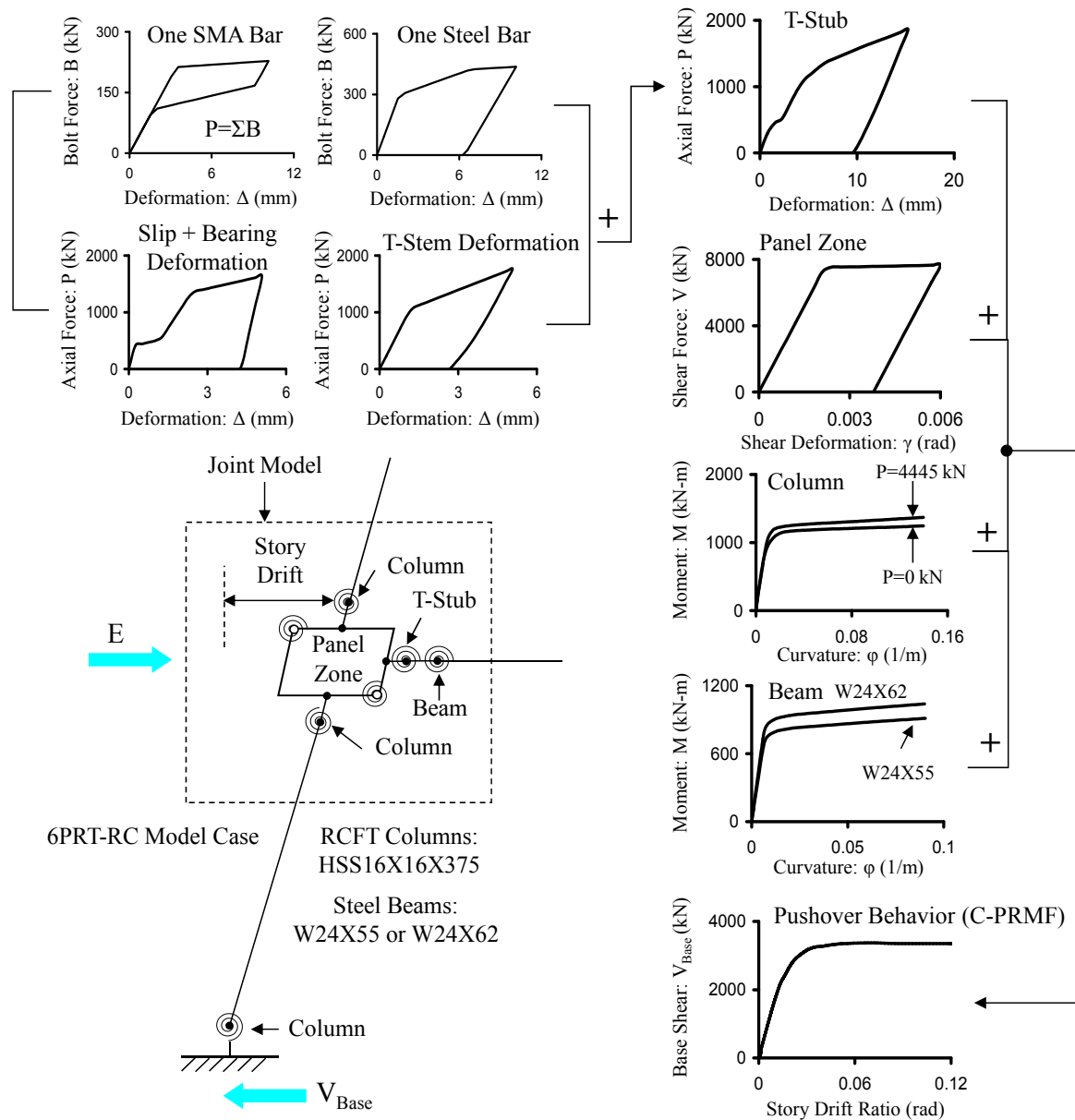


Figure 10. Force-deformation Curves of Individual Components under Static Pushover (6PRT-RC Model Case)

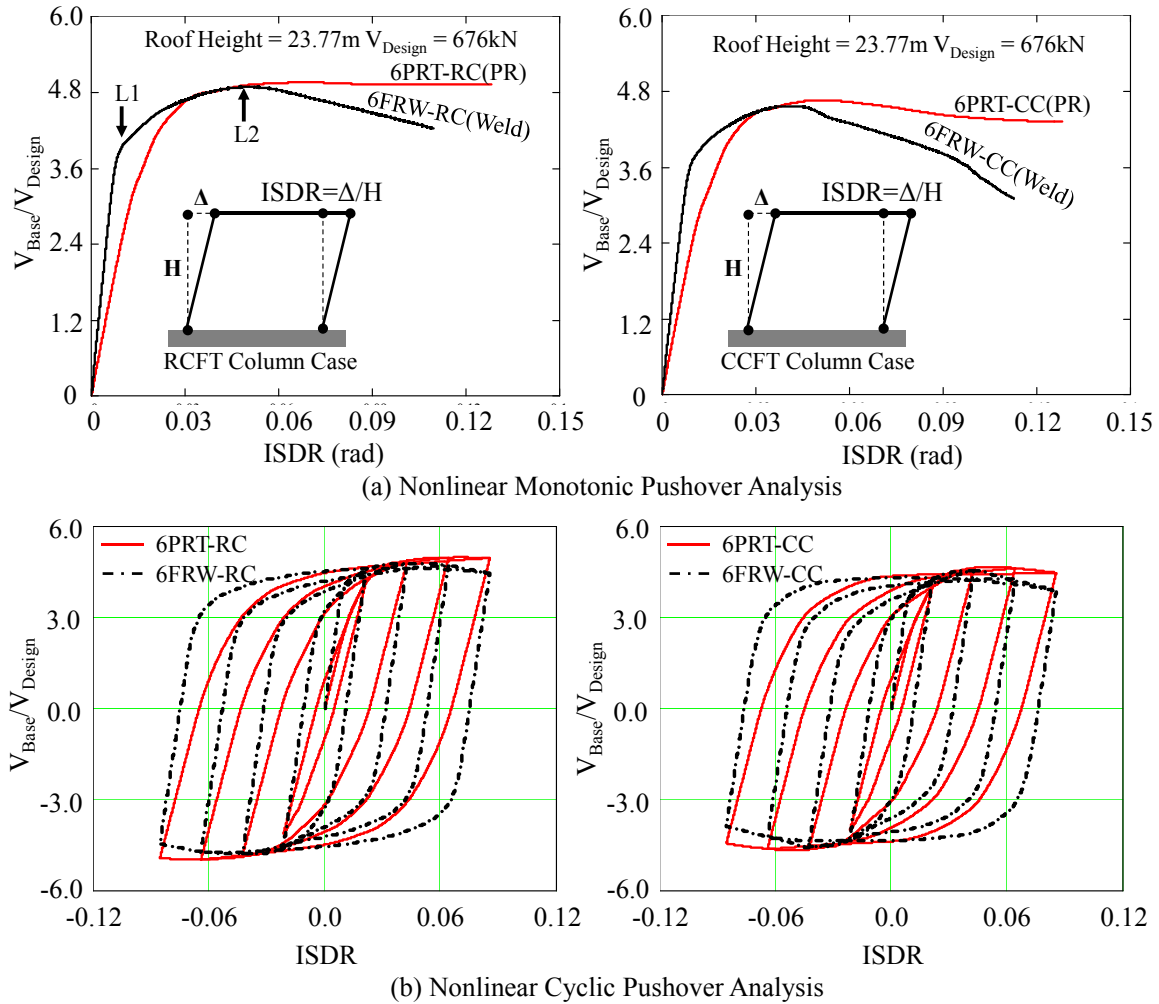
## 4. NONLINEAR ANALYSES AND PERFORMANCE EVALUATIONS

### 4.1 Nonlinear Pushover Analyses

2D nonlinear pushover analyses were conducted on the numerical frame models developed herein to evaluate lateral strength and deformation behavior. The force and deformation relationships obtained from static or cyclic pushover analyses were very useful to investigate the capacity of composite structures subjected to large inelastic excursions. Under the dominant load combination



(LC 5), the resulting pushover curves were plotted as inter-story drift ratios (ISDR:  $\Delta/H$ ) at the roof story vs. the base shear force normalized by the design base shear force ( $V_{\text{Base}}/V_{\text{Design}}$ ), as shown in Figures 11 (a) and (b). These figures show comparisons of pushover curves for composite frames with the same composite column systems but different connection types (e.g. 6PRT-RC vs. 6FRW-RC).



Figures 11 (a) and (b). Results of Nonlinear Pushover Analyses

The elastic range (proportional limit), yield strength (L1), initiation of hardening, ultimate strength (L2), and strength degradation or stability limit can be observed in the static nonlinear pushover curves (see Figure 11 (a)). The 6PRT models with SMA PR-CFT connections show a more flexible initial slope than the 6FRW models with welded FR connections. The stiffness loss due to slip at the bolt holes and the inherent characteristics of the PR connections can cause the C-PRMF to have relatively lower initial stiffness. After arriving at the ultimate strength (L2), the strength of the 6PRT models deteriorated more slowly than that of the counterpart FR model. This indicates that PR connections with more flexible tension bars provide more ductility. The frames with welded connections are susceptible to collapse due to brittle fracture of welded sections and larger P-Delta effects. Therefore, faster strength degradation was observed in the pushover curves of welded moment frames (6FRW models).

Energy dissipation, unloading slope, and permanent displacements can be observed during cyclic pushover analyses (Figure 11 (b)). As we expected, all transition points on the envelope of the monotonic curve coincided with those on the envelope of the cyclic curves when the same models

are tested. Similarly, strength degradations were found in the cyclic behavior of 6FRW models after their ultimate strength was exceeded. This caused a decrease in energy dissipation capacity. Due to the recentering capacities of SMA tension bars, 6PRT models show a smaller permanent roof displacement during unloading than 6FRW models.

## 4.2 Nonlinear Dynamic Analyses

As shown in Figure 12, the LA 21 ground motion with 6.9 magnitude and 60 second duration was chosen to examine the seismic response of the overall structure for two frame systems (6PRT vs. 6FRW). This ground motion was scaled to 1.283g peak ground acceleration (PGA). The time-histories for the roof story displacement and the normalized base shear vs. ISDR plots at the roof level are shown in Figures 13 (a) and (b).

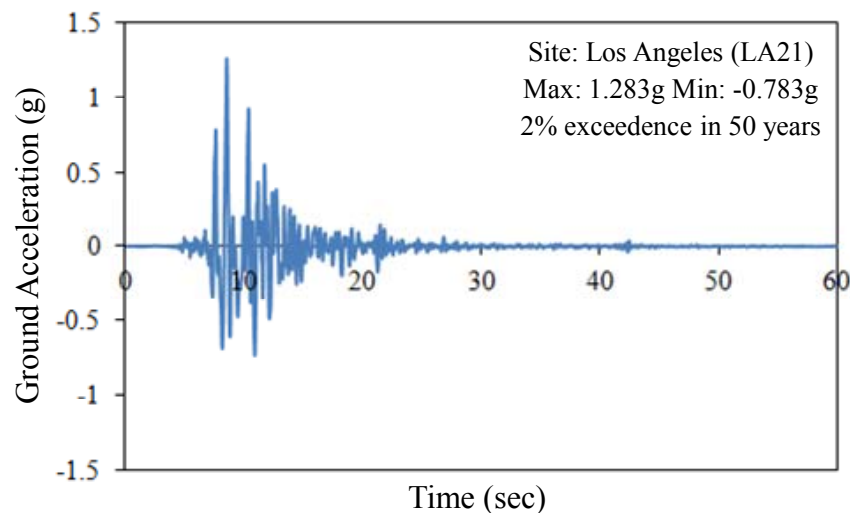
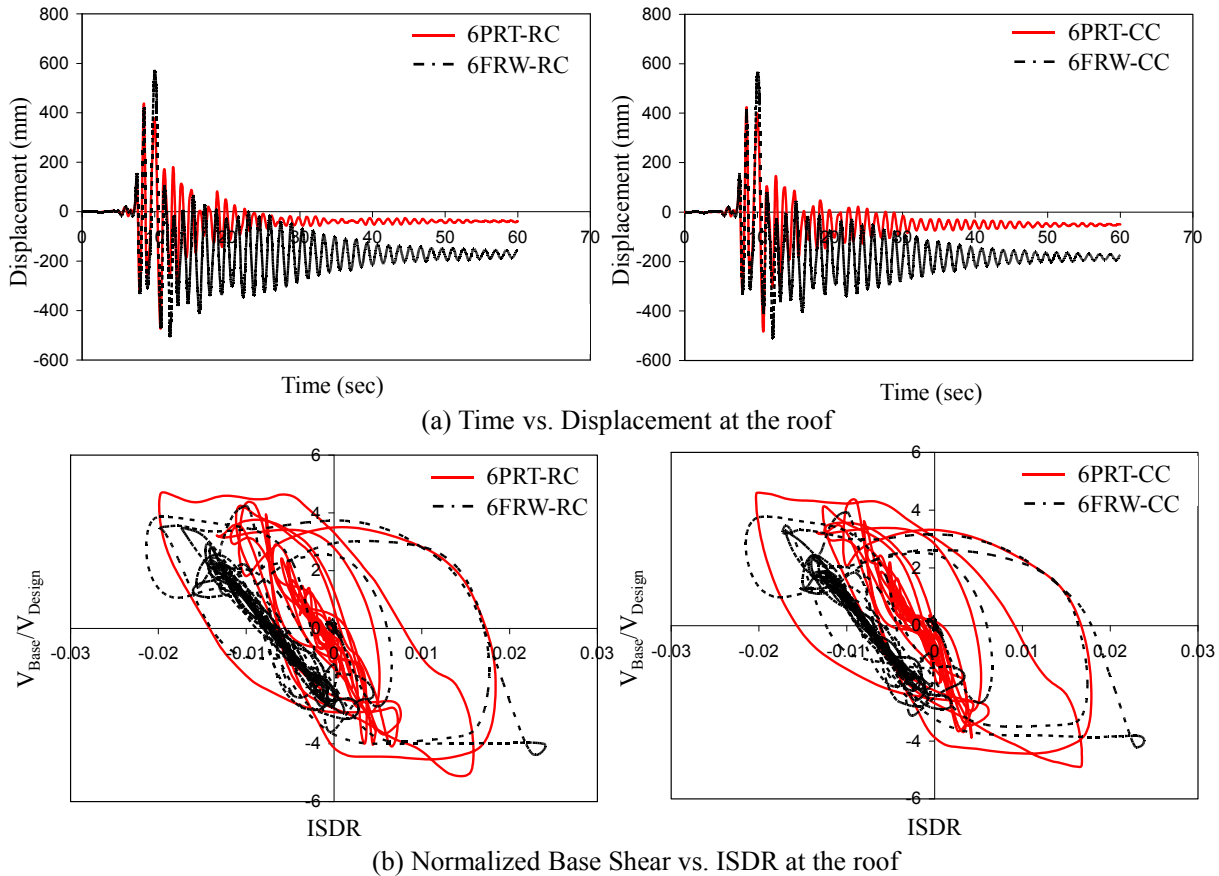


Figure 12. Ground Motion used for Nonlinear Dynamic Time-history Analyses

The peak roof displacements for the 6PRT-RC and 6FRT-RC models are about 590 mm and 450 mm, which indicate a roof ISDR of 2.5% and 1.9%, respectively (see Figure 13 (a)). The flexibility of the PR connections and the recentering effect of the SMA tension bars enabled the roof displacement to be reduced by approximately 25%. Note that the 6PRT models have a permanent roof displacement of approximately 30 mm, while the 6FRW models have approximately 200 mm at the final time step (60 sec.). This implies that SE SMA components are able to reduce permanent displacement and limit damage to the structural systems. Furthermore, a smaller peak roof ISDR corresponding to relatively higher peak normalized shear was observed for the 6PRT models as compared to the 6FRW models (see Figure 13 (b)). For instance, a peak roof ISDR of 1.9% corresponding to the normalized base shear of  $V_{\text{Base}}/V_{\text{Design}} = 4.5$  occurs in the 6PRT-RC model, while a peak roof ISDR of 2.5% corresponding to the normalized base shear of  $V_{\text{Base}}/V_{\text{Design}} = 4.05$  occurred in the 6FRW-RC model. The superior ability of SMA PR-CFT connections, which provides gentle strength degradation in the pushover behavior, allowed the 6PRT models to undergo strong ground motions with relatively smaller ISDR rather than the 6FRW models.





Figures 13 (a) and (b). Results of Nonlinear Dynamic Time-history Analyses

## 5. CONCLUSIONS

The main conclusions of this study are as follows:

- The proposed joint element includes behavioral properties of the components in the form of a simplified model that reflects the global stiffness, strength, and deformation capacity of the actual connection. This type of joint model results in significant savings in running time for frame analyses.
- Four different prototypes of composite perimeter moment frames with either PR connections or FR connections were presented in this study. 2D numerical frame models were used in nonlinear frame analyses. The behavior of the composite PR connections was successfully simulated using 2D joint elements developed in this study.
- Based on pushover analysis results, composite moment frames with PR connections showed smaller residual displacements than those with welded connections due to the recentering effect of the SMA components. In addition, composite frames with PR connections showed a more gradual degradation in strength.
- From nonlinear dynamic analysis results, composite moment frames with welded connections showed larger peak roof displacements. The outstanding energy dissipation properties of the PR connections resulted in lower drifts. Finally, it can be concluded that composite PR moment frames show superior performance owing to structural advantages for the proposed connection models in comparison with traditional welded ones.

## ACKNOWLEDGEMENTS

This research was supported by Basic Science Research Program through the National Research Foundation of Korea (NRF) funded by the Ministry of Education, Science and Technology (Grant No. 2012R1A1A1041521). The author (J.W. Hu) gratefully acknowledges this support. The author also sincerely thanks Prof. Roberto T. Leon for his academic advice and valuable comments when he was a Ph.D. student and Post-Doctoral Fellow at Georgia Tech.

## REFERENCES

- [1] Tsai, K.C., Hsiao, P.C., Wang, K.J., Weng, Y.T., Hsia, P.C., Lin, K.C., Chen, C.H., Lai, J.W., and Lin, S.L., "Pseudo-dynamic Tests of a Full-scale CFT/BRB Frame-Part I: Specimen Design, Experiment and Analysis", *Earthquake Engineering and Structural Dynamics*, 2008, Vol. 37, pp. 1081-1098.
- [2] Wu, L., Chung, L.L., Tsai, S.F., Lu, C.F., and Huang, G.L., "Seismic Behavior of Bidirectional Bolted Connections for CFT Columns and H-beams", *Engineering Structures*, 2008, Vol. 29, No. 3, pp. 395-407.
- [3] American Institute of Steel Construction (AISC), *Seismic Provisions for Structural Steel Buildings (ANSI/AISC 341-05)*, 2005, Chicago, IL.
- [4] American Society of Civil Engineers (ASCE), *Minimum Design Loads for Buildings and Other Structures (ASCE 7-05)*, 2002, Reston, VA.
- [5] Wu, L.Y., Chung, L.L., Tsai, S.F., Lu, C.F., and Huang, G.L., "Seismic Behavior of Bolted Beam to Column Connections for Concrete Filled Steel Tube", *Journal of Constructional Steel Research*, 2005, Vol. 61, No. 10, pp. 1387-1410.
- [6] Park, T., Hwang, W.S., and Hu, J.W., "Damage Evaluation of Composite-special Moment Frames with Concrete-filled Tube Columns under Strong Seismic Loads", *KSCE Journal of Civil Engineering*, 2011, Vol. 15, No. 8, pp. 1381-1394.
- [7] Hu, J.W., Kang, Y.G., Choi, D.H., and Park, T., "Seismic Design and Behavior of Composite-moment Frames with Steel Beam-to-concrete Filled Tube Column Connections", *KSSC International Journal of Steel Structures*, 2010, Vol. 10, No. 2, pp. 177-191.
- [8] Hu, J.W., Park, J., and Leon, R.T., "Advanced Analysis and Performance based Evaluation of Concrete Filled Tube (CFT) Columns", *International Journal of Advanced Steel Construction*, 2010, Vol. 6, No. 4, pp. 1018-1032.
- [9] Leon, R.T., "Seismic Performance of Bolted and Riveted Connections, Background Reports: Metallurgy, Fracture Mechanics, Welding, Moment Connections, and Frame System Behavior", FEMA Publication No. 288 Federal Emergency Management Association (FEMA), Washington (DC), 1997.
- [10] Green, T.P., Leon, R.T., and Rassati, G.A., "Bidirectional Tests on Partially Restrained, Composite Beam-column Connections", *ASCE Journal of Structural Engineering*, 2004, Vol. 130, No. 2, pp. 320-327.
- [11] Rassati, G.A., Leon, R.T., and Noe, S., "Component Modeling of Partially Restrained Composite Joints under Cyclic and Dynamic Loading", *ASCE Journal of Structural Engineering*, 2004, Vol. 130, No. 2, pp. 343-351.
- [12] Penar, B.W., "Recentring Beam-column Connections using Shape Memory Alloys", Master's Thesis, 2005, Georgia Institute of Technology, 2005.
- [13] Hu, J. W., "Seismic Performance Evaluations and Analyses for Composite Moment Frames with Smart SMA PR-CFT Connections", Ph.D. Dissertation, Georgia Institute of Technology, 2008.

- [14] DesRoches, R., McCormick, J., and Delemont, M., "Cyclic Properties of Superelastic Shape Memory Alloy Wires and Bars", *ASCE Journal of Structural Engineering*, 2004, Vol.130, No.5, pp. 732-740.
- [15] Mazzoni, S., McKenna, F., and Fenves, G.L., "OpenSEES Command Language Manual v. 1.7.3.", Department of Civil Environmental Engineering", University of California at Berkeley, 2006.
- [16] Braconi, A., Salvatore, W., Tremblay, R., and Bursi, O.S., "Behaviour and Modelling of Partial-strength Beam-to-column Composite Joints for Seismic Applications", *Earthquake Engineering and Structural Dynamics*, 2007, Vol. 36, pp. 142-161.
- [17] Kulak, G.L., Fisher, J.W., and Struik, J.H.A., "Guide to Design Criteria for Bolted and Riveted Joint", 2<sup>nd</sup> Edition, Johns Wiley & Sons, 1987.
- [18] Rex, C.O., and Easterling, W.S., "Behavior and Modeling of a Single Plate Bearing on a Single Bolt", Report No. CE/VPI-ST 96/14, Virginia Polytechnic Institute and State University, Blacksburg, VA, 1996.
- [19] Astaneh-Asl, A., "Seismic Design of Bolted Steel Moment-resisting Frames", Technical Information & Product Service, 1995.
- [20] Hu, J.W., Leon, R.T., and Park, T., "Analytical Investigation on Ultimate Behaviors for Steel Heavy Clip-angle Connections using FE Analysis", *ISIJ International*, 2010, Vol. 50, No. 6, pp. 883-892.
- [21] Swanson, J.A., "Characterization of the Strength, Stiffness, and Ductility Behavior of T-stub Connection", Ph.D. Dissertation, Georgia Institute of Technology, 1999.
- [22] Swanson, J.A., "Ultimate Strength Prying Models for Bolted T-stub Connections", *AISC Engineering Journal*, 2002, Vol. 39, No. 3, pp. 136-147.
- [23] Davide, F., "Shape Alloy Devices in Earthquake Engineering: Mechanical Properties, Constitutive Modeling and Numerical Simulations", Master's Thesis, Rose School in Italy, 2003.
- [24] International Code Council (ICC), *International Building Code (IBC 2003)*, Falls Church, VA, 2003.
- [25] American Institute of Steel Construction (AISC), *Manual of Steel Construction: Load and Resistance Factor Design (LRFD)*, 3<sup>rd</sup> Edition, Chicago, IL, 2001.
- [26] Somerville, P. G., Smith, N., Punyamurthula, S., and Sun, J., "Development of Ground Motion Time Histories for Phase 2 of the FEMA/SAC Steel Project", Report No.SAC/BD 97/04, SAC Background Document, 1997.
- [27] Newmark, N.M., "A Method of Computation for Structural Dynamics", *ASCE Journal of Engineering Mechanics Division*, 1959, Vol. 85, No. 3.

# DESIGN OF STEEL AND COMPOSITE OPEN CAR PARKS UNDER FIRE

C. Haremza<sup>1,\*</sup>, A. Santiago<sup>2</sup> and L. Simões da Silva<sup>3</sup>

<sup>1</sup>Ph.D. student, ISISE, Civil Engineering Department, University of Coimbra, Coimbra, Portugal

<sup>2</sup>Assistant Professor, ISISE, Civil Engineering Department, University of Coimbra, Coimbra, Portugal

<sup>3</sup>Full Professor, ISISE, Civil Engineering Department, University of Coimbra, Coimbra, Portugal

\*(Corresponding author: E-mail: haremza@dec.uc.pt)

Received: 2 January 2013; Revised: 21 January 2013; Accepted: 23 January 2013

---

**ABSTRACT:** Steel and concrete are the most commonly used materials for open car park buildings because of their numerous advantages. Open car parks are characterized by high ventilation that keeps the fire limited on the ignition zone, not leading to a flash-over, what justify using fire engineering methodology for assessing the structural behavior of steel and composite open car parks under fire, based on a Natural Fire Concept. The methodology for assessing this structural behavior under fire is presented in this paper, and is characterized by the following steps [1]: i) definition of fire scenario(s), ii) calculation of the rate of heat release and iii) analysis of structural behavior. The research significance of this methodology is justified by the discrepancies on the design requirements for this type of structure in different European countries [2]. At the end of the paper, an example of application of this methodology to fire design an open composite steel-concrete car park with eight floors [3] is presented and is compared to advanced calculation methods.

**Keywords:** Composite steel-concrete structure, Localized fire, Open car park, Rate of heat release, Design methodology

---

## 1. INTRODUCTION

Steel and concrete are the most commonly used materials for car parking, and open car park buildings with unprotected steel or composite steel-concrete structures is a solution frequently used in many countries of the center and north of Europe, or even in United-States, Canada or Japan. There are many advantages of a composite steel-concrete structure for open car park buildings: i) shorter on-site construction schedule due to the prefabricated elements, and consequently lower construction cost as well as lower environmental impacts during construction; ii) flexible column spacing up to around 16 m, allowing to locate the columns at the back of the parking bay which facilitates vehicles maneuvers [4]; iii) reduced column section size in comparison to a concrete structure, which increases the parking spaces; and iv) reduced weight, and smaller foundations, in comparison to concrete structures [5]. Moreover, steel structures are robust, sustainable, of easy maintenance and easily accommodate vertical enlargement [6].

This solution has become quite competitive since the National regulations have been adapted taking into account the document: *Fire safety in open car parks*, the oldest reference in this subject, published in 1993, ECCS – *European Convention for Constructional Steelwork* [7]. This document was a first attempt to clear up the differences between fire safety requirements of open car parks for all European countries, according to information and test results available throughout the world. However, the fire safety requirements, including structural fire ratings and provision of active fire protection system such as sprinklers, still vary between different building codes. In some countries, steel or composite steel-concrete structures are not recommended because steel is required to be fire rated by the building code, and is conditioned by the fire resistance demands (R) from the National regulations. In that case, concrete structure will be more cost effective, despite the numerous advantages of a composite steel-concrete structure.

A car park as part of a building can be classified as open or closed depending on the ventilation condition. In accordance with ECCS, it may be considered as "open" if, for every parking level, the ventilation areas in the walls are: i) located in at least two opposite façades, ii) equal at least 1/3 of the total surface area of all the walls and iii) correspond to at least 5% of the floor area of one parking bay [7]. The main advantages of open car parks are: i) lower energy consumption, ii) natural light that contributes to the human comfort and safety of users, iii) natural ventilation, and iv) attractive architectural design. In addition, open car parks present specific characteristics that must be considered in the fire design.

From experimental tests performed in real steel-concrete car parks in 1968, Butcher *et al.* [8] was the first to conclude that a burning car is unlikely to cause uncontrollable fire spread within a car park and the damage to the car park building is not critical. These results were confirmed by Gewain [9] in 1973, adding that steel provides adequate safety against structural collapse under a car fire. In 1985, Bennetts *et al.* [10] concluded that the probability to involve more than two cars in a fire is very small because the fire brigades arrive before, and the security could be assured with unprotected steel. More recently, in 2000, three car fire tests were carried out in a two-level braced car park with unprotected steel and concrete slabs, by CTICM – *Centre Technique Industriel de la Construction Mécanique*, within the European Project – *Demonstration of real fire tests in car parks and high buildings* ([1];[11]). The aim of these tests was to prove to the French authorities that fire severity achieved by this realistic scenario is lower than the fire severity obtained by the fire curve ISO 834; consequently, reduction or even no fire protection could be accepted. From the two first tests, with three cars and the central one being initially ignited, the authors concluded that the fire engineering methodology based on the scenarios is adequate: the fire spread from one car to another, but structural deformations were far from leading to the collapse of the structure, although some bolt failures were observed. Table 1 presents the peak values of temperatures in steel members according to the previous experimental studies; the older fire tests showed lower temperatures than the recent French test. The evolution of the composition of cars (more plastic, therefore a faster combustion) and the high fuel capacity may explain these higher temperatures.

Table 1. Maximum Steel Temperatures Reached in Fire Tests in Various Countries

Full scale fire tests	Maximum measured steel temperature	
	Beam	Column
UK, 1968 [11]	275°C	360°C
Japan, 1970 [7]	245°C	242°C
USA, 1973 [8]	226°C	-
Australia, 1985 [10]	340°C	320°C
France, 2000 [1]	700°C	640°C

Additionally to the previous tests, some statistics of real fires in car parks were analyzed in Paris, New Zealand, Brussels, etc... based on the reports from fire brigades. In Paris, three is the maximum number of cars involved in fires and it corresponds to only 10% of the fires in open car parks buildings. All fires in car parks (with cars or other fire load) were stopped before 1 hour, with 5.5% of car fires extinguished before the arrival of firemen [1]. In New Zealand, only 3% of fires involved multiple vehicles [12]. From additional statistics collected in Marseille, Toulouse and Brussels in open car parks [13], it was noticed that a maximum of two cars were involved in a fire, and in Toulouse, only 6.1% of the fires happened in open car parks. These previous statistics and experimental tests show that fires in open car parks buildings: i) have never led to any local collapse of the structure, and most of unprotected steel open sided steel-framed car parks has sufficient inherent resistance to withstand the fire effects; ii) are not frequent; iii) rarely involved more than three adjacent vehicles; iv) have never killed someone (only a few persons were

recorded to be injured, and they were the owners of the cars). The main reasons that justify previous evidences are: in contrast to closed car parks, open car parks are characterized by high ventilation that keeps the fire limited on the ignition zone. Indeed, in an open car park building, the fire propagates from a burning car to another by radiation, convection and/or scattering of the fuel: by radiation, fire propagates sequentially from a car to another, but when the fifth or sixth car is burning, the combustion of the first one has already ended; the propagation of the fire by convection in an open car park building well ventilated is unlikely because hot gases have little impact on the cars; and the scattering of the fuel only happens in inclined floors [14].

The structural behavior of the car park under fire can be analyzed by specific combinations of mechanical and thermal loads defined in Eurocode 0 [15] and Eurocode 1, Parts 1.1 and 1.2 ([16], [17]). The methodology proposed in Annex C of Eurocode 1, Part 1.2 [17] for localized fires can be adapted to calculate the thermal loads of open car parks. In this case, fire scenarios are used to define the curve of the real rate of heat release of the burning vehicles, and thus to obtain an adequate fire characterization, against the traditional nominal fire curves defined by Eurocode 1, part 1.2 [17]. The vertical position of the virtual heat source, the height, the diameter of the fire, the rate of heat release and the distance between the fire source and the ceiling define the heat flux to the structural elements. Finally, simplified and advanced calculation methods are presented in Eurocodes 3 and 4, part 1.2 ([18], [19]) for calculating the resistance of structural elements in fire, depending on the fire safety requirements of each country. In France, CTICM validated this computing method to justify the use of unprotected steel frame resistance for the fire design, and the French legislation allowed this design methodology since 2004 (Decree of 22 March 2004).

The objectives of the presented study are: i) to present a fire engineering methodology, for assessing the structural behavior of steel and composite open car parks under fire, based on a Natural Fire Concept; ii) to compare the legislation of several European countries regarding the fire safety in this kind of building; and iii) to illustrate this design methodology through its application to an open composite car park with eight floors [3] and to compare the results with those obtained through advanced calculation methods.

## 2. FIRE SCENARIOS

The fire scenario (position of the vehicles) should represent the most unfavorable situation for the elements (or substructure). The vehicles' type mostly used in fire scenarios are cars, classified according their calorific potential or combustion energy ( $E$ ) [1]; five classes of cars were defined: class 1 -  $E = 6000$  MJ (ex. Peugeot 106); class 2 -  $E = 7500$  MJ (ex. Peugeot 306); class 3 -  $E = 9500$  MJ (ex. Peugeot 406), and classes 4 and 5 -  $E = 12\,000$  MJ (ex. Peugeot 605 or 806). According to statistical studies of actual fires in car parks, 90% of the vehicles involved in a fire are classified as class 1, 2 or 3 [1]. The INERIS - *Institut National de l'Environnement Industriel et des Risques* [14], considers that fire scenarios with cars of class 3 should be used to evaluate the structural stability of the car park under fire, and the fire resistance of the structure should be ensured during the entire fire scenario, or at least, if allowed by National requirements, up to a certain resistance time  $R$  of the elements defined as for the ISO curve. In addition, a scenario including a commercial vehicle (van containing 250 kg of highly flammable material:  $E = 19\,500$  MJ) corresponds to an extreme situation and should only be used to check the global behavior of the structure, assuming local collapse, without progressive collapse [20].

Five fire scenarios recommended or already used for the study of fires in car parks are presented and described. ECCS [7] indicates that one or two vehicles in fire correspond to the most critical scenario in an open car park (Figure 1). One car burning at mid-span under the beam (corresponding

to the maximum bending moment position) is defined as scenario 1. The scenario 2 involves two burning cars, one on each side of the column; this fire event was considered being the most dangerous for the columns [7]. INERIS defines three additional fire scenarios [20]: i) scenario 1 of ECCS, but with a commercial vehicle under the beam, ii) scenario 3 - involving seven class 3-cars, with possibility of a commercial vehicle in places 0 or 1a (Figure 1), iii) scenario 4 - involving four class 3-cars parked face to face, with possibly a commercial vehicle in places 0, 1a, 1b or 2. According to INERIS, and for all scenarios, the fire spread time from a vehicle to another is 12 minutes [20]; the initial document by ECCS [7] recommended a time delay equal to 15 minutes. The evolution of the composition of vehicles may also explain the decrease in the time delay (see Section 1). Another scenario already considered by CTICM [1] is scenario 5 (Figure 1): three class 3-cars, parked side by side. According to the same statistical source [1], a scenario of 3 class 3-cars (scenario 5) involved in a fire is an envelope scenario of around 98.7% of all possible scenarios.

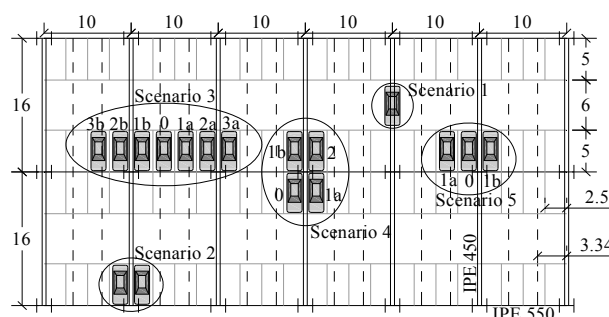


Figure 1. Fire Scenarios  
(Represented in the Car Park Analyzed in this Paper; Dimensions given in m)

### 3. RATE OF HEAT RELEASE FROM VEHICLES

The model of a car under fire presented in the ECCS report [7] is based on experimental fire tests: it was observed that the flames extend out of the car, mainly through the windscreen and the rear window. The hot gases in the flames and above them move upward due to buoyancy; this flow of gases corresponds to the fire plume. The burning car is divided into two plumes which are called as the front and the rear fire plumes (Figure 2), and the sum of the heat releases included in the two fire plumes is equal to the heat release of the vehicle.

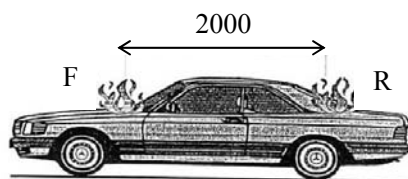


Figure 2. Front (F) and Rear (R) Fire Plumes [7]

In order to calculate the heat release, cars under fire have been experimentally studied in several countries [13]. Most of the tests were performed in closed conditions. The first tests carried out in opened conditions were developed by Mangs and Keski-Rahkonen in the 90's [21]. It was obtained that the total heat release of a European car from the 70's burning in an open car park building is equal to 4000 MJ. Between 1993 and 1996, the European project – *Development of design rules for steel structures subjected to natural fires in closed car parks* [22] – developed a design guide for closed car park structures subject to localised Natural Fires and established more realistic standards in Europe. Within this project, ten full-scale calorimetric fire experiments on old and recent European cars were performed by CTICM. In the first six tests, class 3-cars from the 70's and 80's

were tested, while in the last four tests, newer cars (reference time: 1995) were used to simulate an open car park [14]. Based on these tests, reference curves of rate of heat release for two class 3-cars (one car as fire source and another one subject to the spread of fire with 12 minutes of delay) were defined [22]. These curves allow simulating multiple burning cars: Figure 3 presents the references curves for three consecutive burning class 3-cars, with maximum 8.3 MW. For commercial vehicles, CTICM suggests a maximum value of rate of heat release equal to 18 MW; this value is considered as a "safe value" for design, but this is not a measured value [20].

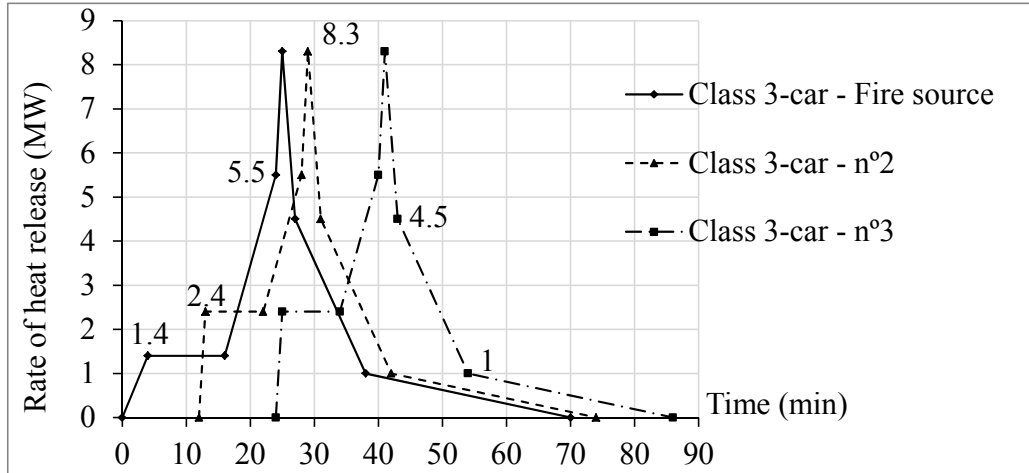


Figure 3. Curves of Rates of Heat Release from Burning of 3 Vehicles, Class 3

## 4. STRUCTURAL BEHAVIOR

### 4.1 Combination of Actions

The combination of actions for car parks under fire corresponds to the accidental design situations presented in Eurocode 0 [15]:

$$\sum_{j \geq 1} G_{k,j} + P + A_d + \psi_{1,1} Q_{k,1} + \sum_{i \geq 2} \psi_{2,i} Q_{k,i} \quad (1a)$$

$$\sum_{j \geq 1} G_{k,j} + P + A_d + \sum_{i \geq 1} \psi_{2,i} Q_{k,i} \quad (1b)$$

where:  $G_{k,j}$  are the characteristic values of permanent actions  $j$ ;  $P$  is the design value of a prestressing load (if available);  $A_d$  is the design value of indirect actions from fire; and  $Q_{k,i}$  are characteristic values of the variable actions  $i$ . The difference between these two equations (1a) and (1b) is the coefficient applied to the leading variable action  $\psi_{k,1}$ : the coefficients for the frequent value  $\psi_1$  and for the quasi-permanent value  $\psi_2$  are considered in expressions (1a) and (1b), respectively. In case of a car park (traffic with vehicles smaller than 30 kN), the coefficient for the frequent value  $\psi_1$  and for the quasi-permanent value  $\psi_2$  are respectively equal to 0.7 and 0.6; guidance may be given in the National Annex. The simplified combination of actions can be written as:

$$1.0 G_k + 0.7 \text{ (or } 0.6) Q_k \quad (2)$$

Note that equation (1b) will lead to the situation where no horizontal action is considered in the fire situation because the quasi-permanent value of the wind  $\psi_2$  is equal 0.0 [23].



## 4.2 Mechanical loads

The load model which should be used, given by the Eurocode 1 part 1.1 [16], is a load  $q_k$  uniformly distributed on the floors for determination of general effects, and a single axis with a load  $Q_k$  applied on two square surfaces for local effects (Figure 4), located in the position which will produce the most adverse effect of the action. Concerning characteristic values of the live loads, the Eurocode 1 part 1.1 [16] recommends that  $q_k$  be selected within the range 1.5 to 2.5 kN/m<sup>2</sup> and  $Q_k$  be selected within the range 10 to 20 kN; the recommended values are underlined, but they may be set by the National Annex.

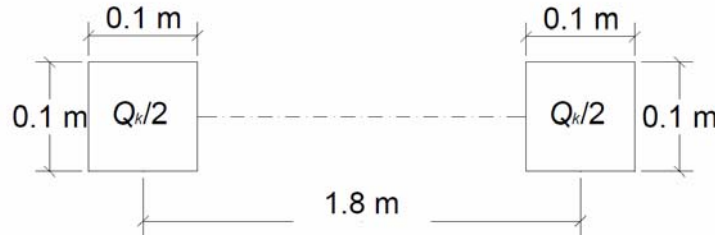


Figure 4. Dimensions of Axis Load

## 4.3 Thermal loads

The steel temperature of structural elements can be calculated in two ways: i) a simplified method that assumes a uniform temperature throughout the steel cross-section, and ii) an advanced method that considers the evaluation of the temperature field in the cross-section using finite element models. In this section, the simplified method given in the Eurocode 1 part 1.2 [17] is considered. The heat flux received by the members located at the ceiling level due to a localized fire is calculated by one of the simplified methods presented in Annex C of this code: i) Heskestad's method, when the flames are not impacting the ceiling, and ii) Hasemi's method, when the flames are impacting the ceiling. The length of the flame  $L_f$  is obtained by:

$$L_f = -1,02D + 0,0148Q^{2/5} \quad [\text{m}] \quad (3)$$

where  $D$  [m] is the diameter of the fire (for a vehicle with an area equal to 12 m<sup>2</sup>,  $D = 3.9$  m [22]) and  $Q$  [W] is the rate of heat release of the fire, established in accordance with Annex E.4 of Eurocode 1, part 1.2 [17]. In this Annex, the heat release for car park occupancy is not specified; however, the experimental values presented in section 3 are considered in this study.

When the flames are not impacting the ceiling ( $L_f < H$ ), Eurocode 1 Part 1.2 [17] suggests that the temperature in the plume along the symmetrical vertical flame axis is given by:

$$\theta_{(z)} = 20 + 0,25Q_c^{2/3}(z - z_0)^{-5/3} \leq 900 \quad [^\circ\text{C}] \quad (4)$$

where the heat flux  $Q_c$  [W] is the convective part of the rate of heat release ( $Q_c = 0.8 Q$ ),  $z$  [m] is the height along the flame axis and  $z_0$  [m] is the virtual origin of  $z$  axis.

When the flame is impacting the ceiling ( $L_f \geq H$ ), the net heat flux  $\dot{h}_{net}$  [W/m<sup>2</sup>] received by the fire exposed unit surface area at the level of the ceiling is given by:

$$\dot{h}_{net} = \dot{h} - \alpha_c(\theta_m - 20) - \Phi \varepsilon_m \varepsilon_f \sigma [(\theta_m + 273)^4 - (20 + 273)^4] \quad [\text{W/m}^2] \quad (5)$$

where  $\dot{h}$  is the heat flux received by the unit of surface area exposed to fire at the ceiling level,  $\alpha_c$  is the coefficient of heat transfer by convection [ $\text{W}/\text{m}^2\text{K}$ ],  $\theta_m$  is the surface temperature of the member [ $^{\circ}\text{C}$ ],  $\phi$  is the configuration factor,  $\varepsilon_m$  is the surface emissivity of the member,  $\varepsilon_f$  is the emissivity of the fire and  $\sigma$  is the Stephan Boltzmann constant ( $5.67 \times 10^{-8} \text{ W}/\text{m}^2\text{K}^4$ ). Hasemi's method is a simple tool for the evaluation of the localized effect of a fire on horizontal elements located above the fire. The background of the method is experimental and based on tests made by Hasemi in Japan: a gas burner was placed under an unconfined flat ceiling, the height of the ceiling was adjusted in each test, and the heat flux to the ceiling surface was recorded [24]. This method cannot be used for the columns. The net heat flux from the fire of each vehicle to the horizontal structural members depends of the following parameters (Figure 5) [1]:  $H_s$  [m] is the vertical distance between the fire source and the floor (equal to 0.3 m [7]);  $H_f$  [m] is the vertical distance between the floor and the ceiling;  $H$  [m] is the vertical distance between the fire source and the ceiling (or the lower flange of the beam);  $r$  [m] is the horizontal distance between the vertical axis of the fire and the point along the ceiling where the thermal flux is calculated;  $y$  is a parameter that depends on the diameter  $D$ , the rate of heat release  $Q$  and on the distances  $H$  and  $r$ . The net heat flux ( $\dot{h}$ ) is calculated according the following expression [17]:

$$\begin{aligned} \dot{h} &= 100\,000 & \text{if } y \leq 0.3 \\ \dot{h} &= 136\,300 - 121\,000 y & \text{if } 0.3 < y \leq 1 \\ \dot{h} &= 15\,000 y^{-3.7} & \text{if } 1 < y \end{aligned} \quad [\text{W}/\text{m}^2] \quad (6)$$

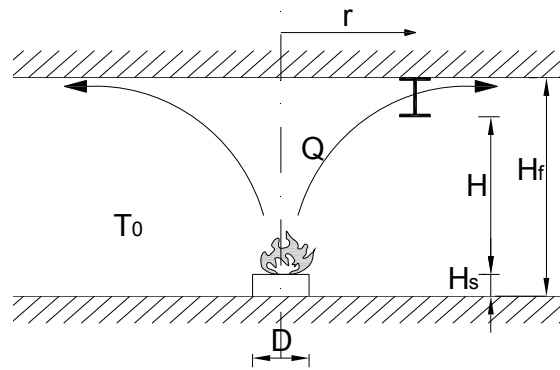


Figure 5. Parameters used in the Hasemi's Method to Calculate the Heat Flux from the Vehicle to the Beam

The net heat flux ( $\dot{h}$ ) may be multiplied by a correction factor equal to 0.85 to account that the flame is deviated under the beam [24]. The heat flux from several localized fires is the sum of the heat fluxes obtained for each fire, with a maximum value of  $100 \text{ kW}/\text{m}^2$  (see Equation 6); this limit was deduced from experimental tests made by Hasemi [25].

#### 4.4 Fire Design of Steel Members

According to Eurocodes 3 and 4, part 1.2 ([18], [19]), there are three approaches to design structures exposed to fire: i) fire testing (very expensive and time consuming), ii) simplified methods, and iii) advanced methods. The simplified methods are based on conservative assumptions and only allow the use of nominal temperature-time curves for the design of individual members. The advanced calculation methods apply engineering principles in realistic and specific situations. In these methods, the fire can be modeled by means of Natural Fire curves (Fire Safety Engineering approach), and the indirect effects due to thermal expansions are considered; these advanced calculation methods can be applied to the fire analysis of any structural member. In the application example presented in section 6, advanced calculation methods are used for structural analyses and safety checks, based on the use of natural localized fires.

#### 4.5 Structural Fire Behavior of Steel Members

The best characterization of the structural fire response of open car parks is the real evidence or experimental tests that reproduce closely the reality, such as the study performed in 2000 by CTICM [1]. The three fire tests were performed in a real unprotected composite steel-concrete car park; the first one included three class 3-cars (scenario 5 in Figure 1). The tested structure was defined by beams IPE 550 and columns HEB 200 and a steel-concrete composite slab connected to the beams by shear connectors; no fire protection was considered in the steel profiles. The fire test took 1 hour and 20 min. and the maximum gas temperature near the ceiling reached 1040°C above the vehicle 0; however, the average gas temperature during the 15 minutes of higher temperatures was 510°C, which means that a peak temperature was reached only during a very short time. The maximum temperature in the beam lower flange at a distance of 2.5 m from the column (half length of the vehicle) was 700°C with a gradient of 250°C in the cross-section. The column flange exposed to fire reached 640°C and 480°C respectively at 2 m and 1 m above the ground, with a gradient in the cross-section of 140°C and 150°C respectively. The maximum vertical displacement of the beam was -70 mm (or 0.4% of the length); after cooling phase, a residual deformation of +25 mm was observed. Just above the cars, lateral buckling and local buckling of the lower flange of the beam were observed. In the beam-column joint, 6 bolts (in a total of 8) broke, but no collapse of the structure was observed.

### 5. FIRE REQUIREMENTS IN DIFFERENT EUROPEAN COUNTRIES

The definition of open car park can differ from country to country, as shown in Table 2. This table also presents the limitations, the general requirements for fire ISO 834 and the indication of acceptance or not of alternative design conditions. It is shown that in some countries, this type of building does not require (or very few) any time of resistance under fire (ex.: R0 in Germany or R15 in U.K.). Portugal is one of the countries with the highest requirements for fire resistance of structural elements (from R60 to R180); however, the use of Natural Fire (defining scenarios and using the RHR curves) as an alternative to ISO 834 fire is accepted and it also allows limiting or avoiding any fire protection on steel elements. This table also shows that, actually, still 18% of European countries prescribe long fire time of resistance under the ISO 834 fire, and do not indicate anything about the use of Natural Fire (Hungary, Spain and Poland).

According to the ECCS report [7], steel structures in open car parks do not require fire protection, and therefore have economic advantages. The fire safety of these structures is ensured by the following conditions: i) the design at room temperature (or “cold design”), according to the current rules, is the basic condition for the stability of the structure in the fire situation; no additional measures for fire neither a special “hot” design are required; ii) beams with composite steel concrete section including shear studs should be used; for economic reasons, it is recommended to use light weight sections (IPE, HEAA and UB); iii) large flange sections (HEA, HEB, UC) should be considered for the columns; and iv) horizontal forces must be supported by frames or bracings (protected against fire). Additionally, CTICM [20] indicates: i) the same cross-sections for all columns in the same floor; these columns must be filled with concrete between the flanges, ii) use of concrete stairs to increase the horizontal stability and to be used as emergency stairs; iii) use a minimum steel grade of S355, and minimum concrete class of C30/37; iv) steel beams connected to the concrete slab by shear studs with a minimum degree of connection of 80%; v) concrete slabs built in situ or precast concrete; the essential point is the static and structural integration of the slab in the load-bearing system [7].

Table 2. Resistance Requirements of Open Car Parks in Europe, According to the ECCS [7], and Updated in Accordance with the INERIS [14] and Other Documents

COUNTRY	Limitations						General requirements for fire ISO 834	Alternative design conditions	
	Minimum percentage of openings (%)		Maximum					No fire protection	Natural fire (*3)
	Openings /floor	Openings /walls and façades (*1)	Dist. between opposite façades (m)	n° of stories	Building height (m)	Floor area per story (m <sup>2</sup> )			
Germany	-	33	70	-	22	-	R0	/	/
Austria	-	33	70	-	22	-	Up to R90	Yes	Yes
Belgium[26]	-	17	60	-	-	-	R0 to R120	/	Yes
Denmark	5	-	24	-	-	-	R0 to R60	Yes	Yes
Spain	-	-	-	-	-	-	R60 to R120 (*2)	-	-
Finland	10	30	-	8	-	9000	R60	No (*4)	Yes
France[27]	5	50	75	-	-	-	Up toR90	Yes	Yes
Netherlands	-	30	54	-	20	-	R0 to R30	/	/
Hungary	-	-	-	-	-	-	R30 to R90 (*2)	No	No
Italy[28], [29]	15	60	-	-	-	-	R0 to R90	-	Yes
Luxemburg[30]	-	50	-	-	-	-	R0 to R30	/	/
Norway	-	33	-	-	16	5400	R10 to R60	Yes	-
Poland	-	-	-	-	25	4000	R60	No	-
Portugal [31];[32]	-	-	-	-	-	-	R60 to R180	-	Yes
U.K.[6]	5	-	-	-	30	-	R15	Yes	Yes
Sweden	-	-	-	-	-	-	Up to R90 (*2)	Yes	Yes
Switzerland	-	25	70	-	-	-	R0	/	/

(\*1): Total area of openings / total area of walls and façades surrounding one parking level.

(\*2): General requirements of National Building Code.

(\*3): Use of Natural Fire as an alternative to ISO fire to prove the fire resistance.

(\*4): Bare steel is allowed if this can be proved by tests or scientific studies.

As open car park buildings have general/typical dimensions with few variables, Corus in UK [6], ArcelorMittal in the center of Europe ([5], [30]) and One Steel in Australia [33] have already developed some typical sizing data sheets or examples in order to avoid the advanced sophisticated calculations.

## 6. EXAMPLE OF APPLICATION

The Fire Safety Engineering approach is based on the use of Natural Fires (as localized fires, defined by fire scenarios and their corresponding RHR curves) and then requires the use of advanced calculation methods for the structural analyses and safety checks. This design methodology based on fire scenarios is exemplified in this section by the application to an open composite steel-concrete car park with 8 floors, studied within the European RFCS Project ROBUSTFIRE [3]. The main and secondary beams are defined by IPE 550 and IPE 450, respectively (steel grade equal to S355). The height of each floor is 3 m, and the cross-section of steel columns varies according to the floor (HEB 550 at the bottom two floors, HEB 400 and HEB 300 at the middle floors, and HEB 220 at the top two floors), the steel grade of the columns is S460. The lateral bracing of the structure is ensured by concrete ramps required for the car circulation.

In this paper, four localized fires scenarios are studied in order to check the design of the secondary beam with two spans of 16 m each (IPE 450), the main beam with spans of 10 m (IPE 550) and the column of the fourth floor (HEB 300); cars of class 3 are used in the scenarios. The study of the global behavior of the structure, assuming local collapse without progressive collapse, has been disregarded, so commercial vehicle is not considered in the studied scenarios.

The fire scenario chosen for the secondary beams is scenario 1, with a vehicle under the mid-span of the beam (critical situation for the cross-section with hogging bending moment), whereas scenarios 4 and 5 correspond to the worst scenarios for the column study (Figure 1). Only class 3-cars are considered. The design fire load is calculated according to Equation 7, considering the equation (1a) with  $\psi_I = 0.7$ :

$$1.0 G_k + 0.7 Q_k = 1.0 \times 7.77 \text{ kN/m} + 0.7 \times 8.18 \text{ kN/m} = 13.50 \text{ kN/m} \quad (7)$$

For the main beam (IPE 550), scenario 3 is the worst fire scenario, and the design load is given by:

$$1.0 G_k + 0.7 Q_k = 1.0 \times 25.91 \text{ kN/m} + 0.7 \times 26.16 \text{ kN/m} = 44.22 \text{ kN/m} \quad (8)$$

## 6.1 Design According to the Simplified Methods

In the simplified methods defined in Eurocodes 3 and 4, part 1.2 ([18], [19]), the fire design of a structural element can be performed in the temperature domain, time domain or resistance domain. These simplified methods cannot be used if Natural Fire (based on RHR fire curves) is taken into account, as explained in section 4.4. However, an attempt is made in this section to simplify the fire design of the beams under localized fire, using these simplified methods. In the temperature domain, it is considered that the element has a uniform temperature distribution and the failure is expected to occur when this temperature exceeds the critical temperature ( $\theta_{crit}$ ). In case of a localized fire, temperature is not uniform along the beam and using a critical temperature of the element is very conservative. In the resistance domain, the resistant bending moment of the structural element  $M_{fi,\theta,Rd}$  should be compared to the applied bending moment  $M_{fi,Ed}$  (assuming no lateral buckling because of the concrete slab). These two domains are checked for the study of the secondary beam.

Steel temperatures can be easily determined with program Elefir-EN [34], considering the following data: i) definition of the localized fire according to the number of vehicles included in the scenario, ii) curve of the rate of heat release of each car (Figure 2); iii) diameter of the fire,  $D$  (for each car:  $D = 3.9$  m); iv) distance between the heat source and the ceiling  $H = H_f - H_s - H_{beam}$  (Figure 5), with  $H_s = 0.3$  m; and v) horizontal distance between the vertical axis of the fire and the point along the ceiling where the thermal flux is calculated,  $r$  (m) (Figure 5). For each scenario, the flame length  $L_f$  (see Equation 3) is greater than the height of the floor: the flame impacts the ceiling, so the Hasemi's method is considered.

The critical temperature ( $\theta_{crit}$ ) is also calculated with the program Elefir-EN [34], according to Eurocode 3, Part 1.2 [18]. The beam is exposed on 3 sides (the top flange supports a concrete slab), the adjustment factor  $k_1$  (non-uniformity of temperature in the section) is equal to 0.7 and adjustment factor  $k_2$  (non-uniformity of temperature along the beam) is considered equal to 1. Figure 6a shows the results of the critical fire scenario 1; the critical temperature is equal to 653°C and a maximum temperature ( $\theta_{max}$ ) of 706°C is reached in the beam after 28 min. In this case, it is necessary to protect the beam using 3 mm of cement with vermiculite, for example. If resistance domain is considered, the maximum sagging bending moment is equal to 244.5 kNm (mid-span). At 28 min. of fire (uniform steel temperature of 706°C), the resistant bending moment of the

composite beam section is equal to 255 kNm, which is higher than the applied bending moment; no fire protection is needed. The concrete slab is assumed to be at ambient temperature; this assumption is based on the results from the CTICM tests [1]: maximum temperature equal to 250°C was measured at the bottom of the slab and in an area restricted to the area of fire. Scenario 3 with seven cars (Figure 1) is the critical fire scenario for the main beam (IPE 550). Figure 6b shows the temperature curves: the critical temperature of 724°C is reached after 32 min. and a maximum temperature of 543°C was calculated in the beam; no fire protection is needed, even in the more conservative temperature domain. However, if Portugal regulation is considered, the structure resistance should be R90 [31] (this building has more than 9 m in height, and it is 2<sup>nd</sup> category of risk [32]); moreover, if curve ISO 834 is used to check this structure for the resistance R90, 11 mm and 25 mm of cement with vermiculite are needed to protect main and secondary beams, respectively. Table 3 summarizes and compares these results.

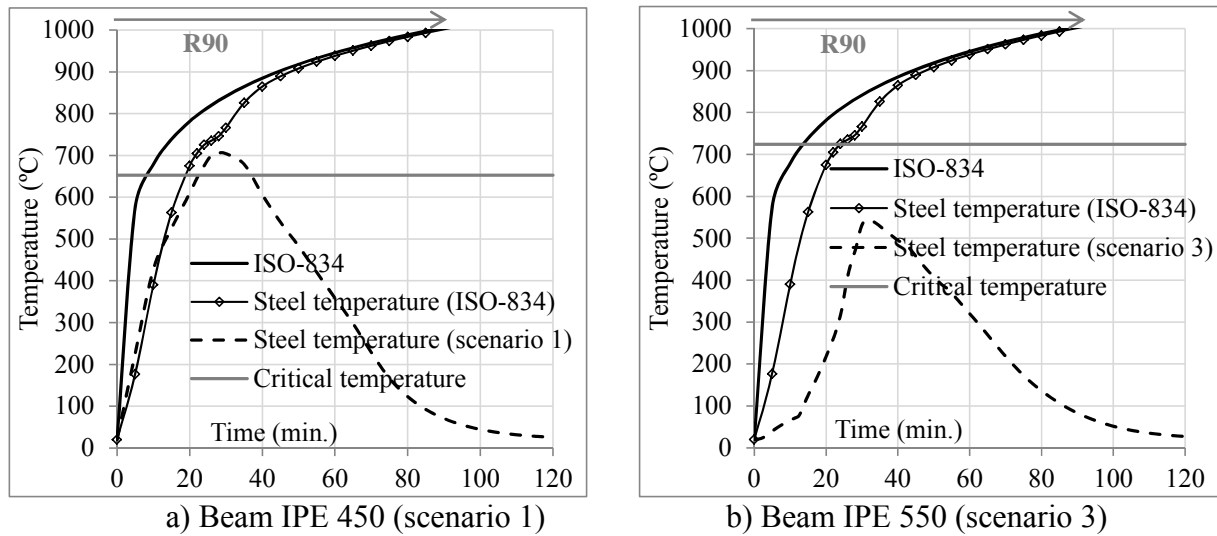


Figure 6. Comparison between the Steel Temperature in Beams IPE450 and IPE550 subject to ISO 834 Fire and to the Most Unfavorable Fire Scenarios for Each Beam

## 6.2 Design According to the Advanced Calculation Methods

The design of the same structure through an advanced calculation method is now presented and the results are compared with those obtained in section 6.1. Since with the method based on fire scenarios and applied in a simplified way, no fire protection is needed to the main beam, advanced calculation method will only be applied to composite secondary beam (scenario 1). Additionally, the advanced calculation methods will also be used to evaluate the fire resistance of the column (scenarios 4 and 5). The finite element program Abaqus [35] is used to perform the thermal and structural analyses.

### 6.2.1 Thermal analysis

The thermal loads for the beams are defined taking into account the following procedure: i) the gas temperatures that surround the beam are calculated using the program Elefir-EN: as the flame impact the ceiling, the Hasemi's method is considered and the gas temperature corresponds to the flame temperature ( $H = 2.25\text{m}$ ); ii) a heat transfer analysis is performed in Abaqus for each composite section located along the beam (emissivity factor equal 0.7 and convection coefficient equal to 35 W/m<sup>2</sup>K); the model of the composite beam is developed using 2D deformable element DC2D4. Figure 7 depicts the temperatures evolution in the steel beam section for each scenario; the presented curves correspond to the cross-sections with maximum temperatures: mid-span of the beam for scenario 1 and at 2.5 m from the column for scenarios 4 and 5.

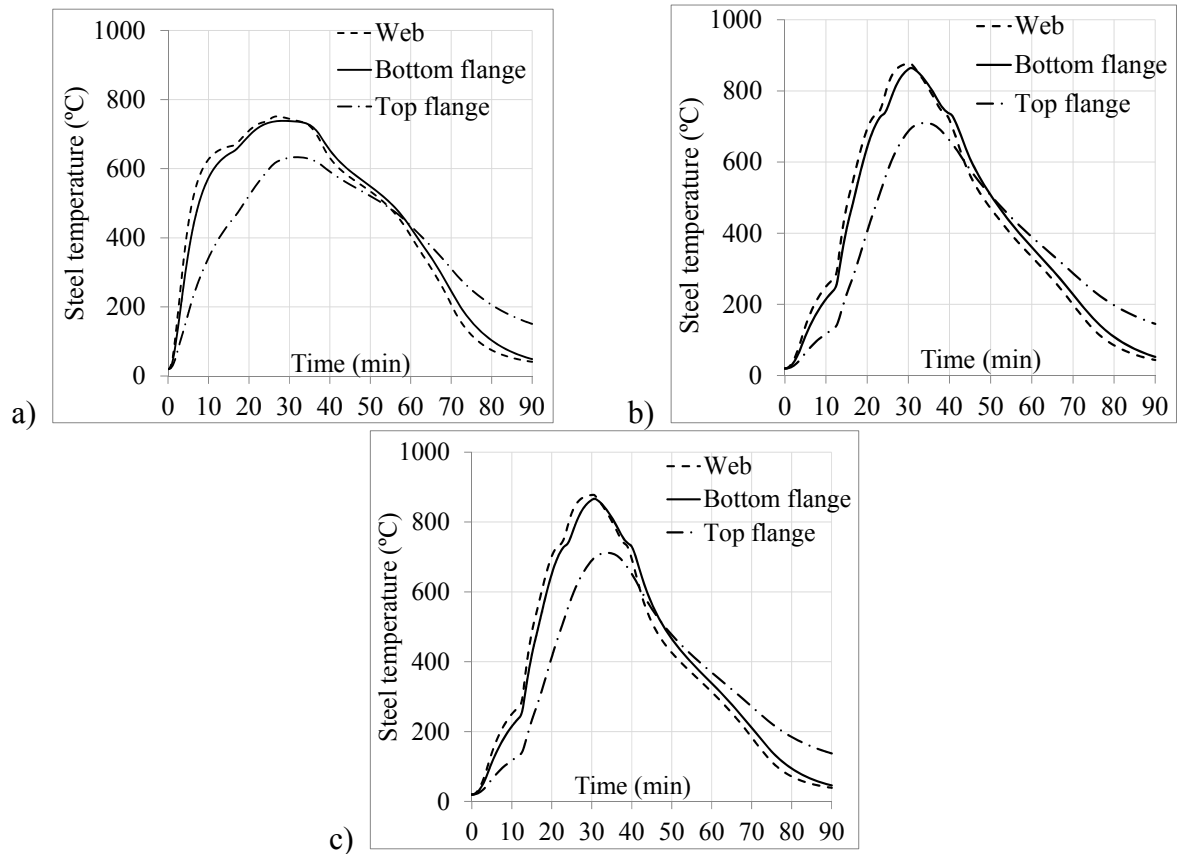
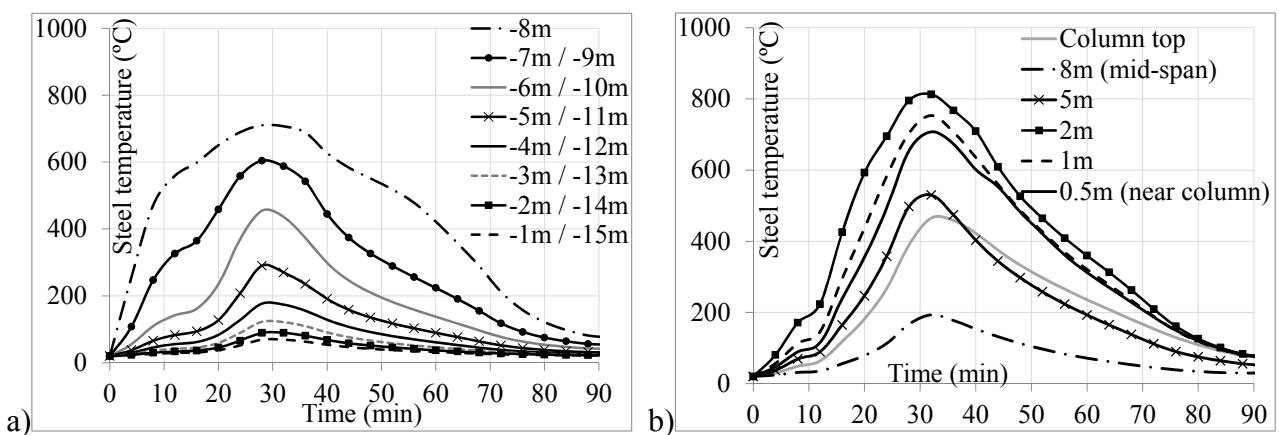


Figure 7. Temperature Evolution in the Secondary Beam IPE 450 under: a) Scenario 1 (Mid-span), b) Scenario 4 (at 2m from the Column) and c) Scenario 5 (at 2m from the Column)

Figure 8 presents the variation of the average temperature in each section of the secondary beam during the fire for each scenario, while Figure 9 presents the variation of the average temperatures in each section of the secondary beam versus the position at 30 min. of fire. In these charts are represented the weighted average temperatures of the steel beam section.



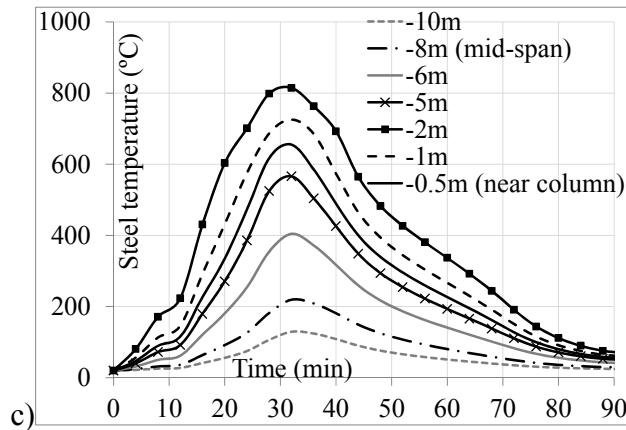


Figure 8. Variation of the Weighted Average Temperatures in Section of the Secondary Beams IPE 450 versus time: a) Scenario 1, b) Scenario 4 and c) Scenario 5

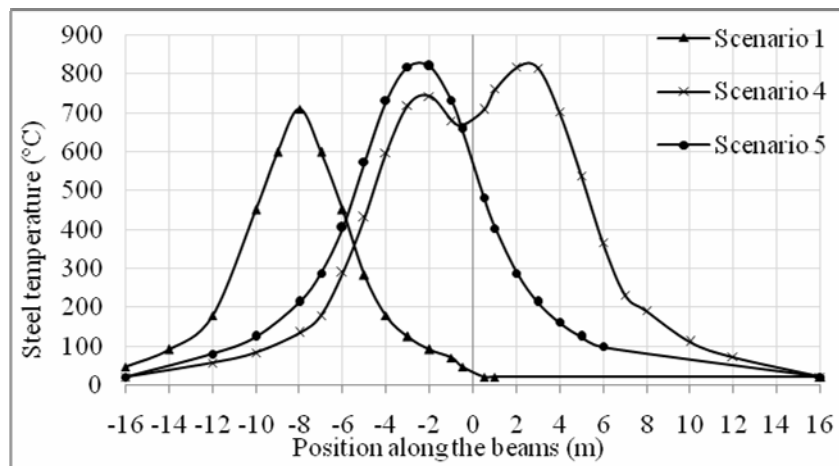


Figure 9. Variations of the Weighted Average Temperatures in Section of the Secondary Beam IPE 450 after 30 min. of Fire Versus Position along the Beams (scenarios 1, 4 and 5)

### 6.2.2 Mechanical analysis

In this example, the two dimensional frame includes the secondary beams of 16 m length each (Figure 10) and the columns (weak axis). The composite beams are modeled with an equivalent rectangular section (identical section and inertia than the real composite beam; additionally inertia considering cracked concrete is considered near the supports). The beams affected by the fire scenarios developed at the fourth floor are modeled by beam elements for the steel profile, and shell elements for the slab (the composite slab is simplified to a reinforced concrete slab of thickness equal to 120 mm). The width of the slab is 3.4 m, which corresponds to the effective width of the mid-span. The initial deformation of  $h/1000$  (3 mm) is applied to the columns. Beams elements are used for the beams and the columns not directly affected by the fire. Mechanical loads correspond to the values presented at the beginning of section 6. Only third, fourth and fifth floors are modeled, taking into account loads from the upper floors.



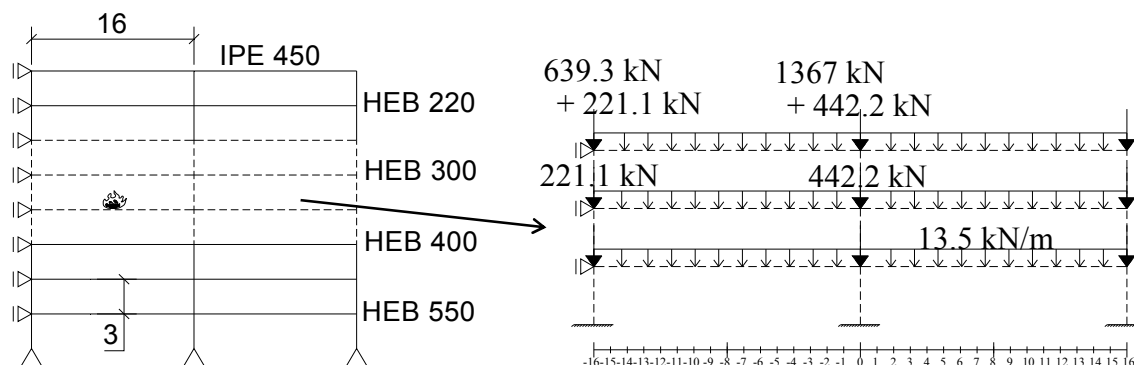


Figure 10. Studied Car Park Versus Numerical 2D Frame (Loaded)

The calculated temperatures gradients are directly applied to the steel beam sections in the static analysis, using the option “predefined fields”. The concrete slab is assumed to be at ambient temperature throughout the analysis, as justified previously. The scenario 4 corresponds to the worst fire scenario for the column, with four class 3-cars burning around it. Because no accurate (and simple) method is defined to calculate the column temperature in case of a localized fire, the temperature at the column top is assumed to be the same than an HEB 300 beam (calculated by Hasemi’s method). This temperature is applied uniformly along the column height (except below the heat source, at 0.3 m above the floor, where 20°C are considered). The concrete properties are set in accordance with Eurocode 2 Part 1.2 [36], and steel properties vary with temperature as defined in Eurocode 3 Part 1.2 [18].

Figure 11 shows the development of the vertical displacement at the beam mid-span for each fire scenario. For the scenario 1, a maximum displacement equal to 122 mm downwards (which includes the initial displacement of 21 mm due to the mechanical loading) is reached after 15 min. of fire. After the fire, the beam shows a residual camber, with a displacement at mid-span equal to 102 mm upwards. Because i) of the high thermal gradients in the cross-section of the composite beam (unheated concrete slab), and ii) the axial restraint to thermal expansion due to the lateral bracing and the unaffected part of the building, high compression loads developed at the beam bottom flange, which inverted the bending moment from sagging to hogging moment. This thermal bowing developed at the beam mid-span after 17 min. of fire. If thermal deformations or expansions were not restrained, the axial compression loads would not have increased and thermal bowing would not have happened. This highlights the importance of using advanced calculation methods within Fire Safety Engineering, where indirect actions due to restrained thermal deformations or expansions are considered.

Under scenario 4, the column is not able to resist to the entire fire and fails by yielding of the cross-section after 28 min. of fire (three plastic hinges are developed at the top, bottom and at the mid-height of the column - Figure 11). However, according to the statistics, this scenario never happened in reality in an open car park building, and the application of uniform temperatures along the column height is a very conservative hypothesis [22]. An additional verification of the column, based on the realistic fire scenario 5 including three burning cars, is performed. For this scenario, the column temperatures measured during the first French test [1] are assumed: average values of 405°C and 570°C were measured at 1m height and at 2m height, respectively. The column and the beams resist to this fire scenario, with maximum 196 mm of beam vertical displacement at 32 min (Figure 11).

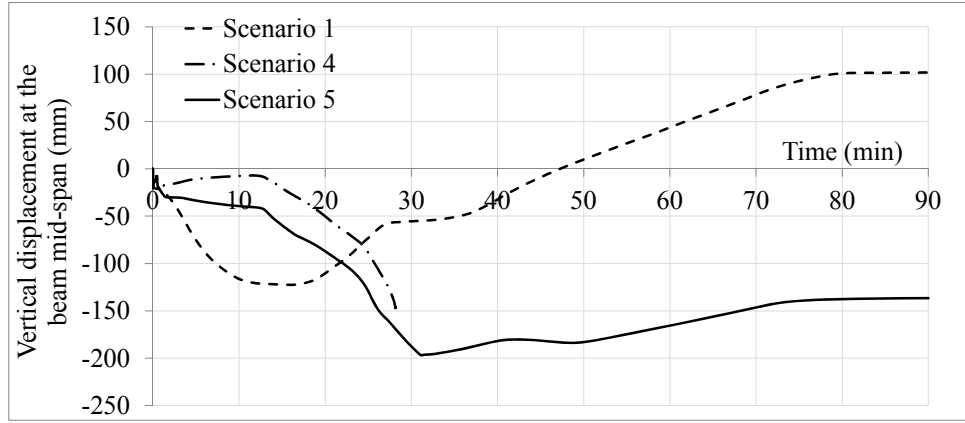


Figure 11. Evolution of the Beam IPE 450 Mid-span Vertical Displacement During Fire

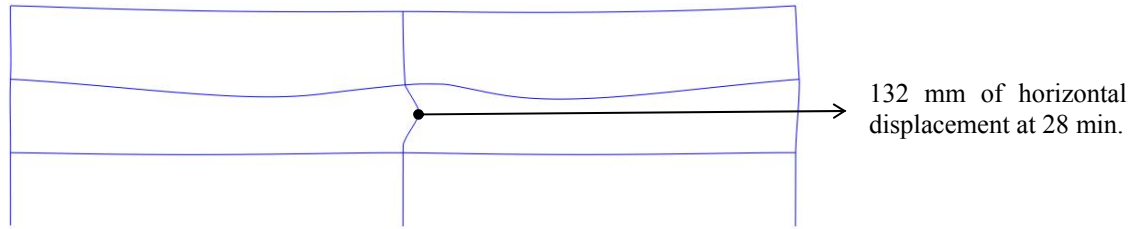


Figure 12. Frame Deformation at 28 min of Fire (Scenario 4): Column Failure (Scale 5)

Standard ISO 834-1 [37] relating to fire resistance tests indicates that failure of an element subject to bending under fire should be considered when the maximum vertical displacement  $\sigma_{max}$  exceeds the values indicated by Equation 9:

$$\delta_{max} \leq \frac{L^2}{400d} = 1123 \text{ mm} \quad (9)$$

Where  $L$  [mm] is the span of the beam and  $d$  [mm] is the distance from the extreme fiber of the design compression zone to the extreme fiber of the design tensile zone of the structural section. The maximum displacements of the studied beam are lower than these values, and it can be considered that the beam does not fail under any of these fire scenarios. For the column, the same standard restricts the maximum axial contraction  $\sigma_{vert,max}$  of axially loaded elements to Equation 10:

$$\delta_{vert,max} \leq \frac{h}{100} = 30 \text{ mm} \quad (10)$$

Where  $h$  [mm] is the initial height. The studied column reached this limit after 28 min. of fire in scenario 4, but reached smaller contraction (max. 24 mm) in scenario 5. French prescriptions [20] usually prescribe to add concrete between the column flanges in order to protect the column (see section 5), which is a solution that could be done if scenario 4 needs to be checked.

### 6.3 Summary of the Results

Table 3 summarizes the results obtained for the beams and the column, according to the simplified and advanced methods.

Table 3. Summary of the Design Results for Beams IPE 450 and IPE 550

	Simplified methods			Advanced methods		
	Temperature / resistance domain					
	Scenario 1	Scenario 3	ISO 834	Scenario 1	Scenario 4	Scenario 5
IPE 550 ( $\theta_{crit.} = 724^{\circ}\text{C}$ )	---	$\theta_{max} = 543^{\circ}\text{C}$ (32 min.)	$\theta_{90min.} = 1001^{\circ}\text{C}$	---	---	---
<i>Prot.*: ex.: cement with vermiculite</i>	---	No need	11 mm thick	---	---	---
IPE 450 ( $\theta_{crit.} = 653^{\circ}\text{C} / M_{fi,Ed} = 244.5$ )	$\theta_{max} = 706^{\circ}\text{C}$ (28 min.) / = 255 kNm	---	$\theta_{90min.} = 1001^{\circ}\text{C}$	$\sigma_{max} = 122$ mm (15 min.)	---	$\sigma_{max} = 196$ mm (32 min.)
<i>Prot.*: ex.: cement with vermiculite</i>	3 mm thick / No need	---	25 mm thick	No need	---	No need
Column HEB 300	---	---	---	---	$\sigma_{vert} > 30$ mm	$\sigma_{vert,max} = 24$ mm
<i>Prot.*: ex.: concrete between flanges</i>	---	---	---	---	Need!	No need

\*Prot. = fire protection

## 7. CONCLUDING REMARKS

The fire design of steel and composite structures from open car park can be made in accordance with Eurocodes: Eurocode 1 Part 1.1 [16] defines the mechanical loads, while Annex C and Annex D of Part 1.2 [17] present a simplified method for determining the flame temperature around the beams. The calculation of these temperatures depends on the total rate of heat release, which is determined based on the fire scenarios. The reference curve for the rate of heat release was defined based on results of experimental tests performed on actual vehicles. Finally, Eurocodes 3 and 4, Part 1.2 ([18], [19]) present the calculation models for these structures.

From previous experimental tests in real open car park buildings, it was concluded that most of unprotected steel open sided steel-framed car parks has sufficient inherent resistance to withstand the effects of any fires that are likely to occur. These results have encouraged to change the legislations in several European countries, allowing to build steel or composite steel-concrete open car parks without fire protection, taking into account a design based on the actual performance of the structure and not on prescribed nominal design curves (that in most of the cases, require fire protection with considerable thickness).

The simplified design methods defined in Eurocodes 3 and 4, part 1.2 ([18], [19]), are based on conservative assumptions and only allow the use of nominal temperature-time curves for the design of individual members. When the structure is subject to Natural Fire defined by RHR fire curves, the choice must involve the use of advanced calculation methods rather than simplified methods in order to consider the indirect effects due to restrained thermal expansions.

Design of columns under localized fires can only be done, for now, using advanced models; no accurate and simple method is available to calculate the column temperature due to a localized fire. Hasemi's method is a simple tool for the evaluation of the localized effect of a fire on horizontal elements located above the fire, but cannot be used for the columns. Finally, the example clearly

showed the advantage of using the design methodology based on fire scenarios against the use of ISO curve; it was verified that the unprotected composite steel-concrete structure resists to the studied fire scenarios.

In conclusion, the design methodology based on fire scenarios allowed optimizing the structure to benefit from an appropriate level of fire safety, reducing the fire protection and therefore the final cost of this type of building.

## ACKNOWLEDGEMENTS

The research leading to these results has received funding from the European Community's Research Fund for Coal and Steel (RFGS) under grant agreement n° RFGS-CT-2008-00036 – project ROBUSTFIRE: “Robustness of Car Parks against Localized Fire”.

## REFERENCES

- [1] Joyeux, D., Kruppa, J., Cajot, L.-G., Schleich, J.-B., Van de Leur, P. and Twilt, L. “Demonstration of Real Fire Tests in Car Parks and High Buildings”, European Commission, Contract No. 7215-PP/025 (1993 – 1996), CTICM, Final Report, EUR 20466 EN, 2002, pp. 168.
- [2] Simões da Silva, L., Santiago, A. and Haremza, C., “ROBUSTFIRE Project, Document 1 – Car Parks – V1(11)”, Internal Document, University of Coimbra, 2009, pp. 71.
- [3] Demonceau, J.F., Huvelle, C., Comeliau, L., Hoang, L.V., Jaspert, J.P. and Fang C., et al. “Robustness of Car Parks Against Localised Fire”, European Commission, Grant Agreement Number RFGS-CT-2008-00036, Final Report, 2012.
- [4] Cajot, L.-G., Mathieu, J. and Thomas, L., “Les Structures Métalliques Pour Les Parking Souverts”, La revue de Métallurgie-CIT, November 2003, pp. 8.
- [5] Arcelor Mittal, “Parkings Aériens métalliques Large Ment ventilés”, Les carnets de l’acier, 2007, No 9, pp. 34.
- [6] Corus, “Steel-framed Car Parks”, Corus Construction & Industrial, 2004.
- [7] ECCS, “Fire Safety in Open Car Parks”, Modern Fire Engineering, Technical Committee 3, n°75, European Convention for Constructional Steelwork: Brussels, Belgium, 1993, pp. 90.
- [8] Butcher, E.G., Langdon-Thomas G.H., Bedford G.K. “Fire Car Park Buildings”, Fire Note 10, HMSO, U.K, July 1968.
- [9] Gewain, R.G. “Fire Experience and Fire Tests in Automobile Parking Structures.” Fire Journal, 1973, Vol. 67, No. 4, pp. 50-54.
- [10] Bennetts, I.D., Proe, D.J., Lewins, R.R. and Thomas I.R. “Fire and Unprotected Steel in Closed Car Parks”. BHP Melbourne, Research Laboratories Report Number MRL/PS98/87/001, August 1987.
- [11] Zhao, B. and Kruppa, J. “Structural Behaviour of An Open Car Park under Real Fire Scenarios”, Second International Workshop “Structures in Fire” - Christchurch – March 2002, Fire and Materials, 2004, Vol. 28, pp. 269-280.
- [12] Li, Y. and Spearpoint, M., “Analysis of Vehicle Fire Statistics in New Zealand Parking Buildings”, Fire Technology, 2007, Vol. 43, pp. 93-106.
- [13] Li, Y. “Assesment of Vehicle Fires in New Zealand Parking Buildings”. Fire Engineering Research Report 04/2, Master Thesis, University of Canterbury, New Zealand, May 2004.
- [14] Cwiklinski, C., “Parcs de Stationnement en Superstructure Large Ment ventilés – Avis d’experts sur les scénarios d’incendie”, Rapport final, INERIS DRA-CCw/MCh-2001-cgr22984, 2001, pp. 26.

- [15] EN 1990:2002, “Eurocode – Basis of Structural Design”, European Committee for Standardization, April 2002, pp. 87.
- [16] EN 1991-1-1:2002, “Eurocode 1: Actions on Structures – Part 1-1: General Actions – Densities, Self-weight, Imposed Loads for Buildings”, European committee for standardization, April 2002, pp. 44.
- [17] EN 1991-1-2:2002, “Eurocode 1: Actions on Structures – Part 1-2: General Actions – Actions on Structures Exposed to Fire”, European Committee for Standardization, November 2002, pp. 59.
- [18] EN 1993-1-2:2005, “Eurocode 3: Design of Steel Structures – Part 1-2: General Rules – Structural Fire Design”, European Committee for Standardization, April 2005, pp. 78.
- [19] EN 1994-1-2:2005, “Eurocode 4: Design of Composite Steel and Concrete Structures – Part 1-2: General Rules – Structural Fire Design”, European Committee for Standardization, August 2005, pp. 109.
- [20] Fraud, C., Zhao, B., Joyeux, D., Kruppa, J., “Guide Pour la Vérification du Comportement au Feu de Parcs de Stationnement Large Mentventilés en Superstructure Métallique”, CTICM, INSI – 03/233d – BZ/PB, 2004, pp. 75.
- [21] Mangs, J. and Keski-Rahkonen, O., "Characterisation of the Fire Behaviour of a Burning Passenger Car. Part I: Car Fire Experiments." Fire Safety Journal, 1994, Vol. 23, pp. 17-35.
- [22] Schleich, J.-B., Cajot, L.-G., Pierre, M., Brasseur, M., Franssen, J.-M. and Kruppa, J. et al., “Development of Design Rules for Steel Structures Subjected to Natural Fires in Closed Car Parks”, European Commission, C.E.C. Research 7210-SA/518. Final Report EUR 18867 EN, 1999, pp. 154.
- [23] Franssen, J.-M. and Vila Real, P. “Fire Design of Steel Structures”, ECCS Eurocode Design Manuals, Ernst & Sohn, 1<sup>st</sup> Edition, 2010.
- [24] Schleich, J.B., Cajot, L.G., Pierre, M., Brasseur, M., Franssen, J.M., Kruppa, J., Joyeux, D., Twilt, L., Van Oerle, J. and Aurtenetxe, G. “Development of Design Rules for Steel Structures Subjected to Natural Fires in Large Compartments”, European Commission, Contract No. 7210-SA/211/318/518/620/933, 1999.
- [25] EC1-1-2/71, “Background Document on Localized Fires According to Annex C of prEN1991-1-2 (24-08-2001)”, Profil ARBED, Centre de Recherches, CEN/TC250/SC1/N339, 2001.
- [26] Arrêté royal fixant les mesures en matière de prévention contre l’incendie et l’explosion auxquelles les parkings fermés doivent satisfaire pour le stationnement des véhicules LPG, Moniteur Belge, Belgisch Staatsblad. Ed. 3, 20 of June, 2007, pp. 33997.
- [27] Arrêté du 9 mai 2006 portant approbation de dispositions complétant et modifiant le règlement de sécurité contre les risques d’incendie et de panique dans les établissements recevant du public (parcs de stationnement couverts), Ministère de l’intérieur et de l’aménagement du territoire, Journal Officiel de la République Française, 8 juillet 2006.
- [28] Ministry of Interior (Italian Government), Decree 9 May 2007. Direttive per l’attuazione dell’approccio ingegneristico alla sicurezza antincendio, GU n. 117 del 22 maggio 2007.
- [29] Nigro, E., Cefarelli, G., Ferraro, A., Manfredi, G. and Cosenza, E., “Fire Safety Engineering for Open and Closed Car Parks: C.A.S.E Project for L’Aquila”, Applied Mechanics and Materials, Vol. 82, pp. 746-751, 2011. ISSN: 1662-7482. doi:10.4028/www.scientific.net/AMM.82.746.
- [30] ArcelorMittal – “Car parks in steel”, Commercial Sections, 1996, 30p.
- [31] Portaria nº1532/2008”, Diário da República, 1<sup>a</sup> série, N.º 250, 29 de Dezembro, 2008, pp. 9050-9127.
- [32] Decreto-Lei nº220/2008, Diário da República, 1<sup>a</sup> série, N.º 220, 2008, pp. 7903-7922.
- [33] Economical Carparks – A Design Guide, Australia, 2<sup>nd</sup> Edition, 2004.

- [34] Vila Real, P. and Franssen, J.M. – Elefir-EN V1.2.3, Software for Fire Design of Steel Structural Members According the Eurocode 3, 2010. <http://elefired.web.ua.pt>.
- [35] ABAQUS – Theory Manual & Users Manuals, v. 6.11, Hibbitt, Karlsson and Sorensen Inc., 2011.
- [36] EN 1992-1-2:2004 - “Eurocode 2: Design of Concrete Structures – Part 1-2: General Rules – Structural Fire Design”, European Committee for Standardization, December 2004, pp. 97.
- [37] ISO 834-1, “Fire-resistance Tests - Elements of Building Construction - Part 1: General Requirements”, International Standard, 1<sup>st</sup> Edition, 1999.

# RESEARCH ON A NEW DOUBLE-WALL STEEL INSULATION SILO WITH MULTIPLE BOLTED JOINTS: PART I, STRUCTURE SYSTEM

Lingfeng Yin<sup>1,\*</sup>, Gan Tang<sup>1,2</sup>, Xiaoming Guo<sup>1</sup> and Haibin Lai<sup>1</sup>

<sup>1</sup> School of Civil Engineering, Southeast University, SiPaiLou 2, Nanjing, China, 210096

<sup>2</sup> Department of Civil Engineering, Nanjing University of Aeronautics and Astronautics,  
YuDao Street 29, Nanjing, China, 210016

\*(Corresponding author: Email: eking@seu.edu.cn)

*Received: 21 September 2011; Revised: 17 January 2012; Accepted: 27 January 2012*

**ABSTRACT:** The objective of this paper is to study a new double-wall steel insulation silo with multiple bolted joints for grain storage, which is designed to improve the insulation effect and mechanical behavior of the traditional silo structure. The silo employs the planar thin-walled steel plate as the internal wall, and the continuous ladder-shaped profiled plate as the external wall. The cavity between the internal and external walls is filled with insulation material. The silo utilizes specifically designed bolt connections to connect the internal and external walls. This paper carefully studied the structural behavior of the silo and the results indicate that the horizontal pressure from the grains is resisted by the internal wall under tension, and that the vertical friction force is mainly carried by both the external and internal walls. The stability of the internal wall is effectively provided by the external wall. The selection of connection model between the internal and external walls has a significant impact on the structural performance of the silo. To make the optimal selection, further verification and experimental studies are needed.

**Keywords:** Steel insulation silo; double-wall; multiple bolted joints; structural behavior; connection model between the internal and external walls

## 1. INTRODUCTION

There are two types of silos for grain storage, the reinforced concrete silos and the steel silos. The steel silos have been more widely applied due to their advantages such as light weight, low cost, short construction period, waterproof property, and outstanding impermeability.

The main loads on the steel silo structures are the horizontal pressure and the vertical friction force from the grains. Janssen[1] first proposed the formula to calculate horizontal pressure and vertical friction force at the end of the 19th century. The formula has been adopted by the standards of many countries (China [2], Australia [3], Europe [4], ISO [5], the United States [6] and so on). The horizontal pressure coefficient  $k$  in the formula has become an important research focus. Many studies and experiments demonstrated the dynamic effects of the horizontal pressure in the process of loading and unloading. Walker [7] and Zhong [8] conducted in-depth studies on dynamic unloading. However, no consensus on the mechanism of the dynamic pressure has been reached. The current studies mainly focus on single-layer thin-walled steel silos. Pincher [9], Teng [10], Sadowski [11] and Zhao [12] studied the stability and initial imperfection of silos. Teng [13], Laier [14], Dogangun [15] and Sadowski [16] studied the collapse behavior and the influence of eccentric load. However, few studies have focused on the steel insulation silo structure.

Most of the steel silos in use are single-layer and thin-walled, which leads to ill-function of the silos. The silo wall is so thin that a temperature difference between the inside and outside of the silo can easily form. Moisture condensation, imbalanced temperature distribution and high grain temperature are observed when the silo is greatly affected by the external environment. These bring a great threat to grain storage safety, to reduce which, the proper ventilation equipment should be installed and the frequency of the grain turnover should be increased. These countermeasures increase the costs and grain consumption.

The commonly used steel silos are constructed of corrugated steel plates and reinforcing ribs with bolted connections, from which some mechanical defects are usually observed. The shape of corrugated plate determines that it can bear only the horizontal pressure. The vertical loads are carried only by the reinforcing ribs. The restraint of the corrugated plate on the flexural buckling of the reinforcing rib is insignificant. The silo is very sensitive to the eccentric loads, which increases the instability of the silo, thus leading to a possible collapse.

In order to improve the insulation effect and mechanical behavior of the traditional silo structure, this paper proposes a double-wall steel insulation silo with multiple bolted joints for grain storage and carefully analyzes its structural behavior. This new silo has been granted patent [17].

## **2. SYSTEM INTRODUCTION**

### **(1) Silo Structure**

The double-wall steel insulation silo with multiple bolted joints proposed in this paper inherits the merits of the existing fabricated steel silo while having the capability of insulation. The silo employs the planar thin-walled steel plate as the internal wall, and the continuous ladder-shaped profiled plate as the external wall. The planar internal wall can effectively reduce the vertical friction force from the grains as well as the cleaning work. The silo utilizes specifically designed bolt connections to connect the internal and external walls. Vertically, several internal and external ring beams are set respectively for the internal and external walls. The section of the silo is shown in Figure 1 and the bolt connection set is shown in Figure 2.

### **(2) Insulation Principle**

The cavity between the internal and external walls is filled with insulation material, which produces an outstanding insulation effect for the silo. Thermal insulation caps at the external side of the bolt connection sets are also employed to cut off the “thermal bridge”, thus further promoting the insulation performance of the silo. Sandwich panels are adopted for insulation and enclosure on the top of silo.

The silo is environmentally friendly, featured with simple structure and high integrity. The design of the silo enables it to save energy and steel consumption with a pleasant appearance. Each construction member can be prepared in factories to facilitate field installation with the “upside-down construction method”. A completed silo is shown in Figure 3.



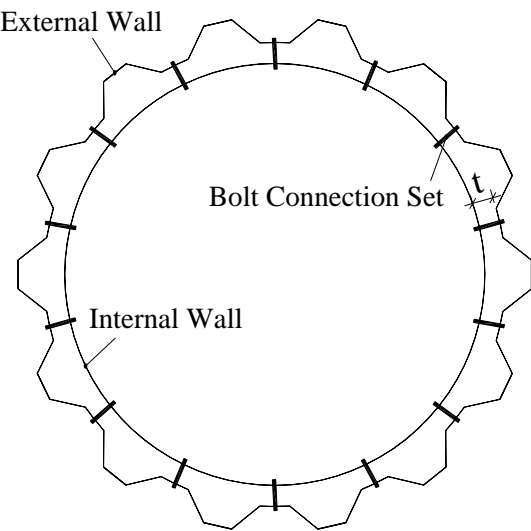


Figure 1. Section Form of the Double-wall Silo

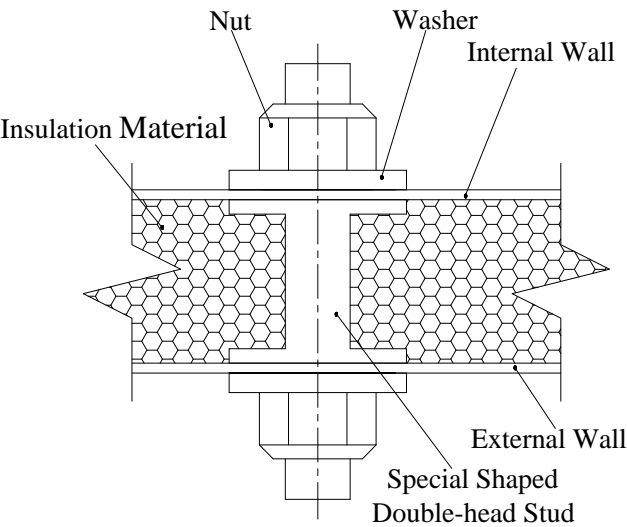


Figure 2. Diagram of Bolt Connection Sets

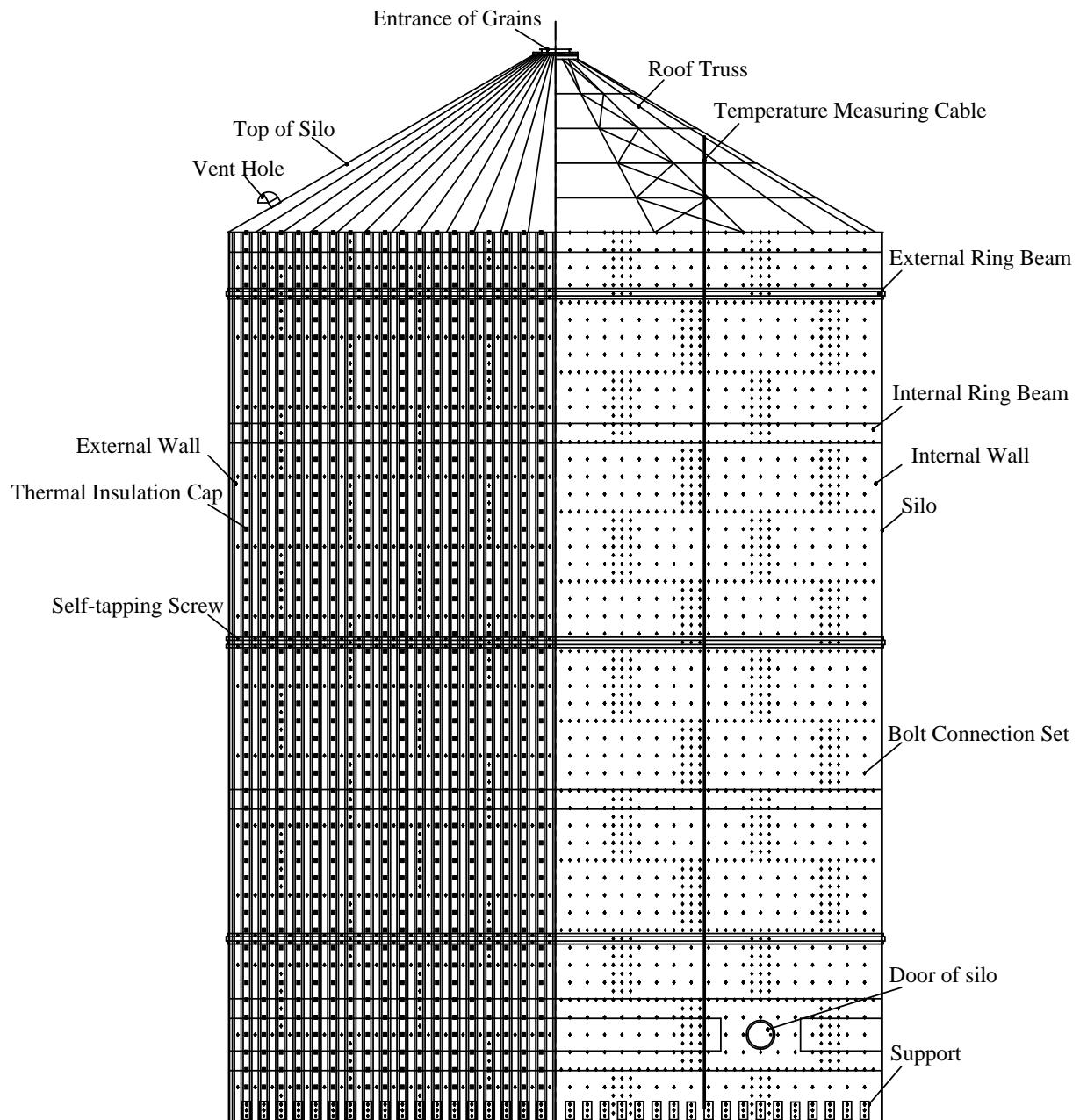


Figure 3. Double-wall Steel Insulation Silo with Multiple Bolted Joints

### 3. STRUCTURE PRINCIPLE

The internal and external walls cooperatively share the loads. The internal wall has a good tensile property, yet still unable to independently bear the large vertical pressure in the plane. Therefore, supports from other external construction members are needed. The external wall performs good bearing capacity along the vertical direction but little bearing capacity in the horizontal direction. A careful configuration and design of the double-head bolts can promote the cooperation between the internal and external walls.

The silo structure is axisymmetric, and its force diagram under grain loads is shown in Figure 4. The horizontal pressure from the grains is resisted by the internal wall under tension; the external wall helps carry the vertical friction force and provides effective supports to the stability of the internal wall.

In addition, the internal and external ring beams can promote the mechanical behavior and stability of the silo. The external and internal walls together resist the wind, snow, and earthquake loads. The roof truss serves as a restraint on the whole top area of the silo walls and delivers the loads on the top of silo to the silo walls.

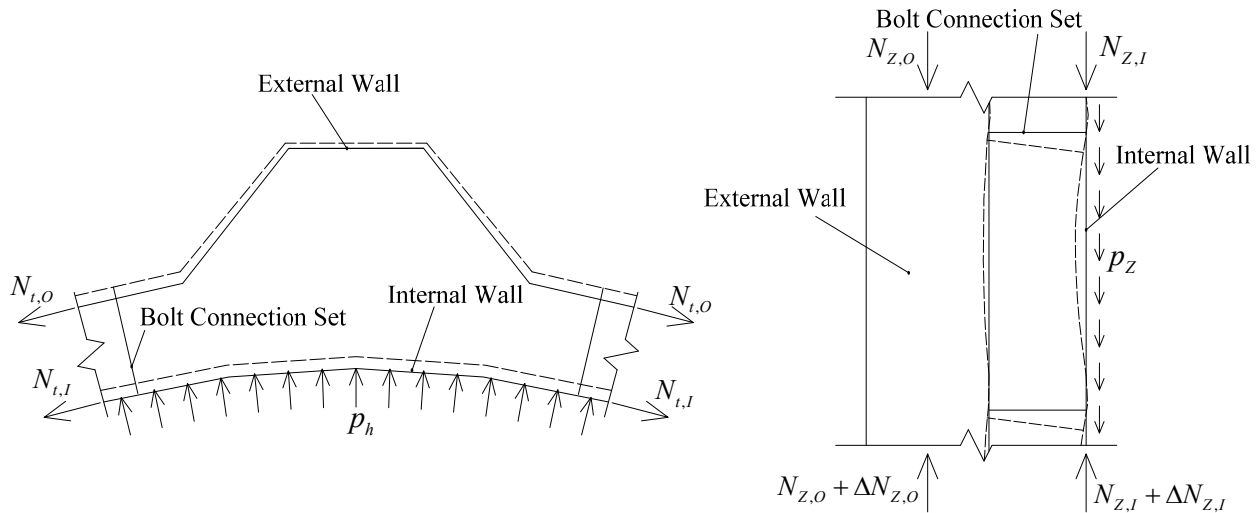


Figure 4. Force Diagram of the Silo under Grain Loads

## 4. STRUCTUREAL BEHAVIOR ANALYSIS

### 4.1 Research Object

The research object is an experimental silo model. Its internal diameter is 500mm, height 1200mm, and the spacing between the internal and external walls 25mm. For more details of the experimental silo model design, experiment process and results analysis, refer to Ref.[18]. In Figure 5, the external wall uses the YX 35-125-750 profiled steel plate, and the internal wall is a thin-walled circular plate of thickness 1mm. The 8-mm-diameter double-head bolts that connect the internal and external walls are placed with the vertical spacing of 100mm and are evenly spaced around a circle.

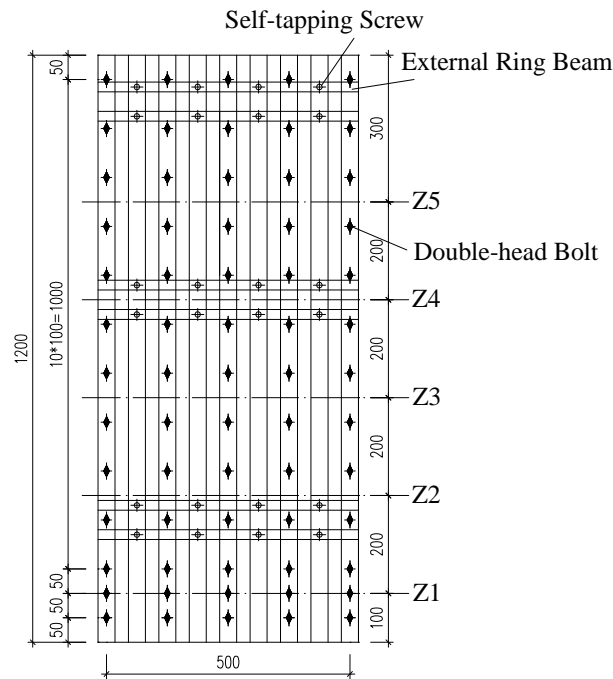


Figure 5. Diagram of the Experimental Silo Model

## 4.2 Study on Connection Model between Internal and External Walls

### 4.2.1 Finite Element Modeling

From the material experiments, the elastic modulus of steel plate is obtained as  $E = 1.90 \times 10^5$  MPa, and the yield strength  $f_y = 195$  MPa. Dry yellow sand of diameter less than 0.25mm is used to replace the grains. The measured gravity density of the sand is  $\gamma = 1.5108 \times 10^4$  N/m<sup>3</sup>, and the internal friction angle is  $\phi = 25.46^\circ$ .

#### (1) Simulation of external ring beams, internal wall, and external wall

The external ring beams are modeled by beam elements with ANSYS, and each ring beam is divided into 28 elements. The internal and external walls are modeled by the shell elements. The vertical edge length of one element is specified as 5mm. The internal wall is divided evenly into 280 elements along its circumference. The wave trough of the external wall is evenly divided into 8 elements to make their nodes coincide with the ones of the virtual beam elements that model the washer. The diagonal section between the wave crest and wave trough is divided into 4 shell elements. The wave crest is divided into 2 elements so that the node at the middle can be coupled with the corresponding node on the external ring beams.

The washers not only distribute the loads of the nuts but also provide additional thickness for the internal wall at the very region. This experimental silo model chooses washers of the thickness 1.4mm, which increases the wall thickness at the region to 3.8mm.

## (2) Boundary Conditions

The vertical and radial displacements of the internal wall, as well as the vertical displacement of the external wall are restrained at the bottom of the finite element model. This study uses shell elements to model the 14 steel angles, the bottoms of which are fixed.

## (3) Loading Mode

According to Ref. [2], the silo is a deep bin if  $h_n \geq 1.5 d_n$ , a shallow bin if  $h_n < 1.5 d_n$ , where  $h_n$  is the computed height of the grains and  $d_n$  the inner diameter of the silo. Therefore, the experimental silo model in this study is a deep bin. At the depth  $S$ , the characteristic values of the horizontal pressure and vertical friction force on the unit area of the silo wall are calculated by the following formulas respectively [2]:

$$p_{hk} = \frac{\gamma \rho}{\mu} (1 - e^{-\mu k S / \rho}) \quad (1)$$

$$p_{fk} = \mu p_{hk} \quad (2)$$


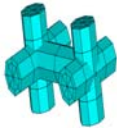


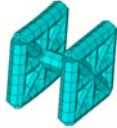

In the above formulas,  $\gamma$  is the gravity density of the grains,  $\rho$  the hydraulic radius  $\rho = \frac{d_n}{4}$ ,  $\mu$  the friction coefficient of the grains to the silo wall, and  $k$  the horizontal pressure coefficient of the grains.

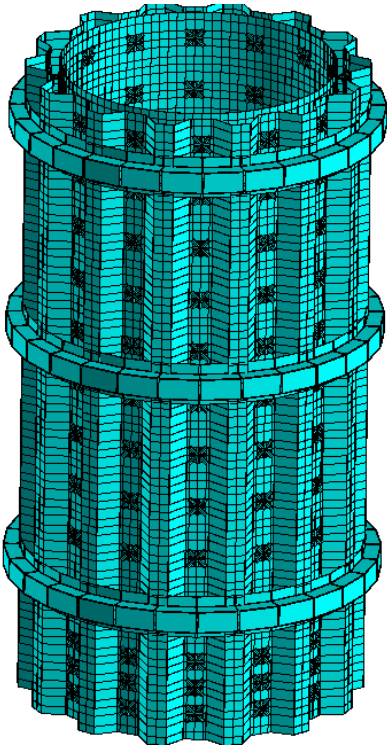
## (4) Connection model between the internal and external walls

The cooperation between the internal and external walls to resist the loads is the most noteworthy feature of the silo, therefore, the selection of the connection model between the internal and external walls is crucial.

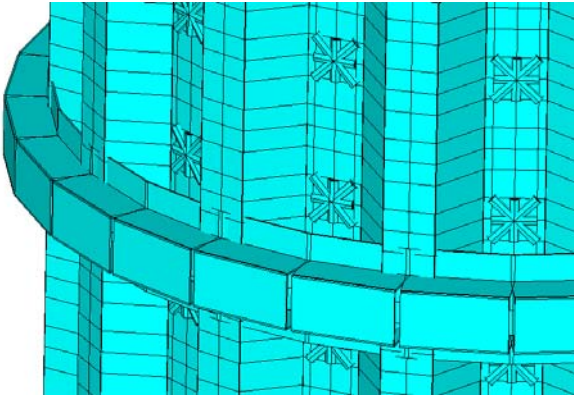
The double-head bolts are the only members transferring force between the internal and external walls. The loading process and transferring mechanism between the bolts and walls are relatively complex, which can be described by the contact nonlinearity in nature. If the contact elements are adopted, enormous work of modeling and computation will make it impractical to complete the design of the silo. To explore a simple and reliable connection model between the internal and external walls, six simulation plans (Table 1) are investigated after the actual bolt connection are carefully analyzed. In Table 1, A1 to A5 adopt the beam elements to simulate the bolts. In A1, either side of the bolt adopts only one node to connect the wall. A2 to A5 adopt different virtual beam elements to simulate the connection area between the washers and the walls. There is no need to model the bolts for A6 since it adopts the direct coupling approach.

Table 1. Six Connection Models between the Internal and External Walls

Model	A1	A2	A3	A4	A5	A6
Simulation shape	—	+	米	田	⊠	Coupling
Bolt illustration						



(a) Whole



(b) Local

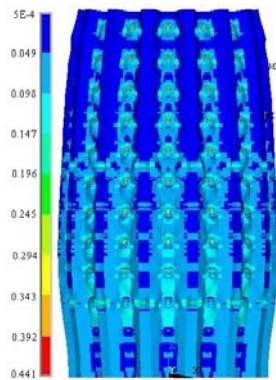
Figure 6. A3 Finite Element Model

#### 4.2.2 Results Analysis

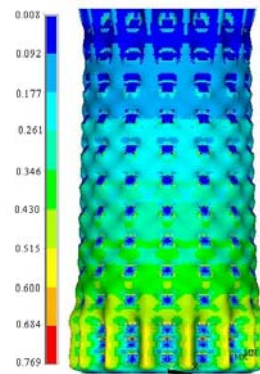
Linear elastic analyses of the six connection models are carried out. The typical Mises stress distributions of the silo walls are shown in Figure 7, and the maximum deformations are shown in Table 2.

From Table 2 and Figure 7 it is worth noting that:

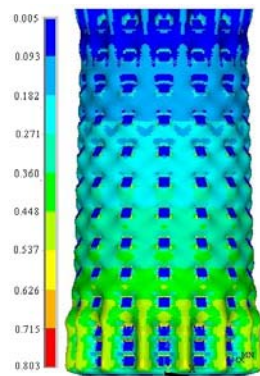
- 1) The stress and deformation of the silo walls are insignificant under the sand loads. The reason is that the silo wall thickness and the bolt diameter cannot be designed and processed with geometric similarity. Hence, a specifically designed loading plan should be adopted to increase the sand loads in the experiment. Although the absolute values of the stress and deformation are small, the relationship of the six models can still reflect some of the behavior rules of the silo.
- 2) The deformation characteristics of the six models are similar (the deformation of A3, A4 and A5 almost the same). The circumferential outward expansion of the walls is observed and the expansion near the external ring beams is relatively small. Local concave-convex deformation is also observed at the connection area between the washers and the walls and the support area.
- 3) Obvious stress concentration is seen at the support area and the connection area between the washers and the walls, however, the degree and distribution of stress concentration are quite different among the models. The most intense stress concentration of the external wall is found in A1 and the most intense stress concentration of the internal wall is found in A5. The stress distribution of the internal and external walls of A6 is the most uniform.
- 4) The circumferential deformations of the six models differ slightly yet the vertical deformations differ greatly. Of the internal walls, the maximum and minimum values of the maximum circumferential deformation are  $8.87\text{E-}04\text{mm}$  (A1) and  $7.71\text{E-}04\text{mm}$  (A6), the ratio of which is 1.15; of the external walls, the values are  $4.57\text{E-}04\text{mm}$  (A2) and  $3.74\text{E-}04\text{mm}$  (A6), the ratio 1.22. Of the internal walls, the ratio of the maximum value to the minimum value of the maximum vertical deformation is 1.68; of the external wall, the ratio is 1.56.



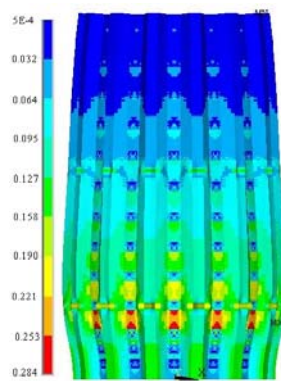
(a) A1's External wall



(b) A3's Internal wall



(c) A5's Internal wall



(d) A6's External wall

Figure 7 Typical Mises Stress Distribution of the Silo Walls (MPa)



Table 2. Maximum Deformation of the Silo Walls (mm)

Models	Internal wall		External wall	
	Circular	Vertical	Circular	Vertical
A1	8.87E-04	-8.11E-04	4.32E-04	-3.06E-04
A2	8.76E-04	-7.05E-04	4.57E-04	-3.69E-04
A3	8.67E-04	-6.77E-04	4.34E-04	-3.86E-04
A4	8.32E-04	-6.56E-04	4.06E-04	-3.71E-04
A5	8.34E-04	-6.47E-04	4.05E-04	-3.75E-04
A6	7.71E-04	-4.82E-04	3.74E-04	-4.76E-04

### 4.2.3 Bearing Patterns

Some results are obtained to further examine the bearing patterns of the internal and external walls of the six models, as shown in Table 3, Table 4 and Figure 8. In Table 3, the bearing efficiency of the horizontal pressure is defined as  $\rho_t = N_{t,I} / (N_{t,I} + N_{t,O})$ , where  $N_{t,I}$  is the hoop force of the internal wall,  $N_{t,O}$  the hoop force of the external wall in Figure 4. In Table 4, the bearing efficiency of the vertical friction force is defined as  $\rho_z = N_{z,O} / (N_{z,I} + N_{z,O})$ , where  $N_{z,I}$  is the vertical force of the internal wall,  $N_{z,O}$  the vertical force of the external wall in Figure 4. Due to the existence of supports at Z1, the results at Z1 are not taken into consideration.

Table 3.  $N_{t,I}$ ,  $N_{t,O}$  and  $\rho_t$  of Six Models

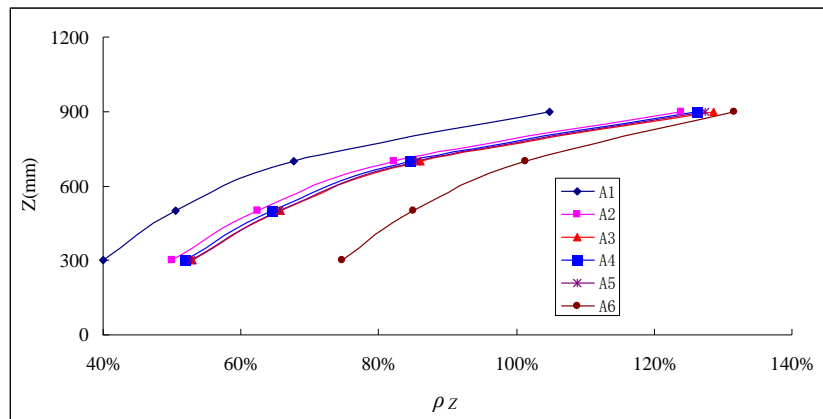
Position	A1			A2			A3		
	$N_{t,I}$	$N_{t,O}$	$\rho_t$	$N_{t,I}$	$N_{t,O}$	$\rho_t$	$N_{t,I}$	$N_{t,O}$	$\rho_t$
Z5	0.154	2.0E-04	99.9%	0.154	2.0E-04	99.9%	0.155	2.8E-04	99.8%
Z4	0.227	8.2E-04	99.6%	0.227	1.1E-03	99.5%	0.227	1.1E-03	99.5%
Z3	0.286	4.5E-04	99.8%	0.286	4.7E-04	99.8%	0.287	6.6E-04	99.8%
Z2	0.327	4.3E-04	99.9%	0.328	4.7E-04	99.9%	0.329	7.4E-04	99.8%
Position	A4			A5			A6		
	$N_{t,I}$	$N_{t,O}$	$\rho_t$	$N_{t,I}$	$N_{t,O}$	$\rho_t$	$N_{t,I}$	$N_{t,O}$	$\rho_t$
Z5	0.155	3.7E-04	99.8%	0.155	3.8E-04	99.8%	0.154	1.5E-04	99.9%
Z4	0.229	1.2E-03	99.5%	0.229	1.2E-03	99.5%	0.227	1.1E-03	99.5%
Z3	0.287	8.5E-04	99.7%	0.287	8.8E-04	99.7%	0.286	6.1E-04	99.8%
Z2	0.329	9.9E-04	99.7%	0.329	1.0E-03	99.7%	0.329	7.7E-04	99.8%

Note:  $N_{t,I}$ ,  $N_{t,O}$  in N/mm.

Table 4.  $N_{Z,I}$ ,  $N_{Z,O}$  and  $\rho_Z$  of Six Models

Position	A1			A2			A3		
	$N_{Z,I}$	$N_{Z,O}$	$\rho_Z$	$N_{Z,I}$	$N_{Z,O}$	$\rho_Z$	$N_{Z,I}$	$N_{Z,O}$	$\rho_Z$
Z5	2.8	-61.6	104.7%	14.0	-72.8	123.8%	16.8	-75.6	128.6%
Z4	-49.9	-104.3	67.7%	-27.4	-126.7	82.2%	-21.4	-132.8	86.1%
Z3	-139.4	-142.6	50.6%	-105.9	-176.1	62.5%	-96.5	-185.5	65.8%
Z2	-261.1	-173.7	40.0%	-217.2	-217.7	50.1%	-204.5	-230.3	53.0%
Position	A4			A5			A6		
	$N_{Z,I}$	$N_{Z,O}$	$\rho_Z$	$N_{Z,I}$	$N_{Z,O}$	$\rho_Z$	$N_{Z,I}$	$N_{Z,O}$	$\rho_Z$
Z5	15.4	-74.2	126.2%	16.1	-74.9	127.4%	18.6	-77.4	131.5%
Z4	-23.9	-130.3	84.5%	-22.2	-132.0	85.6%	2.1	-156.3	101.4%
Z3	-99.9	-182.1	64.6%	-97.3	-184.7	65.5%	-42.1	-239.9	85.1%
Z2	-208.9	-226.0	52.0%	-205.2	-229.6	52.8%	-110.5	-324.4	74.6%

Note:  $N_{Z,I}$ ,  $N_{Z,O}$  in N.

Figure 8.  $\rho_Z$ -Z Curves of Six Models

Note: Z is the height from the silo bottom

Results in Table 3, Table 4 and Figure 8 indicate the following conclusions:

1) The bearing patterns of the horizontal pressure of the six models are the same. The horizontal pressure is mainly resisted by the internal wall under tension, while the external wall does not resist much of the pressure. Among all the  $\rho_t$ 's of all the six models, the minimum is 99.5 % and the maximum is 99.9%. In addition, the hoop force of the external wall  $N_{t,O}$  is slightly greater at Z4, as affected by the external ring beam.

2) The bearing patterns of the vertical friction force of the six models are the same, where the vertical friction force is carried by the external wall and the internal wall together, however, the efficiency varies at different height. The bearing efficiency of the vertical friction force increases along the upward direction of the silo. It even exceeds 100% at the upper part of the silo, where the internal wall is under vertical tension. In this situation, the external wall carries all the vertical friction force while balancing the vertical tensile force of the internal wall.

3) The performances of carrying the vertical friction force of the six models vary markedly. A1 delivers the worst performance, due to that it does not take into full consideration the stiffness of the connection area, thus resulting in a weak cooperation between the internal and external walls. A6 delivers the best performance due to that it ensures the deformation consistency of the coupled nodes of the internal and external walls, thus resulting in a great cooperation. The performances of A2 to A5 are in between.

The selection of connection model between the internal and external walls has a significant impact on the structural performance of the silo. To make the optimal selection, further verification and experimental studies are needed. For more details, refer to Ref. [18].

## 5. CONCLUSION

In this paper, a double-wall steel insulation silo with multiple bolted joints for grain storage is proposed, which is designed to improve the insulation effect and mechanical behavior of the traditional silo structure. Based on the study of its structural behavior, the following conclusions can be drawn:

- 1) The silo employs the planar thin-walled steel plate as the internal wall, and the continuous ladder-shaped profiled plate as the external wall. The cavity between the internal and external walls is filled with insulation material. The silo utilizes specifically designed bolt connections to connect the internal and external walls. The silo is environmentally friendly, featured with simple structure and high integrity. The design of the silo enables it to save energy and steel consumption with a pleasant appearance. The external and internal walls can together resist the wind, snow, earthquake and grain loads and the ring beams can promote the mechanical behavior and stability of the silo.
- 2) The horizontal pressure from the grains is mainly resisted by the internal wall under tension and the vertical friction force is carried by both the external and internal walls. The external wall helps carry the vertical friction force and provides effective supports to the stability of the internal wall.
- 3) The stiffness of the connection area must be appropriately simulated and the selection of connection model between the internal and external walls has a significant impact on the structural performance of the silo. To make the optimal selection, further verification and experimental studies are needed.

## ACKNOWLEDGEMENTS

The presented work was supported by the National Natural Science Foundation of China (NO.51008067), NUAA Research Funding (NO.NS2010018), Jiangsu provincial Six Talent Peaks (NO.2010-JZ-007) and the Priority Academic Program Development (PAPD) of Jiangsu Higher Education Institutions.

## REFERENCES

- [1] Sperl, M., "Experiments on corn pressure in silo cells—translation and comment of Janssen's paper from 1895", 2006, Vol. 8, No. 3, pp. 59-65.
- [2] National Standard of the People's Republic of China, "Code for Design of Grain Steel Silos (GB 50322-2001)", Beijing, 2001.
- [3] Standards Australia, "Loads on Bulk Solids Containers (AS 3774-1990)", Sydney, 1990.
- [4] European Committee for Standardisation, "Eurocode 1: Basis of Design and Actions on Structures, Part 4: Actions in Silos and Tanks (ENV 1991-4)", Brussels, 1995.
- [5] International Organization for Standardization, "Bases for Design of Structures—Loads Due to Bulk materials (ISO 11697)", Switzerland, 1995.
- [6] American Concrete Institute, "Standard Practice for Design and Construction of Concrete Silos and Stacking Tubes for Storing Granular Materials (ACI 313-97)", Michigan, 1998.
- [7] Reimbert, M. and Reimbert, A., "Silos Theory and Practice", Trans Tech Publications, 1st ed., 1976, Clausthal, Germany.
- [8] Zhong, Z., Ooi, J.Y. and Rotter, J.M., "The Sensitivity of Silo Flow and Wall Stresses to Filling Method", *Engineering Structures*, 2001, Vol. 23, pp. 756–767.
- [9] Pincher, M. and Bridge, R.Q., "Buckling of Thin-walled Silos and Lands under Axial Load—Some New Aspects", *Journal of Structure Engineering*, 2001, Vol. 10, pp. 1129-1136.
- [10] Teng, J.G. and Chan, F., "Plastic Buckling Strength of T-section Ring Beams in Steel Silos", *Engineering Structures*, 2000, Vol. 23, No. 3, pp. 280-297.
- [11] Sadowski, A.J. and Rotter, J.M., "Buckling of Very Slender Metal Silos under Eccentric Discharge", *Engineering Structures*, 2011, Vol. 33, pp. 1187-1194.
- [12] Zhao, Y., Yu, J. and Ye, J., "Structural Behavior of Column-supported Steel Silos with Engaged Columns", *Engineering Mechanics*, 2006, Vol. 23, No. 11, pp. 63-69. (in Chinese)
- [13] Teng, J.G. and Rotter, J.M., "Collapse Behavior and Strength of Sheel Silo Transition on Junctions. Part I : Collapse Mechanics", *Journal of Structural Engineering*, 1991, Vol. 117, No. 12, pp. 3587-3604.
- [14] Laier, J.E, Cowles, G.D.E. and White, M.E., "Anatomy of Foundation Performance Involving Three Grain Silos Systematically Loaded to Impending Failure", *Research to Practice in Geotechnical Engineering Congress*, 2008, pp. 507-521.
- [15] Dogangun, A., Karaca, Z., Durmus, A. and Sezen, H.M., "Cause of Damage and Failures in Silo Structures", *Journal of Performance of Constructed Facilities*, 2009, Vol. 23, No. 2, pp. 65-71.
- [16] Sadowski, A.J and Rotter, J.M., "Steel Silos with Different Aspect Ratios: II—Behaviour under Eccentric Discharge", *Journal of Constructional Steel Research*, 2011, Vol. 67, pp. 1545-1553.
- [17] Yin, L.F., Tang, G., Zhu, X.P. and Yao, Z.S., "A Double-wall Steel Insulation Silo", People's Republic of China Ministry of Construction: ZL201010106084.9, 2012.1.18. (in Chinese)
- [18] Tang, G., Yin, L.F, Guo, X.M. and Lai, H.B., "Research on a New Double-Wall Steel Insulation Silo with Multiple Bolted Joints: Part II, Experimental Verification". *Advanced Steel Construction*, 2013, Vol. 9, No. 4, pp. 383-394.

# RESEARCH ON A NEW DOUBLE-WALL STEEL INSULATION SILO WITH MULTIPLE BOLTED JOINTS: PART II, EXPERIMENTAL VERIFICATION

Gan Tang<sup>1,2</sup>, Lingfeng Yin<sup>2,\*</sup>, Xiaoming Guo<sup>2</sup> and Haibin Lai<sup>2</sup>

<sup>1</sup> *Department of Civil Engineering, Nanjing University of Aeronautics and Astronautics,  
YuDao Street 29, Nanjing, China, 210016*

<sup>2</sup> *School of Civil Engineering, Southeast University, SiPaiLou 2, Nanjing, China, 210096*  
*\*(Corresponding author: Email: eking@seu.edu.cn)*

*Received: 26 September 2011; Revised: 21 January 2012; Accepted: 28 January 2012*

**ABSTRACT:** An experimental model of a double-wall steel insulation silo with multiple bolted joints is designed. The experiment results and the finite element results are compared and analyzed, and the following conclusions are reached. The cooperation between the internal and external walls is outstanding. Among the six proposed models, A3, A4 and A5 present almost the same results, which satisfyingly coincide with the experiment results. The horizontal pressure is mainly resisted by the internal wall under tension during the whole loading process. Before the force  $P$  reaches  $P_{u-in}$ , the vertical friction force is carried by both the internal and external walls. When the force  $P$  reaches  $P_{u-in}$ , the internal wall at the area between the first external ring beam and the supports shows a sudden elastic-plastic buckling. After that, the external wall bears more and more vertical friction force, then it also shows an elastic-plastic buckling at the same area. Finally, the walls at this area are destroyed and the model loses the bearing capability.

**Keywords:** Steel insulation silo; double-wall; experiment; cooperation between the internal and external walls; elastic-plastic buckling

## 1. INTRODUCTION

In the former paper [1], a new double-wall steel insulation silo with multiple bolted joints for grain storage is proposed. The silo employs the planar thin-walled steel plate as the internal wall, and the continuous ladder-shaped profiled plate as the external wall. The cavity between the internal and external walls is filled with insulation material. The silo utilizes specifically designed bolt connections to connect the internal and external walls. The silo is environmentally friendly, featured with simple structure and high integrity. The design of the silo enables it to save energy and steel consumption with a pleasant appearance. An experimental silo model is studied and the results show that the horizontal pressure from the grains is resisted by the internal wall under tension, and that the vertical friction force is mainly carried by both the external and internal walls. The stability of the internal wall is effectively provided by the external wall. The stiffness of the connection area must be appropriately simulated and the selection of connection model between the internal and external walls has a significant impact on the structural performance of the silo. Based on the above, this paper designs the experimental silo model and examines its structural behavior. The experiment results and the finite calculation results are compared and analyzed to make an optimal selection of connection model between the internal and external walls. The bearing patterns during the whole loading process are also researched.

Brown et al. described the design, conduct and verification of a series of experiments on a square planform funnel-flow unstiffened steel silo containing free-flowing granular solids [2]. The results of model tests with a steel silo at the University of Karlsruhe are summarised by Tejchman and Ummenhofer [3]. The results of five tests on cone-cylinder-skirt-ring junctions under simulated bulk solid loading were presented by Zhao and Teng [4] and the finite element modeling of the experiments was given in the companion paper [5]. Yin and Huang performed dynamic experiments of thin-walled silo models on different foundations [6]. Zhang and Shu conducted a discharging

experiment for floor-type steel silo model, in which time-dependent stresses of silo walls with 8 different discharge opening diameters and positions were studied [7]. The plans and results of the above researches have provided valuable insights into the design and study in this paper.

## 2. MODEL EXPERIMENT OF STEEL INSULATION SILO

### 2.1 Model Design and Manufacture

The internal diameter and the height of the experimental silo model are 500mm and 1200mm respectively. The spacing between the internal and external walls is 25mm. Three external ring beams are set at the height of 250mm, 750mm and 1105mm respectively. The external wall uses the YX 35-125-750 profiled steel plate, and the internal wall is a circular plate, the thickness of both walls 1mm. The 8-mm-diameter double-head bolts that connect the internal and external walls are placed with the vertical spacing of 100mm and are evenly spaced around a circle. The internal wall, external wall and external ring beams are all spliced by the high-strength bolts. Dry yellow sand of diameter less than 0.25mm is used to replace the grains. To avoid leaking of the sand, this design employs a bottom plate of diameter 640mm for the experimental silo model. 14 steel angles are welded by one leg on the bottom plate. The other legs are between the internal and the external walls and are connected with them by three rows of bolts. The completed experimental silo model is shown in Figure 1.

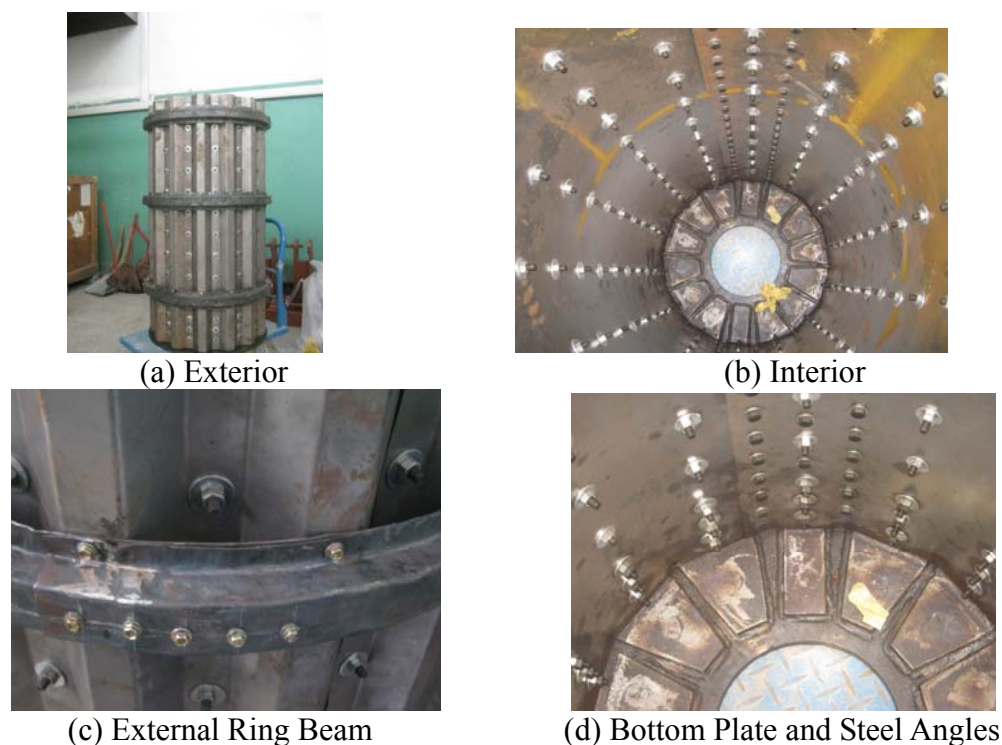


Figure 1. The Completed Experimental Silo Model

### 2.2 Basic material properties

The screened sand is quickly dried in a drier. The average gravity density of the sand  $\gamma = 1.5108 \times 10^4 \text{ N/m}^3$  is obtained after the sand volume and quality are measured by a graduated cylinder and electronic balance. The average internal friction angle of the sand  $\phi = 25.46^\circ$  is obtained by a direct shear apparatus.

From the material experiments by an universal testing machine, the elastic modulus of steel plate is obtained as  $E=1.90\times10^5$  MPa , the yield strength  $f_y=195$  MPa , the ultimate strength  $f_u=247$ MPa, the initial yield strain  $\varepsilon_y=1.0263\times10^{-3}$ , the strain at initial strengthening  $\varepsilon_{st}=4.292\times10^{-3}$  and the ultimate strain  $\varepsilon_u=9.292\times10^{-3}$ .

### 2.3 Loading and Measurement Plans

#### (1) Loading Plan

The sand loads are too small to destroy the silo or cause an obvious strain of the silo walls [1]. Therefore, the original loads from the sand are ignored and a force transmission device, which is composed of an upper plate, a steel tube and a lower plate, is installed above the model to evenly apply the force  $P$  from the press machine to the sand in the model, as shown in Figure 2.

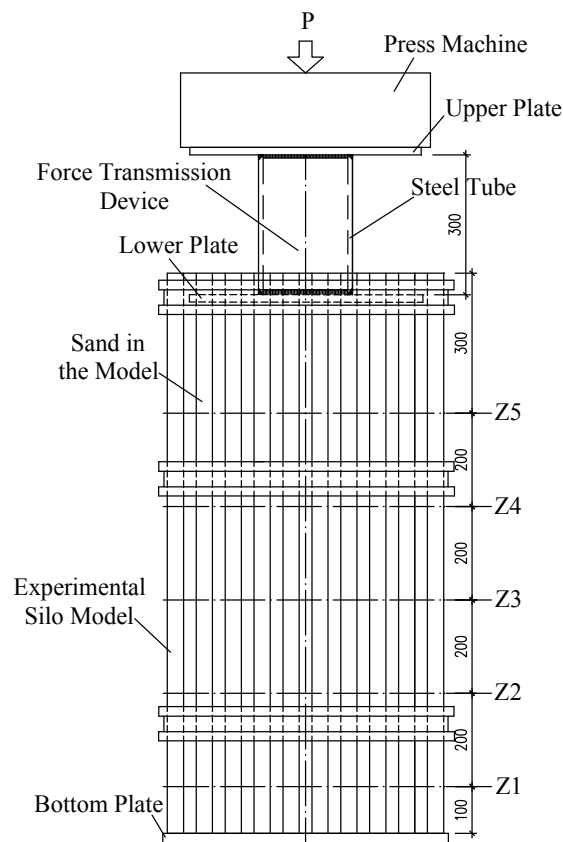


Figure 2. Loading Plan



Figure 3. Protection of Pressure Cells and Strain Gauges

## (2) Horizontal Pressure Measurement

Pressure cells are used to measure the horizontal pressure from the sand to the internal wall. The pressure cells are placed at Z1 to Z5, the same heights as the strain observation points. Plastic boxes are used to fix and protect the pressure cells during the loading process (Figure 3). Glass adhesive is used to seal the plastic box to avoid the leaking-in of the sand that can interfere with data collection.

## (3) Strain Measurement

Along the circles at Z1 to Z5, right angle strain rosettes are attached to the interior surface of the internal wall to measure the horizontal and vertical strains, as shown in Figure 4(a). Similarly, in Figure 4(b), vertical strain gauges are attached to the exterior surface of the external wall. Note that some vertical strain gauges are replaced with right angle strain rosettes at Z3 to Z5, and that the positions of some strain observation points on the external wall are slightly adjusted due to the existence of the bolts.

## (4) Deformation Measurement

A displacement meter is set at every 200mm along the vertical direction to measure the deformation of the external wall and a displacement meter is set on each of the three external ring beams.

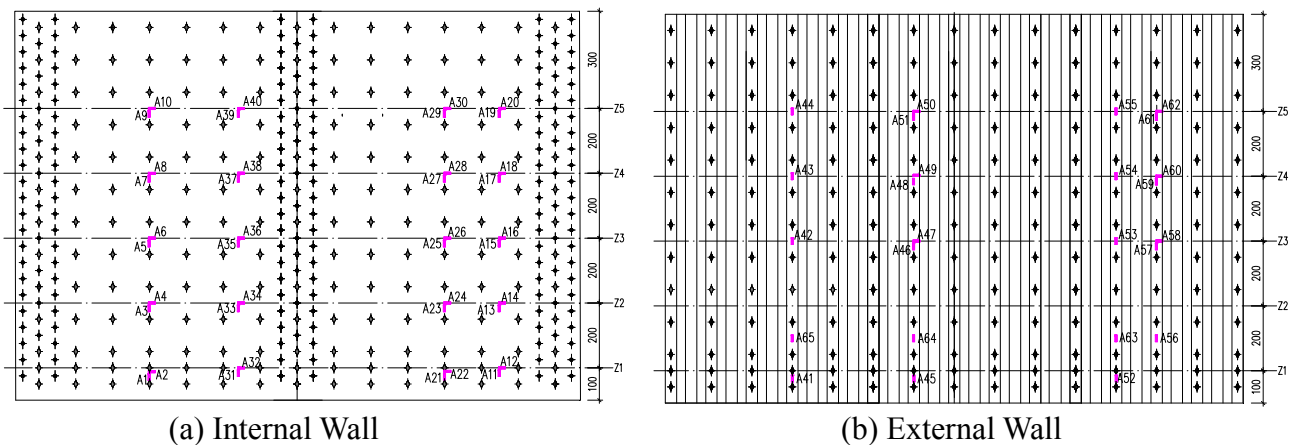


Figure 4. Strain Observation Points on the Internal and External Walls

## 2.4 Experiment Process and Results

First, the strain gauges, strain rosettes and pressure cells are connected by wires to two DH3816 static strain collecting instruments and their proper operation states are checked. Then the dried yellow sand is charged into the model. After that, the force transmission device is hoisted and then placed on the sand. It has to be checked that the wires are not pressed by the force transmission device. The model is lifted onto a steel platform. A pressure sensor between the press machine and force transmission device and the displacement meters are placed and then connected to the static strain collecting instruments. For the site ready for the experiment, see Figure 5.

An actual loading is performed level by level after three pre-loadings, each level increasing 5KN from the previous level. The strain, deformation, force P and horizontal pressure at each level are synchronously collected.



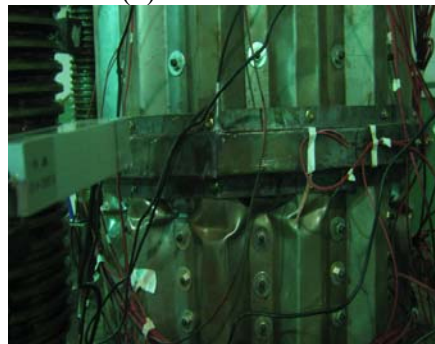
A slight noise, which is created by the sand being squeezed against the internal wall, is heard at the initial loading stage. As the force  $P$  increases, the horizontal and vertical strains of the internal wall are increased apparently, and so is the vertical strain of the external wall, yet the horizontal strain of the external wall is not noticeably increased. When the force  $P$  is increased to around 300kN, slight wrinkles occur on the external wall between first external ring beam and the supports. With the force  $P$  increased further, the wrinkled area expands. When the force  $P$  reaches 410kN, the model loses its bearing capacity. The failure mode is shown in Figure 6 and the specific data is given in section 3.2 and 3.3.



Figure 5. Experiment Site



(a) Internal Wall



(b) External Wall

Figure 6. Failure Mode of the Experimental Silo Model

### 3. NONLINEAR FINITE ELEMENT ANALYSIS

#### 3.1 Finite Element Modeling

To compare with the experiment results, the geometrical and material nonlinear analysis of the FE model is carried out, where the modeling of the internal wall, external wall, external ring beams, boundary conditions and the connection models between the internal and external walls are the same as in Ref.[1] while the material constitutive relation and loading mode are obtained from the experiment.

##### (1) Material Constitutive Relation

A trilinear model is achieved from the simplification of results of the material experiment, as shown in Figure 7, where  $f_y = 195\text{MPa}$ ;  $f_u = 247\text{MPa}$ ,  $\varepsilon_y = 1.0263 \times 10^{-3}$ ,  $\varepsilon_{st} = 4.292 \times 10^{-3}$ ,  $\varepsilon_u = 9.292 \times 10^{-3}$ .

##### (2) Loading Mode

During the loading process, the horizontal pressures at Z1 to Z5 of the internal wall, measured by the pressure cells, basically take the form of linear growth, as shown in Figure 8. To facilitate calculation, linear regression is used for the data in Figure 8 and the results in Figure 9 are obtained, based on which the horizontal pressures at other heights are achieved by linear interpolation. The vertical friction force is the horizontal pressure (at the same height) multiplied by the friction coefficient  $\mu$  and  $\mu = 0.4$ . In the FE model, all the loads are applied to the nodes of the internal wall.

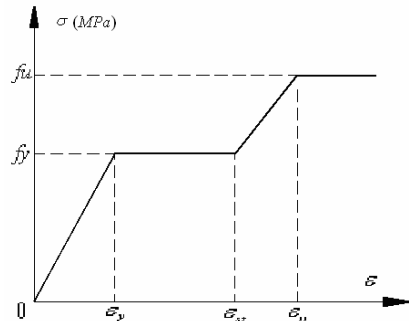


Figure 7. Material Constitutive Relation

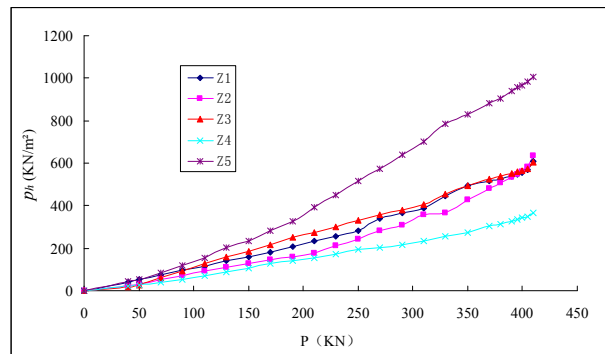


Figure 8. Horizontal Pressures by Pressure Cells

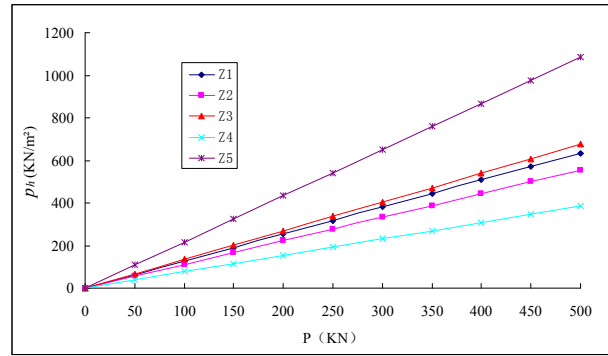


Figure 9. Horizontal Pressures after Linear Regression

### 3.2 Results Analysis

Nonlinear analysis of six connection models A1 to A6 (Ref.[1]) are conducted. The typical values of the force  $P$  are listed in Table 1, where  $P_{y-in}$  and  $P_{y-ex}$  are the respective values of the force  $P$  when the maximum Mises stresses of the internal and external walls reach the yield strength (195 MPa),  $P_{u-in}$  and  $P_{u-ex}$  the respective values of the force  $P$  when the maximum Mises stresses of the internal and external walls reach the ultimate strength (247 MPa); “—” indicates that the ultimate strength is not reached;  $P_{max}$  is the value of the force  $P$  when the model loses its bearing capacity. The typical Mises stress distributions of the internal and external walls are shown in Figure 10. The typical maximum deformations are shown in Table 2.

In Table 1,  $P_{y-in}$  and  $P_{y-ex}$  of the experiment are the respective values of the force  $P$  when the maximum stresses measured on the internal and external walls reach the yield strength. Given the limited number of strain observation points, the experiment results cannot reflect the entire strain distribution of the internal and external walls, especially that of the stress concentration region. Hence,  $P_{y-in}$  and  $P_{y-ex}$  of the experiment are larger than the actual values. For the same reason,  $P_{u-in}$  and  $P_{u-ex}$  of the experiment cannot be determined but it does not indicate that the maximum Mises stresses of the internal and external walls do not reach the ultimate strength during the loading. However,  $P_{max}$  of the experiment is an actual value.

Table 1. Typical Values of Force  $P$  /kN

	A1	A2	A3	A4	A5	A6	Experiment
$P_{y-in}$	180.0	150.0	160.0	160.0	160.0	290.0	<b>205.0</b>
$P_{y-ex}$	200.0	280.0	225.0	220.0	220.0	360.0	<b>310.0</b>
$P_{u-in}$	—	—	324.0	322.8	336.9	472.8	—
$P_{u-ex}$	—	—	418.8	414.9	417.1	488.1	—
$P_{max}$	282.1	311.1	434.0	433.6	433.7	488.1	410.0

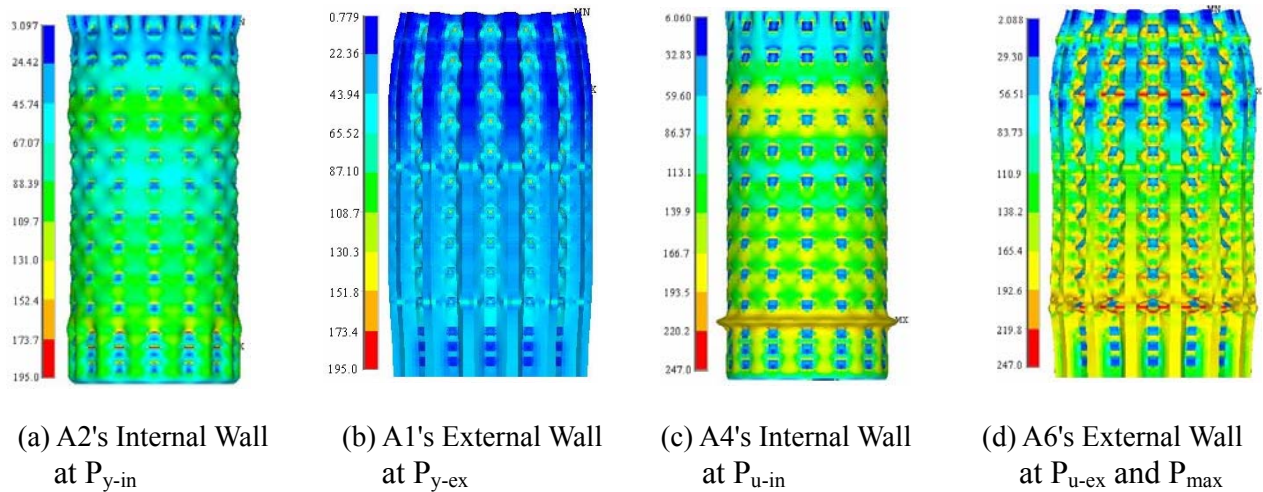


Figure 10. Typical Mises Stress Distribution of the Silo Walls (MPa)

Table 2. Typical Maximum Deformations (mm)

Models	$P_{y-in}$				$P_{y-ex}$				$P_{max}$			
	Internal Wall		External Wall		Internal Wall		External Wall		Internal Wall		External Wall	
	Circular	Vertical	Circular	Vertical	Circular	Vertical	Circular	Vertical	Circular	Vertical	Circular	Vertical
A1	0.012	-0.334	0.026	-0.119	0.013	-0.372	0.028	-0.133	0.018	-0.544	0.040	-0.194
A2	0.011	-0.241	0.023	-0.119	0.020	-0.457	0.044	-0.227	0.022	-0.523	0.050	-0.260
A3	0.011	-0.248	0.025	-0.133	0.016	-0.357	0.036	-0.192	0.068	-1.748	0.432	-0.875
A4	0.011	-0.241	0.024	-0.129	0.015	-0.332	0.033	-0.178	0.068	-1.727	0.423	-0.855
A5	0.011	-0.238	0.024	-0.130	0.015	-0.328	0.033	-0.180	0.068	-1.753	0.480	-0.896
A6	0.007	-0.337	0.045	-0.318	0.009	-0.425	0.057	-0.399	0.041	-0.952	0.195	-0.913

It can be seen from Table 1, Table 2 and Figure 10 that:

1) The bearing processes of the six models are similar because the material constitutive relation, simulation of silo walls and ring beams, boundary conditions, loading mode and finite element analysis are identical. At the initial loading stage, the circumferential outward expansion is observed and obvious stress concentration is seen at the support area and the connection area between the washers and the walls. With the force  $P$  increasing, the maximum Mises stress of the internal wall reaches the yield strength and then that of the external wall does. As the force  $P$  is further increased, the yield area of the internal wall gradually expands, especially the area near Z5 and the area between the first external ring beam and the supports, then a sudden buckling at the latter area occurs. After that, at the area between the first external ring beam and the supports in all six models except A1 and A2, the maximum Mises stress of the internal wall rapidly reaches the ultimate strength, and the yield area of the external wall further expands and then a buckling also occurs, next, the maximum Mises stress of the external wall reaches the ultimate strength. Finally, the walls at this area are destroyed and the model loses the bearing capability.

2) The typical values of the force  $P$  of the six models vary significantly.  $P_{y-in}$  of A1 to A5 are similar but much smaller than that of A6. The differences among  $P_{y-ex}$  of A1 to A5 are enlarged and  $P_{y-ex}$  of A1 to A5 are also much smaller than that of A6.  $P_{u-in}$  and  $P_{u-ex}$  of A1 and A2 do not exist while  $P_{u-in}$  and  $P_{u-ex}$  of A3 to A5 are much smaller than that of A6.  $P_{max}$  of A1 is the smallest,  $P_{max}$  of A6 the largest, and  $P_{max}$  of A2, A3, A4 and A5 are in between.

$P_{\max}$  of A1 and A2 are much smaller than  $P_{\max}$  of the experiment due to that they do not take into full consideration the stiffness of the connection area. A6 ensures the deformation consistency of the coupled nodes of the internal and external walls, which overestimates the cooperation between the internal and external walls, so  $P_{\max}$  of A6 exceeds  $P_{\max}$  of the experiment by about 20% and  $P_{y-in}$  and  $P_{y-ex}$  are larger than those of the experiment. The differences among all the typical values of the force  $P$  of A3, A4 and A5 are insignificant.  $P_{\max}$  of A3, A4 and A5 differ slightly from  $P_{\max}$  of the experiment (less than 6%), and  $P_{y-in}$  and  $P_{y-ex}$  of A3, A4 and A5 are fairly reasonable. Therefore, A3, A4 and A5 can effectively reflect the cooperation between the internal and external walls.

3) The overall stress distributions and deformation characteristics of the six models under typical values of the force  $P$  are similar due to their similar bearing processes, but the details vary. Before the force  $P$  reaches  $P_{y-in}$ , the differences among the circular stresses and deformations of A1 to A5 are insignificant while the differences among the vertical values are significant, however, both circular and vertical values are significantly different from those of A6. After the force  $P$  exceeds  $P_{y-in}$ , the stress and deformation differences between A1/A2 and A3/A4/A5 are exaggerated, yet all the stresses and deformations of the five models still differ greatly from those of A6. During the whole loading process, the stresses and deformations of A3, A4, and A5 are almost the same.

### 3.3 Further Comparison between A3 Results and Experiment Results

The A3 results and experiment results are further compared as shown in Figure 13 and 14.

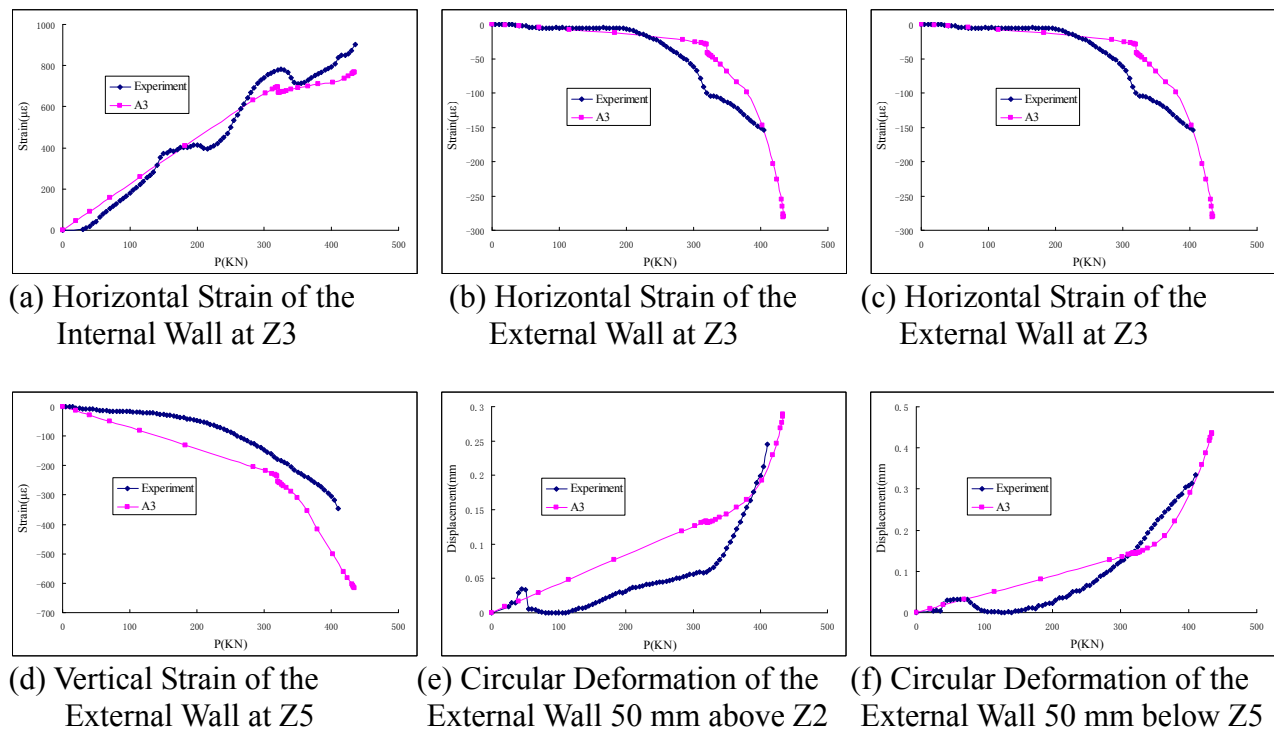
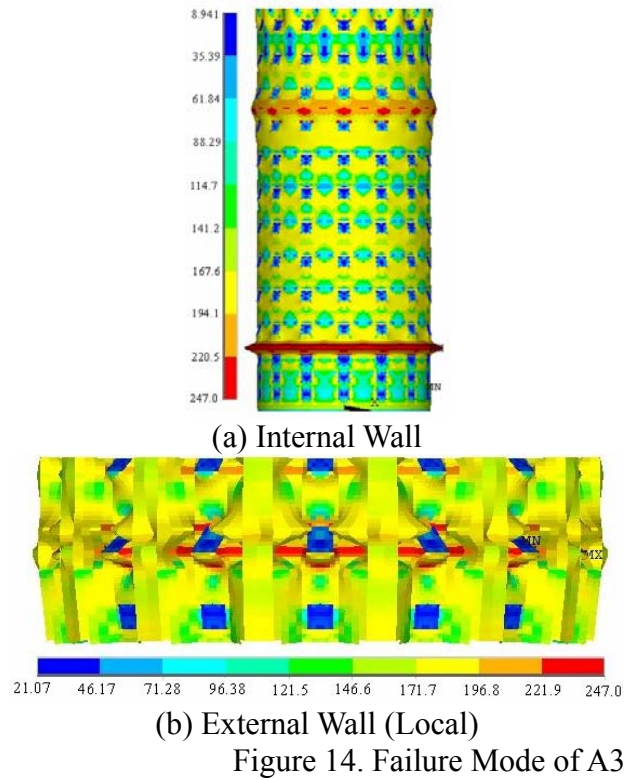


Figure 13. Comparison between A3 Results and Experiment Results

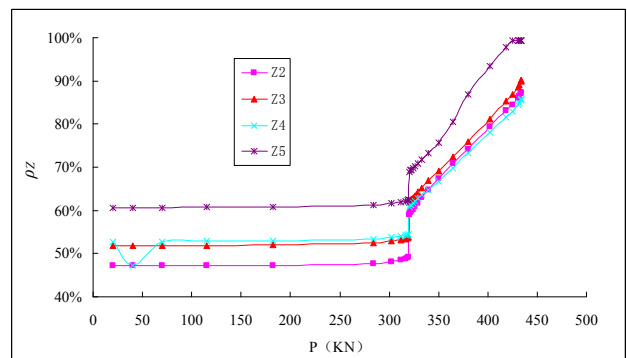
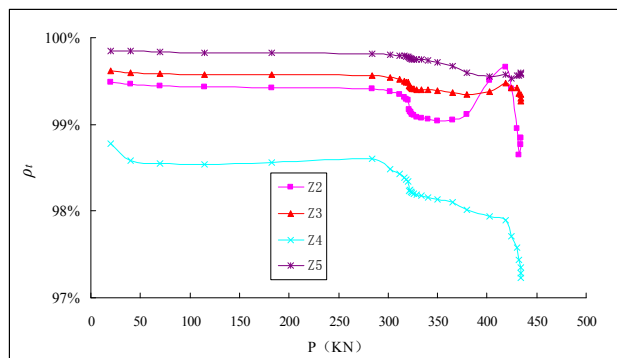


From the results in Figure 6, Figure 13 and Figure 14 it is worth noting that:

- 1) During the loading process, both the internal and external walls generally undergo circular tensions and vertical pressures. The vertical strain of the external wall is smaller than that of the internal wall. Due to the existence of the external ring beams, local area of the external wall undergoes a circular pressure.
- 2) The strain, deformation, failure mode of A3 are consistent with those of the experiment, indicating that A3 is a reasonable connection model.

### 3.4 Bearing Patterns during the Loading Process

Some results of A3 are obtained to examine the bearing patterns of the internal and external walls during the loading process, as shown in Figure 15 and Figure 16.



Note: for the definition of  $\rho_t$  and  $\rho_z$ , refer to Ref.[1]



It can be indicated from Figure 15 and 16 that:

- 1) During the loading process, the pattern of resisting the horizontal pressure remains the same, where the horizontal pressure is mainly resisted by the internal wall under tension while the external wall does not resist much of the pressure.  $\rho_t$ , the bearing efficiency of the horizontal pressure, exceeds 97% at each height during the loading process. All the  $\rho_t$  increase slightly along the upward direction of the silo, except that at Z4, where the hoop force of the external wall  $N_{t,o}$  is slightly greater as affected by the external ring beam.  $\rho_t$  at each height remains unchanged before the force P reaches  $P_{u-in}$ , after that, it slightly drops.
- 2) Before the force P reaches  $P_{u-in}$ ,  $\rho_z$ , the bearing efficiency of the vertical friction force, basically remains unchanged at each height. All the  $\rho_z$  increase slightly along the upward direction of the silo, the values between 47% and 63%. These indicate that the pattern of carrying the vertical friction force remains the same, where the vertical friction force is carried by both the internal and external walls. When the force P reaches  $P_{u-in}$ ,  $\rho_z$  sees a dramatic increase because a sudden elastic-plastic buckling of the internal wall sharply decreases its capacity of carrying the vertical friction force. After that, the external wall bears more and more vertical friction force, thus  $\rho_z$  increasing sharply.
- 3) Compared with Ref. [1], in this paper, the increasing rate of  $\rho_z$  along the upward direction of the silo at the initial loading stage is smaller. The major reason is that the loading modes in the two papers are different, as shown in Figure 17. Thus the loading mode has a great impact on the bearing pattern of the vertical friction force.

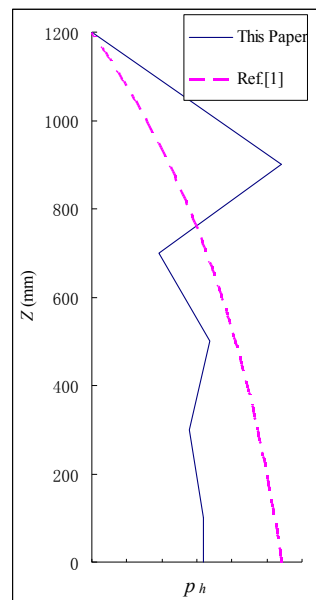


Figure 17. Comparison of the Loading Modes

#### 4. CONCLUSIONS

In this paper, an experimental model of a double-wall steel insulation silo with multiple bolted joints is designed. An experiment is carried out to get its strain, deformation, horizontal pressure, ultimate bearing capacity and failure mode. The experiment plan and results may shed light on future studies of steel insulation silo. Based on the experimental and numerical study, the following conclusions can be drawn:

1) The cooperation between the internal and external walls is outstanding. Among the six proposed models, A3, A4 and A5 present almost the same results during the whole loading process. Their strain, deformation, failure mode are consistent with those of the experiment, indicating they are all reasonable connection models. A3 is recommended due to its simplicity in modeling and calculation.

2) The pattern of resisting the horizontal pressure keeps unchanged during the loading process, where the horizontal pressure is mainly resisted by the internal wall under tension while the external wall does not resist much of the pressure.

3) Before the force  $P$  reaches  $P_{u-in}$ , the pattern of carrying the vertical friction force remains the same, where the vertical friction force is carried by both the internal and external walls. When the force  $P$  reaches  $P_{u-in}$ , a sudden elastic-plastic buckling of the internal wall at the area between the first external ring beam and the supports sharply decreases its capacity of carrying the vertical friction force. After that, the external wall bears more and more vertical friction force, then it also shows an elastic-plastic buckling at the same area. Finally, the walls at this area are destroyed and the model loses the bearing capability.

## ACKNOWLEDGEMENTS

The presented work was supported by the National Natural Science Foundation of China (NO.51008067), NUAU Research Funding (NO.NS2010018), Jiangsu provincial Six Talent Peaks (NO.2010-JZ-007) and the Priority Academic Program Development (PAPD) of Jiangsu Higher Education Institutions.

## REFERENCES

- [1] Yin, L.F, Tang, G., Guo, X.M. and Lai, H.B., "Research on a New Double-Wall Steel Insulation Silo with Multiple Bolted Joints: Part I, Structure System". *Advanced Steel Construction*, 2013, Vol. 9, No. 4, pp. 369-382.
- [2] Brown, C.J., Lahlouh, E.H. and Rotter, J.M., "Experiments on a Square Planform Silo", *Chem Engng Sci.*, 2000, Vol. 55, No. 20, pp. 4399-4413.
- [3] Tejchman, J. and Ummenhofer, T., "Bedding Effects in Bulk Solids in Silos: Experiments and a Polar Hypoplastic Approach", *Thin-Walled Structures*, 2000, Vol.37, pp.333-361.
- [4] Zhao, Y. and Teng, J.G., "Buckling Experiments on Steel Silo Transition Junctions, I: Experimental Results", *Journal of Constructional Steel Research*, 2004, Vol. 60, pp. 1783-1801.
- [5] Zhao, Y. and Teng, J.G., "Buckling Experiments on Steel Silo Transition Junctions. II: Finite Element Modeling", *Journal of Constructional Steel Research*, 2004, Vol. 60, pp.1803-1823.
- [6] Ying, G.S. and Huang, Y., "An Experimental Study on the Vibration Characteristics of Thin-walled Silo Models", *Journal of Experimental Mechanics*, 2002, Vol. 17, No. 2, pp. 191-199. (in Chinese)
- [7] Zhang, C. and Shu, G.P., "Experimental Research of Ground-supported Steel Silo Model's Discharge", *Journal of Southeast University (Natural Science Edition)*, 2009, Vol. 39, No. 3, pp. 531-535. (in Chinese)